Neutral Particle Detection Methods Using Noble Gases in LAGUNA-LBNO and MODES-SNM

Thesis submitted in accordance with the requirements of
the University of Liverpool for the degree of Doctor in Philosophy

by

Thomas Michael Stainer

Oliver Lodge Laboratory,

University of Liverpool

July 2015

Abstract

Neutral particles, particularly neutrons, gammas and neutrinos are difficult to detect and measure due to their lack of electric charge. Noble fluids are a powerful medium when detecting such particles due to their ability to collect charge and scintillation light. The LAGUNA-LBNO and MODES-SNM projects are two independent projects that focus on using this concept to detect neutral particles of interest. The two projects are consecutively discussed in this thesis.

A study on a potential near detector design to be used within the proposed LAGUNA-LBNO experiment is presented. We introduce a novel design for the near detector based on a pressurised gas Argon TPC at 20 bar surrounded by layers of plastic scintillator, encompassed in a pressurised gas chamber. Monte Carlo studies form the basis of the study with focus on detector interaction rates and assessment of the basic detector properties and parametrisation. Based on a $2 \times 2 \times 2 \times$ m^3 TPC we estimate 0.1785 ± 0.0003 (stat) ν p.p.p interactions for a 400 GeV neutrino beam in positive focusing and 0.0628 ± 0.0002 (stat) ν_μ p.p.p interactions for energies 0-10 GeV in a $1.8 \times 1.8 \times 1.8 \times$ m^3 fiducial volume. Conversely we can expect high muon backgrounds in the TPC at 44.5 ± 0.5 μ (stat) p.p.p, arising from neutrino interactions with external detector components (non TPC) and surrounding rock interactions. With the inclusion of the muons arising from the beam directly at 70 p.p.p (estimated) we can expect $\sim$1-2 μ tracks in the TPC / 700 cm^2 / spill.

Within the MODES-SNM section of the thesis a prototype system is designed, tested and analysed using ^{4}He, instead of the commonly favourable ^{3}He, for fast neutron detection. A neutron-gamma discrimination analysis is performed based on a pulse shape discrimination technique from the collected scintillation light of PuBe and ^{60}Co sources in laboratory conditions. For high levels of gamma contamination (up to 76%) detection efficiencies exceeding 96% can be achieved with the prototype system while maintaining reasonable false alarm rates (< 1 per hour).

Acknowlegements

I would like to firstly acknowledge my supervisors, Dr Neil McCauley and Dr Jon Coleman, for their wealth of knowledge on the subject of neutrinos and particle physics. You have provided me with much needed help though the entirety of my PhD. I would also like to thank the neutrino group, especially Prof. Christos Touramanis, for his wisdom and guidance throughout my PhD. The neutrino weekly meetings were an important date in my calendar and although they often ran far too long they were key in helping me resolve some problems along the way.

Fellow PhD students, both young and old, too many to name here but a few who made it an enjoyable experience, thanks Mike, Allan, Adrian, Oliver, Matt, Rob, John, Aaron, James, Abdi, Graham. Also some notable thanks to the post doctoral community at Liverpool: George, Matt, Steve, Joe, Kostas.

I would also like to acknowledge the Hep football team for the enjoyable but sometimes dangerous weekly football games that helped me survive the tough weeks at work. However it leaves me with some regret that over the three years we did not win the Bubble Chamber tournament, but playing in the final gives me some solace.

Of course this thesis would never have happened if it was not for the support of my family and my girlfriend Els, thank you.

Declaration

I declare that the work presented in this thesis is my own, other than where clearly stated. The work done by others has been explicitly referenced accordingly, this includes passages of text, figures, plots and images. Some of this work has been the result of collaborative work and all participants have been identified within this thesis.

Chapters 1 and 2 describe the history, background and theoretical motivation for the subject of this thesis. These chapters are then a summary of the vast amount of work conducted by others, gathered from scientific journals, papers, documents and published books, which have been referenced accorindinly.

Chapters 3 and 4 then focus on the LAGUNA-LBNO project and its aims, development and work, with the latter chapter focusing on the near detector within LAGUNA-LBNO. The work has been conducted within the collaboration, with the published work and internal documents referenced when applicable. Chapter 4 involves a smaller collaborative effort within LAGUNA-LBNO, in which I have contributed significantly.

Chapter 5 represents the analysis work regarding the near detector within LAGUNA-LBNO. This chapter describes the simulation framework, the detector geometry design and modelling, simulation studies and data analysis. I made significant contributions to the software framework as one of two main developers and I also made major contributions to the detector design. The rest of the work in the chapter, involving the modelling and analysis, represents my effort and work. An introductory background is presented at the start of this chapter motivating Monte Carlo simulations and describes the third party software used, all of which is referenced accordingly. This work has been presented to the collaboration internally, represented in internal documents and presented outside the collaboration to members of the scientific community.

Chapter 6 presents the MODES-SNM project in a similar fashion to chapter 3, where it represents the work of the MODES-SNM collaboration. The work shown in this chapter is a summary of published work and internal documents from members

of the collaboration. These have been referenced accordingly and members are noted in this chapter.

Chapter 7 describes the detectors and the integration of the MODES-SNM system. Much of this work was conducted at the University of Liverpool, where I made significant contributions to the design, construction and integration of the system. The majority of the work conducted by myself is represented by the simulation studies and the integration.

Chapter 8 describes the MODES-SNM system demonstrations in various locations across Europe in a real life environment. For all the demonstrations described in the chapter I was only present for one, the demonstration at London Heathrow Airport, which I was significantly involved in the majority of the data collection and the demonstration report. Other demonstrations described in this chapter are based on shared collaboration documents and files.

Chapter 9 forms the MODES-SNM analysis chapter, which presents my analysis framework and implementation. The data used was collected by other members of the MODES-SNM collaboration and was shared within the group. This has been referenced. The initial part of the chapter presents the work conducted by other members of the MODES-SNM collaboration used to motivate the remaining part of the chapter and is necessary for the analysis. This first section is based on internal documents within the collaboration and is explicitly stated so in the chapter, referenced accordingly.

Thomas Michael Stainer
July 2015

Glossary of Terms

- CC - Charge Current
- CPV - Charge Parity Violation
- CCQE - Charge Current Quasi Elastic
- DIS - Deep Inelastic Scattering
- FAR - False Alarm Rate
- FD - Far Detector
- FND - Fast Neutron Detector
- FSPL - Final State Primary Lepton
- FSS - Final State Secondaries
- FWHM - Full Width Half Maximum
- GAr - Gas Argon
- HPGe - High Purity Germanium
- IAEA - International Atomic Energy Agency
- IEC - International Electrotechnical Commission
- IH - Inverted Hierarchy
- IND - Improvised Nuclear Device
- LAr - Liquid Argon
- MC - Monte Carlo

- MPPC - Multi Pixel Photon Counter
- NC - Neutral Current
- ND - Near Detector
- NF - Negative Focusing
- NH - Normal Hierarchy
- NORM - Naturally Occurring Radioactive Material
- PDG - Particle Data Group code
- PF - Positive Focusing
- PMT - Photo Multiplier Tube
- p.o.t - protons on target
- ppp - per proton pulse
- PSD - Pulse Shape Discrimination
- RES - Resonance
- RPM - Radiation Portal Monitor
- SND - Slow Neutron Detector
- SNM - Special Nuclear Material
- TAS - Totally Active Scintillator
- TPC -Time Projection Chamber
- WLS - WaveLength Shifter

Contents

Chapter 1

Introduction

The issue of neutral particle detection is one that can be very problematic and concerns both LAGUNA-LBNO and MODES-SNM. Photons, neutrons and neutrinos collectively form the family of particles of interest. They are introduced sequentially in this chapter to motivate their relevance in these two disparate and apparently unrelated projects.

1.1 Neutral Particles

Particles pertaining no net electrical charge are considered neutral. Neutrons, gammas and neutrinos are all stable or long-lived neutral particles. Although their difficulty in detection can be troublesome it is also what makes them very attractive to study. This family of particles will not leave tracks in ionisation detectors and poses the ability to pass through materials unscathed. Such a property is useful for monitoring systems that cannot be physically examined and allows for non intrusive methods in detection. Examples of this are reactor monitoring using neutrinos [1] and radiation monitoring using neutrons and gammas [2]. The former is a modern idea proposed and proof of concept has been shown, with the latter very much the focus of this thesis.

1.2 The Photon

The idea of the photon arose on the turn of the 20^{th} century when Max Planck was working on blackbody radiation. He coined the term 'energy elements' [3] to describe electromagnetic waves released in energy packets. Planck found that quantising the radiation in such a way, the energy, E, was proportional to the frequency of the

radiation, ν, equation 1.1. The constant of proportionality, Planck's constant, is $h = 6.63 \times 10^{-34}$ Js.

$$E = h\nu \tag{1.1}$$

It was not until 1905 that it was understood why this happened to be the case, when Einstein put forward his idea, stemming from Planck's initial findings [4]. He suggested it was an inherent property of the electromagnetic radiation itself, opposed to Plancks emission process idea. In turn this led Einstein to the Nobel Prize in 1921 for an explanation of the photoelectric effect. Following this revelation a further publication in 1909 justified that these light quantum should be considered as particles themselves [5].

Arthur Compton confirmed Einstein's theory and his controversial claims in 1923 with his work on X-ray scattering off light elements [6]. For an incident wavelength λ, on a target of mass m, scattered through an angle θ, with final wavelength $\lambda^{'}$, he found that this shift was in accordance with equation 1.2. The Compton wavelength of the target particle is then $\lambda_c = h/mc$. Kinematically this is equivalent to a particle of zero rest mass, thus confirming that light can carry momentum and hence behaves as a particle with zero rest mass.

$$\lambda^{'} - \lambda = \frac{h}{mc}(1 - cos\theta) \tag{1.2}$$

The name, photon, is accredited to chemist Gilbert Lewis [7] and since becoming a well established particle, it has opened up our view on the physical world and helped forge Quantum Field Theory. The photon is now considered as a quantum of light.

1.2.1 Gamma Radiation

Photons of energy > 100 keV are considered gamma rays. Such energies correspond to extremely high frequencies of the order 10^{10} GHz and above. In many nuclear gamma emissions energies are of the order of 1 MeV, corresponding to a wavelength of $\sim$1.2 pm. This distance is extremely small, much smaller than the radius of an atom and for energies exceeding 1 GeV it is comparable with the radius of the nucleus. Gamma emission can arise from many radiative processes, it is useful to discuss the key types.

1.2.1.1 Nuclear Transition Radiation

Gamma ray emission can occur through the excitation of nuclei and the subsequent transition to a lower nuclear energy state, with the energy of the photon equal to the difference between energy levels. Radionuclides can decay in several ways but most processes will leave the nucleus in an excited state. Although these processes can have large half-lives the de-excitation happens very quickly, over the order of picoseconds. Due to this process the energy spectrum of the gamma radiation gives an indication of the energy structure of the daughter nucleus while the rate gives an indication of the half-life of the parent nucleus. As nuclear energy levels are discrete and well defined this can yield almost mono energetic gamma rays, making their sources perfect candidates for the energy calibration of detectors. ^{60}Co is a perfect example of this, as it decays via β-decay leaving the nucleus in an excited state. Upon de-excitation of the remnant ^{60}Ni, two photons of 1.173 and 1.332 MeV respectively are emitted every time [8].

1.2.1.2 Annihilation Radiation

In the case when a positron is emitted, under β^+ decay, it will usually annihilate with a electron in a nearby atom once it has lost its kinetic energy. This will then produce two photons equal in energy and opposite in direction, each with energy of $m_e = 0.511$ MeV. Annihilation radiation generally occurs with other radiative processes and will be superimposed in the spectrum.

1.2.1.3 Bremsstrahlung Radiation

Accelerating charged particles produce electromagnetic radiation. An electron passing through matter will interact electromagnetically with the material and thus radiate. This is Bremsstrahlung radiation. Unlike nuclear de-excitation, Bremsstrahlung radiation yields a continuous energy spectrum and is not useful for energy calibration of detectors.

1.2.2 Interactions

Gamma rays interact via three main processes: Photoelectric Absorption, Compton Scattering and Pair Production. Their interaction probabilities are then proportional to $\mathrm{Z}^5/E^{7/2}$, Z/E and $\mathrm{Z}^2\ln(2E)$ respectively [9], where Z is the atomic number of

the material and E is the incident gamma energy. This then describes the dominant processes in ascending order of gamma energy, with the photoelectric absorption dominating at low energies, Compton scattering at intermediate energies and then pair production dominating at energies above $2m_e = 1.022$ MeV.

1.2.2.1 Photoelectric Absorption

Photoelectric absorption involves the complete conversion of a photon to an energetic electron. The photon will interact with the absorber atom as a whole and cannot occur with the electrons in the bound shell. When the photon is absorbed a photoelectron is emitted from one of the bound shells on the atom. The most probable shell origin for such a photoelectron is the K shell, the most tightly bound shell of the atom. The kinetic energy of the photoelectron is simply,

$$E_e = h\nu - E_0 \tag{1.3}$$

where E_0 represents the binding energy of the electron in its shell. Due to conservation of momentum however some energy is lost to nuclear recoil, but such considerations are negligible.

With binding energies of the order of ∼40 keV for the K shell in Xenon [9], when the incident gamma energy exceeds a few hundred keV, the photoelectron gives a good indication of the original gamma energy. It is therefore an ideal process when concerned with measuring the energy spectrum of gamma sources.

1.2.2.2 Compton Scattering

Kinematic restrictions infer that a Compton scattered photon will produce an electron with kinetic energy

$$E_e = h\nu - h\nu^{'} = h\nu \left[\frac{h\nu/m_e(1-\cos\theta)}{1+h\nu/m_e(1-\cos\theta)} \right], \tag{1.4}$$

following from equation 1.2. Therefore a continuum of energies result from a mono energetic gamma ray due to the scattering angle θ, for which any angle can occur. In the extreme case of shallow grazing ($\theta \sim 0$) then $E_e \sim 0$ and no interaction is observed. For the other case when maximum scattering occurs ($\theta = \pi$), i.e backscattering, the incident gamma cannot transfer all of its energy to the electron and a Compton edge

can be seen in the electron energy distribution. Only at energies well exceeding $h\nu \gg m_e/2$ can it be considered very close to the incident gamma energy.

1.2.2.3 Pair Production

As gamma energies reach several MeV pair production becomes the dominant process. In pair production the entire photon is converted to an electron and positron pair due to the intense electric field of the protons in the absorber nuclei. Once the energy threshold of $2m_e$ is exceeded then the process in energetically viable and the total kinetic energy of the pair is then

$$E_{e^+} + E_{e^-} = h\nu - 2m_e. \tag{1.5}$$

The emitted electron positron pair will only travel a short distance, losing all their kinetic energy to the absorbing material. The positron will come to rest, comparable to the thermal energy of the electrons in the material, and subsequently annihilate with such an electron. Annihilation results in the emission of two photons, each of energy 511 keV $= m_e$, with opposite and equal momenta due to conservation laws.

1.3 The Neutron

It was in 1920 when Ernest Rutherford first introduced the notion of the neutron [10] to explain the discrepancy between the atomic mass and the atomic number of the atom. It also introduced the rational to explain the prevention of the positively charged protons in the nucleus from repelling each other. After some years of considering that this could actually be due to nuclear electrons, the proton-electron nuclear model was rejected subject to proof by V. A. Ambartsumain and D. Ivanenko [11]. Deducing that a neutral particle must also exist in the nucleus. It was not until twelve years after Rutherford first theorised the neutron that it was confirmed by James Chadwick [12]. This discovery had enormous and explosive implications to modern society, introducing threats that are still very much imminent today.

With the ability to traverse many centimetres of dense materials they can be very difficult to detect. Neutrons can interact in a manner of ways but the three main processes of concern are; elastic scattering, inelastic scattering causing an excited nuclear state and absorption. It is considered useful to divide neutrons into two categories, slow (thermal) and fast, as certain interactions are favourable in these two

classes.

1.3.1 Slow Neutrons

Neutrons with kinetic energies of ∼0.5 eV and below are considered slow neutrons. Although this definition is not exact, it is used as a rough approximation to define the transition from fast to slow neutrons. At room temperature, ∼300 K, a neutron will have $\sim kT$ kinetic energy, that is around 0.026 eV. This is then a thermal neutron.

Slow neutrons exhibit elastic scattering but due to the low kinetic energy of the neutron, very little is transferred to the recoil nucleus. Multiple elastic scatterings can then bring the neutron into thermal equilibrium with the material. At these energies, their cross section for many materials is much larger and they are more readily absorbed. Upon absorption of the neutron the nucleus is altered and it subsequently recoils. In addition to this the emission of an alpha particle, proton, or some fission fragments also occur. This can be summarised by equations 1.6 and 1.7, given a target nucleus, X, with the absorption of a neutron, n, yielding nucleus, Y, with the emission of an alpha particle, α, or a proton, p.

$$ {}^{A}_{Z}X + {}^{1}_{0}\,n \rightarrow {}^{A-3}_{Z-2}\,Y + {}^{4}_{2}\,\alpha \tag{1.6} $$

$$ {}^{A}_{Z}X + {}^{1}_{0}\,n \rightarrow {}^{A}_{Z-1}\,Y + {}^{1}_{1}\,p \tag{1.7} $$

From these reaction products the recoiling nucleus, proton or alpha particle can then cause ionisation. In most of these cases the energy liberated is far greater than the energy of the incident neutron so that the energy of the products are essentially independent of the neutron energy.

1.3.2 Fast Neutrons

When dealing with fast neutrons, typically with kinetic energies of 1 MeV and above, elastic scattering is the dominant interaction type. In this case the recoil nucleus is usually energetic enough to be visible in a detector. However certain kinematic restrictions impede on the energy transfer to the recoil nucleus. Following energy and momentum conservation the maximum amount of kinetic energy that a non-relativistic neutron ($T_n \ll m_n$) can transfer per elastic scatter is given by equation 1.8.

$$ T_A = T_n - T_n^{'} = \frac{4A}{(1+A)^2} T_n \tag{1.8} $$

Where T_A is the recoil kinetic energy of the nucleus, of mass number A, T_n and $T_n^{'}$ are the kinetic energies of the neutron before and after elastic scatter respectively.

1.3.3 Neutron Emission

Neutron sources originate from either spontaneous fission or decay products of nuclear reactions. Multiple fast neutrons can be emitted per fission event, along with other products such as α, β and γ particles and heavy fission fragments. Shielding such fissile sources in thick material prevents the majority of these from leaving and only the fast neutrons and gammas can emerge.

^{252}Cf is a good source of fast neutrons, with ∼3.8 neutrons on average emitted per fission [13]. The neutron energy spectrum of ^{252}Cf peaks at ∼1 MeV with it extending to 8 MeV. Other examples of fissile neutron sources are ^{235}U and ^{239}Pu.

Sources emitting alpha radiation can be used to induce neutron emission when paired with a suitable target material. A common material fit for purpose is ^{9}Be, due to its high neutron yield, with the following reaction occurring,

$$ {}^{4}_{2}\alpha + {}^{9}_{4}\,Be \rightarrow {}^{12}_{6}\,C + {}^{1}_{0}\,n. \tag{1.9} $$

There are various choices of alpha emitting materials but some can contribute a large gamma background in addition. Considering this and other factors such as availability, half lives and cost, ^{241}Am is a widely used alpha emitter for when high neutron yields are required [8].

It is also possible for neutrons to be emitted from a source upon excitation by gamma rays. These type of sources are called photoneutron sources. They benefit from the fact that near mono energetic neutrons are produced if mono energetic photons are used. However only two sources, ^{2}H and ^{9}Be, are practically feasible. These then require very large gamma activities to ascertain neutron sources of reasonably intensity, as 1 in every $\sim 10^6$ gammas incident on the target will interact and produce a neutron.

1.4 The Neutrino

Electrically neutral, extremely small and vastly abundant, the neutrino is certainly one of the most intriguing and unknown particles in particle physics today. The current climate surrounding it is very positive and the future looks extremely bright. However

our understanding is still in its infancy and with its discovery date less than 60 years old, a brief introduction seems apt.

1.4.1 Small Beginnings

Initially postulated by Wolfgang Pauli in 1930 in order to conserve momentum, energy and spin in beta decay, the neutrino was theoretically conceived [14]. It was to possess no electrical charge and have little mass, and once after the discovery of the neutron, these properties governed its name, neutrino, little neutral one. It was not until 26 years later that its existence was experimentally confirmed by Clyde Cowan and Frederick Reines [15]. In their experiment electron anti-neutrinos were produced from a nuclear reactor via β-decay. These anti-neutrinos interact with protons, via inverse beta decay, in a scintillator detector to emit a neutron and a positron.

$$\bar{\nu_e} + p \rightarrow n + e^+ \tag{1.10}$$

The positron annihilates with a nearby electron producing two gamma rays and the capture of the neutron on a nucleus releases a gamma ray. A unique signature of the interaction then results from the coincidence of the two events.

After confirmation that such a lepton existed, further experiments developed to probe into detection methods for the other two neutrino flavours, the muon neutrino, ν_μ, and the tau neutrino, ν_τ. These were experimentally discovered in 1962 [16] and 2001 [17] respectively, conforming to the three flavour model of the leptons in the Standard Model.

With both the electron and muon neutrino both established in the late 1960's, solar studies were conducted to determine the flux of the emitted neutrinos from the sun. This was met with a large discrepancy with that predicted by the Standard Solar Model, in which approximately only one third of the predicted electron neutrino flux was measured [18]. Named the Solar Neutrino Problem, this deficit in flux could not be resolved and the problem lasted for almost 40 years. The solution came in 2001, when the Sudbury Neutrino Observatory (SNO) in Canada could experimentally measure the rate of ν_e and $\nu_{tot} = \nu_e + \nu_\mu + \nu_\tau$ [19]. It confirmed that only $\sim$35% of the Solar neutrinos reaching the earth were electron neutrinos with the remainder being muon and tau neutrinos. Since all the neutrinos created in the Sun should be electron neutrinos this implied that neutrinos oscillate.

The three flavour model is widely accepted, as fourth or higher generations of light

neutrinos, <45 GeV/c^2, have been ruled out by measurements conducted by the Large Electron Positron Collider (LEP) on the Z mass resonance [20].

1.4.2 Neutrino Oscillations in a Vacuum

Neutrino oscillations were first formulated by Bruno Pontecorvo in 1957 [21] and arise due to the weak eigenstates of neutrinos composing of a mixture of mass eigenstates. Thus for a neutrino to oscillate it must have non zero mass, showing physics beyond the Standard Model.

The weak eigenstates of a neutrino can be written as a linear combination of mass eigenstates,

$$|\nu_\alpha\rangle = \sum_j U^*_{\alpha j}|\nu_j\rangle \tag{1.11}$$

and for the inverse case

$$|\nu_j\rangle = \sum_\alpha U_{j\alpha}|\nu_\alpha\rangle \tag{1.12}$$

Here $U_{\alpha j}$ represents the Maki–Nakagawa–Sakata–Pontecorvo (MNSP) mixing matrix and indices $\alpha = e, \mu, \tau$ represent the flavour with $j = 1, 2, 3$ mass indicies. Similarly for anti-neutrinos the unitary MNSP matrix is replaced by its complex conjugate $U^*_{\alpha j}$.

At time t = 0 we know the neutrino is in a flavour eigenstate as it is produced by the weak interaction, so we can make the assertion

$$|\nu(t=0)\rangle = |\nu_\alpha\rangle = \sum_j U^*_{j\alpha}|\nu_j\rangle. \tag{1.13}$$

In a vacuum these massive neutrino states $|\nu_j\rangle$ are eigenstates of the Hamiltonian, with eigenvalues of

$$E_j = \sqrt{\mathbf{p}_j^2 + m_j^2}. \tag{1.14}$$

Evolving these massive states in time by applying the time dependant Schrödinger equation yields

$$|\nu_j(t)\rangle = e^{-iE_j t}|\nu_j\rangle. \tag{1.15}$$

The neutrino flavour state can then be described at a time t after creation as

$$|\nu_\alpha(t)\rangle = \sum_j U^*_{\alpha j} e^{-iE_j t}|\nu_j\rangle. \tag{1.16}$$

If we then rewrite our massive state $|\nu_j\rangle$ in terms of our flavour state $|\nu_\alpha\rangle$, using equation 1.12, we obtain it in terms of a superposition of flavour states.

$$|\nu_\alpha(t)\rangle = \sum_\beta \sum_j U^*_{\alpha j} e^{-iE_j t} U_{j\beta} |\nu_\beta\rangle \tag{1.17}$$

The probability of a flavour eigenstate neutrino ν_α transforming to a different flavour ν_β is given as

$$P(\nu_\alpha \to \nu_\beta, t) = |\langle \nu_\beta | \nu_\alpha(t) \rangle|^2 \tag{1.18}$$

Using the orthonormality condition of the massive states $\langle \nu_i | \nu_j \rangle = \delta_{ij}$, and hence $\langle \nu_\alpha | \nu_\beta \rangle = \delta_{\alpha\beta}$ for the flavour states leaves us with

$$P(\nu_\alpha \to \nu_\beta, t) = \sum_k \sum_j U^*_{\alpha j} U_{j\beta} U_{\alpha k} U^*_{k\beta} e^{-i(E_k - Ej)t}. \tag{1.19}$$

As neutrinos are highly relativistic and of negligible mass $m << p$ the approximation,

$$E_j = \sqrt{\mathbf{p}_j^2 + m_j^2} \simeq E + \frac{m_j^2}{2E} \tag{1.20}$$

can be made, where $E = |\mathbf{p}|$. Then using the unitarity of the matrix U and the fact that $t = x/c = x = L$, we can write

$$P(\nu_\alpha \to \nu_\beta) = \sum_k \sum_j U^*_{\alpha j} U_{j\beta} U_{\alpha k} U^*_{k\beta} \exp\left(-i \frac{\Delta m^2_{jk} L}{2E}\right), \tag{1.21}$$

for a baseline of length L and neutrino energy E. Here $\Delta m^2_{jk} \equiv m^2_j - m^2_k$ where m_1, m_2 and m_3 label the mass eigenvalues. However it is more convenient to write it in the following form,

$$\begin{aligned} P(\nu_\alpha \to \nu_\beta) &= \delta_{\alpha\beta} - 4 \sum_{j>k} \mathrm{Re}(U^*_{\alpha j} U_{\beta j} U_{\alpha k} U^*_{\beta k}) \sin^2\left(\frac{\Delta m^2_{jk} L}{4E}\right) \\ &\quad + 2 \sum_{j>k} \mathrm{Im}(U^*_{\alpha j} U_{\beta j} U_{\alpha k} U^*_{\beta k}) \sin\left(\frac{\Delta m^2_{jk} L}{2E}\right). \end{aligned} \tag{1.22}$$

It can be easily seen in this form that if neutrinos are massless or if no mixing occurs ($U = I$) then the transition probability is simply $P(\nu_\alpha \to \nu_\beta) = \delta_{\alpha\beta}$. For the case of antineutrinos, the kinematics are the same as for neutrinos and so the derivation

follows the same lines. However our initial state for antineutrinos is written as

$$|\overline{\nu}_j\rangle = \sum_j U_{\alpha j}|\overline{\nu}_j\rangle. \tag{1.23}$$

Now we have the elements in the mixing matrix complex conjugated, so equation 1.19 now reads

$$P(\overline{\nu}_\alpha \to \overline{\nu}_\beta, t) = \sum_k \sum_j U_{\alpha j} U^*_{j\beta} U^*_{\alpha k} U_{k\beta} e^{-i(E_k - Ej)t}. \tag{1.24}$$

Ultimately this only changes the sign of the imaginary part of equation 1.22 [22].

For a two flavour neutrino approximation (ν_e, ν_μ), the unitary mixing matrix U is 2 x 2 with just one single parameter θ [23]. Then P($\nu_\mu \to \nu_e$) is given as:

$$P(\nu_\mu \to \nu_e) = \sin^2 2\theta \sin^2 \left(\frac{\Delta m^2 L}{4E} \right), \tag{1.25}$$

and the disappearance transition is simply P($\nu_\mu \to \nu_\mu$) = 1 - P($\nu_\mu \to \nu_e$).

For a more accurate calculation, three flavour neutrinos $(\nu_e, \nu_\mu, \nu_\tau)$ are considered. The unitary mixing matrix U then becomes 3 x 3 which is then parameterised by three mixing angles $(\theta_{12}, \theta_{13}, \theta_{23})$ and a single CP-violating phase δ [23].

$$U = \begin{pmatrix} c_{12}c_{13} & s_{12}c_{13} & s_{13}e^{-i\delta} \\ -s_{12}c_{23} - c_{12}s_{23}s_{13}e^{i\delta} & c_{12}c_{23} - s_{12}s_{23}s_{13}e^{i\delta} & s_{23}c_{13} \\ s_{12}s_{23} - c_{12}c_{23}s_{13}e^{i\delta} & -c_{12}s_{23} - s_{12}c_{23}s_{13}e^{i\delta} & c_{23}c_{13} \end{pmatrix}, \tag{1.26}$$

where $c_{ij} = \cos\theta_{ij}$ and $s_{ij} = \sin\theta_{ij}$.

1.4.3 Neutrino Oscillations in Matter

When Lincoln Wolfenstein predicted in 1978 that neutrinos propagating in matter alter their mixing [24], it introduced a new way to probe the nature of neutrinos. He noticed that as they propagate in matter they are subject to forward elastic scattering off electrons, as ordinary matter does not consist of μ or τ. Hence introducing an effective mass-squared term in the neutrinos Hamiltonian. This effective potential causes interference with the original mass-squared term and alters mixing angles and neutrino masses, ultimately modifying the oscillation probabilities. This difference in probability in matter compared to the vacuum is known as the Mikheev-Smirnov-Wolfenstein (MSW) effect [25]. The change induced by the interference depends on

the sign of the mass-squared difference, thus depending on the mass hierarchy [26].

The are two types of neutrino interaction that occur with matter, Charged Current (CC) and Neutral Current (NC), these are shown in figure 1.1. The exchange of a charged W boson indicates a CC interaction, while a Z boson exchange indicates a NC interaction. These two processes can be expressed by the following leptonic currents [22],

$$j^{\sigma}_{W,CC} = \sum_{\alpha=e,\mu,\tau} \overline{\nu}_{\alpha}\gamma^{\sigma}(1-\gamma^{5})l_{\alpha}, \tag{1.27}$$

$$j^{\sigma}_{Z,NC} = \sum_{\alpha=e,\mu,\tau} \overline{\nu}_{\alpha}\gamma^{\sigma}(1-\gamma^{5})\nu_{\alpha}. \tag{1.28}$$

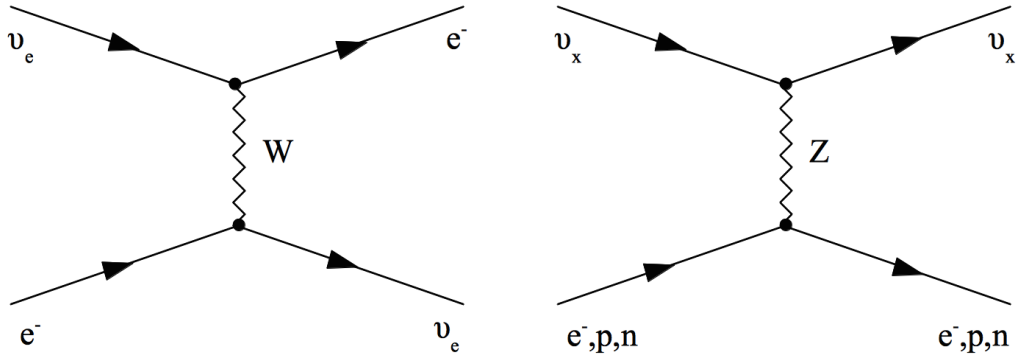

Fig. 1.1 Feynman diagrams of coherent forward scattering processes, CC on the left and NC on the right.

The average effective Hamiltonian term, $\overline{\mathcal{H}^{(CC)}_{\text{eff}}}(x)$, corresponding to the CC interactions in matter is

$$\overline{\mathcal{H}^{(CC)}_{\text{eff}}}(x) = V_{CC}\overline{\nu_{eL}}(x)\gamma^{0}\nu_{eL}(x). \tag{1.29}$$

Where our CC potential term V_{CC} is

$$V_{CC} = \sqrt{2}G_{F}N_{e} \tag{1.30}$$

with G_F being the Fermi constant and N_e the electron density of the medium. The NC contribution must consider all neutrino flavour interactions with protons, neutrons and electrons.

$$V^{f}_{NC} = \sqrt{2}G_{F}N_{f}g^{f}_{V} \tag{1.31}$$

Here $f = e^{-}$, p, n and g^{f}_{V} is the coefficient associated with the fermion, f. However these coefficients are equal and opposite for protons and electrons and with electrical

neutrality of atoms in matter these terms do not contribute and only the neutron term persists.

$$V_{NC} = -\frac{1}{\sqrt{2}} G_F N_n \tag{1.32}$$

With N_n as the neutron density of the medium. We then have

$$V_\alpha = \sqrt{2} G_F \left(N_e \delta_{\alpha e} - \frac{1}{2} N_n \right), \tag{1.33}$$

as our total potential. Now the Hamiltonian reads,

$$\mathcal{H} = \mathcal{H}_0 + \mathcal{H}_1 \tag{1.34}$$

with our vacuum Hamiltonian term $\mathcal{H}_0$ and $\mathcal{H}_1$ arising due to the effective potential from matter effects. These matter effects are negligible in most practical cases as $G_F/(\hbar c)^3 = 1.17 \times 10^{-5}$ GeV^{-2}, but over large enough distances through a medium, where matter densities are high, these effects can be quite considerable. Indeed such vast distances do occur in the Sun and in proposed long baseline experiments such as LAGUNA-LBNO, with the aim to use these matter effects to probe the nature of neutrinos.

In the context of LAGUNA-LBNO, a muon (anti)neutrino beam is proposed. Both the appearance ($\nu_\mu \to \nu_e$) and disappearance ($\nu_\mu \to \nu_\mu$) channels are examined to include these matter effects. Implementing the 3×3 matrix the probability for the appearance transition can be approximated as equation 1.35 [27].

$$\begin{aligned} P(\nu_\mu \to \nu_e) \;=\; & 4c_{13}^2 s_{13}^2 s_{23}^2 \left(1 + \frac{2\alpha}{\Delta m_{31}^2}(1 - 2s_{13}^2) \right) \sin^2\Delta_{31} \\ & + 8c_{13}^2 s_{12} s_{13} s_{23} (c_{12} c_{23} \cos\delta - s_{12} s_{13} s_{23}) \cos\Delta_{32} \sin\Delta_{31} \sin\Delta_{21} \\ & - 8c_{13}^2 c_{12} c_{23} s_{12} s_{13} s_{23} \sin\delta \sin\Delta_{32} \sin\Delta_{31} \sin\Delta_{21} \\ & + 4s_{12}^2 c_{13}^2 (c_{12}^2 c_{23}^2 + s_{12}^2 s_{23}^2 s_{13}^2 - 2c_{12} c_{23} s_{12} s_{23} s_{13} \cos\delta) \sin^2\Delta_{21} \\ & - 8c_{13}^2 s_{13}^2 s_{23}^2 \frac{\alpha L}{4E_\nu} (1 - 2s_{13}^2) \cos\Delta_{32} \sin\Delta_{31} \end{aligned} \tag{1.35}$$

Wheres for disappearance transition probability is shown by equation 1.36 [23].

$$\begin{aligned} P(\nu_\mu \to \nu_\mu) &= 1 - 4s_{23}^2c_{13}^2(c_{12}^2c_{23}^2 + s_{12}^2s_{13}^2s_{23}^2 - 2c_{12}c_{23}s_{12}s_{13}s_{23}\cos\delta)\sin^2\Delta_{23} \\ &\quad - 4s_{23}^2c_{13}^2(s_{12}^2c_{23}^2 + c_{12}^2s_{13}^2s_{23}^2 + 2c_{12}c_{23}s_{12}s_{13}s_{23}\cos\delta)\sin^2\Delta_{13} \\ &\quad - 4(c_{12}^2c_{23}^2 + s_{12}^2s_{13}^2s_{23}^2 - 2c_{12}c_{23}s_{12}s_{13}s_{23}\cos\delta) \\ &\quad \times (s_{12}^2c_{23}^2 + c_{12}^2s_{13}^2s_{23}^2 + 2c_{12}c_{23}s_{12}s_{13}s_{23}\cos\delta)\sin^2\Delta_{12} \end{aligned} \tag{1.36}$$

Here $\Delta_{ij} = \frac{1.27\Delta m_{ij}^2}{eV^2}\frac{L}{km}\frac{GeV}{E_\nu}$. In the ν_e appearance channel matter effects have been included with $\alpha = 2\sqrt{2}G_f n_e E_\nu = 7.56 \times 10^{-5} eV^2 \frac{\rho}{g/cm^3}\frac{E_\nu}{GeV}$, where the density of the earth is taken as $\rho = 2.8 g/cm^3$, G_f is the Fermi constant and n_e is the electron density [23] [27].

Examining the expressions for the probability, the baseline L and the energy E are the only free parameters. Optimisation of these values and hence of L/E, will result in a maximal probability for the desired channel.

1.4.4 Current Status

Current values for the 3 mixing angles and the mass difference oscillation parameters have been well established [28][29], shown in table 1.1.

Parameter	**Best Fit $\pm$ 1σ**	**2σ**	**3σ**
$\Delta m_{21}^2[10^{-5}eV^2]$	$7.59^{+0.20}_{-0.18}$	7.24-7.99	7.09-8.19
$\Delta m_{31}^2[10^{-3}eV^2]$ (NH)	2.54 ± 0.09	2.28-2.64	2.18-2.73
$\Delta m_{31}^2[10^{-3}eV^2]$ (IH)	-($2.34^{+0.10}_{-0.09}$)	-(2.17-2.54)	-(2.08-2.64)
$\sin^2\theta_{12}$	$0.312^{+0.017}_{-0.015}$	0.28-0.35	0.27-0.36
$\sin^2\theta_{23}$	0.51 ± 0.06	0.41-0.61	0.39-0.64
$\sin^2\theta_{13}$	0.024 ± 0.08	0.012-0.036	0.010-0.038

Table 1.1 The current neutrino oscillation parameters with best fit, 2 σ and 3 σ values, from [28], with the recent result from Daya Bay of θ_{13} [29].

Of the parameters in table 1.1 that which has been of most recent interest is θ_{13}. It remained the last mixing angle to be determined and initial evidence from T2K [30] indicated that it had a non-zero value. More recent results are the Daya Bay θ_{13} value shown in table 1.1 and the even more recent result from RENO of

$\sin^2 2\theta_{13} = 0.103 \pm 0.013(stat) \pm 0.011(syst)$ [31]. These combined efforts to determine θ_{13} have shown that this parameter is no longer of key interest to future experiments and focus can be moved onto the remaining undetermined parameters, δ_{CP} and the sign of Δm^2_{31}.

Current global analysis of the six independent parameters, $\sin^2\theta_{12}$, $\sin^2\theta_{13}$, $\sin^2\theta_{23}$, $\delta m^2 \equiv \Delta m^2_{21}$, $\Delta m^2 \equiv m^2_3 - (m^2_1 + m^2_2)/2$ ($+\Delta m^2$ for NH and -Δm^2 for IH) and δ_{CP} are shown with their corresponding $N\sigma$ bounds in figure 1.2 [32]. The constraints of the parameters $\sin^2\theta_{13}$ and δ_{CP} can be seen in figure 1.3 when examining the combination of Long Baseline (LBL) accelerator experiments, Solar experiments, KamLAND, and Short Baseline (SBL) reactor experiments and Atmospheric detectors.

1.4.5 CP Violation

From the MNSP mixing matrix there then remains one unknown parameter, the CP-violating phase, δ, which can now be determined as the mixing angle θ_{13} is shown to be non zero (or integer multiples of π) to larger than 5σ. The measurement of a large θ_{13} was crucial for probing δ_{CP} as it is coupled with $\sin\theta_{13}$ in the MNSP. By comparing neutrino with anti-neutrino beams in Positive Focusing (PF) and Negative Focusing (NF) run modes respectively, asymmetries in their oscillation amplitudes will show a direct observation of CP Violation (CPV) in the leptonic sector. One can define the CP asymmetry as equation 1.37.

$$A^{CP}_{\alpha\beta} = P(\nu_\alpha \to \nu_\beta) - P(\overline{\nu}_\alpha \to \overline{\nu}_\beta) \tag{1.37}$$

1.4.6 The Mass Hierarchy

It is clear from looking at the oscillation probabilities that they depend on Δm^2_{ij} but the problem lies in the sign of these. Is $m^2_3 > m^2_1$? This is a question that remains unresolved. In a vacuum these probabilities cannot discriminate between the sign as they arise in sine and cosine terms which cancel out the sign effects. However with the inclusion of the effective matter potential and the MSW effect, terms arise in the oscillation probability to make it possible to observe this sign. It is well established that Δm^2_{21} is positive [33]. This is due to matter effects of the Sun. The mass hierarchy problem is the problem of resolving the sign of Δm^2_{13}, illustrated in figure 1.4. This sign can only be determined through the appearance channel as the disappearance channel involves squared terms of the sign.

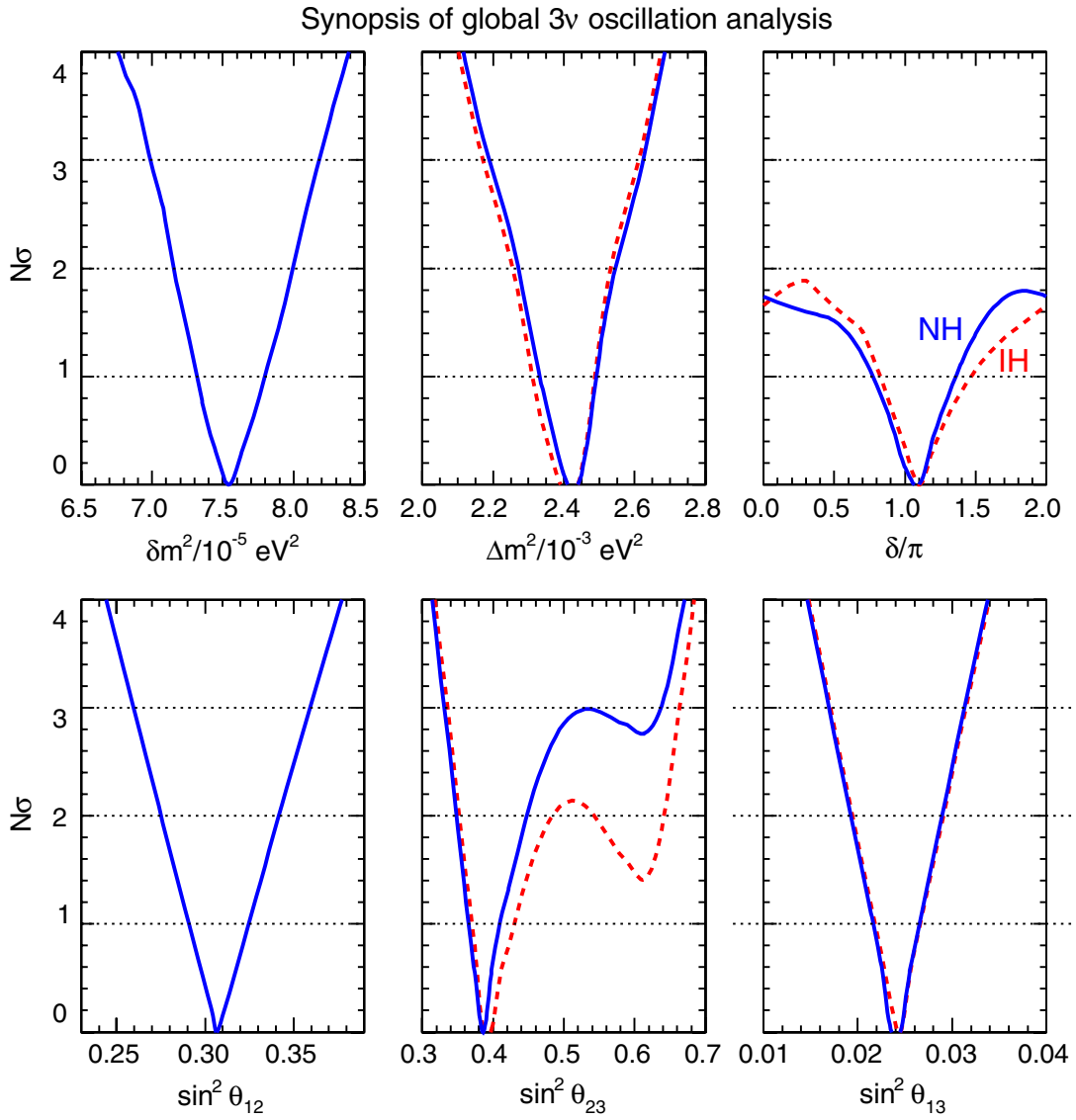

Fig. 1.2 The six parameters, $\sin^2\theta_{12}$, $\sin^2\theta_{13}$, $\sin^2\theta_{23}$, $\delta m^2 \equiv \Delta m^2_{21}$, $\Delta m^2 \equiv m^2_3 - (m^2_1 + m^2_2)/2$ ($+\Delta m^2$ for NH and $-\Delta m^2$ for IH) and δ_{CP} are shown from a global analysis with their corresponding $N\sigma$ bounds, for 3ν flavour neutrinos. Blue solid lines indicate NH and red dashed lines indicate IH. Plots taken from [32].

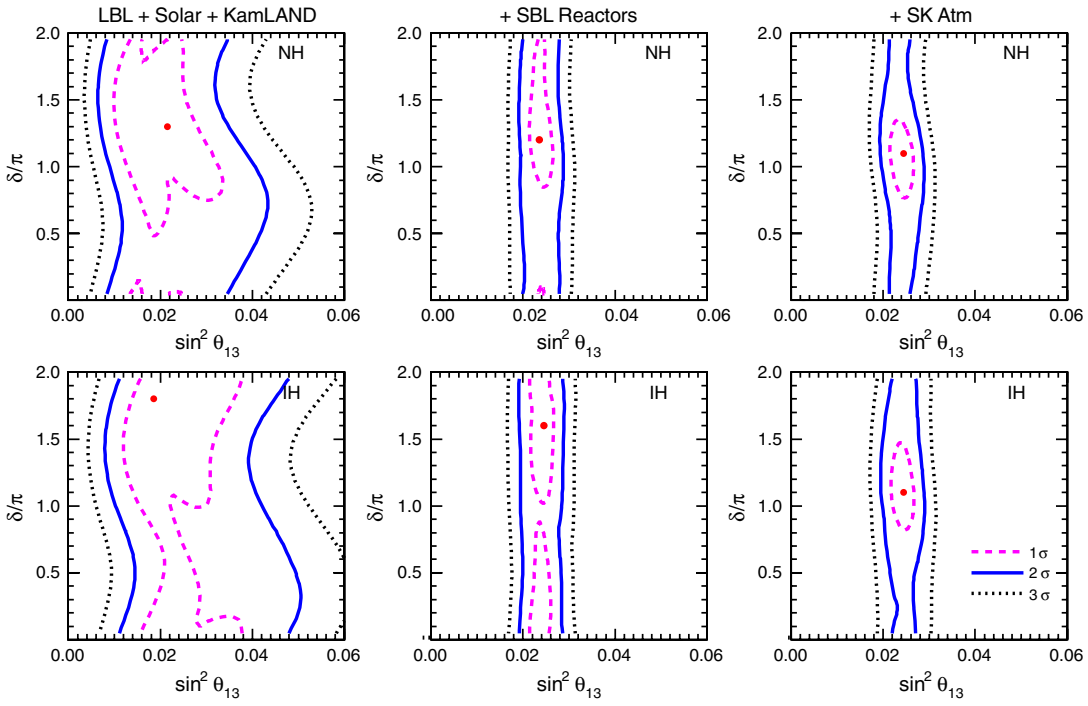

Fig. 1.3 Global results in the plane of $\sin^2\theta_{13}$ and δ_{CP}. The left plots show analysis using LBL + Solar + kamLAND, the middle plots include the addition of SBL reactor experiments and the right plots include Atmospheric results. 1, 2 and 3 σ levels are shown in dashed red, solid blue and dashed black lines respectively. Plots taken from [32].

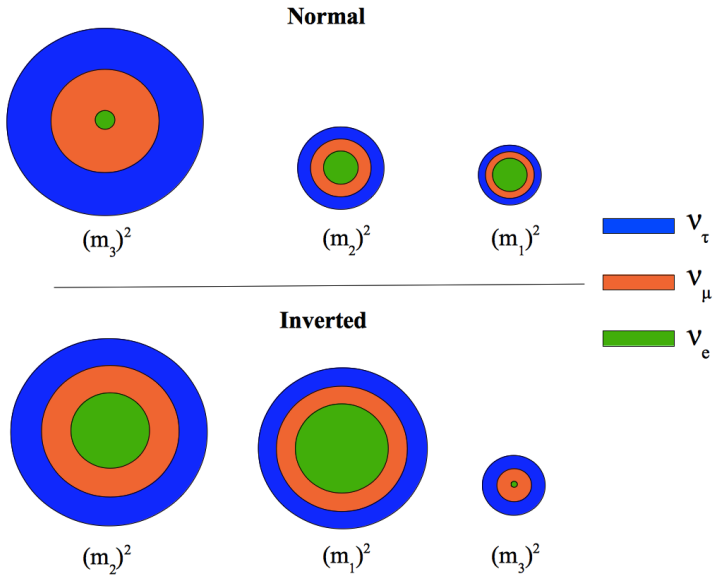

Fig. 1.4 The mass hierarchy of neutrinos, the normal hierarchy (NH) on the top and the inverted hierarchy (IH) on the bottom. This graphic shows the larger the circle the larger the value of m_i^2.

1.4.7 Sterile Neutrinos

Neutrinos could in theory oscillate to other flavours that do not interact weakly, unlike the 3 flavours we currently observe. This would then alter observed oscillation probabilities and could give an indirect indication to such a family of neutrinos. These particular variety of theorised neutrinos are named sterile neutrinos and as of yet are to be experimentally confirmed.

1.4.8 Neutrino Interactions

Neutrinos can only interact in one way (ignoring gravity), that is, weakly. These interactions are well described processes in the Standard Model. Although neutrino oscillations are not described in the Standard Model, there have been no experimentally observed deviations from the Standard Model for neutrino interactions. Of course oscillations imply neutrino mass, and the Standard Model does not account for this but with neutrino mass limit $m_{\nu_e} < 2.3$ eV/c^2 at 95% confidence [34], the kinematic effects of this small mass are negligible for oscillation experiments and are only relevant for mass measurement experiments.

In order to perform accurate oscillation measurements, neutrino interactions need

to be well understood. LAGUNA-LBNO and most long baseline experiments are concerned in the intermediate energy scale of 0.1 to 100 GeV [35]. In this energy range several important physical process contribute. There are three main neutrino interactions concerning this intermediate energy scale. They consist of Elastic/Quasi-Elastic (E/QE), Resonance (RES) and Deep Inelastic Scattering (DIS) interactions.

Elastic and Quasi Elastic: Considered the simplest and most well understood interaction type in detectors, elastic scattering occurs with an electron or a nucleon. In either of these cases however it impossible to detect the final state neutrino in the detector and only the lepton/nucleon can be seen.

QE interactions are not elastic but considered semi elastic due to low momentum transfer. They involve the production of new particles in the final state if above the production threshold. Charge Current Quasi Elastic (CCQE) interactions are prevalent below the ∼1 GeV regime, with neutrino-nucleon scatterings of

$$\nu_l + n \rightarrow p + l^-, \tag{1.38}$$

$$\overline{\nu}_l + p \rightarrow n + l^+, \tag{1.39}$$

where l represents the charged lepton, $l = e, \mu, \tau$, and interacting with the proton, p, or the neutron, n in the nucleon. In practice only electron and muon (anti)neutrinos are feasible with tau neutrino beams originating from astrophysical events. CCQE interactions are favourable in experiments as the neutrino energy can be solely reconstructed from the momentum of the lepton, by conservation of momentum and energy we have

$$E_{\nu_l} = \frac{E_l m_N c^2 - m_l^2 c^4/2}{m_N c^2 - E_l + p_l c \cos\theta}. \tag{1.40}$$

Here E_{ν_l} and E_l are the energies of the neutrino and lepton respectively, m_N denotes the mass of the proton or neutron (depending on neutrino or antineutrino case). The transverse momentum of the charged lepton is given by p_l, with the angle between the lepton and the incident neutrino as θ. Determination of the angle cannot be done from the lepton alone and without accurate measurement of the final state nucleons momentum it is assumed that angle is taken with respect to the beam axis.

Resonance: In the region between elastic and inelastic processes, around 1 GeV, RES events are common. Through the excitation of baryon resonances pions are produced via,

$$\overset{(-)}{\nu}_l + N \rightarrow l^{\pm} + N^*, \tag{1.41}$$

where $N^{(*)}$ denotes a nucleon in a non-resonant/resonant state. The excited state N^*

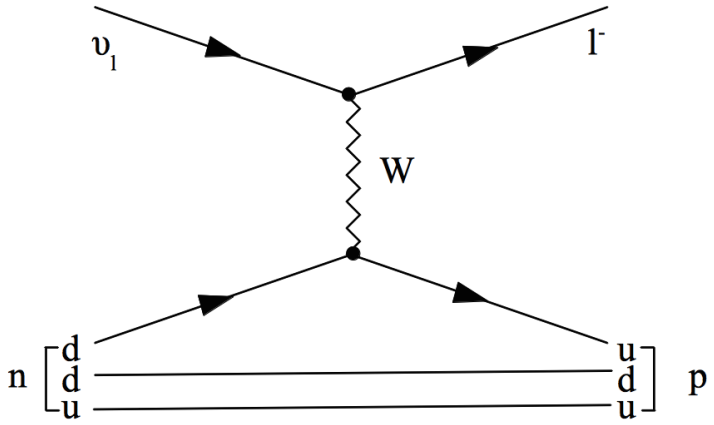

Fig. 1.5 CCQE interaction at tree level.

then decays with pions in the final state.

Deep Inelastic Scattering: When neutrino energies are high enough that they well exceed the proton/neutron mass, $E_\nu >> m_N$, DIS interactions dominate. These processes are defined as

$$\overset{(-)}{\nu_l} + N \rightarrow l^{\pm} + X, \tag{1.42}$$

with N = proton or neutron and X represents a set of final state hadrons. Such interactions are notoriously difficult to fully reconstruct in detectors as they usually results in high multiplicities. Determining cross sections of such events require the use of structure functions, $F_i(x, Q^2)$ which are given in terms of two Lorentz invariants, $x \equiv Q^2/2p_N \cdot q$ and $Q^2 \equiv -q^2$ [22].

Quantum ChromoDynamics (QCD) and nuclear effects make understanding neutrino interactions difficult. Neutrinos can interact on the atomic scale, nuclear scale or quark scale. Due to the non perturbative nature of these interactions several models are used to describe the various interaction processes. Current experimental measurements of neutrino cross sections are not well known in the low GeV range, with several different models and calculations driving most oscillation measurements. These current measurements are shown in figure 1.8 [35].

1.4.9 Types of Neutrino Experiment

Neutrino oscillation experiments can be divided into several classifications depending on their associated L/E value for the experiment. This quantity can determine the

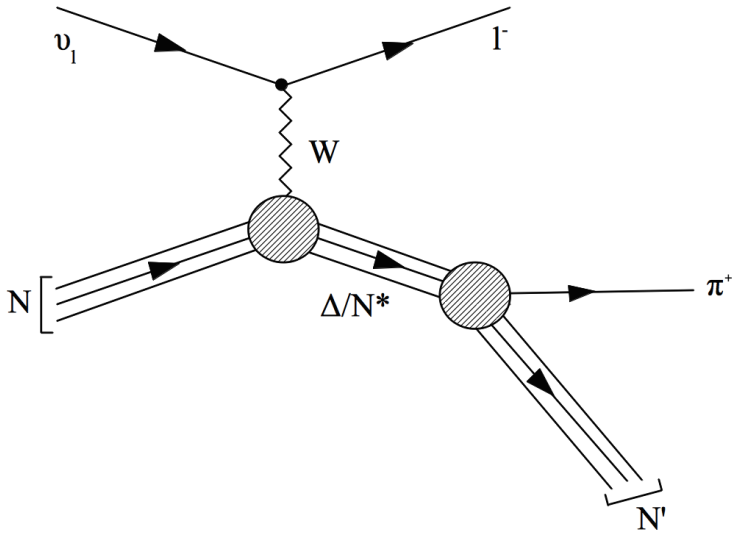

Fig. 1.6 RES interaction with single pion production at tree level.

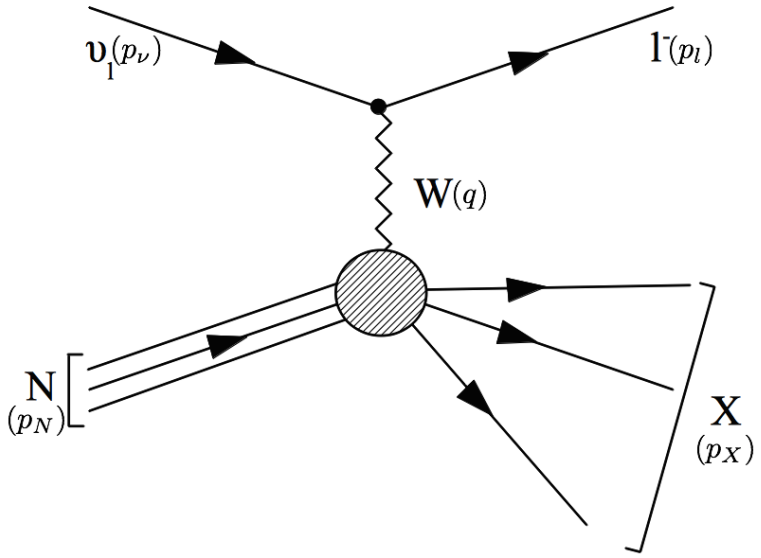

Fig. 1.7 DIS interaction at tree level.

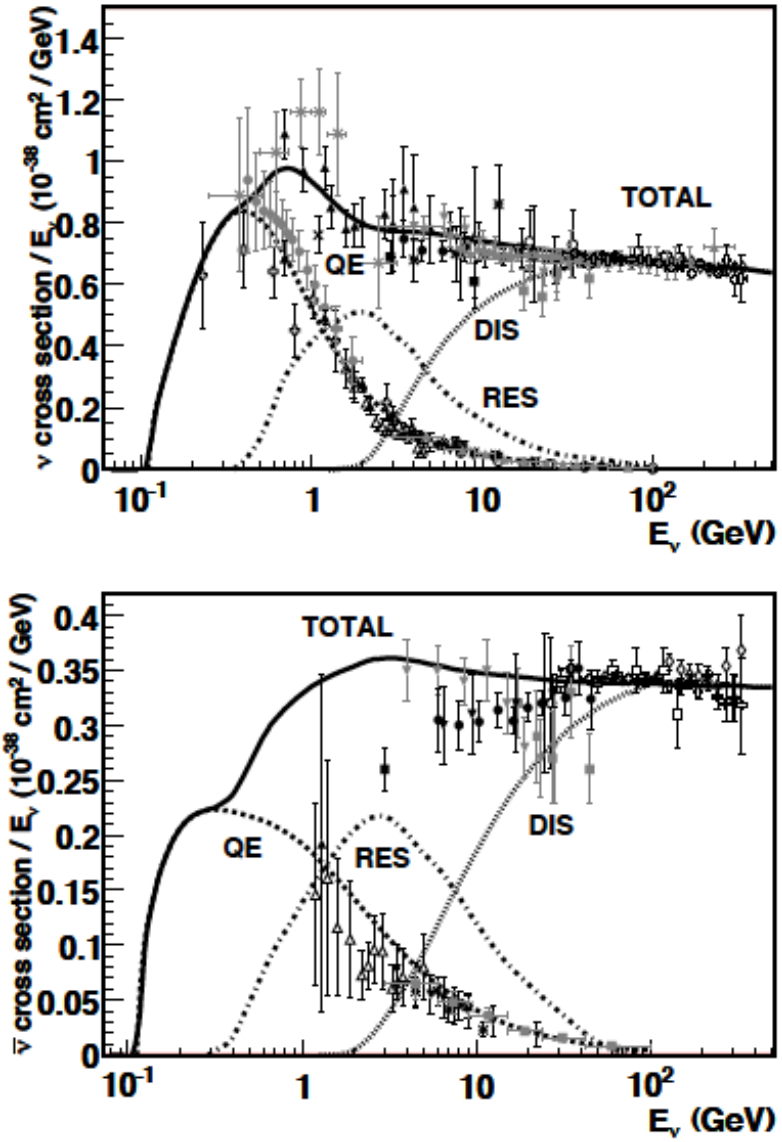

Fig. 1.8 CC neutrino cross sectional data divided by neutrino energy as a function of neutrino energy for neutrino (upper) and antineutrino (lower). QE, RES single pion and DIS data is shown against predictions from an event generator. Images taken from [35].

sensitivity of Δm^2, which is defined as equation 1.43 [22]. The longest baseline is described first, that is neutrino experiments using the Sun as their source.

$$\Delta m^2 \sim \frac{2E[GeV]}{L[km]} \tag{1.43}$$

1.4.9.1 Solar Neutrino Experiments

The Sun is a rich and powerful source of electron neutrinos due to fierce fusion processes in its core. Copious amounts of neutrinos at energies of several MeV are produced, but consist of only electron flavour, arising from reactions shown in figure 1.9. Large amounts of these neutrinos are produced with a neutrino flux of about 6×10^{10} $cm^{-2}s^{-1}$ on the Earths surface [22]. The predicted neutrino flux emitted from the Sun as a function of energy is shown in figure 1.10.

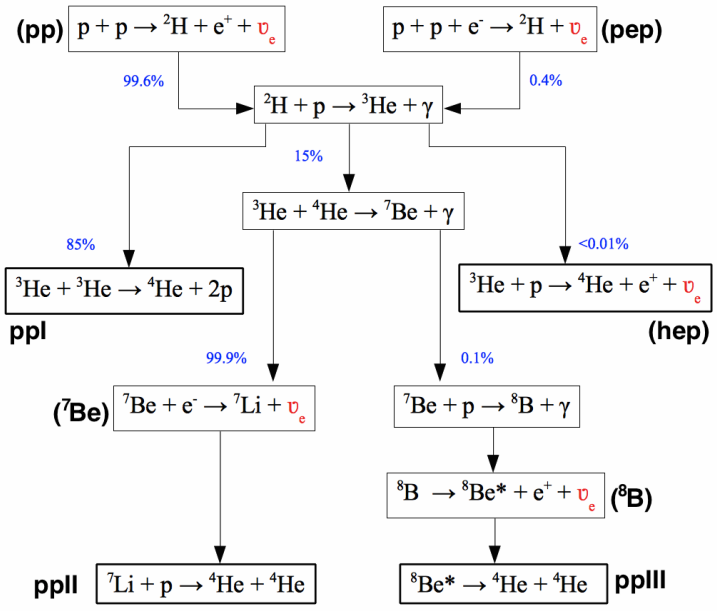

Fig. 1.9 The fusion reactions that occur in the sun. Process chain based on [22].

The first solar neutrino experiment was the Homestake experiment conducted by R. Davis in 1968 [18] (the origin of the Solar Neutrino Problem). Several experiments have since been conducted, providing a direct probe to the interior of the Sun. Experiments such as Kamiokande [37], GALLEX [38], SAGE [39], GNO [40] and SNO [41] have all confirmed the Homestake observations. The latter of course resolving the Solar

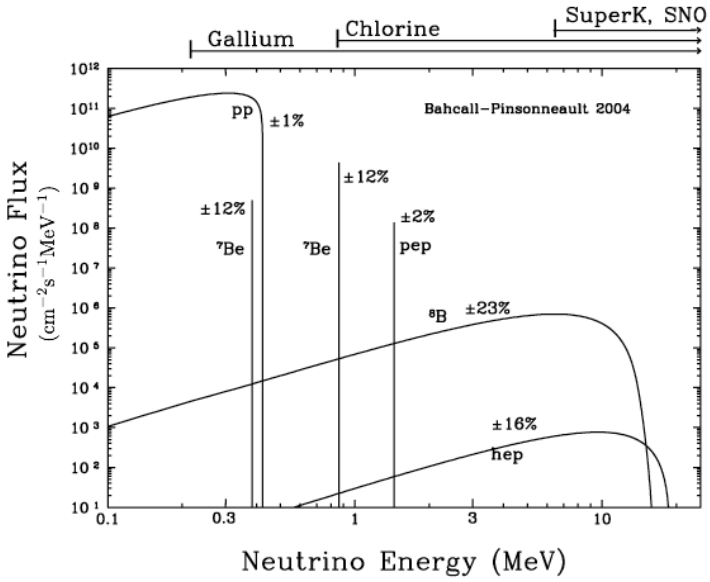

Fig. 1.10 The neutrino flux from the solar fusion processes. The percentages indicate the uncertainties in the values. Figure taken from [36].

Neutrino problem by measuring CC interactions for the ν_e rate and NC interactions to yield the total ν rate.

The distance between the Sun and the Earth is approximately 1.5×10^{11} m. With the energy spectrum ranging between 0.1 - 15 MeV this gives an upper bound of L/E $\sim 10^{12}$ m/MeV, corresponding to a sensitivity of $\Delta m^2 \sim 10^{-12}$ eV^2. Although with the radius of the Sun at roughly 7×10^8 m they can experience considerable matter effects inside the Sun before reaching the surface.

1.4.9.2 Atmospheric Neutrino Experiments

Another source of naturally occurring neutrinos is from the atmosphere. Cosmic high energy particles, primarily protons, interact in the upper atmosphere producing muons, pions and kaons. These all subsequently decay into neutrinos via several different modes, with one example shown in figure 1.11. Charged pions decay >99.9% of the time via process 1.44 [42], producing muon (anti)neutrinos. These muons then decay via processes 1.45 and 1.46. Kaons have several decay modes which all result in the production of pions, muons and neutrinos. Neutrinos of atmospheric origin have

a wide range of energies varying from 500 MeV to 100 GeV.

$$\pi^{\pm} \rightarrow \mu^{\pm} + \overset{(-)}{\nu_{\mu}} \tag{1.44}$$

$$\mu^{-} \rightarrow e^{-} + \overline{\nu}_{e} + \nu_{\mu} \tag{1.45}$$

$$\mu^{+} \rightarrow e^{+} + \nu_{e} + \overline{\nu}_{\mu} \tag{1.46}$$

Measurements using atmospheric neutrinos require different techniques than solar experiments as they no longer originate from one localised source. As neutrinos can originate from anywhere in the atmosphere then directional information is key in studying these neutrinos.

With distances varying dramatically depending on the several atmospheric levels, the baseline is anywhere between 10 - 10,000 km. Taking the lower bound gives a sensitivity of $\Delta m^2 \sim 10^{-4}$ eV^2. Kamiokande [37] and IMB [43] are two experiments that have measured atmospheric neutrinos.

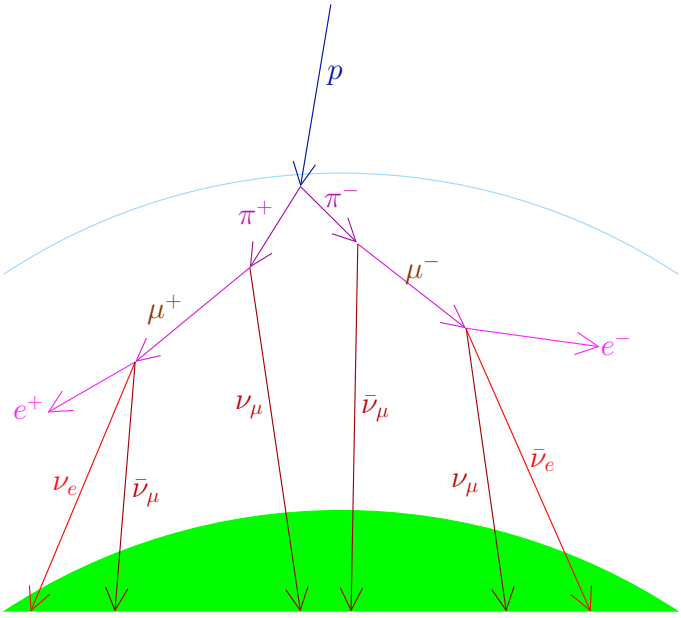

Fig. 1.11 An illustration of how cosmic protons interact in the atmosphere and produce various flavours of neutrinos reaching the Earth's surface. Image taken from [22].

1.4.9.3 Reactor Neutrino Experiments

Fission reactors are another powerful source of neutrinos, producing electron antineutrinos in large amounts $\sim 2 \times 10^{20}$ s^{-1}. Arising from the β-decay of fission products from reactions between ^{235}U, ^{238}U, ^{239}Pu and ^{241}Pu they have typical energies of the order of several MeV. Such energies result in shorter baselines but considering the isotropic nature of the flux this is beneficial for experiments using reactor neutrinos as a source. Only disappearance experiments are feasible as such energies are not sufficient to produce μ's or τ's in a detector through CC interactions. The common method to detect reactor neutrinos is via inverse beta decay.

Reactor neutrino experiments can be short or long baseline, with sensitivities of $\Delta m^2 \sim 0.1$ eV^2 and $\Delta m^2 \sim 10^{-3}$ eV^2 respectively. Experiments that employ this method are Daya Bay[44], RENO[45] and CHOOZ[46].

1.4.9.4 Accelerator Long Baseline Experiments

Muon (anti)neutrino beams are common in present day LBEs with the ability to perform both appearance and disappearance measurements. Neutrinos are specifically created at accelerators and aimed towards a detector at some considerable distance away, $>10^3$ km. LAGUNA-LBNO is a proposed LBE with one of the largest baselines considered in the world of 2300 km. Energies of such beams are in the regime of between 500 MeV and several GeV. At 2300 km the sensitivity to Δm^2 is then $\sim 10^{-6}$ eV^2. Current accelerator LBEs are T2K[47], K2K[48], MINOS[49] and NOνA[50].

Chapter 2

Detection in Noble Fluids

Noble fluids are very attractive materials for use when particle and radiation detection is required. They are commonplace in current detector technologies, with argon being the most prolific. It is hard to imagine in this modern era designing detectors and experiments without the use of noble fluids, and this chapter aims to motivate and describe their use.

2.1 The Noble Gases

The five naturally occurring noble elements, excluding the radioactive radon (Rn), are helium (He), neon (Ne), argon (Ar), krypton (Kr) and xenon (Xe). Being chemically inert provides them with unique attributes that are key for particle detectors, specifically for detectors which collect charge and scintillation light. However some noble gas detectors can require extremely high purities, in excess of the order of 0.1 part per billion (ppb). Their properties relevant to detector design are shown in table 2.1.

Natural abundance and ease of production drives the price of the gases. The lightest of the noble gases, He, Ne and Ar are the most abundant in the Earth's atmosphere. High abundance can result in low production costs and makes these three the most easily attainable of the noble gases. They are popular candidates for use in detectors, as vast quantities can be required for large detector volumes and for purification processes. Kr and Xe are much less abundant in the atmosphere and as a result are more expensive to produce. The global production of Xenon is ∼5 tonnes per year[54], costing ∼£1500 / liquid litre compared to Ar at ∼700,000 tonnes per year[55], costing ∼£1.3 / liquid litre.

Other considerations must be taken into account for their use in detectors. The

	He	**Ne**	**Ar**	**Kr**	**Xe**
Atomic number, Z	2	10	18	36	54
Molar mass [g mol^{-1}]	4.00	20.2	39.9	83.8	131
Density (273 K, 1 atm) [kg m^{-3}]	0.179	0.888	1.76	3.70	5.90
Boiling point (1 atm) [K]	4.40	27.1	87.3	112	169
Critical point:					
Temp [K]	5.25	44.4	151	209	290
Pressure [MPa]	0.226	2.69	4.90	5.43	5.76
Triple point:					
Temp [K]	2.18	24.6	83.8	115	161
Pressure [kPa]	5.04	43.4	68.8	73.4	81.8
First excitation energy (293K, 1 atm) [eV]	19.8	16.7	11.6	10.5	8.4
Ionisation energy (293K, 1 atm) [eV]	24.6	21.6	15.7	13.0	12.1
Scintillation wavelength [nm]	78	80	128	147	175
Radiation length [g cm^{-2}]	89.9	28.9	19.9	11.7	8.49
Abundance in atmosphere [ppm]	5.20	18.2	9340	1.10	0.09

Table 2.1 The properties of the 5 natural occurring non-radioactive nobel gases. Data taken from [51] and [9]. Radiation lengths correspond to the most naturally abundant isotopes (^{4}He, ^{20}Ne, ^{40}Ar, ^{84}Kr and^{129}Xe) and are calculated from an experimental fit from [52]. Abundance in Earth's atmosphere given by [53].

most important trait for use as a detector medium is the ability to absorb and efficiently measure energy transfer of incident particles or radiation. Heavier noble gases are preferable for this, with higher atomic numbers making it favourable for electromagnetic interactions. Noble fluids are usually implemented in either liquid or gaseous states, however since all the stable noble gases have boiling points below room temperature and pressure, cryogenics are usually required to maintain them in a liquid state. Gases can avoid the need for this, but require high pressures to achieve adequate detector efficiencies. The pressure is then a measure of controlling the density and hence their stopping power.

It is also worth noting that some of these noble gases contain radioactive isotopes which can introduce unwanted backgrounds in detectors. Argon contains traces of ^{39}Ar, which decaying via β-decay releases an energy of $\sim$0.5 MeV, which is a large background relevant for lower energy detectors. Krypton contains small amounts of ^{78}Kr and ^{81}Kr, which are also radioactive. Xenon has three naturally occurring isotopes that are radioactive, ^{124}Xe, ^{134}Xe and ^{136}Xe, however these have such long lifetimes they can be considered stable. Traces of ^{85}Kr (β-decay at 687 keV) are the most problematic of the radioactive contaminates for low energy xenon detectors.

The two main implementations of noble fluids as detector media are as Ionisation Detectors and Scintillation Detectors. These detection methods rely on the interaction of charged particles with atoms in the medium, causing ionisation or excitation. Neutral particles can be detected indirectly also by inferring their interaction from the propagation of charged particles in the volume. While ionisation and scintillator detectors are presented sequentially and independently, it can be beneficial to incorporate the two into a single detector technology, with some current and proposed detectors operating to utilise both methods of particle detection.

2.2 Noble Gases as Ionisation Detectors

Charged particles interact primarily with electrons in atoms while traversing matter. Moderately relativistic ($0.05 < \beta\gamma < 500$) heavy charged particles such as μ, α, protons and nuclear ions, lose their energy according to the well described equation 2.1, the Bethe-Bloch formula[52].

$$-\left\langle \frac{dE}{dx} \right\rangle = 4\pi N_A r_e^2 m_e c^2 z^2 \frac{Z}{A} \frac{1}{\beta^2} \left[\frac{1}{2} \ln\left(\frac{2m_e c^2 \beta^2 \gamma^2 T_{max}}{I} \right) - \beta^2 - \frac{\delta}{2} \right] \tag{2.1}$$

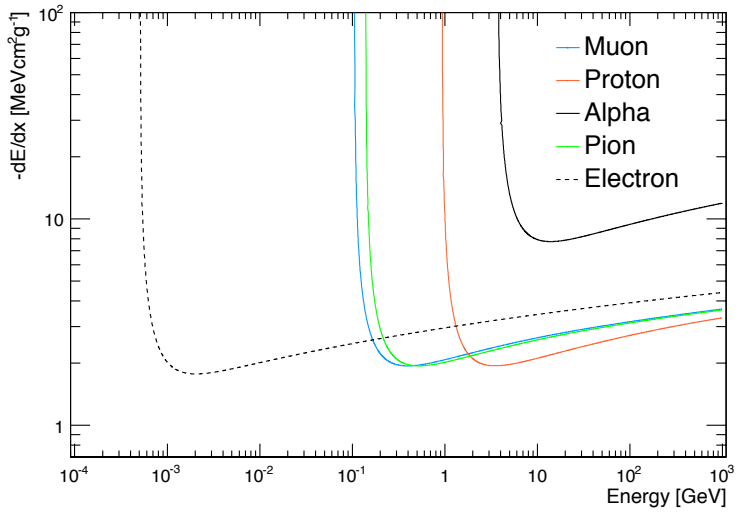

Fig. 2.1 The mean energy loss per unit length, $\langle dE/dx \rangle$, calculated from equation 2.1, shown for muons, protons, charged pions, alpha particles and electrons in Argon at 293 K and 1 atm, which 11.6 eV was used as the excitation energy and $\delta = 0$.

Here $\langle dE/dx \rangle$ is the mean rate of energy loss per unit length, where $N_A = 6.02214179(30) \times 10^{23}$ mol^{-1} is the Avogadro constant, r_e is the classical electron radius, z is the charge of the incident particle in units of e and with $\beta = v/c$. The Lorentz factor is $\gamma = 1/\sqrt{1-\beta^2}$ and I represents the mean excitation energy of the atom. The maximum kinetic energy that can be transferred from the incident particle, of mass M, to an electron, mass m_e, in a single collision is represented by T_{max}. This is determined by equation 2.2 [52]. The δ factor is a correction factor for density effects.

$$T_{max} = \frac{2m_e c^2 \beta^2 \gamma^2}{1 + 2\gamma m_e/M + (m_e/M)^2} \tag{2.2}$$

The energy loss for electrons in denser materials is mainly due to Bremsstrahlung and is not well described by the Bethe-Bloch equation but for cases when the mean free path is high then it can be considered minimum ionising. Application of this equation for heavy charged particles of interest such as muons, protons, pions, alpha particles and electrons can be seen over the energy range of 0.1 to 10^7 GeV in figure 2.1 for them traversing Argon.

The Bethe equation only describes the mean energy loss for moderately relativistic heavy charged particles. Particles with $\beta\gamma \lesssim 0.05$ fall outside this description with nuclear effects more important and no analytical description of their energy loss is

given. For highly relativistic charged particles of $\beta\gamma \gtrsim 500$, radiative effects begin to have greater influence, with pair production and Bremsstrahlung the dominant processes. For muons and pions this limit is reached at around several hundred GeV. Such large energies are not considered in this thesis and focus is on the 0.2 to 10 GeV scale, in the minimum ionising regime.

The heavy charged particle will interact with the electrons in the gas losing energy according to the equation 2.1 through the exchange of virtual photons. If the energy of such a photon is above the ionisation potential then this will cause ionisation. Further ionisation can occur from energetic electrons that escape the molecule, namely δ-rays. The majority of δ-rays will have small ranges compared to that of the incident charged particle, and ionisation remains close to the track.

On production of an ionisation pair, an electron and an ion, an electric field can be applied to the volume to introduce the drift of the electrons/ions, thus overcoming the Coulomb electron-ion attraction and ultimately reducing the recombination process. If purities and electric fields are high enough it then allows for the ability to drift over vast distances (several meters). Once charges have been drifted they can then be collected and read out, producing a two dimensional representation of the ionisation.

The equation of motion of charged particles subject to electric, $\mathbf{E}$, and magnetic, $\mathbf{B}$, fields can be described by equation 2.3, for a particle of velocity $\mathbf{v}$ of mass m and charge e. A frictional force proportional to the velocity is represented by $K\mathbf{v}$ to allow for interactions within the gas. The constant K is given in terms of the mean time between collisions, τ, with $K = m/\tau$, and drift velocities are calculated at times, $t \gg \tau$. It can be seen that if the magnetic field is non existent or perpendicular to the electric field then cross product effects are removed, resulting in a drift velocity that is independent of the magnetic field strength. This is a powerful technique as magnetic fields can also be required for momentum measurements in detectors.

$$m\frac{d\mathbf{v}}{dt} = e(\mathbf{E} + \mathbf{v} \times \mathbf{B}) - K\mathbf{v} \tag{2.3}$$

The magnitude of the drift velocity can then be written as proportional to the electric field strength in the drift direction, $|\mathbf{E}|\cos\phi$, as in equation 2.4. The mobility is then defined as $\mu = e\tau/m$ [56].

$$|\mathbf{v}| = \frac{e}{m}\tau|\mathbf{E}|\cos\phi \tag{2.4}$$

With electrons far lighter than ions, they are favourable for drifting, this not only increases their mobility and acceleration due to the electric field but also reduces

the energy loss due to collisions during drifts. The ability to drift electrons is a popular technique employed in many modern particle detectors. One of the dominant technologies in this field is the Time Projection Chamber (TPC). Argon and Xenon are the most favoured of the nobel gases for use in TPCs, due to their high densities and radio purities. Argon is far more common however, as it is far more abundant and therefore much cheaper for experiments requiring large detection volumes.

2.2.1 The Time Projection Chamber

Since the implementation of the Multi-Wire Proportional Chamber (MWPC) in 1968 [57] modern descendants of this technology such as the TPC are rife in many particle physics experiments. The MWPC revolutionised detector capabilities, yielding better resolutions and allowing for increased interaction rates. The MWPC uses a mesh of wires acting as anodes, equally spaced, placed between two cathodes to provide an electric field across the chamber [52]. Fairly constant electric fields can be established over the majority of the volume and electrons/ions are drifted along these field lines. As electrons are drifted towards the anode wires the intense electric field causes an avalanche and the charge is collected on the wires.

Drift chambers were introduced shortly afterwards which exploited the use of the time taken for the electrons to reach the anode wires. The introduction of cathode wires between anodes caused a reduction in the field between anodes, providing a more uniform field and increased charge collection. This can be seen in figure 2.2. Several geometries have been developed for detectors but they all rely on the measurement of the drift position from the drift time. With timing precisions of a few ns, resolutions of $\sigma(x)$ $\sim$100 μm can be achieved. Diffusion of electrons is the main limitation to this device which is increased over large drift distances.

The TPC is considered the improved drift chamber with the concept introduced in 1976 [51]. They employ both concepts of the MWPC and Drift Chambers, using MWPCs to readout charge after being drifted. As a result TPCs can provide a 3-dimensional view of charged particles traversing the detector. Using a uniform electric field applied across the volume ionisation can be drifted, produced from a passing track, to a readout end plate. This provides a 2-dimensional view of the track with the third determined from the drift time. Knowledge of the electron drift velocity, the diffusion in the medium and accurate modelling of the electric field must be well understood in order to provide an accurate description of the track.

Argon is commonly implemented for TPCs, and with drift speeds of the order of

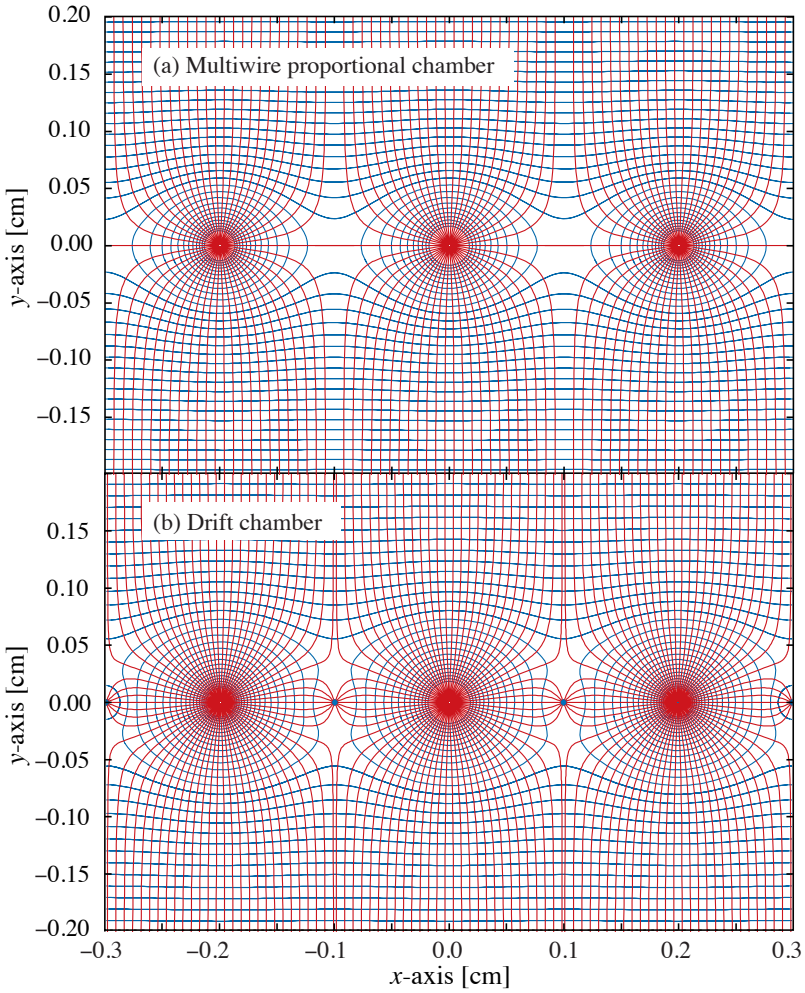

Fig. 2.2 The difference between MWPC and Drift Chamber field lines. Image from [52].

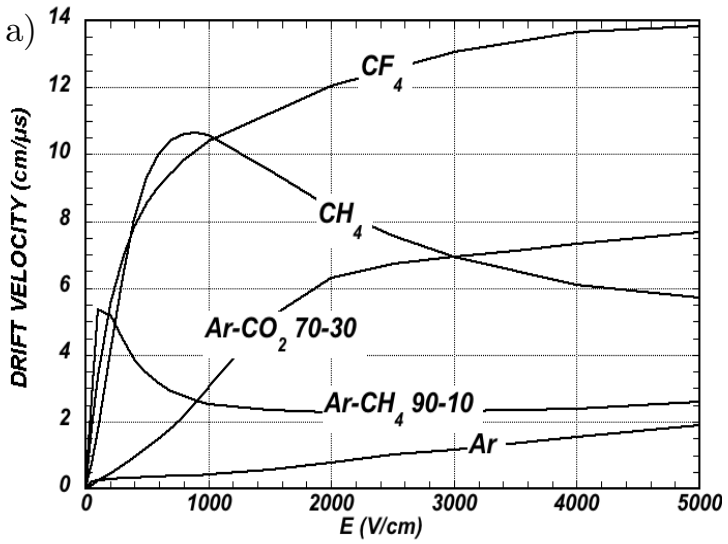

Fig. 2.3 The electron drift velocities for various gases including combinations with Argon. Ar, Ar (90%) + CH_4(10%), Ar (70%) + CO_2(30%), CH_4 and CF_4 are shown. Image from [51].

cm/μs for LAr, good resolutions can be achieved in the drift direction $\sigma(z)$ ~100 μm. However with large drifting volumes of 1 m and above, high voltages are required. Also coupled with slow drift times ~100 μs and slow readout, pileup can become an issue with this detector technology. Hence they are not well suited as detectors where high event rates are possible.

It is best to operate these detectors in proportional mode, so that the number of electrons produced remains proportional to the measured signal. However during amplification, avalanches occur that cause further ionisation and further photon emission, introducing additional charge that can result in the loss in proportionality. The removal of these photons is done by the additional of quench gases (such as isobutane, methane or CO_2) to the noble gas. The high Ultra Violet (UV) photon cross sections of these molecules results in the absorption of the scintillation light and helps maintain proportionality. Another benefit of the addition of the quench gases is the increase in electron drift velocity due to the reduction of the electrons energy and its scattering cross section. The use of quench gases restricts the detection method to ionisation but the implementation of noble gases as scintillation detectors can be employed when high purities are obtained. The effect on the drift velocity in Argon can be seen in figure 2.3 [51].

2.3 Noble Gases as Scintillation Detectors

The notion to use noble gases as scintillation materials first arose in 1951 when Grün and Schopper implemented the first noble gas scintillation counter[58]. Since then the technology has developed to facilitate the use for nuclear radiation spectrometers, high energy calorimeters and other implementations. The attractiveness of their use as scintillation media is due to several reasons:

- High light yields
- Transparency to own scintillation light
- Fast scintillation light decay times
- Good linearity of scintillation yield over E and dE/dx
- Attainable high purities
- Scalability in detectors

When a particle deposits energy in the detector medium it transfers its energy to the atoms within the noble gas and will either excite or ionise them. Upon excitation an electron is raised to higher potential, they then can de excite or in denser materials collide with neighbouring atoms and combine to form an excited diatomic molecular state. This excited molecule then subsequently de excites emitting a Ultra Violet (UV) photon, via the process

$$A^* + A \rightarrow A_2^* \tag{2.5}$$

$$A_2^* \rightarrow 2A + h\nu \tag{2.6}$$

where A represents the noble gas atom, and A^* represents the excited state. The excited diatomic state, A_2^*, can also be formed via ionisation. Upon ionisation a free electron and charged ion pair are created. Again neighbouring atoms can combine to form an ionised molecule, which in turn follows a recombination process with a free electron, via the process

$$A^+ + A \rightarrow A_2^+ \tag{2.7}$$

$$A_2^+ + e^- \rightarrow A_2^* \tag{2.8}$$

Here A^+ and e^- represent an ionisation state and electron respectively. Upon recombination, an excited molecule remains which de excites again producing a UV photon.

The two processes produce a fast and slow scintillation component with relaxation times of the order of 6 ns and 1-1.6 μs respectively in liquid argon [59]. This process leading to the photon emission is shown in figure 2.4. The fast and slow components of the scintillation light can allow for Pulse Shape Discrimination (PSD) analysis, which can provide information on incident particles and help discriminate between them in the detector.

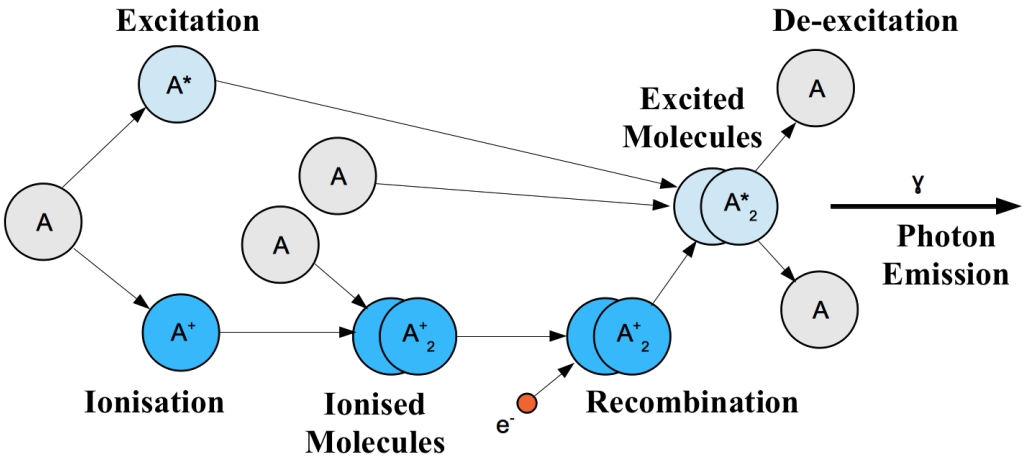

Fig. 2.4 A graphical representation of the excitation and ionisation processes in noble gases to produce scintillation light. Image based on figure from [59].

High light yields have been achieved for noble gases with scintillation yields of ~46,000 γ/MeV for gas xenon and ~40,000 γ/MeV for gas argon [59]. Coupled with the ability to have very pure gases allows for transport of the scintillation light with the medium. However with wavelengths below 180 nm, it is difficult to detect these photons with current Photo Multiplier Tubes (PMT's) and most detectors employing noble gases use wavelength shifters to absorb and emit the light to a lower frequency, with wavelengths of around 400 nm.

Xenon is considered the most favourable option of the noble gases for scintillator detectors, mainly due to its high atomic number, high density and it containing no radioactive isotopes. Being the most expensive to produce, as the least abundant of the 5, it is therefore best suited for small scale detectors. Argon is a more suitable candidate for larger detector volumes as it is far cheaper and also has good scintillation properties. Contrary to this low atomic numbers can also be favourable for detectors that rely on elastic scattering, such as neutron detection. In this case helium is the

superior choice of the noble gases due to its low atomic mass number. As from equation 1.8, it can be seen that up to 64% of its kinetic energy can be transferred per scatter for ^{4}He. Table 2.2 shows the energy transfer ratios for various noble gas isotopes, calculated from equation 1.8.

Noble Gas	**Maximum energy transfer per scatter**
^{4}He	64.0%
^{20}Ne	18.1%
^{40}Ar	9.5%
^{84}Kr	4.7%
^{129}Xe	3.1%

Table 2.2 The maximum kinetic energy transfer kinematically permitted for various noble gas isotopes. Values based on calculations from equation 1.8.

Chapter 3

The LAGUNA-LBNO Experiment

LAGUNA-LBNO (Large Apparatus studying Grand Unification and Neutrino Astrophysics and Long Baseline Neutrino Oscillations) is a feasibility study for the design and implementation of a next generation neutrino experiment [60]. With the existence of massive neutrinos showing the only experimentally observed deviation from the Standard Model, they can be key to probing our deeper understanding of the universe. The experimental project of LAGUNA-LBNO is discussed in this chapter to give an overview of the aims, setup and its relevance to neutrinos.

3.1 The CERN-Pyhäsalmi Baseline

The LAGUNA-LBNO experiment consists of a neutrino beam originating from a facility within CERN (European Organisation for Nuclear Research) in Geneva, aimed to a Far Detector based in Pyhäsalmi, Finland, at a distance of 2300 km away. A Near Detector (ND) of gas argon technology is proposed while the FD technology is uncertain with either liquid argon, Water Cherenkov or liquid scintillator design suggested, respectiviely GLACIER [61], MEMPHYS [62] and LENA [63].

The Pyhäsalmi mine in Finland is the host site for the FD and at -1440 m the mine is the deepest in Europe, allowing unique opportunities for neutrino and astrophysics. With an extremely large baseline of 2300 km neutrino oscillation matter effects are no longer negligible and can be exploited to determine the mass hierarchy of neutrinos. It can also provide the most accurate measurement of the CP-violating phase factor, δ, given that θ_{13} is now found to be large. With a distance close to the bimagic baseline[26] it puts us in a unique position to exploit the $P(\nu_\mu \rightarrow \nu_e)$ transition. Figure 3.1 shows the appearance channel as a function of incoming neutrino energy for the

CERN-Pyhäsalmi baseline, with oscillation parameters from table 1.1 used. The two hierarchies are shown with varying values for δ. The vacuum oscillation is also plotted for which matter effects are not considered and shows the 1^{st} oscillation maximum around 4.6 GeV. The difference between the two hierarchies becomes apparent above 4 GeV when using matter effects, regardless of the value of δ. Figure 3.2 shows the $P(\nu_\mu \rightarrow \nu_\mu)$ transition and it can be seen that it is independent of δ, so to measure CP-violation the appearance channel must be used.

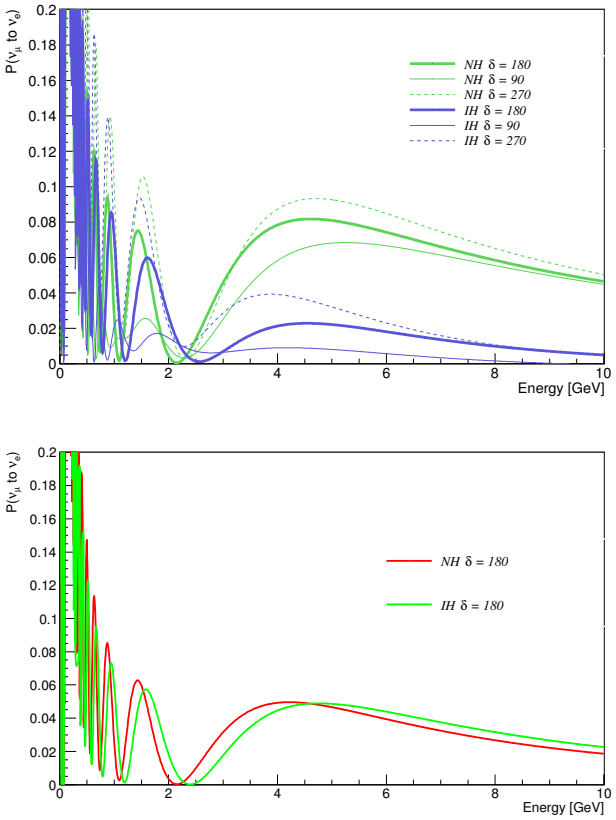

Fig. 3.1 The appearance channel probability as a function of incoming neutrino energy for the Pyhäsalmi baseline with matter effects (upper) and without (lower).

To quantify CP violation is it useful to define asymmetries between the oscillation probabilities for neutrinos and antineutrinos. These are given for vacuum and matter probabilities in equations 3.1 and 3.2 respectively. These two asymmetry variables are plotted in the neutrino energy against baseline plane and are shown in figure 3.3 [64] for fixed values of $\delta_{CP} = 270$ °and Earth matter density of 2.8 gcm^{-3}. At 2300 km clear separation between the first and second maxima is noticeable and achievable for

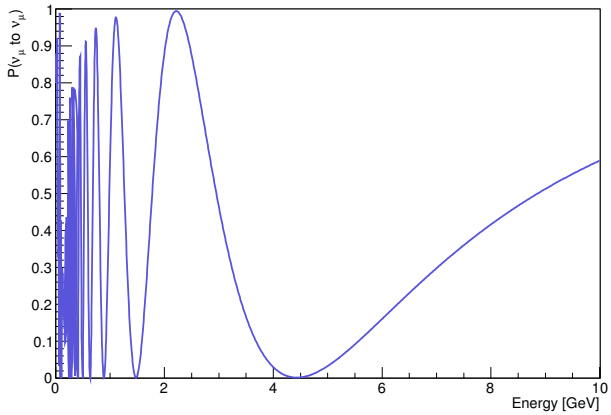

Fig. 3.2 The disappearance channel probability as a function of incoming neutrino energy for the Pyhäsalmi baseline for which is independant of δ_{CP}.

a wide band beam.

$$A_{CP}^{vac}(\delta_{CP}) = abs\left(\frac{P^{vac}(\nu) - P^{vac}(\bar{\nu})}{P^{vac}(\nu) + P^{vac}(\bar{\nu})}\right) \tag{3.1}$$

$$A_{CP}^{mat}(\rho) = abs\left(\frac{P^{mat}(\nu) - P^{mat}(\bar{\nu})}{P^{mat}(\nu) + P^{mat}(\bar{\nu})}\right) \tag{3.2}$$

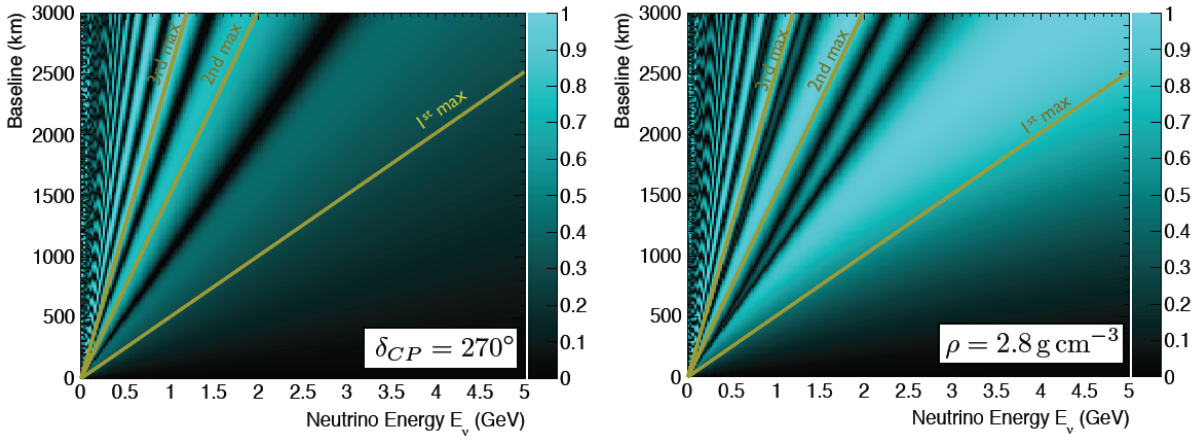

Fig. 3.3 The two asymmetries in vacuum (left) and in matter (right) of density 2.8 gcm^{-3} as a function of neutrino energy and baseline. First, second and third maxima are shown for constant L/E values. Plots taken from [64].

Considering that the Pyhäsalmi site provides the largest baseline of the seven, the

required neutrino energy must be large due to the L/E optimisation. This baseline does not favour MEMPHYS, as Water Cerenkov detectors are used for energies below the 1 GeV region. In this energy region CCQE events dominate and Water Cerenkov's can reconstruct such events well, with general CCQE events producing a single ring for muons and multiple rings for electrons. For the energies required for a 2300 km baseline with 1^{st} oscillation maximum at 4.6 GeV, dominant processes are then resonance (RES) and Deep Inelastic Scattering (DIS). This is not favourable to Water Cerenkov technology as this produces large amounts of rings which cannot be reconstructed. Liquid Scintillator poses to overcome these problems with current studies [63] arguing that reconstruction can work for energies above 1 GeV, although this technology is limited by Neutral Current (NC) backgrounds. The technology that is preferred for such a baseline is the LAr detector, GLACIER, due to its reconstruction properties at high energies.

3.2 Physics Potential

The 2300 km baseline coupled with the GLACIER detector offers a rich and broad physics program for neutrino oscillations and other particle physics studies, including nucleon decay searches. In terms of neutrino physics the LAGUNA-LBNO experiment offers unrivalled opportunities to precisely measure and resolve the neutrino mass hierarchy, reaching this to beyond a 5σ confidence level (C.L) within $\sim$4 years of running [65], shown in figure 3.4. It also has the potential to discover evidence for CP violation in the leptonic sector, with a 20 ktonne GLACIER detector covering $\sim$45% of possible CP values at 3σ C.L. This is shown in figure 3.5. Current experiments like T2K and NOνA are less sensitive to these effects due to shorter baselines and lower neutrino energies.

3.3 Generating Neutrinos

Unlike solar, atmospheric and reactor neutrino oscillation measurements, long baseline oscillation experiments are tailored to the physics requirements, where neutrinos are created and controlled at a source. Neutrinos are generated from the decay of short lived particles, and depending on the type of the parent particle then defines the neutrino beam type. Conventionally, high energy protons are fired into a target to create secondaries, consisting of charged mesons, which in turn decay into neutrinos. This is a conventional neutrino beam. The dominant decay chain from this type of

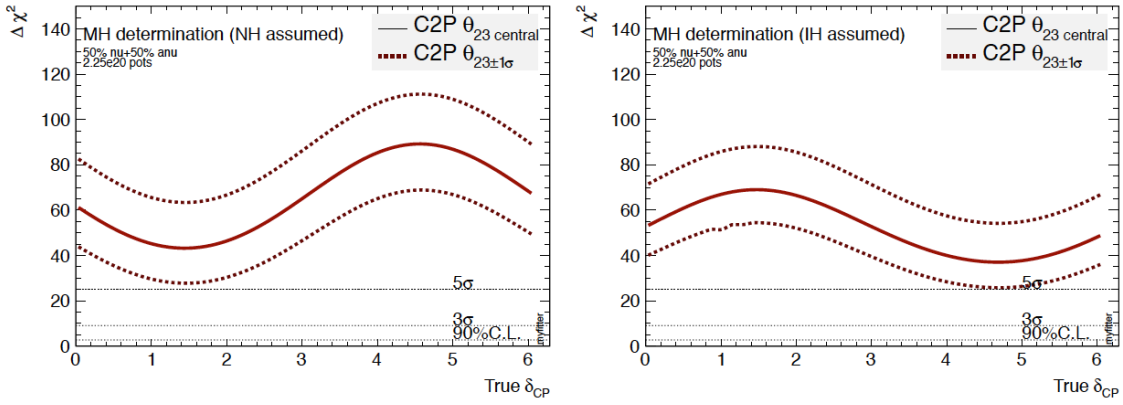

Fig. 3.4 The mass hierarchy determination for normal (left) and inverted (right) hierarchies. Showing in excess of a 5σ C.L for both cases. Plots taken from [65].

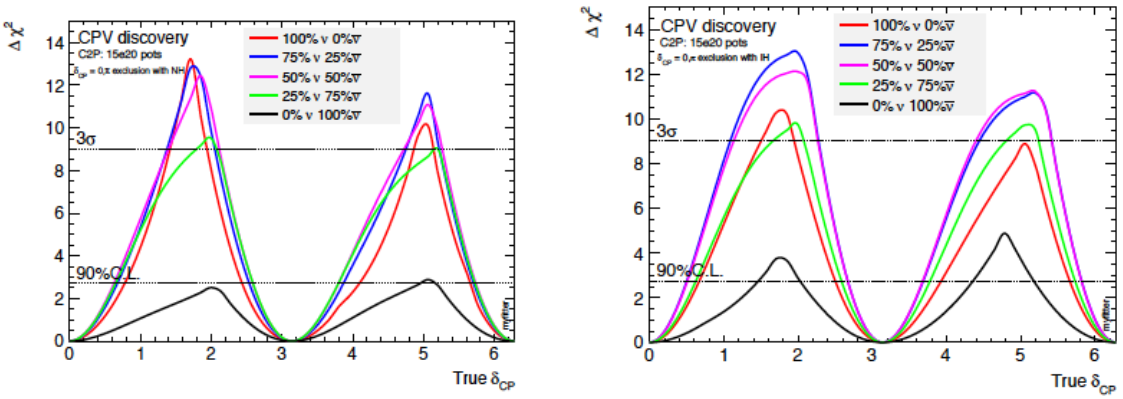

Fig. 3.5 The CPV sensitivity for various ν and $\bar{\nu}$ beam sharing modes for a 20 ktonne GLACIER detector. The different contours show the CPV discovery potential for various levels of beam sharing modes (ν,$\overline{\nu}$), red indicates (100%,0%), blue (75%,25%), purple (50%,50%), green (25%,75%), black(0%,100%). The left plot shows the discovery potential for NH with the right plot showing it for the IH. Plots taken from [65].

beam is,

$$\pi^{\pm} \rightarrow \mu^{\pm} + \overset{(-)}{\nu}_{\mu} \tag{3.3}$$

but it is also possible to have,

$$\pi^{\pm} \rightarrow e^{\pm} + \overset{(-)}{\nu}_{e} \tag{3.4}$$

however this decay mode is helicity suppressed and has a small branching ratio measured as $(1.230 \pm 0.004) \times 10^{-4}$ [42]. Kaons can also decay via these chains generating a leptonic pair of a muon and neutrino, however they can also decay via other modes involving three body decays, generating larger amounts of electron neutrinos. Table 3.1 shows the main decay modes with their corresponding branching ratios observed from experiments [66].

Decay Mode	**Branching Ratio (%)**
$\mu^{+}\boldsymbol{\nu_{\mu}}$	63.55 ± 0.11
$\pi^{+}\pi^{0}$	20.66 ± 0.08
$\pi^{+}\pi^{+}\pi^{-}$	5.59 ± 0.04
$\pi^{0}e^{+}\boldsymbol{\nu_{e}}$	5.07 ± 0.04
$\pi^{0}\mu^{+}\boldsymbol{\nu_{\mu}}$	3.353 ± 0.034
$\pi^{+}\pi^{0}\pi^{0}$	1.761 ± 0.022

Table 3.1 The main decay modes (>1%) of K^{+} with its corresponding branching ratios. K^{-} decay modes are the same but are charge conjugated. Data taken from [66].

Muons produced from these mesons can decay before being stopped and they introduce further contamination to the beam via

$$\mu^{-} \rightarrow e^{-} + \overline{\nu}_{e} + \nu_{\mu} \tag{3.5}$$

$$\mu^{+} \rightarrow e^{+} + \nu_{e} + \overline{\nu}_{\mu}. \tag{3.6}$$

Contaminations of other neutrino flavours can cause problems for oscillation searches due to these wrong flavour neutrinos reaching the far detector.

Neutrino factories aim to remove this contamination by using only the decays of muons to create neutrinos. From the pion decays, muons are collected in storage rings and accelerated to the desired momentum. They are then optimised for $\nu_{\mu} \rightarrow \nu_{e}$ and $\overline{\nu}_{\mu} \rightarrow \overline{\nu}_{e}$ searches as a magnetised detector can then identify the sign of the muon and hence measure oscillation parameters. Unfortunately currently neutrino factories are a relatively new idea and are extremely expensive. Ongoing studies are working towards developing the technology and maximising their sensitivities but there is no immediate

demand to implement these beams in the near future. This technology would indeed provide a very clean beam and dramatically reduce the systematical uncertainties that arise from the beam, but as θ_{13} has recently been measured to be non-zero makes the mass hierarchy and CP violation accessible with conventional beams.

3.4 The Beam Facility

LAGUNA-LBNO proposes to use a conventional neutrino beam approach from a new facility Cern Neutrinos to Pyhäsalmi (CN2PY). The current layout of the main accelerators at CERN are shown in figure 3.6. Two beam options exist, a 50 GeV proton extraction from a newly proposed synchrotron, the High Power Proton Synchrotron (HP-PS) or 400 GeV proton extraction from the existing Super Proton Synchrotron (SPS) beam line at CERN. Both Positive Focusing (PF) and Negative Focusing (NF) options are required for each beam line yielding ν_μ and $\bar{\nu}_\mu$ runs respectively.

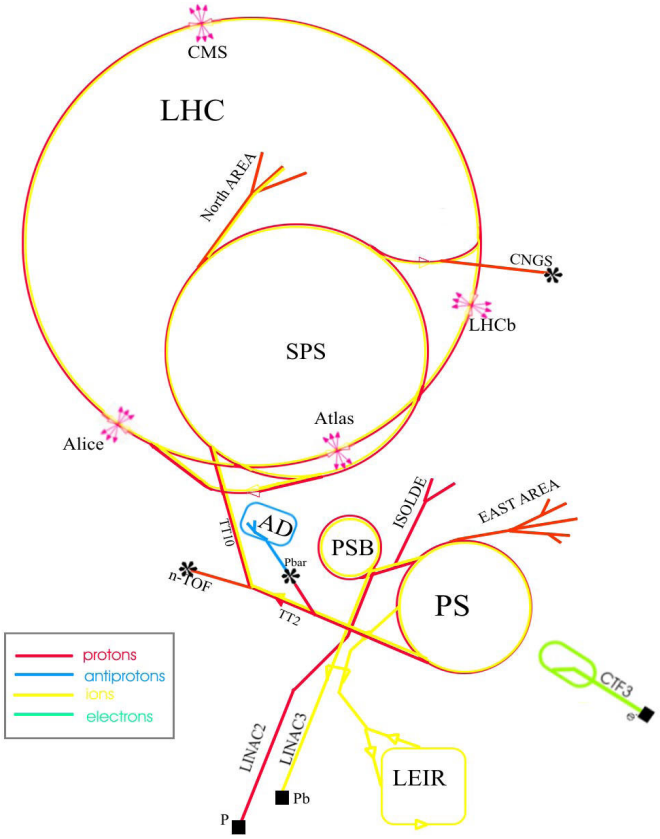

Fig. 3.6 The accelerator and beam complex at CERN. Image from [67].

3.4.1 400 GeV Option

The first step in the beam is the Linear Accelerator 2 (Linac 2), consisting of cylindrical conductors operating at radio frequency. Protons are created from a hydrogen gas source at one end of the Linac 2, by initially passing the hydrogen through an electric field the removal of its electrons leaves only the protons. The protons are then accelerated to energies of 50 MeV upon reaching the other end of the Linac 2. Small quadrupole magnets are required to ensure that the beam is kept tight. The protons are extracted in pulses from the hydrogen source over periods of up to 100μs per pulse.

Upon leaving the Linac 2, they then enter the Proton Synchrotron Booster (PSB) to increase their energy. The PSB consists of four superimposed synchrotron rings which accelerate the protons to 1.4 GeV for injection into the Proton Synchrotron (PS). The PS then accelerates the protons to 25 GeV to which they are subsequently injected into the SPS to reach energies of 400 GeV, at which point they are extracted from the SPS.

It is proposed that per 10.5 μs extraction from the SPS a rate of 7×10^{13} protons on target (p.o.t) per proton pulse (ppp) can be achieved. This is based on two extractions per 6 s cycle of 3.5×10^{13} p.o.t from the SPS, separated by 50 ms intervals. The corresponding instantaneous SPS beam intensity is then $\sim 1.2 \times 10^{13}$ protons per second at 400 GeV, equivalent to a beam power of $\sim$750 kW.

Assuming a pessimistic operation with 60% beam sharing, 85% accelerator efficiency and yearly run period of 200 days its expected to obtain $\sim 1.0 \times 10^{20}$ p.o.t / year [64].

3.4.2 50 GeV Option

The 50 GeV option relies on the new Linear Accelerator (Linac 4) which is expected to be completed for 2018. This will use negative Hydrogen ions (H^-), which are Hydrogen atoms with an additional electron, as the source. Again the electrons will be removed upon passing an electric field but this will accelerate them to 160 MeV. Besides the higher proton energy, the Linac 4 will allow more protons to accumulate with a simpler injection and therefore provide a better beam.

Upon leaving the Linac 4, the protons are injected into the High-Power Proton Synchrotron (HP-PS) upon which they are accelerated to 50 GeV. This design is very much in progress with technical studies ongoing, however some basic estimations can be made. It is assumed that a beam power of 2 MW can be achieved with 2.5×10^{14}

ppp and a superior extraction rate of 1 Hz compared to the 400 GeV option.

3.4.3 Layout

Both beam options require similar design layouts, although there is a higher level of uncertainty for the 50 GeV option due to the location of the HP-PS. The beam layout for the 400 GeV option is discussed only, as this is beam option of choice for the majority of the studies in this thesis. The proposed location for the beam facility is in the north area of CERN, and it can be seen in figure 3.7 where the extraction point and ND will be placed.

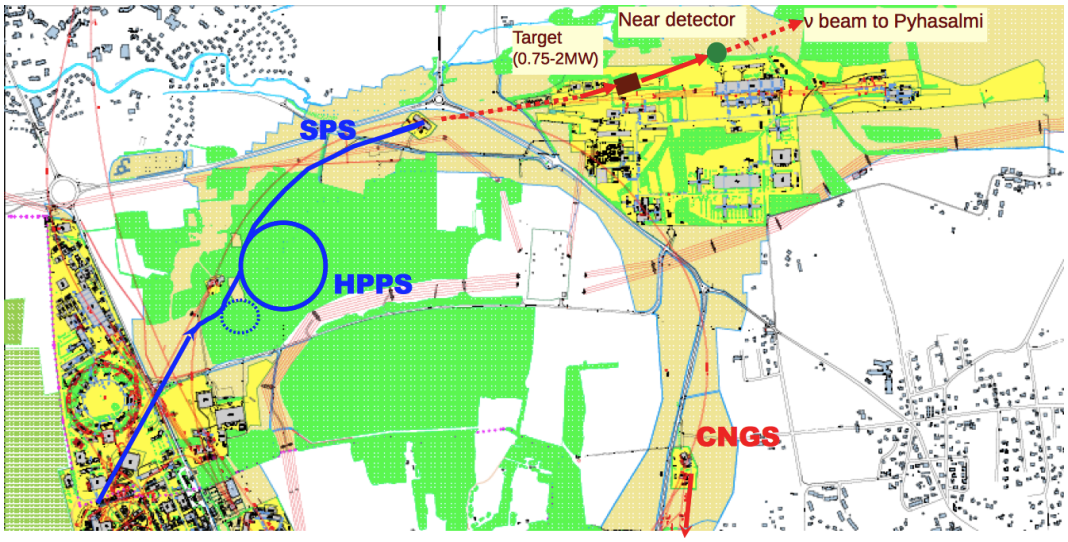

Fig. 3.7 The expected location for the beam facilities and ND in the north area of CERN [65].

3.4.4 Design

A 10.4° inclination angle is required to reach the Pyhäsalmi site, after extraction from the SPS the protons are bent to this angle shortly before hitting the beam target. A 1 m long graphite cylinder of density 1.85 gcm^{-3} and radius of 2 mm forms the beam target. Shortly after the target magnetic parabolic horns are used to focus the secondaries into the decay pipe. The horns are optimised primarily for the ν_μ energy at the first oscillation maximum, with consideration to incorporate the flux at the second oscillation maximum also, at 1.44 GeV.

A 300 m long decay pipe allows for the decay of the mesons produced with a hadron stop at the end of the pipe to collect all non decayed hadrons. With muons passing through the hadron stop a muon monitor is placed at 30 m downstream to this in order to measure the muon flux.

The path the neutrinos will follow to Pyhäsalmi can be seen in figure 3.8. This shows the estimated matter composition and approximate densities of the Earth's crust according to geological studies [68].

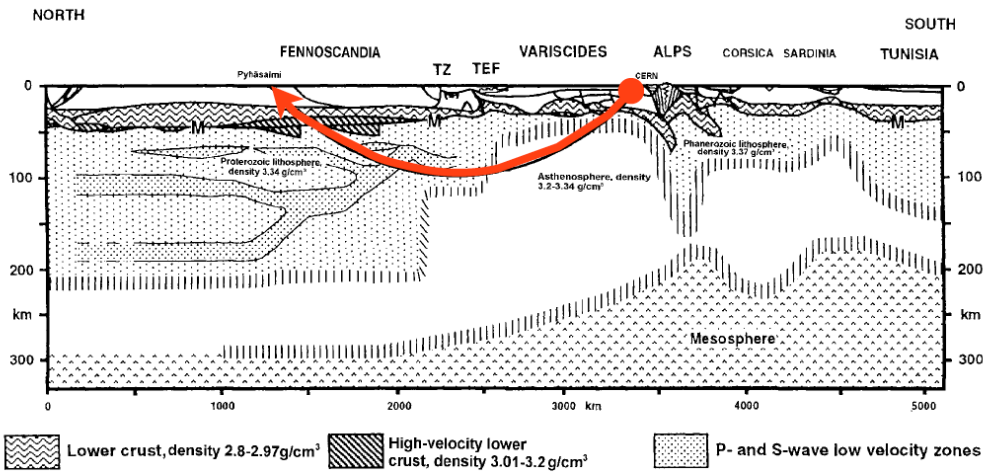

Fig. 3.8 The path of the neutrinos from CERN to Pyhäsalmi (red) shown against the main tectonic elements of Western Europe with the corresponding densities [68][65].

3.5 The Expected Neutrino Flux

Following from the implementation of the beam design into the simulation package FLUKA[69], the unoscillated neutrino fluxes expected at the FD can be determined as a function of neutrino energy. The expected neutrino flux at both the ND (placed at 800 m from the target, 3 m radius cut) and FD (2300 km from the target and 1 km radius cut) is then shown in figure 3.9 for both beam options and positive focusing runs. Each beam option is normalised to the beam power. It can be noticed that for both beam options the fluxes at both the near and far detectors are very similar in shape and hence will provide a fairly constant Near/Far ratio.

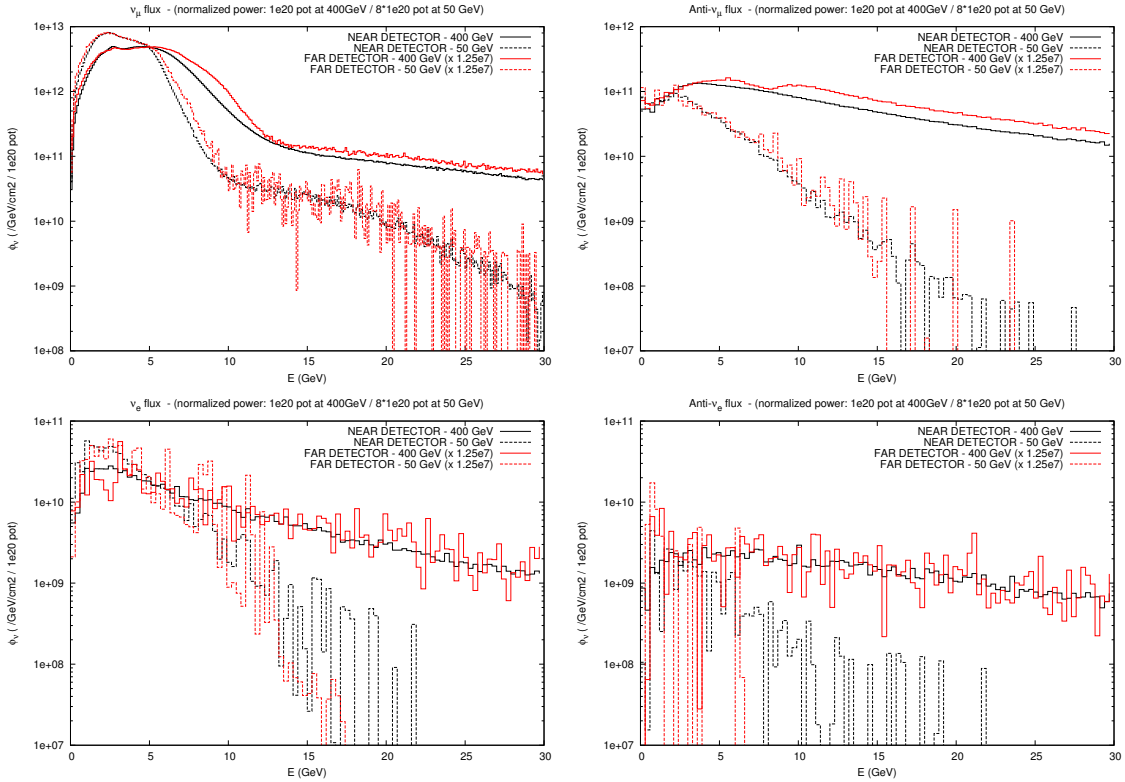

Fig. 3.9 Clockwise from top left: ν_μ, $\overline{\nu}_\mu$, $\overline{\nu}_e$ and ν_e spectra for horns set to positive focusing (ν_μ run). Both beam options, 50 and 400 GeV beams are shown for near and far detectors (unoscillated) with a 3 m and 1 km radius cut respectively. The beams are normalised to equivalent beam power [65][70].

3.6 The Near Detector

Fundamentally the ND is required to perform measurements on the neutrinos before oscillation and is used to extrapolate the flux to the FD. This however introduces systematic errors but which can be reduced by matching target materials of both near and far detectors. A Gas Argon (GAr) TPC design in proposed as the ND and the feasibility of such an instrument is the focus of this thesis. GAr is chosen as the target material instead of its liquid counterpart due to its lower density (∼40 times less at 20 bar), resulting in fewer neutrino interactions in the ND and avoiding pile up, improved charged track reconstruction and also benefits from the lack of cryogenics. However implementing a pressurised GAr TPC introduces some technical and engineering problems that must be also be considered. Details of the ND are covered in the following chapter.

With the ND completing the facilities at CERN a summary of the estimated distances of each instrument is shown in table 3.2.

Component	**Distance [m]**	**Depth [m]**
Beam Target	0	0
Hadron Stop	300	-54.2
Muon Monitor	330	-59.6
Near Detector	800	-144.4

Table 3.2 The relative distances and depths for each beam and detector component at the CERN facility.

3.7 The Far Detectors

3.7.1 GLACIER

An incremental approach is taken for the FD design, initially considering a 20 ktonne detector, with 50 ktonne and 100 ktonne options available for future upgrades. However due to cavern excavation restrictions, a cavity big enough to host a 100 ktonne detector is not possible, so it would comprise of two 50 ktonne detectors. The 20 ktonne detector is assumed for this study and its concept is described. Larger volumes would follow from this design with all three sizes employing a 20 m drift distance but with larger volumes having increased vessel diameters.

The 20 ktonne GLACIER detector is of cylindrical design, with the flat ends forming the top and bottom of the detector, with the design shown in figure 3.10. The inner vessel diameter of 37 m and inner height of 22 m yields a volume of 23654.6 m^3 of Argon. At a depth of 1400 m in the Pyhäsalmi mine the pressure is approximately 1.2 bar, this corresponds to a density of 1.38 gcm^{-3} for liquid Argon. The total mass is then 32.7 ktonnes assuming constant density across the whole volume. An active instrumented mass of the detector is then 22.8 ktonnes. [64]. Due to hydrostatic pressure of the Argon in the vessel the pressure on the bottom of the vessel is 4.2 bar.

The detector operates in double-phase (liquid-vapor) using charge readout and amplification in the vapour phase. An octagonal field cage creates a uniform electric field in the vertical direction. The cage is composed of equally spaced stainless steel rings which are held in place with a series of mechanical structures. The support structure is then suspended by stainless steel ropes from the outer deck of the detector. To acquire drift velocities of electrons at $\sim$2 mm/μs a field strength of 1 kV/cm is required. Over a 20 m drift distance this corresponds to a high voltage of 2MV.

The charge is read out at the top of the detector which also functions as the anode, with the cathode at the bottom of the tank. The charge readout consists of 804 square panels, each of 1 m^2 and 40 triangular panels of 0.5 m^2 for the curved ends. 416 signal feedthroughs are required to channel the readout signals, these are located in the roof of the vessel.

In addition to charge readout the design implements the collection of scintillation light also, with an array of PMTs placed below the cathode. One 8" PMT is placed per 1 $\times$ 1 m^2 area, resulting in 804 PMTs on the base of the vessel. They each have a buoyancy of $\sim$4 kg in liquid Argon and are anchored to the bottom of the tank to compensate for this. They must also be able to withstand the 4.2 bar hydrostatic pressure.

3.7.2 Magnetised Iron Neutrino Detector

The Magnetised Iron Neutrino Detector (MIND) is also proposed as a FD in addition to GLACIER. It is a sampling calorimeter consisting of alternating iron and scintillator layers. This follows from the MINOS detector design [49], which is a well proven technology for neutrino detection. It is proposed to complement the primary FD as, unlike GLACIER, it is magnetised so it can perform charge identification and momentum measurements. The majority of high energy muons (>5 GeV) produced from neutrino interactions in the Argon will not be contained within the GLACIER

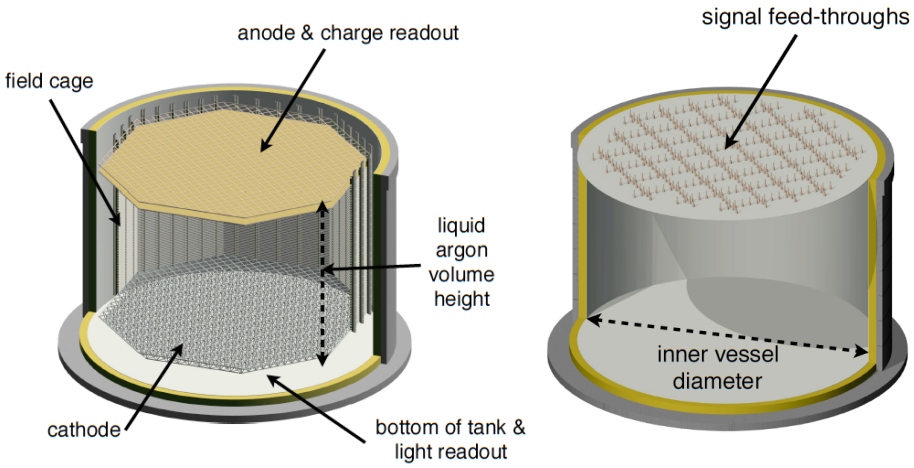

Fig. 3.10 The labelled components of the GLACIER detector design. Image from [65].

detector. Placement of the MIND downstream of the GLACIER detector is then necessary.

A 40 m × 20 m × 10 m MIND is considered, with a width and height to match that of the GLACIER detector. Each iron layer is of 3 cm thickness and each scintillator layer thereafter is 2 cm thick. This corresponds to a mass of ∼38 ktonne of iron and ∼9 ktonne of scintillator if a box shape is employed. Values and parameters of the design are at a preliminary stage as little effort has been put into the MIND design. It is estimated that a magnetic field strength of between 1.5 and 2.5 T is required [65]. A sketch of the design is shown in figure 3.11 with its proposed integration with the GLACIER detector shown in figure 3.12.

3.8 The Pyhäsalmi Site

The site itself is currently a working mine but is planned to be decommissioned around 2018 enabling the mine to be fully devoted to the experiment after this date. The mine has excellent existing infrastructure, with excavated roads allowing vehicles to drive to the maximum depth of the mine. The existing infrastructure layout is shown in figure 3.13. Excavations will still be need to be performed in order to host the detectors however, with costs estimated at ∼100 million EUR [65].

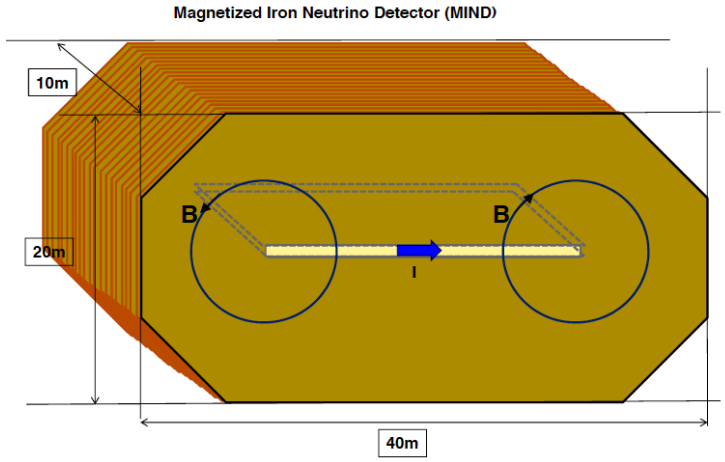

Fig. 3.11 The sketch of the potential MIND design. Image from [65].

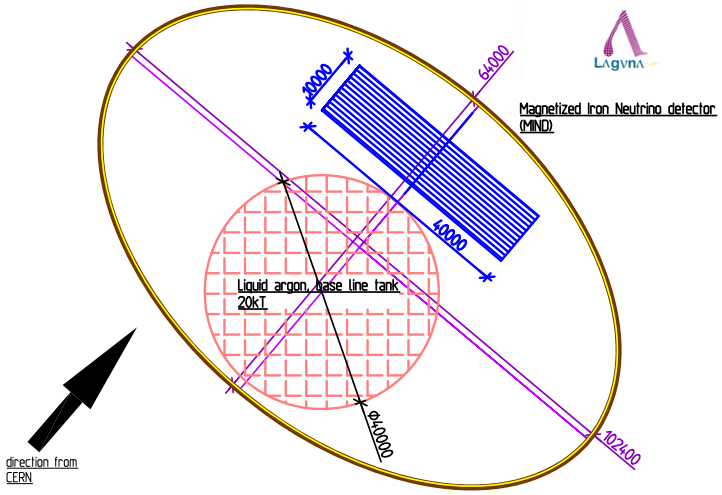

Fig. 3.12 The proposed layout for both the GLACIER and MIND far detectors with dimensions in mm. Image from [65].

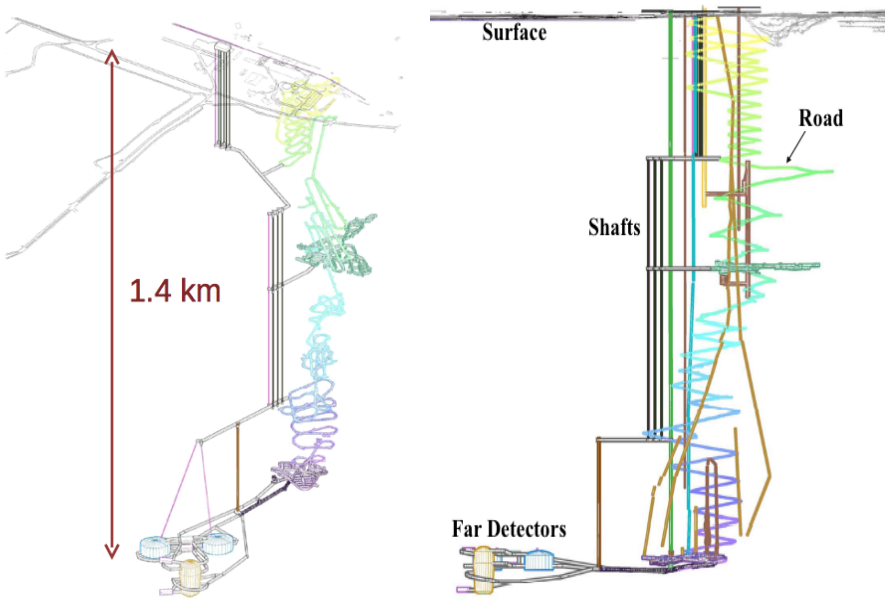

Fig. 3.13 The current layout of the Pyhäsalmi mine with possible implementation of the detectors at a depth of 1400 m. Image from [65].

Chapter 4

The LAGUNA-LBNO Near Detector Concept

The ND is a crucial instrument for neutrino oscillation measurements. It provides details of the unoscillated flux, including measurements of the neutrino beam direction and profile. Measurements of the energy spectrum and electron neutrino contamination are also monitored with the ND. The systematics and accuracy of the ND can constrain the precision of the whole experiment, so great care must be taken in the design and construction of such a detector. With little neutrino cross sectional data in the medium energy regime, the ND can also function to perform such precision measurements.

With LAGUNA-LBNO being a feasibility study, there is no concrete design of the ND. Liverpool University was heavily involved with the ND design since the formation of the LAGUNA-LBNO collaboration and proposed the initial detector design and technology. With collaborations within the LAGUNA-LBNO project this design was refined and investigated, with Liverpool the driving force in the design. I was personally involved with all ND efforts and represented the University of Liverpool within the collaboration. For the LAGUNA-LBNO experiment we propose a Gas Argon (GAr) Time Projection Chamber (TPC) with surrounding scintillator layers and this chapter hopes to introduce the overall concept of the detector with a discussion on the requirements imposed on the ND.

4.1 Requirements

The ND must be able to:

- **Measure the absolute neutrino flux:** The Near/Far ratio is used to extrapolate the flux at the ND to the FD without oscillation. Many factors are required for an accurate measurement of this, with descriptions of the beam profile, direction and neutrino energies of big concern.

- **Monitor the beam contamination:** It is important to know the electron neutrino contamination of the beam, as an accurate understanding of the beam composition reduces the uncertainty on oscillation measurements in the FD. The electron contamination of the beam is a large background for electron neutrino appearance measurements and must be well understood. Using a magnetised ND will allow for charge identification and will discriminate between charged leptons produced from CC interactions.

- **Perform cross sectional measurements:** With a poor understanding of neutrino cross sections on different materials, it is important for present and future experiments to understand their interactions better. There is a need within the neutrino community to perform accurate cross sectional measurements in the medium energy regime (several GeV). Without new and improved measurements then experiments will be limited by these systematical uncertainties. The FD cannot perform such measurements due to neutrino oscillations and hence must be performed at the ND.

4.2 The Detector Design

As a result of the requirements imposed, the ND must poses the ability to reconstruct the energy of the neutrino, the interaction point (vertex) and flavour of the neutrino. In order to perform this a multilayer detector is proposed, consisting of two main sections, the TPC and the scintillator layer (TAS):

- **Primary Detector - Time Projection Chamber (TPC):**
  - Vertex location and tracking
  - Perform momentum measurements on charged particles

  - Charged particle identification

- **Secondary Layer - Totally Active Scintillator (TAS):**

  - Additional particle identification
  - Neutral particle energy reconstruction, π^0's and γ's

These sub detectors are discussed sequentially.

4.3 The Time Projection Chamber

Both beam options offer neutrinos with a broad energy spectrum, peaking between 1-7 GeV, and in this energy regime DIS events dominate. In order to deal with the high multiplicities of such interactions the primary detector must be able to resolve and reconstruct multiple tracks. A clear candidate for the detection medium in the ND is argon, primarily due to its ability to deal with high multiplicity events with very good position reconstruction. It is also important for the target material to match that of the FD to reduce systematical uncertainties in oscillation measurements, avoiding nuclear effects and uncertainties in material cross sections. With the FD chosen to be of either GLACIER or LENA technology then argon and carbon are likely candidates for the ND target material. Considerable favour has fallen to the former technology in the LAGUNA-LBNO study and coupled with the many benefits of using noble gases as detection media, argon is implemented as the primary detector medium.

The FD of GLACIER technology comprises of LAr with a GAr amplification phase, operating in both charge and light collection modes. However such a design is not recommended for the ND with GAr used as the sole medium. Argon is liquid below 87.26 K and hence requires cryogenics to maintain it in this state. Such additional instrumentation increases costs and can require cumbersome extra infrastructure. Using GAr does not require the same instrumentation and avoids the difficulties cryogenics introduces. Such comparisons are albeit rather negligible when considering the difference in densities however. The difference in density between gas and liquid phases results in a factor of $\sim$1000 difference, with LAr at 1.4 gcm^{-3} and GAr at 1.7 $\times$ 10^{-3} gcm^{-3} (at boiling point). With the ND far closer to the beam origin the neutrino beam is far more intense at the ND, $\sim$8 $\times$ 10^6 larger, assuming an inverse square law dependance. The difference in densities is then crucial when considering detector

performance, as pileup becomes a serious issue, with the event rate scaling proportionally to the density. The detector event rate per unit volume can then be tailored to the desired rate by altering the GAr pressure. Studies within LAGUNA-LBNO have shown that tracking in GAr (20 bar) is successful and can be superior to liquid [71], as can be seen in figure 4.1.

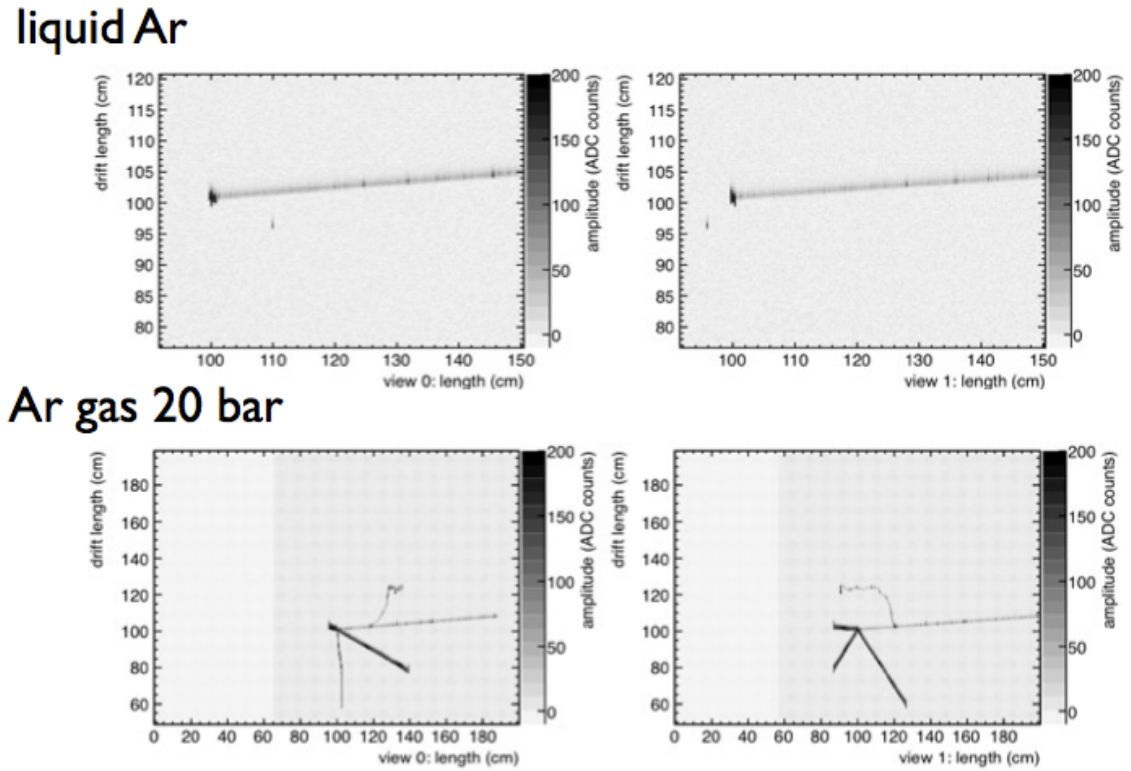

Fig. 4.1 Comparing quasi-elastic charged current interactions in LAr (upper) and 20 bar GAr (lower). The three protons from the interaction vertex are apparent in the GAr TPC, but cannot be resolved in the LAr. Image taken from [70].

The most common and powerful technology utilising argon as its medium is the TPC, this follows suit from the FD design. A $2 \times 2 \times 2$ m^3 GAr TPC is implemented for the ND primary target, pressurised to 20 bar. At this pressure the density of argon is 0.035 gcm^{-3}, yielding a detector mass of 280 kg. This design is loosely based on the T2K ND, ND280 [27], where three TPCs, each of volume $1808 \times 2230 \times 854$ mm, are used as the sensitive volume in the detector. The proposed LAGUNA-LBNO ND is smaller, largely due to restrictions on the pressure vessel, which is discussed later.

4.3.1 Momentum Measurements

The majority of muons generated in the TPC will leave the volume, as a peak energy ∼3 GeV μ^- will travel ∼3 m in argon. A magnetised TPC will allow the measurement of charged particles momentum given a large enough sagitta measurement. When a charged particle passes through the magnetic field, $\boldsymbol{B} = (0,0,B_z)$, it will cause a curved trajectory, ignoring scattering, as shown in figure 4.2. The sagitta, s, is given

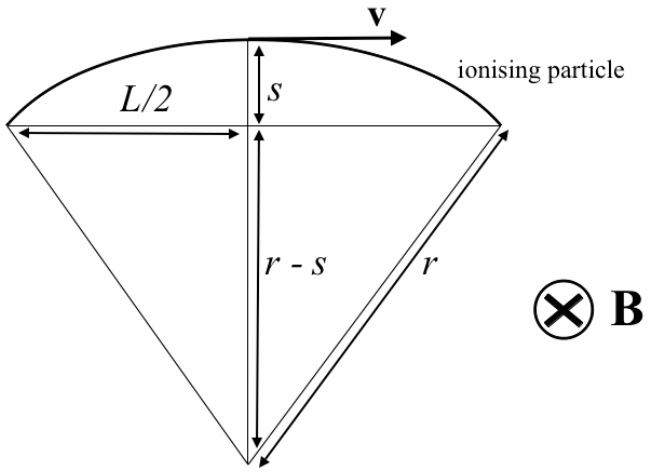

Fig. 4.2 An illustration showing a charged particle passing through a magnetic field $\boldsymbol{B}$ at a velocity $\boldsymbol{v}$ following curvature parametrised by the sagitta s, of radius r, and of track length L.

in terms of the radius of curvature, r ,and track length, l, in equation 4.1. To a good approximation ($s \ll l$) the strength of the magnetic field strength can be estimated as equation 4.2 in terms of the transverse momentum, $p^{trans} = \sqrt{p_x^2 + p_y^2}$.

$$s = r - \sqrt{r^2 - (l/2)^2} \simeq \frac{l^2}{8r} \tag{4.1}$$

$$B_z = \frac{8sp^{trans}}{el^2} = \frac{26.7s[m]p^{trans}[GeV/c]}{l^2[m^2]} \tag{4.2}$$

Thus an estimation of the magnetic field required can be established by determination of an adequate measurement of the sagitta. Based on the T2K ND280 detector design the space point resolution of the TPC is approximately 300 μm [27], which translates to roughly the same value for δs given $N_p = 5$ equidistantly spaced points per track using

the Gluckstern formula [72] as shown in equation 4.3. Here we consider uncertainties on the magnetic field and the track lengths to be negligible. Using this value and assuming a $\delta p/p \sim 5\%$ provides $s \sim 6$ mm. Given a 3 GeV/c muon, with the majority of its momentum in the transverse direction, leaving a track length of ∼1 m in the TPC, translates to a magnetic field strength of ∼0.5 T.

$$\delta p^{trans}/p^{trans} \sim \delta s/s = \frac{\sigma_{xy} p^{trans}}{8s}\sqrt{\frac{720}{N_p+4}} \tag{4.3}$$

4.4 Total Active Scintillator

The TAS will instrument the volume outside the TPC. It is to complement the TPC measurements and is envisaged to contribute to the reconstruction of neutrino interactions in the TPC. Its function is primarily to reconstruct neutral particles such as photons, with many originating from the decay of neutral pions. Its secondary function is to involve cross-section measurements for neutrino interactions in plastic.

To define the amount of matter traversed by high energy photons and electrons for interactions relating to pair production and Bremsstrahlung respectively, the radiation length, X_0, is used. It is usually measured in gcm^{-2} and can be interpreted as the mean distance at which the electron has lost all but $1/e$ of its original energy by Bremsstrahlung and 7/9 of the mean free path for pair production of photons. The radiation length is given by equation 4.4 which originates from fits to experimental data [52].

$$X_0 = \frac{716.4[\mathrm{gcm}^{-2}]A}{Z(Z+1)\ln(287/\sqrt{Z})} \tag{4.4}$$

Here A and Z are the atomic mass number and proton number respectively. When considering a composition of materials or chemicals, then a total radiation length can be approximated by equation 4.5. Here w_i is the weight fraction of element i in the material and X_i is the radiation length of element i.

$$\frac{1}{X_0} = \sum_i \frac{w_i}{X_i} \tag{4.5}$$

Plastic scintillator bars are proposed with Wave Length Shifting (WLS) fibres and compact Multi Pixel Photon Counters (MPPCs) to readout the scintillation light. Once again this design follows from the T2K ND280 scintillator detector implemen-

Material	**A**	**Z**	$\boldsymbol{X_0}$ **[gcm^{-2}]**
Hydrogen	1	1	63.3
Carbon	12	6	43.0
Oxygen	16	8	34.5
$C_5O_2H_8$	-	-	40.8

Table 4.1 The radiation lengths, X_0, for ${}^{1}_{1}H$, ${}^{12}_{6}C$, ${}^{16}_{8}O$ and $C_5O_2H_8$. The results are calculated from the use of equation 4.4 and equation 4.5.

tation, which is well established technology. A chemical composition of $C_5O_2H_8$ is assumed for the scintillator bars and the resulting radiation length of this, along with that of ${}^{12}C$,${}^{16}O$ and ${}^{1}H$ individually, is shown in table 4.1. The bars themselves can be seen in figure 4.3 and have dimensions of $10 \times 10 \times 900$ mm^3.

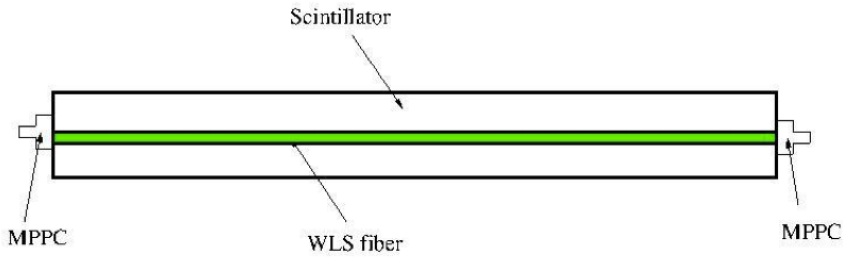

Fig. 4.3 The proposed design of the scintillation bars used in the ND. Image taken from [65].

The MPPCs to be used for scintillation light readout are manufactured by Hamamatsu and customised for the T2K experiment. Each MPPC consists of 667 pixels with a total sensitive area of 1.3×1.3 mm^2 and can be seen in figure 4.4. The use of MPPCs, as opposed to PMTs, is due to the large size of PMTs, typically ∼10 cm diameter, making it very difficult to integrate two for each scintillator bar but also because PMTs cannot operate in magnetic fields. MPPCs however can operate perfectly fine in magnetic fields and require much lower operation voltages, 70 V, compared to 2 kV for PMTs. MPPCs rely on the detection of photons via the photoelectric effect, as a photon after being wavelength shifted will reach a pixel and generate photoelectrons. The subsequent production of further electrons via an avalanche, amplifies the signal, as the amount of electron-hole pairs increases the voltage drops across the diode. If the voltage drop is over the set threshold then a signal is generated for the pixel. Each pixel is then a binary system, with the number of pixels triggered proportional to the

number of photons incident on the MPPC.

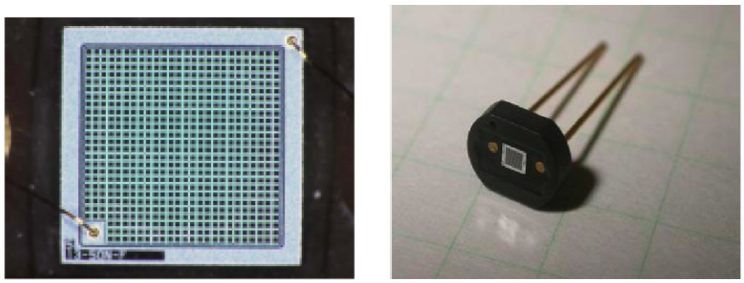

Fig. 4.4 The MPPC proposed for use within the scintillator bars. Image taken from [64].

4.5 Other Detector Components

The TPC imposes additional instrumentation of the detector, mainly a pressure vessel required for the GAr TPC and a magnet to perform momentum measurements and charge identification.

4.5.1 Pressure Vessel

To maintain 2 MPa of pressurised GAr in the TPC a pressure vessel is required. Pressure vessels are commonly of cylindrical shape, other than a sphere this shape provides the best structural support. The material composition of the vessel is aluminium. The vessel has an outer diameter of 5 m, a length of 5 m, and is of thickness 50 mm. With little engineering focus on the pressure vessel the dimensions are approximate with an estimated internal volume of $\sim$90 m^3.

Due to the pressure vessel the scintillator bars will need to be placed inside the vessel to provide continuity in the detector and avoid neutrino interactions within the vessel contaminating the signal. This will cause particular engineering difficulties but would not prove impossible to implement.

4.5.2 Magnet

With no studies performed on the magnet design and no engineering effort established for its development, a very simple implementation is considered for the ND. It is

proposed that a dipole magnet is implemented which is capable of providing a magnetic field strength of 0.5 T. Such a magnet will surround the whole detector assembly to enable momentum measurements in the TPC. The magnetic field must be parallel to the drift direction for charge carriers in the TPC to avoid $\mathbf{B} \times \mathbf{v}$ cross effects from the Lorentz Force.

4.6 Location

The position of the ND from the beam target is not a trivial matter. Several factors govern its distance from the target: cost, engineering and particle rates. Due to cost restrictions and engineering difficulties an upper bound of 1000 m from the target is set. At this distance excavation to a depth of -220 m is needed and becomes unfeasible for depths greater than this. Beam requirements also cause heavy restrictions on the ND placement, with muons originating from the beam, decay pipe and horns creating extremely large muons rates to the ND. The reduction of this rate can be controlled by increasing the distance between the ND and the target or deflecting them via use of a magnet. The latter would require high magnetic fields and is too expensive to be considered, with it far more viable to increase the target ND distance. Due to costs the ND position is at 800 m from the target, at this distance a rate of $\sim$2.5 $\mu/\mathrm{m}^2/10^{13}$ can be expected based on beam simulation studies [65].

4.7 Neutrino Flux at the Near Detector

The neutrino flux is optimised for the FD, not the ND, and so the flux may vary significantly from what is expected at the FD. The ND is an on axis detector in order to cover a wide energy range. Some other long baseline experiments such as T2K, use off-axis beam placement to tune the neutrino energies to narrower energy regime, however this is not the case for LAGUNA-LBNO.

Simulations have been conducted by the beam group within the LAGUNA-LBNO study to estimate the neutrino flux at the ND. Using FLUKA[69], the expected 2 flavour (μ and e flavour) neutrino flux with their antiparticle counterparts expected at the ND is determined in the energy range 0 - 30 GeV. Above this energy the neutrino flux is negligible and can be approximated as zero. Considering the two beam options, 50 and 400 GeV beam, both are shown in figure 4.5 for positive horn (ν_μ run) and negative horn ($\bar{\nu}_\mu$ run) focusing.

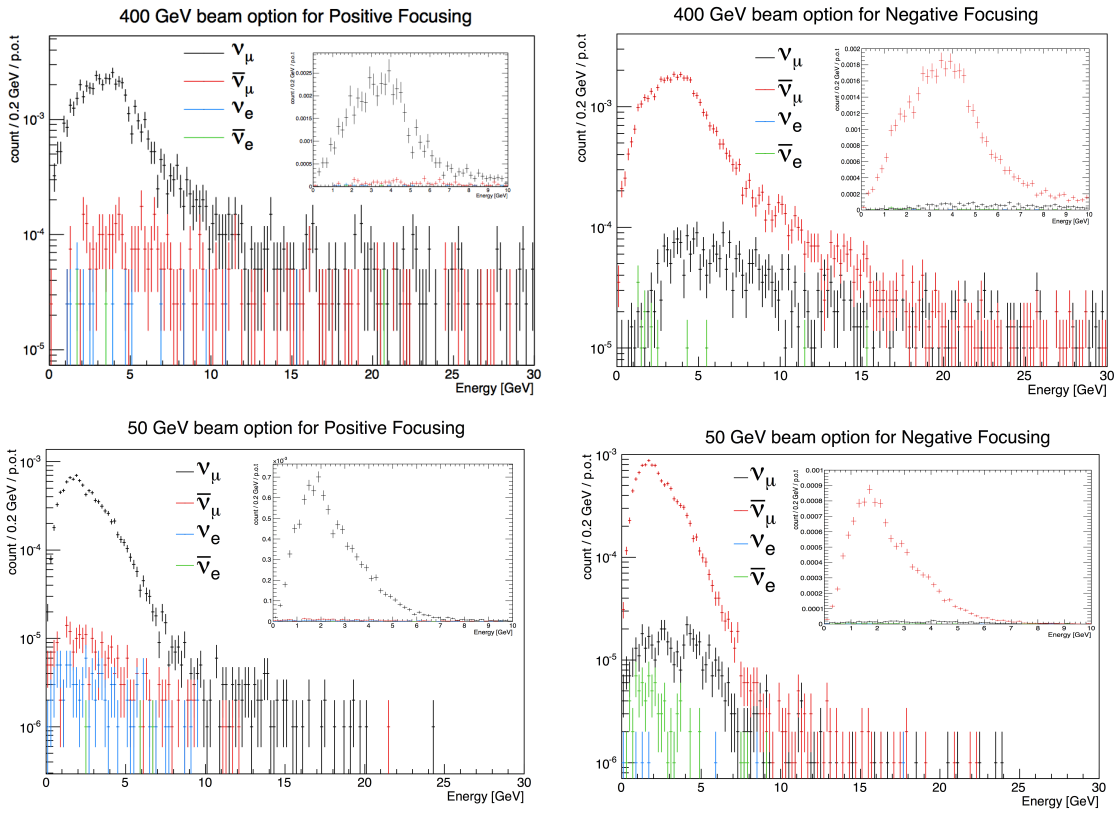

Fig. 4.5 Expected neutrino flux as a function of neutrino energy for positive focusing (left) and negative focusing (right) for beam options of 400 GeV (upper) and 50 GeV (lower). These plots show a 2.5 m radius cut selection, covering an area of 19.6 m at 800 m from the beam target. Errors bar show statistical error of $\pm$ 1σ.

The flux at the ND does not follow a simple inverse square law ($1/r^2$) due to the finite dimensions of the decay pipe, as neutrinos are generated at various positions in this pipe. However for very good approximation this can be used for the FD as the distance is so great, the source can be seen as point like. This can cause problems for the extrapolation of the neutrino flux to the FD given information only on the ND flux. To give a comparison of this between ND placements, the ν_μ expected flux at the ND for the 400 GeV PF is shown for 800, 900 and 1000 m distances from the beam target in figure 4.6. The integrated flux at distances from 800 m to 1000 m deviates slightly from the extrapolated flux following an inverse square law as figure 4.7 shows.

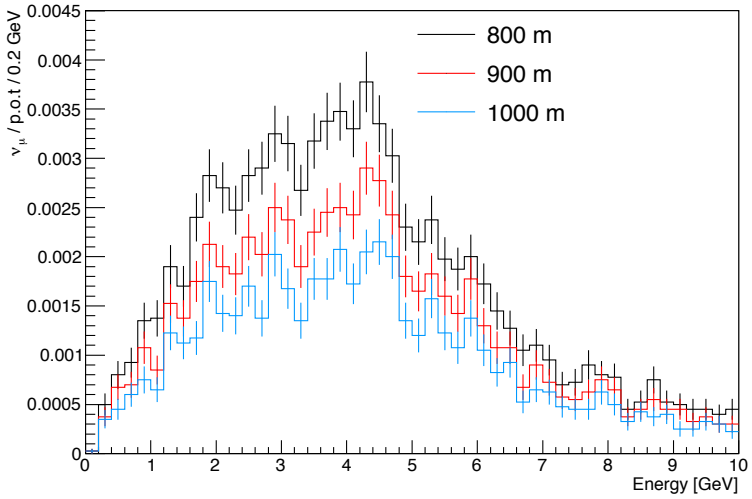

Fig. 4.6 Expected neutrino flux as a function of neutrino energy for the 400 GeV beam in positive focusing mode. These plots show a 2.5 m radius cut selection, covering an area of 19.6 m at 800 m from the beam target. Errors bar show statistical error of $\pm$ 1σ.

The neutrino flux is vastly reduced and its spectrum is broadened upon decreasing the radius cut selection. Figure 4.8 shows the ν_μ flux at 800 m from the target incident on circular areas of radii 1.5, 2.5, 10.0 and 30.0 m. The first two cuts are of particular significance to the ND, a radius cut of 1.5 m (7.1 m^2 area) covers the TPC and at 2.5 m (19.6 m^2 area) covers the whole ND vessel. The larger radius cuts are relevant for understanding background neutrino interactions in the surrounding detector environment and the rock.

The electron neutrino contamination of the beam as a function of cumulative radius selection can be seen on the left of figure 4.9. A radius selection of $\sim$1.5 m covers the

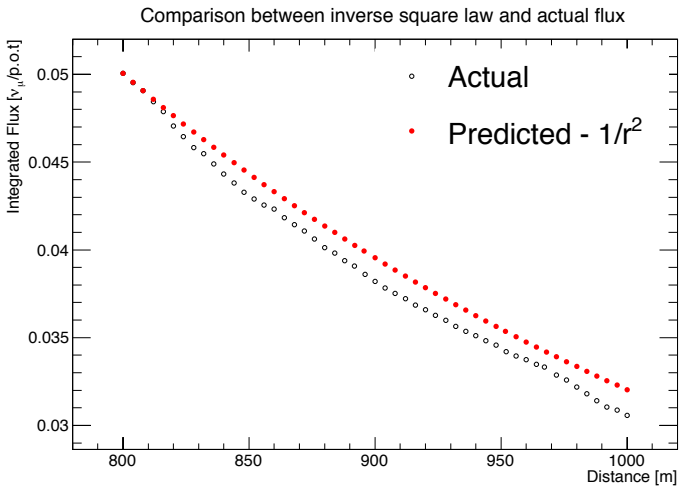

Fig. 4.7 The comparison between actual integrated flux (0 to 10 GeV) at distances from 800 to 1000 m from the beam target to the predicted flux extrapolated from the 800 m value, based on a $1/r^2$ law. Results based on 400 GeV PF beam option only.

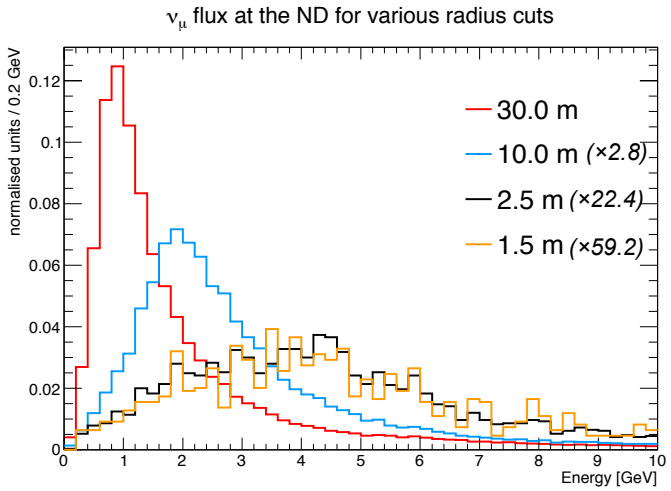

Fig. 4.8 The expected muon neutrino flux at 800 m from the target for radius selections of 1.5 m in orange, 2.5 m in black, 10 m in blue and 30 m in red. Each radius selection is normalised to the number of entries such that the integral is equal to 1, scale factors of 2.8, 22.4 and 59.2 are used for 10, 2.5 and 1.5 m radii respectively to compare rates with the 30 m radius cut. Results based on 400 GeV PF beam option only.

TPC and at this radius the electron neutrino contamination, $\alpha_{\nu_e}^{cont} = (\nu_e + \bar{\nu}_e)/(\nu_\mu + \bar{\nu}_\mu + \nu_e + \bar{\nu}_e)$ is $0.7^{+0.4}_{-0.3}\%$ (stat error only). The statistical errors are rather large for the electron neutrino contamination due to the limited statistics of the beam flux file for the 1.5 m radius selection. The generation of larger statistics is computational intensive and is done externally by the LAGUNA-LBNO beam group, given their time constraints, we are subsequently limited to these low statistics. As the main focus of the studies in this thesis are concerned with the muon neutrino interactions primarily, it is not an issue however. Increasing the radius selection to 30 m increases the statistics of ν_e and $\bar{\nu}_e$ by a factor of 165 (from 6 to 990 $\nu_e + \bar{\nu}_e$ passing the radius selection) and how this contamination varies with energy selection can be seen in the right of figure 4.9. The inclusion of the $\bar{\nu}_\mu$ contamination is shown in figure 4.10.

4.8 Prediction of Event Rates

The neutrino event rate, R_ν, at the detector can be estimated by equation 4.6, which is summed over all neutrino flavours.

$$R_\nu = \frac{\rho V \epsilon}{m_{Ar}} \sum_{\alpha=\mu,e,\tau} \int_0^{E_{max}} \sigma_{\nu_\alpha}^{TOT}(E')\phi_{\nu_\alpha}(E')\mathrm{d}E' \tag{4.6}$$

This equation is established assuming a 100% argon detector with the a density ρ, efficiency ϵ, total cross section (CC and NC) $\sigma_{\nu_\alpha}^{TOT}$ and flux ϕ_{ν_α}, both as a function of neutrino energy. Where the total cross section for ν_μ on ^{40}Ar for CC and NC interactions is shown in figure 4.11. The mass of an argon atom is $m_{Ar} = 6.67 \times 10^{-26}$ kg.

Multiplying the cross section with the neutrino flux on a binned basis and then summing each resultant bin gives an approximate estimate of the integral in equation 4.6. Calculating rates for both LAr and GAr of volumes used in the ND, V = 8 m^3, with maximal efficiency are shown in table 4.2, with various gas pressures and for both beam options.

4.9 Detector Concept

The basic design of the ND, omitting the magnet is shown by an artists impression in figure 4.13.

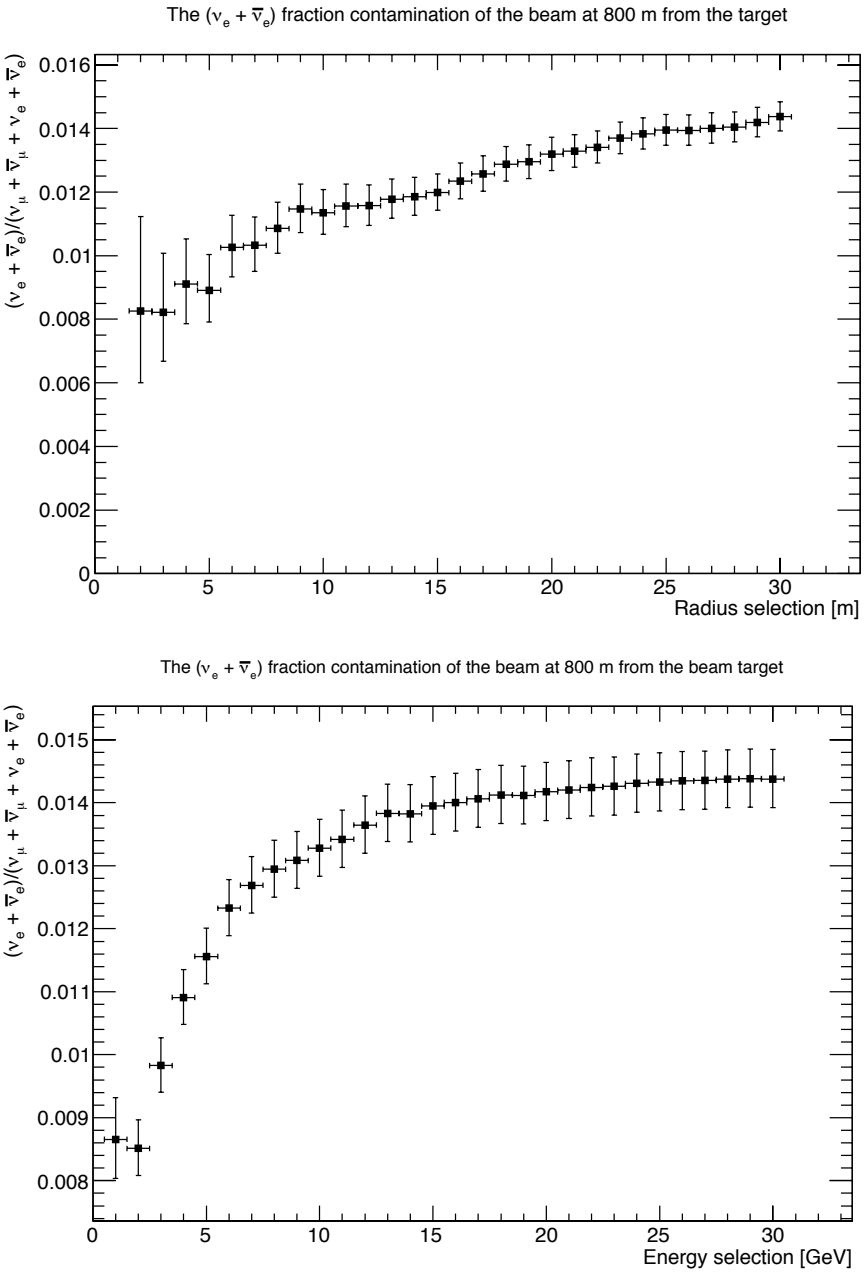

Fig. 4.9 The electron neutrino contamination, $\alpha_{\nu_e}^{cont} = (\nu_e + \bar{\nu}_e)/(\nu_\mu + \bar{\nu}_\mu + \nu_e + \bar{\nu}_e)$ for cumulative radius selections ranging from 1 to 30 m (top) and for cumulative energy selections from 1 to 30 GeV (bottom). No ν_e or $\bar{\nu}_e$ pass the radius selection for 1 m and hence no point is shown. Results based on 400 GeV positive focusing (PF) beam option only.

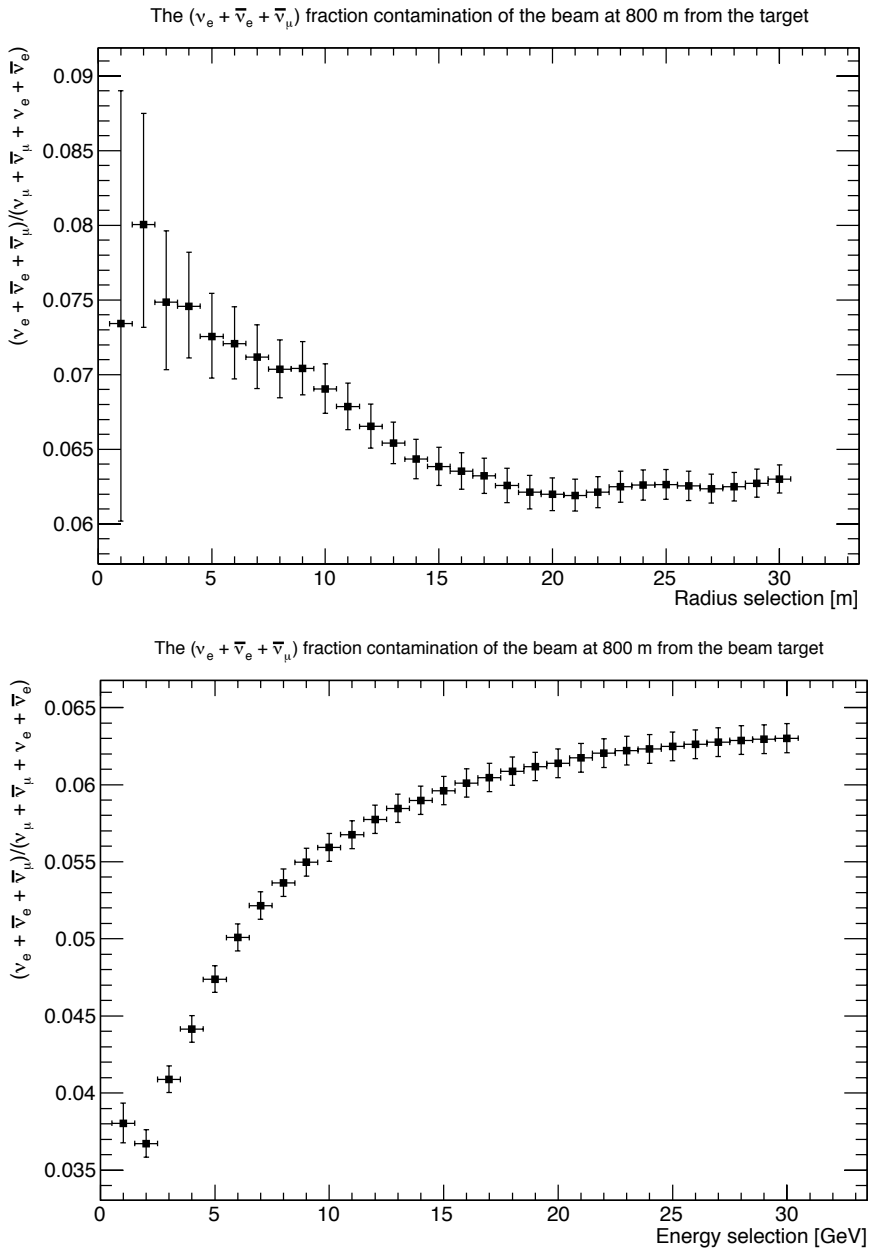

Fig. 4.10 The full neutrino contamination, $\alpha^{cont}_{\nu_{e,\mu}} = (\nu_e + \bar{\nu}_e + \bar{\nu}_\mu)/(\nu_\mu + \bar{\nu}_\mu + \nu_e + \bar{\nu}_e)$ for cumulative radius selections ranging from 1 to 30 m (top) and for cumulative energy selections from 1 to 30 GeV (bottom). Results based on 400 GeV positive focusing (PF) beam option only.

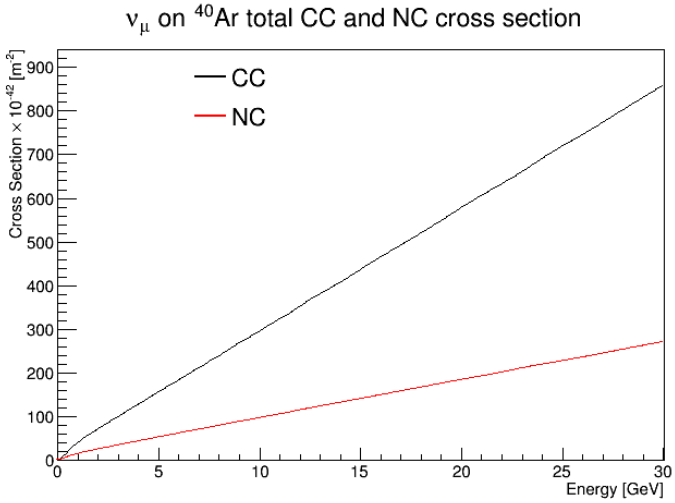

Fig. 4.11 The muon neutrino CC and NC total cross sections on ^{40}Ar for energies up to 30 GeV. The prediction is based on extrapolated data taken from the Monte Carlo generator GENIE 2.6.6 [73].

State	**Pressure**	**Temperature**	**Density**	**50 GeV beam rate**	**400 GeV beam rate**
-	[MPa]	[k]	[kg m^{-3}]	[ν_μ / 10^{14} p.o.t]	[ν_μ / 10^{14} p.o.t]
Liquid	-	87.3	1400	4.61 ± 0.11	39.7 ± 2.5
Gas	10.0	280	184	0.605 ± 0.014	5.22 ± 0.32
Gas	5.0	280	89.3	0.294 ± 0.007	2.53 ± 0.16
Gas	2.0	280	34.9	0.0115 ± 0.003	0.989 ± 0.061
Gas	1.0	280	17.6	0.058 ± 0.001	0.499 ± 0.031
Gas	0.5	280	8.7	0.029 ± 0.001	0.247 ± 0.015

Table 4.2 Estimated ν_μ rates using equation 4.6 for a ND of 2 × 2 × 2 m^3 at 800m from the target. Uncertainties relate to 1σ statistical errors propagating from neutrino flux estimation only, other parameters are assumed to have negligible errors. Densities and pressures for argon taken from [74].

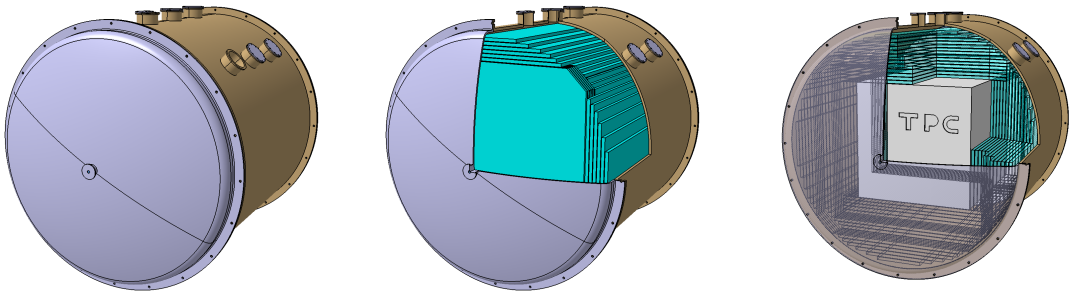

Fig. 4.12 A graphical representation of the current ND design, showing the pressure vessel (left), scintillator bars/layers (middle) and the TPC (right). The magnet is omitted from this sketch.

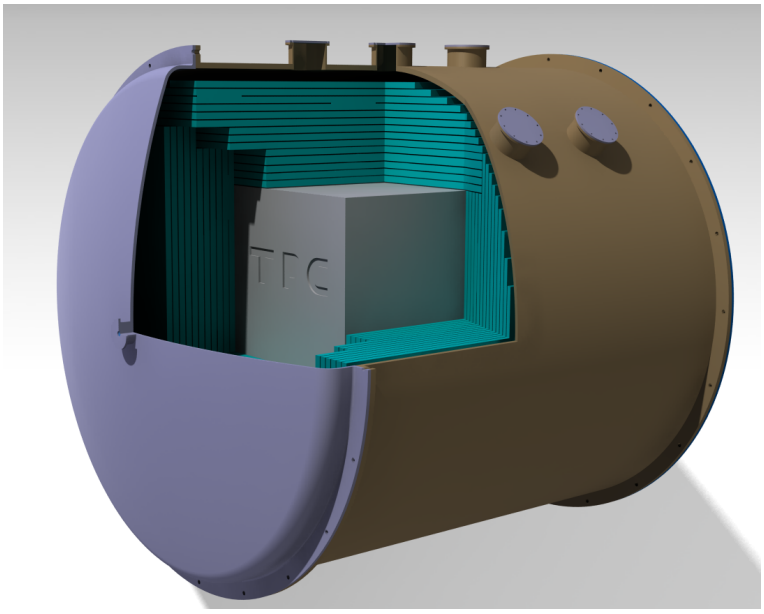

Fig. 4.13 A graphical interpretation of the current ND design for the proposed LAGUNA-LBNO experiment. The magnet is omitted from this sketch.

Chapter 5

Monte Carlo Studies in LAGUNA-LBNO

Monte Carlo (MC) studies are a powerful tool for estimating and assessing proposed experiments or potential detector designs. With that very much the case for LAGUNA-LBNO, MC simulations form the basis of the ND study. The previous chapter described the ND concept and design, acting as a precursor to this chapter, which then presents the parameterisation, implementation and results of the detector using an integrated software framework.

5.1 Monte Carlo Generation

Problems that cannot be solved analytically require other methods to provide a solution, Monte Carlo (MC) simulations can provide a probabilistic approach to this. Fundamentally the principle behind their implementation relies on the generation of random numbers based on some underling probability distribution. This random number, or series of random numbers, then defines a particular result or event. When repeated many times the events will represent the underlying probability distributions and allow conclusions to be drawn within a statistical analysis.

With a poor understanding of how neutrinos interact with nuclei, it becomes an impossible task to analytically solve and analyse their interactions. It is much easier to use neutrino models, based on cross sectional measurements and other experimentally determined parameters, to perform simulations used to predict how neutrinos will interact. MC simulation techniques therefore form the basis of the feasibility study for the ND in LAGUNA-LBNO. When employing this method statistical significance

is very important which can often result in large numbers of events being generated.

Several external software packages currently exist that employ the use of MC simulation for particle physics experiments. Two independent packages are used within the studies described in this chapter, GENIE[73] and Geant4[75].

5.1.1 GENIE

GENIE (Generates Events for Neutrino Interaction Experiments) [73] is an external open source software package based on Object Orientated (OO) design (C++). It is developed by an international collaboration of scientists with expertise in neutrino physics. As a universal neutrino MC generator, its primary function is the generation of neutrino interactions in different materials and geometries. It covers a wide energy regime of ∼1 MeV to ∼1 PeV neutrinos, covering all known neutrino flavours and a variety of nuclear targets.

The energies of concern in LAGUNA-LBNO involve the sub 10 GeV range, this is considered the transition period between perturbative and non-perturbative models of neutrino nucleus scattering. Nuclear physics is paramount to these scattering processes at these energies and GENIE implements a Relativistic Fermi Gas (RFG) nuclear model to cope with this. However scattering kinematics can be vastly different for free nucleons when compared to combined nucleons. GENIE applies a nuclear modification factor which is based on observed differences between both cases to overcome this effect.

For event generation pre-calculated total cross sections are used to initially determine which interaction type will occur with a given probability, given an input flux. From this, differential cross sections are calculated at run time on an event by event basis to establish the event kinematics, given an interaction model. The key interactions of interest in the LAGUNA-LBNO study and their implementation in GENIE are briefly described with their corresponding parameterisations.

5.1.1.1 Quasi-Elastic Scattering

The Llewellyn-Smith model [76] is implemented for these interactions. This model uses Lorentz-invariant form factors to model the hadronic weak current, of which only one remains unknown, the axial form factor, $F_A(Q^2)$. Where the axial form factor is parameterised by $Q^2 = -q^2$, the momentum transfer from the neutrino. This depends on the axial vector mass parameter, M_A, assuming a dipole form, given by equation

5.1. This is free to be altered within the GENIE framework and is set to its default value of $M_A = 0.99$ GeV.

$$F_A(Q^2) = \frac{F_A(0)}{(1 + Q^2/M_A^2)^2} \tag{5.1}$$

5.1.1.2 Elastic Neutral Current Scattering

An axial form factor, $G_A(Q^2)$, is used for modelling this interaction and is given by equation 5.2. The free parameter in this is η which is set to the default value of $\eta = 0.12$.

$$G_A(Q^2) = \frac{G_A(0)}{2(1 + Q^2/M_A^2)^2}(1 + \eta) \tag{5.2}$$

5.1.1.3 Non-Resonance/Deep Inelastic Scattering

A leading order Bodek and Yang model [77] is implemented to describe low Q^2 scattering. Parton Distribution Functions (PDFs) are used to model proton and neutron quark distributions, based on values obtained from high energy experimental data fits. A scale factor of 1.032 is applied to the predictions of the Bodek and Yang model to provide coherence between measured values of neutrino cross sections.

5.1.1.4 Coherent Neutrino-Nucleus Scattering

Coherent neutrino-nucleus scatterings follow descriptions of the Rein and Sehgal model [78]. In such scatterings a pion is produced via the CC channel ($\nu_\mu + N \rightarrow \mu^- + N + \pi^+$) or NC channel ($\nu_\mu + N \rightarrow \nu_\mu + N + \pi^0$). This model assumes a dipole dependance on Q^2, with $M_A = 1$ GeV. Cross sectional data from pion scattering on protons and deuterium are used for pion-nucleus interactions.

5.1.1.5 Baryon Resonance Scattering

The Rein and Sehgal model[79] is implemented in GENIE for baryon resonances. The default value of $M_A = 1.12$ GeV is used for the resonance axial mass vector.

5.1.2 Geant4

Geant4 [75] is a common particle physics third party software package used to simulate the propagation of particles through matter. It follows an OO design framework, again written in C++. It allows complex geometries to be defined within the simulation and

visualisation of events and particle tracks is also possible. Geant4 is not a black box software package and allows the user the freedom to implement any of its extensive tools in a bespoke simulation. However this requires heavy user input with strong definitions of physics lists and models to provide an accurate simulation. User defined classes can inherit from Geant4 default classes to provide control and implementation to the simulation, tailored to the users requirements.

During particle transport within the simulation a particle is propagated on a step by step basis. The mean free path of the particle, λ, is determined given the material properties (density, ρ, molar mass, A and atomic number, Z) and the total cross section given a particular physics model, $\sigma(Z, E)$. In a material/geometry consisting of many elements the mean free path is given by equation 5.3 [80]. Where N_A is the Avogadro constant, ω_i is the proportion of mass of the i^{th} element in the material to the total mass of the material and A_i is the molar mass of the i^{th} element in the material.

$$\lambda(E) = \left(\sum_i \left[\frac{N_A \rho \omega_i}{A_i} \sigma(Z_i, E) \right] \right)^{-1} \tag{5.3}$$

The number of mean free paths a particle travels before reaching the interaction point, n_λ, is determined from a random number uniformly distributed along (0,1). After each step of length, Δx, n_λ is updated such that, $n_\lambda \rightarrow n_\lambda$ - $\Delta x/\lambda(x)$. The interaction point is then determined from minimising $n_\lambda \lambda(x)$. The step length is determined by the user and in order to gain an accurate simulation a small step length must be considered. A compromise between computing processing times and accuracy must be reached for realistic simulations while maintaining large statistics. A step length of 0.1 mm is used throughout the simulations as this yields adequate simulation speeds and with detector resolutions higher than this, it provides no extra benefit if Δx is decreased.

5.1.2.1 Physics Model

The physics models used within the simulations are the standard EM list for electromagnetic processes and QGSP_BIC_HP for hadronic physics. QGSP is the basic physics list in Geant4 which uses a quark gluon string model for interactions concerning protons, neutrons, pions and nuclei within the range of between 5 and 25 GeV. The QGSP_BIC_HP version uses a Binary cascade for protons and neutrons with energies less than 10 GeV and has a precision model for neutrons below 20 MeV.

5.2 Software Framework

The requirements for a full simulation of a ND in a long baseline neutrino experiment are extremely heavy and can be technically intricate. It is therefore natural to subdivide the full simulation into several steps.

1. Simulation of the target station, the focusing system and the decay pipe
2. Modelling of the detector geometry and its environment
3. Simulation of neutrino interactions in different materials
4. Tracking and propagation of secondary particles inside and outside the detector
5. Digitisation and modelling the detector response
6. Reconstruction of the neutrino events
7. Analysis of the results

A bespoke software framework is used to provide the desired functionality and address the described steps. However it is far from a complete simulation package. The main focus of the ND study covers steps 2, 3, 4, 6 and 7, which are described extensively in this chapter. The simulation of the beam, step 1, is done externally by the beam group within LAGUNA-LBNO and has been discussed in the previous chapter. Step 5 is not implemented and basic detector modelling is incorporated into step 6, the reconstruction.

Several third party libraries and software packages exist which are designed specifically to tackle some of these tasks. MC generators GENIE and Geant4 are implemented in the framework with the addition of another package used for analysis, ROOT[81].

5.2.1 All Third Party Dependancies Versions

Other third party packages and libraries are required as dependancies for GENIE and Geant4. All third party software packages and their respective versions that are implemented in the software framework are shown in table 5.1.

Third party software	Version
ROOT [81]	5.34.05
GENIE [73]	2.6.6
Geant4 [75]	4.9.6.p01
CLHEP	2.1.3.1
Pythia	v6.424
LHAPDF	5.8.7

Table 5.1 An extensive table showing all third party software and versions used for current simulation studies.

5.3 Software Structure and Processors

The software designed and implemented for the MC studies on the ND is written in the OO language C++. The design architecture follows a processor and algorithm model, in which processors provide the interfaces and algorithms perform the desired tasks and procedures. The nature of the software allows one processor to have many algorithms. Three main processors are defined for the simulation of the ND and are processed sequentially within the software.

5.3.1 Neutrino Flux Processor

An external neutrino flux file in ROOT format is provided for input. The file contains data relating to neutrinos produced from meson decays within the beam decay pipe, with the neutrino flavour, vertex position $X_0 = (x_0, y_0, z_0)$ and the neutrino 3-momentum $\mathbf{p} = (p_x, p_y, p_z)$ provided. The neutrino energy is simply $E = |\mathbf{p}|c$. Given the corresponding exposure (p.o.t) of the input file, ϵ_0, the number of iterations over the input entries, n, is calculated from a desired simulation exposure, ϵ, by scaling the events as $n = n_0\epsilon/\epsilon_0$. A random variable, using TRandom3 from ROOT, is then used to pick an index relating to a neutrino entry in the file.

The neutrinos are projected along straight line paths to a plane perpendicular to the beam axis, z-axis, at a distance, L from the target. Equation 5.4 shows the projection in cartesian co-ordinates. A radius cut, R, is determined to improve simulation speed so that for all projections where $x^2 + y^2 > R^2$ the neutrinos are rejected.

$$\mathbf{X} = \begin{pmatrix} x \\ y \\ z \end{pmatrix} = \begin{pmatrix} x_0 \\ y_0 \\ L \end{pmatrix} + \frac{(L - z_0)}{p_z} \begin{pmatrix} p_x \\ p_y \\ 0 \end{pmatrix} \tag{5.4}$$

All neutrinos that pass the radius selection are recorded into the output root file under a branch Neutrino Hits. Each neutrino is recorded with its flavour, projected position **X** and momentum **p**, along with a corresponding event identification number and backtracer.

5.3.2 Neutrino Event Processor

The ND geometry is read from an external ROOT file and is loaded into the simulation software. The virtual construction of this geometry is discussed later. Entries are then read from the Neutrino Hit branch sequentially until the number of iterations reaches the entries in the branch. The projected position of the neutrino is transformed to the local co-ordinate system of the geometry by a translation along the beam axis to the minimum z value in the geometry, -$d/2$, where d represents the length of the total ND geometry. The x and y co-ordinates are not altered and z simply transforms as $z \rightarrow z' = -d/2$. The GENIE flux (GFluxI) and geometry (ROOTGeomAnalyzer) drivers are implemented within the processor to interface the ROOT geometry and incident neutrino information into GENIE. Events are then generated within a selected sub section of the ND geometry or the whole geometry, governed by user input.

Upon generation of a neutrino event, truth information on the neutrino interaction and the Final State Secondaries (FSS) is recorded. FSS are considered particles that have left the interaction atom determined to be secondaries by GENIE, this does not include particles that are absorbed inside the nucleus. The Particle Data Group (PDG) [82] coding system is employed to identify particle types and hereafter PDG refers to particle type identification. The extensive list of truth information recorded on the neutrino interaction is:

- Final State Primary Lepton (FSPL): (PDG, 4-Momentum, Mass)
- Final State Secondaries (FSS): (PDG, 4-Momentum, Mass)
- Hit nucleon: (PDG, 4-Momentum, Mass)
- Interaction type (QEL, RES, DIS, and others)
- Scattering process (CC or NC)
- Interaction vertex position
- Node in geometry where interaction occurred

This information is recorded on an event basis and is stored in the output root file under a branch Neutrino Events. Once again an event identification and back tracer are also stored for each event.

A global probability value used to scale the input exposure to a realistic exposure is implemented by GENIE. This is performed in order to provide quick simulation times, which would otherwise be unfeasible due to the extremely small cross sections of neutrinos. This scale factor, η, is determined by scaling the maximum interaction probability for the maximum energy neutrino per simulation to 1. For event rates to correspond to correct and realistic exposures the user defined exposure, ϵ, is then translated to the true exposure, $\epsilon^{true} = \epsilon/\eta$.

5.3.3 Secondary Tracking Processor

The ND geometry is once again initialised and loaded in the software in GDML (Geometry Description Markup Language)[83] format, as implementation of this format is easier than ROOT format. GDML is a description heavily based on XML and is designed for use within Geant4 and ROOT. Iterating over the event entries from the Neutrino Event branch, the FSPL and all FSS are loaded into Geant4 with their initial vertex position set to the neutrino interaction position. They are initialised with their 4-Momentum, p_i^{μ}, and propagated with Geant4.

During propagation of a particle Geant4 will iteratively step through the geometry in increments equal to the step length. Only upon reaching the geometry boundaries or if the track has zero kinetic energy, or is killed by user implementation, the propagation of the particle is stopped. Truth information can be collected at each step and can be processed for later analysis. However due to the large production of particles and small step lengths, it can be computationally demanding to record everything. Energy cuts are used to help reduce this and are particularly useful for electromagnetic showering. An overall energy cut of 1 keV is used, for which tracks are killed below this kinetic energy threshold.

Detector hits are recorded from the implementation of the TPC and the TAS as sensitive detectors, defined by Geant4. A detector hit is defined as a step at which energy was deposited, that is above the user defined threshold, in the sensitive detector. From this, information on the position and the amount of energy deposited is recorded along with the particle identification number, information on the parent particle and the PDG code. One particle transversing the detector can have multiple hits and defining the step length impedes on the amount of hits.

Particles crossing detector boundaries are also monitored, with information on the original neutrino, the particle crossing the boundary and the volume where the interaction originally occurred recorded.

5.3.4 Software Overview

The implementation of a backtracer in the software allows for each event to be tracked through each processor, ultimately relating secondary particles to the original neutrino vertex. The whole structure and process cycle of the software is summarised by figure 5.1.

5.4 Modelling the Near Detector Environment

Modelling the geometry and its surrounding environment is done within the ROOT geometry package which also provides visualisation of the detector. For neutrino studies it is crucially important to model the materials and orientations of the basic ND components. Finer details are omitted in the geometry, such as structural supports and cabling, as they are assumed to have negligible effect on neutrino interactions. Following from the ND design a close representation is implemented in the software and can be seen in figure 5.2. Upon construction the details of the geometries material composition and dimensions is written to both .root and .gdml file formats.

5.4.1 TPC

The $2 \times 2 \times 2$ m^3 TPC contains GAr at 20 Bar, with a density of 35 kgm^{-3}. Quench gases are included at ratios matching that of T2K ND280 [84]. The pressurised gas is then a mixture consisting of 95% ^{40}Ar, 3% CH_4 and 2% Isobutane (C_4H_{10}). The introduction of cathode and anode plates in the TPC reduces this active volume by $\sim$5 kg, with each plate of thickness of 13.2 mm and length and width of 1.9 m with the material composition also based on the ND280 design. The total mass of the gas in the TPC is then 275 kg.

5.4.2 Pressure Vessel

The vessel is of cylindrical design with the addition of slightly curved ends. This is modelled in the software as a cylinder of 5 m outer diameter as the main section,

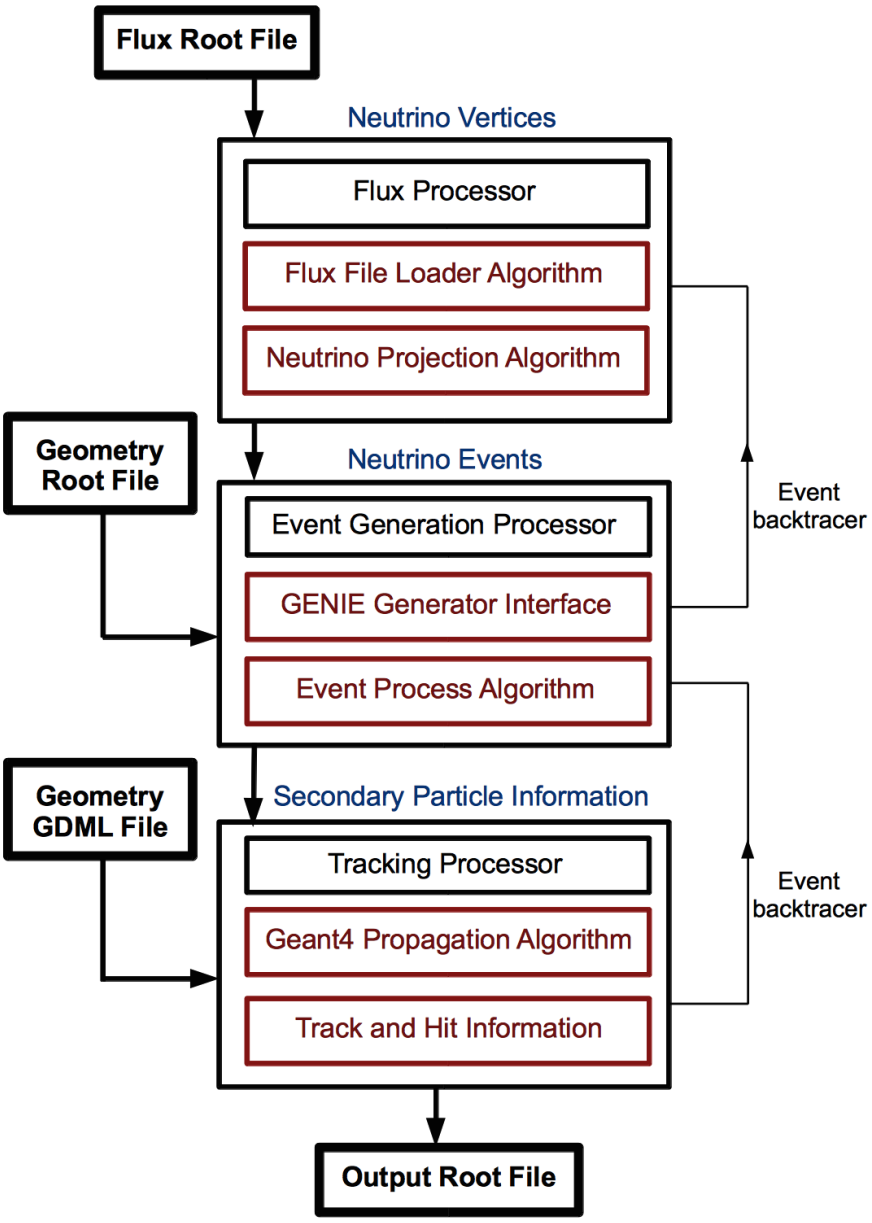

Fig. 5.1 The software architecture used for the MC simulation study for LAGUNA-LBNO.

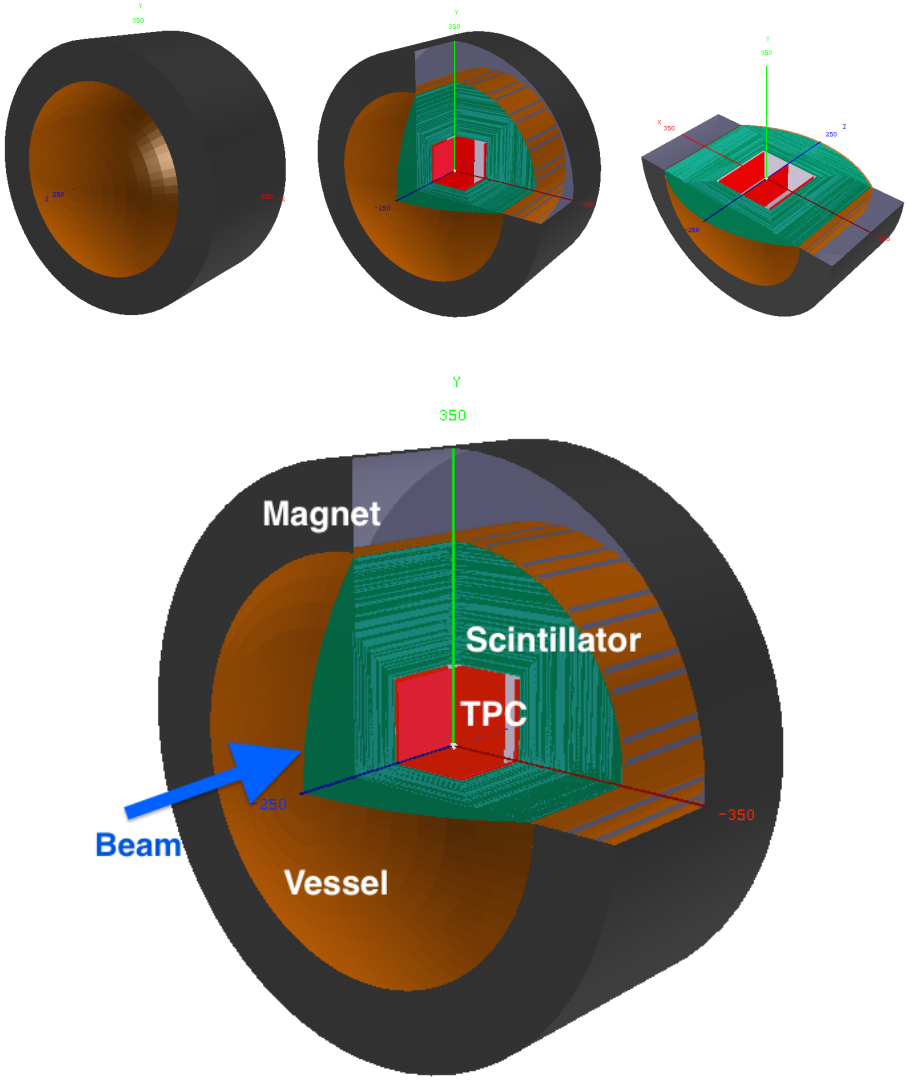

Fig. 5.2 Top: Images of the ND geometry in the ROOT display for closed (left), partly open (middle) and cross section (right). Bottom: A fully labelled image showing dimensions in cm with detector chambers labelled.

appended with a spherical cap on each end of total inner radius 4.05 m. This results in a protrusion of 0.825 m for each end. To maintain a 5 m length, the cylinder is of length 3.35 m. A sketch of this implementation with dimensions is shown in figure 5.3. 50 mm thick aluminium of density 2700 kgm^{-3} is used as the vessel material. The pressure vessel then has a considerable mass of ∼8.2 tonnes.

The inner vessel is filled with the same gas composition and pressure as the TPC, with the TPC centred in the middle of the vessel.

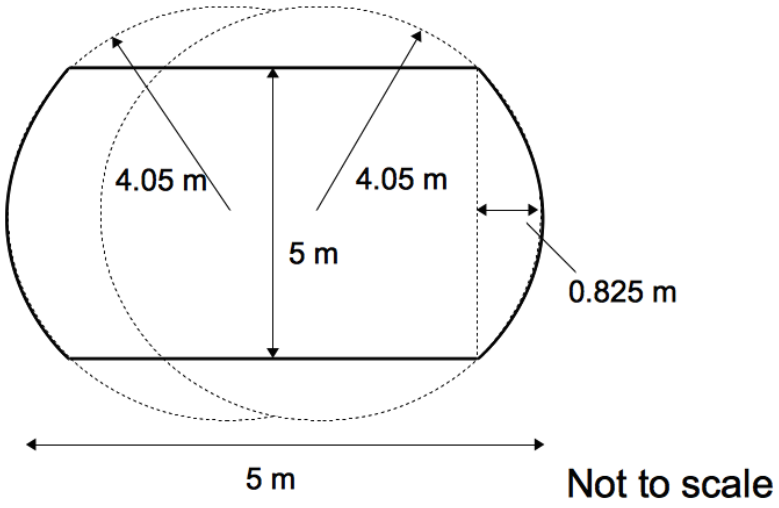

Fig. 5.3 The basic sketch of the side view of the pressure vessel with dimensions in meters. The bold lines indicate the implemented volume. The drawing is not to scale.

5.4.3 Scintillator

The scintillator layers are modelled with plastic of composition $C_5O_2H_8$ and of density 1.18 gcm^{-3}. Individual scintillation bars are not implemented in the model, instead layers of 10 mm thickness are used. The first layer consists of six blocks to fully enclose the TPC, covering each face, with additional layers covering each previous layer. Dividing the six faces into pairs of X, Y and Z faces the dimensions of the n^{th} box layer $t \times l_n \times h_n$ are given by equations 5.5 to 5.7. This procedure is followed until the scintillators layers reach the vessel edges or enter the curved ends. In the curved ends the layers are then modelled with circular disc layers of the same thickness but with decreasing radius to match that of the inner vessel radius. However less scintillator

layers are added upstream of the TPC to avoid introducing dense material which would increase neutrino interactions upstream of the TPC. Following this implementation strategy the ND scintillator can be summarised by figure 5.4 with the total dimensions of the detector. The yellow region inside of the pressure vessel then refers to the volume in which scintillator was omitted, remaining as a GAr region at the same pressure as the TPC, as the whole volume inside the vessel is pressurised at 20 bar. The total mass of all the introduced scintillator is then 73.1 tonnes.

$$X_n = 0.01 \times 2(1 + 0.01(n-1)) \times 2(1 + 0.01(n-1)) \text{ m}^3 \tag{5.5}$$

$$Y_n = 0.01 \times 2(1 + 0.01(n-1)) \times 2(1 + 0.01n) \text{ m}^3 \tag{5.6}$$

$$Z_n = 0.01 \times 2(1 + 0.01n) \times 2(1 + 0.01n) \text{ m}^3 \tag{5.7}$$

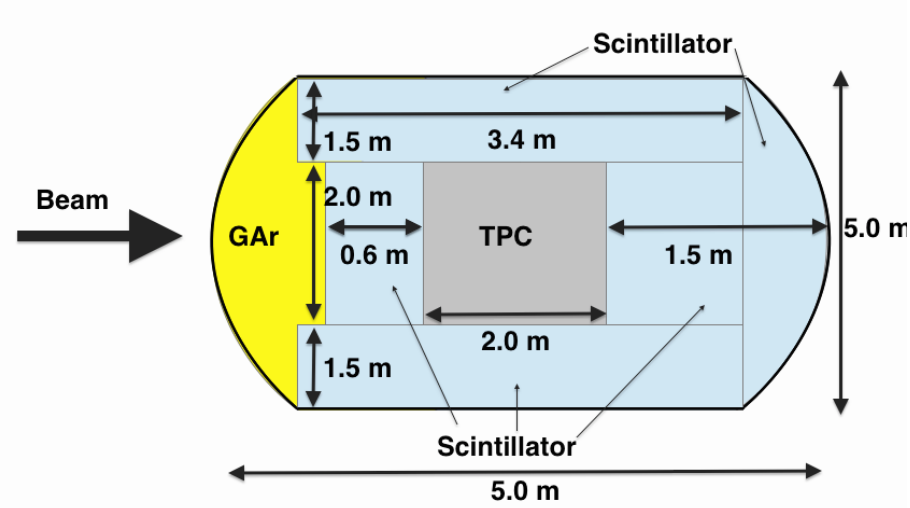

Fig. 5.4 The cross sectional view of the ND vessel with dimensions in meters. The drawing is not to scale.

5.4.4 Magnet

The dipole magnet is modelled as a simple solid cylindrical iron tube. The inner radius is 2.5 m and outer radius of 3.5 m, yielding a thickness of 1 m and has a length of 3.35 m. At a density of 7870 kgm^{-3} the magnet has a mass of 496.7 tonnes.

The magnetic field is simulated as a dipole of constant magnetic field strength of 0.5 T. The magnetic field is only implemented across the TPC as this is the only area

of concern for this study. Taking the beam direction as (0, 0, 1), the electron drift is then perpendicular to this in the (-1, 0, 0) direction and the magnetic field of $\boldsymbol{B}$ = (0.5, 0, 0) T is then anti-parallel to the electric field.

5.4.5 The Surrounding Environment

It is also necessary to model the surrounding environment of the ND to perform background studies on the ND. Specifically this relates to neutrino interactions in the surroundings producing muons which can then reach the ND TPC. A simple model is used composing of a rock environment with an air cavity.

5.4.5.1 Cavity

The cavity replicates the excavation hole needed to insert the ND underground. This is a cylindrical hole of 9 m in diameter and the ND is situated at the bottom of the 23.5 m long hole, giving a volume of 1494.2 m^3. A simple composition of air (78% N and 22 % O) and of density 1.29 kgm^{-3} is used as the medium for the cavity.

5.4.5.2 Rock

Previous excavations at CERN and geological studies have shown that the rock beneath the surface at the proposed ND location consists of mainly sandstone [85]. Sandstone is modelled as a composition of 53% Oxygen and 47% Silicon and of constant density 2323 kgm^{-3}. This is a simplification but small fluctuations in densities and chemical composition would have negligible effect on background neutrino interactions. With high energy muons capable of passing through large quantities of dense material, ∼30 m for 10 GeV muons, the surrounding environment must be extremely large. A 40 × 40 × 200 m^3 = 320,000 m^3 cuboid volume is implemented to give a modest estimate of the actual environment. Removing the cavity volume, which is centred in the middle of the rock and extends to the top of the rock, then gives a total rock mass of 7.4×10^8 kg.

The materials implemented in the geometry are summarised in table 5.2 with the overall masses and volumes of each ND component shown in table 5.3.

Detector Component	**Mass Composition** (%)	**Density** [kgm^{-3}]
TPC Gas Mixture - 20 Bar	Ar(95), C(2.1), H(0.3), F(2.6)	35
TPC Cathode/Anode	C(36), O(26), Si(15), H(6), Cu(17)	287
Scintillator	C(60), O(32), H(8)	1180
Vessel	Al (100)	2700
Magnet	Fe (100)	7870
Cavity	N (78), O (22)	1.29
Rock	O (53), Si (47)	2323

Table 5.2 The material compositions based on mass and densities of each of the materials implemented in the ND geometry in the software model.

Detector Component	**Total Volume** [m^3]	**Total Mass** [tonnes]
TPC Gas Volume	7.86	0.275
TPC Cathode/Anode	0.143	0.040
Scintillator	62.0	73.1
Vessel	3.02	8.17
Magnet	63.1	497
Cavity	1.49×10^3	1.93
Rock	320×10^3	7.40×10^5

Table 5.3 The total volumes and masses of each of the ND components and surrounding environment used in the software model.

5.5 Event Displays and Visualisation

Example event displays of neutrino interactions in the ND geometry as seen within the software are shown in figure 5.5. Three interactions are shown, all within the TPC gas: $\nu_\mu + Ar \rightarrow \mu^- + n + n + n + p$ (Upper), $\nu_\mu + Ar \rightarrow \mu^- + p + \pi^+ + \pi^-$ (Middle) and $\nu_\mu + Ar \rightarrow \nu_\mu + n$ (Lower). The left displays show the X and Z directions which are the magnetic field and beam directions respectively. The right images shows the Y and Z directions. The beam is incident from the left on all event displays. A colour scheme is used to illustrate the different particle types and is described in the figure caption, however all red circles indicate a detector hit, regardless of the particle type which deposited energy in the TPC or TAS.

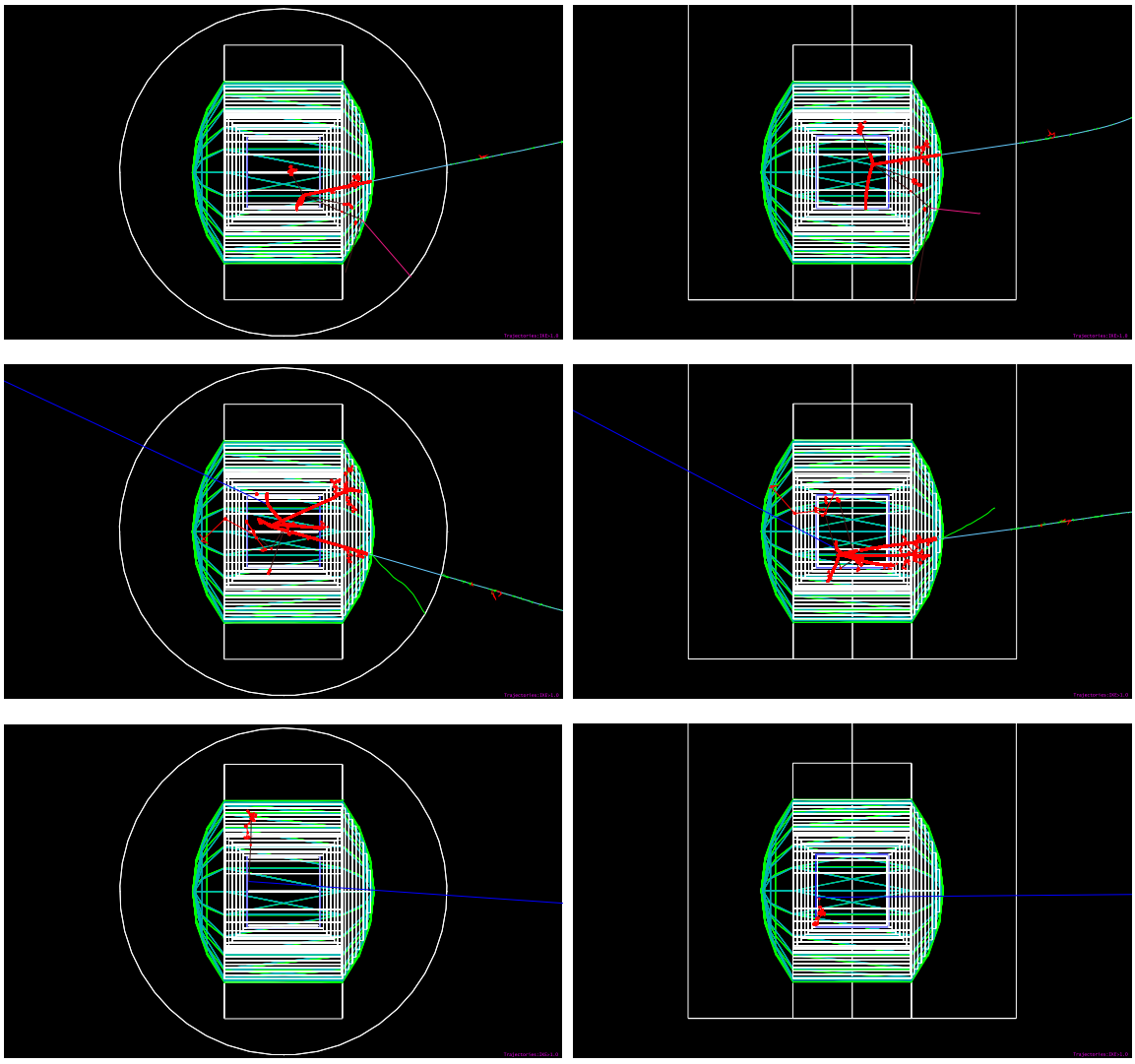

Fig. 5.5 Several event displays are shown for interactions: $\nu_\mu + Ar \rightarrow \mu^- + n + n + n + p$ (Upper), $\nu_\mu + Ar \rightarrow \mu^- + p + \pi^+ + \pi^-$ (Middle) and $\nu_\mu + Ar \rightarrow \nu_\mu + n$ (Lower). A colour scheme is used for particle types, neutrons are brown, protons are pink, muons are light blue, electrons are green, neutrinos are dark blue and red circles indicated detector hits from any particle type. The left displays show the X and Z directions which are the magnetic field and beam directions respectively. The right images shows the Y and Z directions. The beam is incident from the left on all event displays.

5.6 The TPC Rates

When designing a detector it is of primary concern to estimate and understand the number of particle interactions (event rates) occurring. The TPC is the primary target of the detector and it is therefore important to understand all potential particles that can interact or enter the TPC. There are four main contributions that can be considered to estimate these rates, they are:

1. Particles arising from direct neutrino interactions in the TPC
2. Particles arising from neutrino interactions from the rock and detector surroundings
3. Particles arising from neutrino interactions from outer detector components
4. Muons originating from the beam that penetrate through to the TPC

These four areas are summarised in figure 5.6. Except for neutrino interactions directly in the TPC the remainder are all background events. While it will be impossible to eliminate these backgrounds entirely, it may be possible to reduce them with an aim to improve the performance of the TPC.

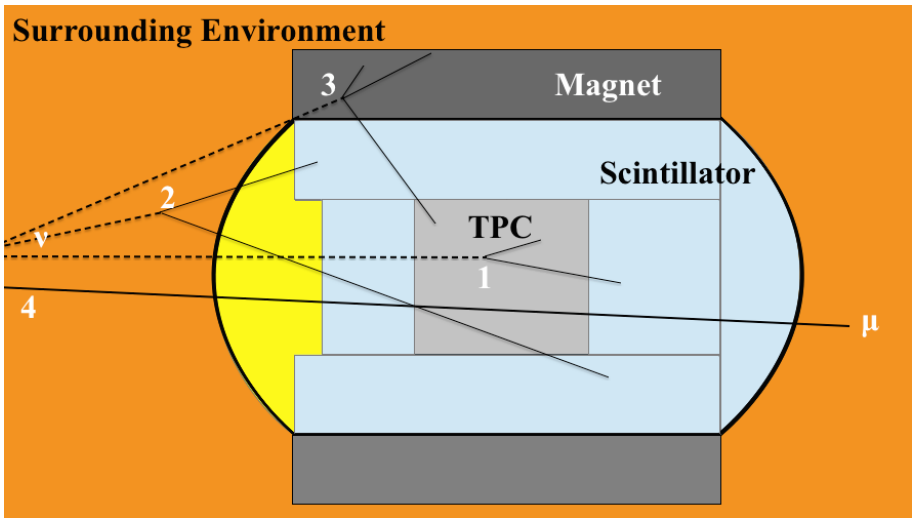

Fig. 5.6 A graphic showing the different contributing factors of particles reaching the TPC. 1. Particles arising from direct neutrino interactions in the TPC. 2. Particles arising from neutrino interactions from the rock and detector surroundings. 3. Particles arising from neutrino interactions from outer detector components. 4. Muons originating from the beam that penetrate through to the TPC.

5.7 Neutrino Event Rates in the TPC

Given the two beam options and two polarities (ν_μ and $\bar{\nu}_\mu$ runs), four different estimations were performed by generating MC events. Only interactions in the TPC were considered and the Secondary Tracking Processor could be omitted for this study, as only the number of neutrino interactions is needed. Although not propagated, the Final State Secondaries (FSS) initial properties were recorded.

The neutrino interaction rates for each of the beam options is shown in the upper of table 5.4, along with the neutrino flavour breakdown. These event rates correspond to 10^{20} p.o.t to provide a normalised comparison between the beam options.

It is clear from these numbers that the 400 GeV beam option is superior in terms of events per p.o.t which is expected due to higher energy protons. However the 50 GeV option provides a cleaner beam, with a greater percentage of the beam composition consisting of its primary neutrino flavour. It is more important to realise these numbers in terms of ppp, which can then declare whether the TPC can cope with these rates. The 400 GeV option can provide 7×10^{13} ppp while the 50 GeV option can provide 2.5×10^{14} ppp. The former option yields 0.1785 ± 0.0003 ν ppp and the latter is a factor $\sim$2.5 smaller at 0.0707 ± 0.0005 ν ppp, for positive focusing. Negative focusing yields neutrino interaction rates of 0.0880 ± 0.0006 ν ppp and 0.0360 ± 0.0005 ν ppp for 400 and 50 GeV options respectively.

The 400 GeV beam with positive focusing provides the highest neutrino rate. With one pulse extracted every 6 seconds (2 spills separated by 50 ms, each of 10.5 μs) and drift times in Argon of the order of 100 μs over 1 m means pile up is not an issue in the gas TPC for these rates.

Certain selections can be made on the events which are then useful for reconstruction purposes. The event rates already discussed include a selection on the TPC itself, requiring that the events are within the gas and not the cathode/anode plates placed within the TPC. Omitting this selection yields an original neutrino rate of 0.2189 ± 0.0004 ppp for the 400 GeV PF beam. Taking this event rate as the basis, a series of selections are performed on this and shown in table 5.5. Selecting only events within the gas result in a 18.1% loss in rate.

Fiducial cuts are necessary for reconstruction purposes as events near the TPC boundaries will be difficult to reconstruct the event with some charged particles leaving the TPC without sufficient track lengths inside the TPC. A 20 cm fiducial cut is applied to each TPC boundary such that event vertices falling within less than 20 cm from

	Positive Focusing				Negative Focusing			
	400 GeV		50 GeV		400 GeV		50 GeV	
Neutrino	**Incident Neutrino Counts / 10^{20} p.o.t (% of Total)**							
ν_μ	239500 ± 400	(93.9%)	27700 ± 200	(98%)	38500 ± 400	(30.6%)	2070 ± 70	(14.2%)
$\bar{\nu}_\mu$	14800 ± 100	(5.8%)	320 ± 22	(1%)	84600 ± 600	(67.2%)	12300 ± 200	(84.8%)
ν_e	665 ± 23	(0.3%)	299 ± 21	(1%)	1760 ± 100	(1.5%)	20 ± 6	(0.2%)
$\bar{\nu}_e$	0	(0%)	6 ± 3	(<0.1%)	876 ± 66	(0.7%)	98 ± 14	(0.7%)
Total	**255.0 ± 0.5 [×10^3]**		**28.3 ± 0.2 [×10^3]**		**125.7 ± 0.8 [×10^3]**		**14.4 ± 0.2 [×10^3]**	
Particle	**Primaries at Vertex Counts / 10^{20} p.o.t (% of Total)**							
μ^-	179200 ± 400	(10.8%)	20700 ± 200	(13.5%)	28400 ± 400	(3.6%)	1570 ± 60	(2.1%)
μ^+	10600 ± 100	(0.6%)	236 ± 18	(0.15%)	60500 ± 500	(7.7%)	8560 ± 140	(11.6%)
p	475700 ± 600	(28.6%)	50940 ± 400	(33.6%)	217000 ± 1000	(27.5%)	22300 ± 230	(30.3%)
n	391700 ± 600	(23.5%)	38500 ± 200	(25.4%)	199000 ± 1000	(25.2%)	20900 ± 220	(28.5%)
π^+	207800 ± 400	(12.5%)	14800 ± 200	(9.8%)	70300 ± 600	(8.9%)	3680 ± 90	(5.0%)
π^0	199500 ± 400	(12.0%)	13100 ± 200	(9.0%)	91300 ± 700	(11.6%)	6150 ± 120	(8.4%)
π^-	112100 ± 300	(6.7%)	5850 ± 90	(4.0%)	79500 ± 600	(10.1%)	6710 ± 120	(9.1%)
γ	19000 ± 100	(1.2%)	527 ± 29	(0.3%)	7670 ± 190	(1.0%)	278 ± 25	(0.4%)
e^-	621 ± 23	(<0.1%)	241 ± 20	(0.2%)	1340 ± 80	(0.2%)	5 ± 3	(<0.1%)
e^+	114 ± 10	(<0.1%)	14 ± 5	(<0.1%)	653 ± 57	(0.1%)	62 ± 12	(0.1%)
other	66700 ± 200	(4.0%)	6210 ± 90	(4.0%)	33000 ± 400	(4.1%)	3310 ± 90	(4.5%)
Total	**1663 ± 1 [×10^3]**		**151.6 ± 0.6 [×10^3]**		**788 ± 2 [×10^3]**		**73.6 ± 0.4 [×10^3]**	
Multiplicity	6.52 ± 0.01		5.36 ± 0.04		6.30 ± 0.03		5.08 ± 0.07	

Table 5.4 These rates correspond to neutrino interactions in the TPC GAr volume, based on simulations of various exposures and scaled to a common exposure of 1×10^{20} p.o.t. No fiducial cuts are employed. Statistical errors of $\pm\sigma = \sqrt{n}$ are shown.

a TPC wall are rejected. This dramatically reduces the event rate to 42.2% which follows in accordance with the volume ratio of 4.05/7.86 = 0.515.

The energy regime of the neutrino beam is taken from 0 to 30 GeV in the simulations but reconstruction of neutrinos at the high energy end will be more difficult to reconstruct, primarily due to high momentum secondaries having low sagitta values. For oscillation purposes LAGUNA-LBNO is concerned with neutrino energies up to ∼10 GeV, a selection of this energy range yields a further reduction of events to 29.7%. Including only muon neutrinos (ν_μ only, not $\bar{\nu}_\mu$) reduces this by a further 1%. With CC interactions making up ∼75% of events, we are then left with 21.6% of neutrino events in the TPC matching all criteria. CCQE interactions account for just 3.6% of events in the TPC after all the selections but are useful for reconstruction as a measurement of the muon's momentum alone can determine the neutrino energy from equation 1.40.

	count [1× 10^{20}]	**count [ppp]**	**% of original**
In TPC	313000 ± 600	0.2189 ± 0.0004	100.0
Gas Only	255000 ± 500	0.1785 ± 0.0003	81.9
20 cm Fiducial Cut	132000 ± 400	0.0924 ± 0.0002	42.2
0 - 10 GeV	92800 ± 300	0.0650 ± 0.0002	29.7
ν_μ	89800 ± 300	0.0628 ± 0.0002	28.7
CC	67500 ± 300	0.0473 ± 0.0002	21.6
CCQE	11100 ± 100	0.00779 ± 0.00007	3.6

Table 5.5 Event rates for neutrino interactions in the TPC after a series of selection criteria are imposed on the events. All events correspond to 400 GeV PF beam option.

5.7.1 Secondary Particle Production

The Final State Primary Lepton (FSPL) and Final State Secondaries (FSS) generated at each neutrino vertex are shown in the lower of table 5.4. High multiplicites can be expected from the neutrino interactions with average particle multiplicites of 6.52 ± 0.01 (stat) for the 400 GeV beam option. This is largely due to the high number of DIS events which can be seen from the particle interaction types in table 5.6. Concerning the number of muons per neutrino interaction, we can expect a muon to be generated at ∼70% of the time, that is 0.1254 ± 0.0003 (stat) μ ppp. The energy spectrum of the muons can be seen in figure 5.7 and illustrates that the majority of the muons

	% of Total Interactions	
Type	**CC**	**NC**
QEL	9.7	3.1
RES	14.2	5.7
DIS	50.3	16.4
Coherent	0.4	0.2

Table 5.6 The different interaction types that the neutrino can undergo in GENIE for both CC and NC interactions. The percentage of each type is shown for the number of total interactions.

generated in the TPC have energies less than 5 GeV while the mean energy is 4.8 GeV.

The kinetic energy that each of the secondary particles carries away from the neutrino interaction needs to be understood to establish the ND capabilities for neutrino energy reconstruction. Only charged particles are visible in the TPC whereas other particles of concern such as neutrons and photons are not. By defining the ratio of kinetic energy devoted to charged particles per neutrino event, T_c, as $\epsilon_c = T_c/T_{TOT}$ we can understand what is achievable within the TPC. Similarly for neutrons and photons (including those originating from π^0s) we can define ratios as $\epsilon_n = T_n/T_{TOT}$ and $\epsilon_\gamma = T_\gamma/T_{TOT}$ respectively. Figure 5.8 shows these ratios for both CC and NC interactions. In NC interactions the outgoing neutrino carries away a significant amount of energy in the majority of interactions and this cannot be detected. Whereas in CC interactions most of the energy is carried by charged particles with little going to photons and neutrons. With ∼75% of neutrino interactions of CC type, the TPC alone will be instrumental in neutrino energy reconstruction.

5.8 Particles Reaching the TPC

Particles reaching the TPC from neutrino interactions within the rock surroundings and other detectors components are a background that need to be well understood in order to estimate the TPC performance. These rates can be significant with rock muons (muons originating from neutrino interactions in the rock and the detector environment) produced with high energies (up to 30 GeV). As a result these muons can travel vast distances, up to 60 m, as figure 5.9 shows the distances that the muons have travelled to reach the TPC. This is not an indication to their full range as propagation after leaving the TPC is not included in these results. The number of

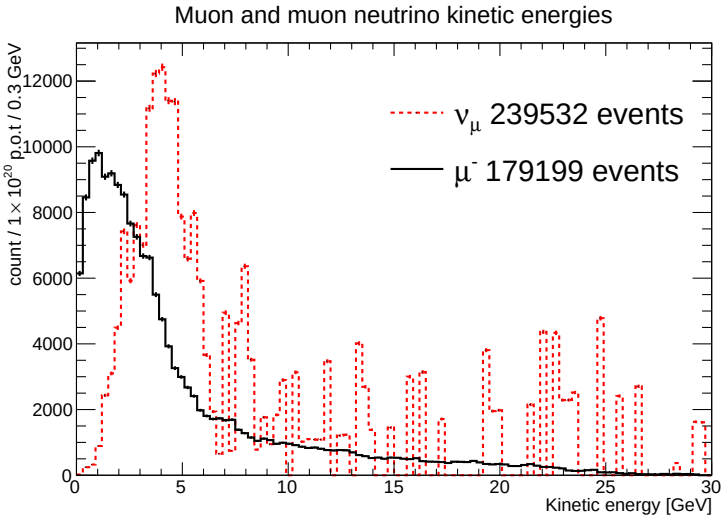

Fig. 5.7 The kinetic energy spectrum of primary muons (in black) generated at the neutrino vertex in the TPC. The red dashed line indicates the ν_μ energy spectrum for those causing interactions in the TPC, hence is not simply the flux but is convoluted with the cross section. Counts are normalised to 1×10^{20} p.o.t for 400 GeV PF beam option.

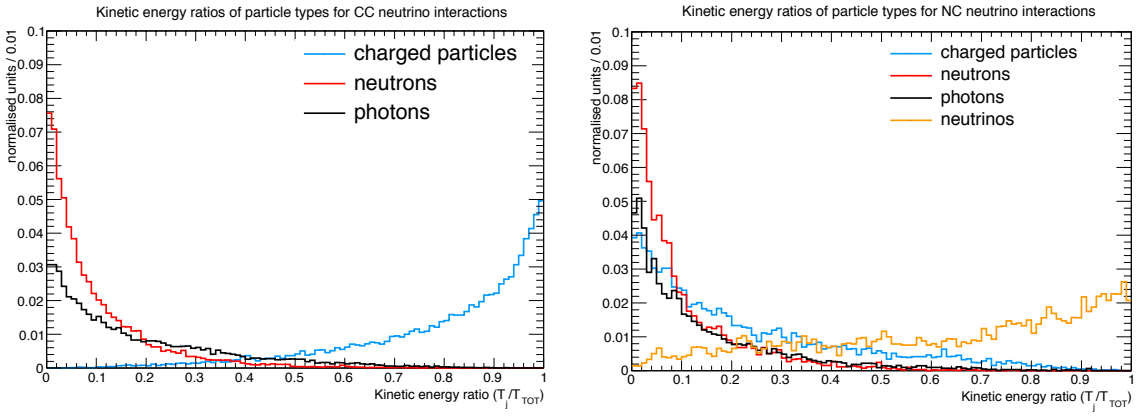

Fig. 5.8 The kinetic energy ratios showing the proportion of kinetic energy devoted to charged particles, ϵ_c in blue, neutrons, ϵ_n in red and photons, ϵ_γ in black for CC (left) and NC (right) neutrino interactions. The orange line represents the neutrino energy ratio for NC only. Counts are normalised to the number of neutrino events for CC (64238 events) and NC (21292 events) channels. Particles with zero kinetic energy ratios are omitted such that $0 < \epsilon_j \leq 1$.

these muons reaching the TPC is considerable at 44.5 ± 0.5 (stat) ppp for the 400 GeV PF beam option, that is over 350 times that of the muons generated in the TPC. However if only neutrinos with energy of 10 GeV or less are considered this number is more than halved to 19.9± 0.2 (stat) ppp, as their range is reduced dramatically. The energy distribution of the muons from the full simulation (up to 30 GeV neutrinos) is shown in figure 5.10. The energy distributions are very similar when compared to the muons produced inside the TPC but almost all of the muons originating from outside the TPC will enter and leave the TPC and hence have no interaction vertex.

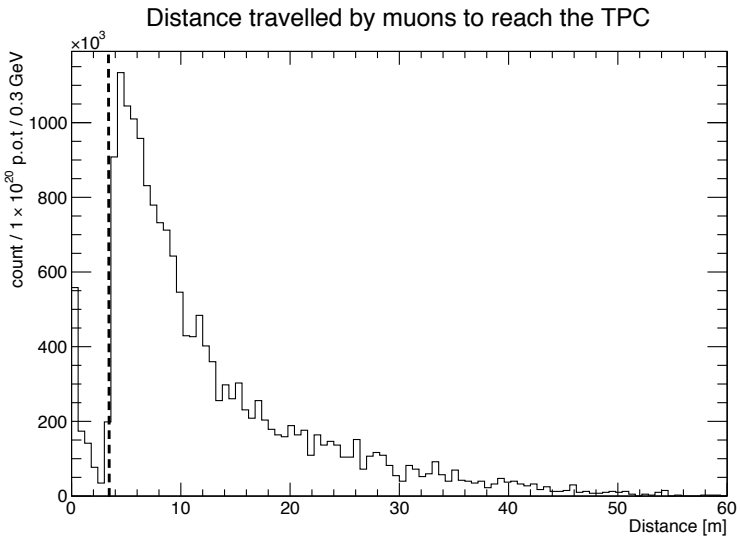

Fig. 5.9 The distance travelled by muons to reach the TPC originating from neutrino interactions outside the TPC. Showing only the magnitude of the distance travelled until the TPC is reached, and therefore does not represent their true range, as the distance after leaving the TPC is excluded. The dashed line at 3.5 m indicates the edge of the cavity and distances greater than this represent muons originating from the rock only.

Other particle types, with kinetic energies greater than 1 MeV, reaching the TPC are shown with their corresponding rates in table 5.7. Figure 5.11 shows the original vertex position of the neutrino interaction for all secondary particles that reached the TPC. These results do not show subsequent interactions in the TPC but show any possible particle that reaches the TPC.

The majority of the particles arriving at the TPC originate from the surrounding rock at 75.6%. A considerable amount also arise from neutrino interactions within the scintillator layers at 20.1%. The rock level is irreducible but removal of some

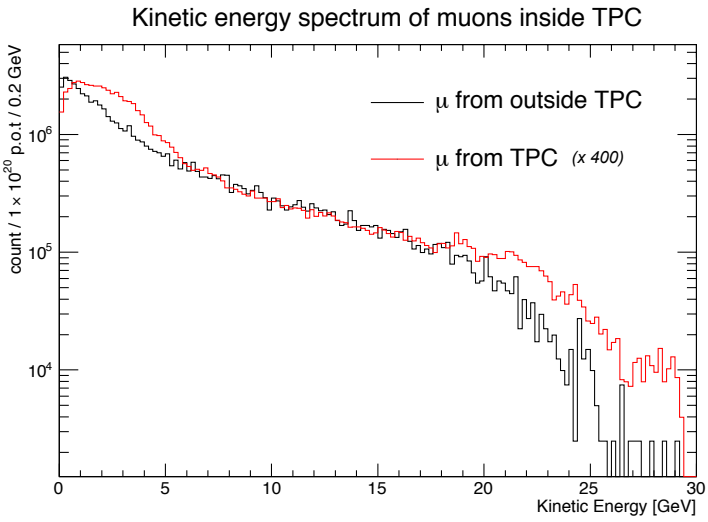

Fig. 5.10 The kinetic energy spectrum of the muons reaching the TPC from neutrino interactions within the rock and surrounding detector components in black and those that are generated in the TPC in red. With a larger muon rate due to interactions outside the TPC the muon rate from inside the TPC is scaled by a factor of 400. After the scale factor both are normalised to 1×10^{20} p.o.t.

Particle Type	**Rate [ppp]**	**%**
Photons	125.0 ± 0.9	40.8
Muons	44.5 ± 0.5	14.5
Electrons	24.7 ± 0.4	8.1
Neutrons	21.0 ± 0.4	6.9
Charged Pions	6.0 ± 0.2	2.0
Protons	4.2 ± 0.2	1.4
Other	13.4 ± 0.3	4.3
Neutrinos	67.2 ± 0.6	22.0
Total	306 ± 1	100

Table 5.7 Particle types of interest reaching the TPC with kinetic energies above 1 MeV. Note that the majority of the photons (>99%) leaving the TPC originate from π^0 decays and are low energy (<1 GeV). Errors indicate statistical ±1 σ only.

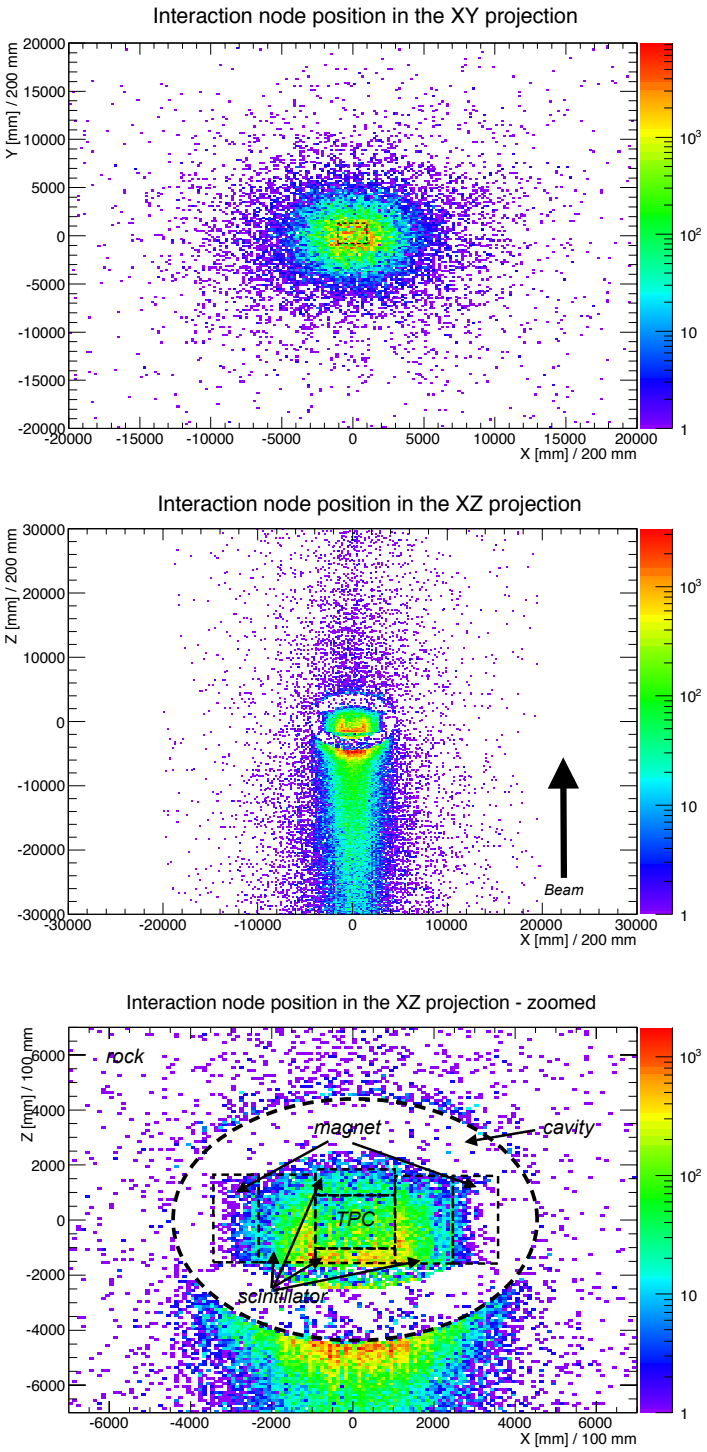

Fig. 5.11 Upper: The XY projection (beam into page) of the node positions of the original neutrino interaction for which a secondary reached the TPC (highlighted by the dashed line). Middle: The XZ projection (beam upwards) of the node positions of the original neutrino interaction for which a secondary reached the TPC. Lower: A zoomed in version of the middle plot to illustrate the various detector components with respect to the node positions. Counts are normalised to 4×10^{16} p.o.t.

scintillator layers, especially upstream of the TPC, could decrease the background muon rate at a cost to the energy reconstruction of photons. Other detector layers and environment surroundings show their contributions in addition to the rock and scintillator layers in table 5.8.

Detector/Environment Node	Contribution (%)
Cavity	<0.1
TPC	0.1
Inner Vessel (GAr)	0.4
Magnet	1.5
Vessel	2.3
Scintillator	20.1
Rock	75.6

Table 5.8 All the detector/environment nodes in the geometry with their contributing percentages to secondary particles reaching the TPC where the neutrino interaction occurred originally.

5.8.1 Muons Originating from the Beam

The rate of muons originating from the beam, decay pipe and focusing horns has been estimated by the LAGUNA-LBNO beam group independently to be 2.5 $\mu/m^2/10^{13}$ p.o.t (400 GeV PF) at 800 m from the beam target [65]. Extrapolating this value to an area of 4 m^2 for the TPC ppp yields 70 μ ppp. This is $\sim$1.6 times larger than the muons originating from the rock and detector surroundings. Estimates for the remaining beam options have not been considered by the LAGUNA beam group.

5.8.2 Total Muons Expected in the TPC

Referring back to figure 5.6 it was shown there are 4 possible areas for muons to reach the TPC. Values have been calculated/estimated for all 4 areas of concern and are summarised in table 5.9. The total muon flux in the TPC is then 114.6 $\pm$ 0.8 μ ppp. Areas 1 and 3 can be controlled to some extent by ND design but areas 2 and 4 are irreducible from the ND design aspect. The latter are of course the largest contributing factors to the muon rates at 112.1 μ ppp (97.8% of the total contribution) and therefore a reduction in areas 1 and 3 will not dramatically increase the performance.

To estimate if pile up is an issue the number of muon tracks in the TPC per unit area (2 $\times$ 2 m^2) shows that $\sim$14 μ tracks/m^2/spill will pass through the TPC. With

Muon origin	**Rate [ppp]**	**Contribution [%]**
ν interactions in TPC	0.1254 ± 0.0003	0.1
ν interactions in outer detector + cavity	2.4 ± 0.1	2.1
ν interactions in rock	42.1 ± 0.5	36.7
Beam + decay pipe + horns	70	61.1
Total	**114.6 ± 0.8**	**100**

Table 5.9 A table showing the four main sources of muons reaching the TPC with their associated rates determined from simulations. These numbers are translated into how much each contributes to the total of the four origins. All values are based on the 400 GeV PF beam option. Uncertainties indicate 1 σ statistical errors only.

each spill extraction lasting 10.5 μs this results in ∼1-2 μ tracks/m^2/μs. With drift times of ∼100 μs detector pile up is therefore unavoidable. However if the vertex can be resolved then it can help discriminate between the tracks within the TPC. At ∼1 μ track/700 cm^2/spill the vertex should be easily resolved.

5.9 Particles Leaving the TPC

It is important for other stages of the ND design to realise what particles leave the TPC. This primarily concerns the angular distribution of photons and their associated energy spectrum, as the majority of these photons will originate from π^0s. Figure 5.12 shows the kinetic energies as a function of angular dependance for particles of key concern.

The majority of the particles leaving the TPC are photons at 30.7%, that is 0.5255 ± 0.0008 (stat) ppp. Table 5.10 shows the main particle types of concern that leave the TPC from neutrino interactions within the TPC. Given that the TPC can perform momentum measurements on protons, charged pions and muons, the two other major particle types are photons and neutrons, of which momentum measurements cannot be performed within the TPC. Outer detector layers such as the TAS will hope to tackle these particles.

5.10 Energy Reconstruction of π^0s in the TAS

At this point we have not directly focussed on the ND performance and its reconstruction capabilities, we next examine a selected demonstration of the ND performance focusing on energy reconstruction of π^0s using the TAS. It is clear from the previous

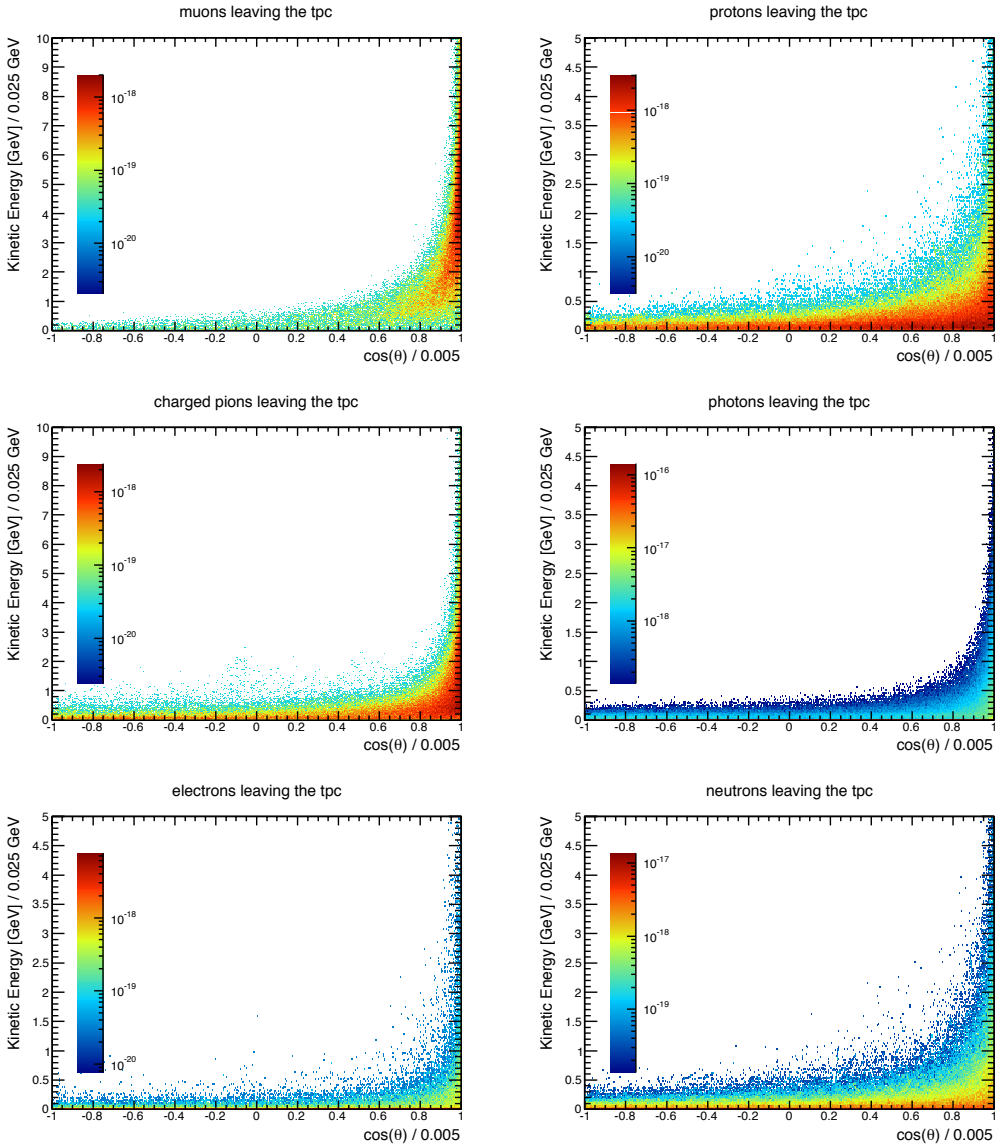

Fig. 5.12 The kinetic energies of the particles of key concern leaving the TPC as a function of angular dependance. The angular dependance is measured by cosθ, which is a measure of the particles momentum in the beam direction, that is cos$\theta = p_z/|\boldsymbol{p}|$. Note the different energy scales for muons and charged pions (0-10 GeV) as they are produced with higher energies, the other scales are 0-5 GeV. Particle counts are normalised to p.o.t.

Particle	**Rate leaving [ppp]**	**Contribution [%]**
Photons	0.5255 ± 0.0008 (stat)	30.7
Neutrons	0.3855 ± 0.0007 (stat)	22.5
Protons	0.2560 ± 0.0006 (stat)	14.9
Charged Pions	0.2291 ± 0.0006 (stat)	13.4
Muons	0.1297 ± 0.0004 (stat)	7.6
Electrons	0.0585 ± 0.0002 (stat)	3.4
Neutrinos	0.0580 ± 0.0002 (stat)	3.4
Other	0.0708 ± 0.0002 (stat)	4.1

Table 5.10 The particle types arising from neutrino interactions in the TPC that then subsequently leave the TPC boundaries. Their associated rates at which they do so is shown per proton pulse (ppp) with their contribution to the total number of particles leaving the TPC. Rates correspond to all particles with kinetic energies in excess of 1 MeV.

sections that this is not only important to detect π^0s but to also reconstruct their energy as photons originating from their decay can carry away a considerable amount of energy in both CC and NC neutrino interactions, as shown in figure 5.8. To reconstruct a π^0 involves the reconstruction of the two photons that led to its decay requiring good knowledge of the photon momentum to give an accurate measurement of the π^0 energy and to locate the neutrino interaction vertex. Particularly the latter is useful in NC interactions where no charged particles can be observed in the TPC.

Inclusion of the TAS aims to complement the TPC by measuring the energy deposited by photons. Almost all photons (∼99%) leaving the TPC arise from π^0 decays via: $\pi^0 \rightarrow \gamma\gamma$. It was shown earlier that also they contribute to 30.7% of the total number of particles leaving the TPC, with neutrons the second majority at 22.5%. This equates to 0.5255 ± 0.0008 (stat) photons ppp. If the momentum of the outgoing photons can be determined it is then possible to reconstruct the original energy of the π^0, of which contribute to 12% of all particles produced at the neutrino vertex (400 GeV PF beam). It is therefore strongly motivated to discuss potential reconstruction techniques for π^0s using the TAS sub detector. Although neutrons contribute heavily to the number of particles leaving the TPC they are not considered in this study, as they require different methods and techniques for reconstruction.

The true kinetic energy spectrum of π^0s from neutrino interactions in the TPC can be seen in the right of figure 5.13 with their multiplicities on the left. High multiplicities of up to 8 π^0s per neutrino interaction can occur, although such occurrences are rare. The average multiplicity is ∼1.2 per neutrino interaction in the TPC, with the

majority of energies of <5 GeV. To understand how these can be reconstructed it is first necessary to understand how photons can be reconstructed within the TAS.

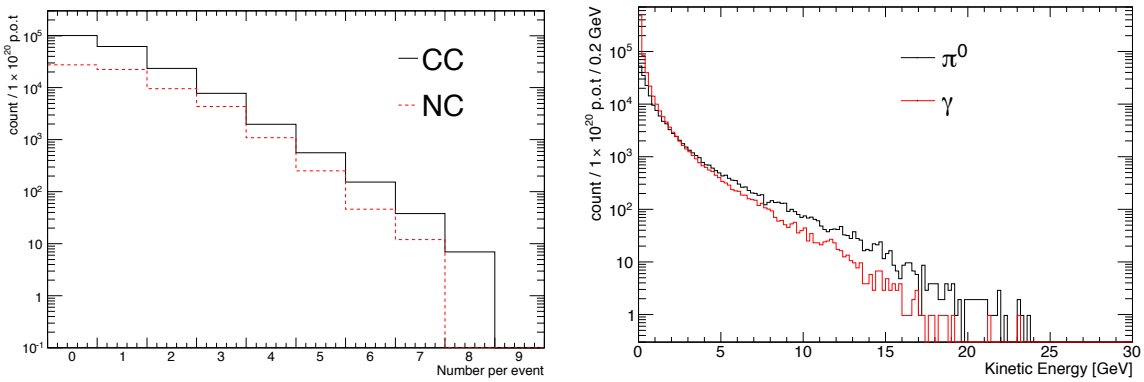

Fig. 5.13 Left: The number of π^0s generated per neutrino interaction in the TPC. Right: The kinetic energy spectrum of π^0s originating from neutrino interactions in the TPC (black line) and the kinetic energy of the photons originating from the π^0s (red line). Both plots show results based on a simulations of 1×10^{20} p.o.t.

5.10.1 Photon Energy Reconstruction

Photons of energies ranging from 0.1 - 5 GeV are generated in the centre of the TPC, directed downstream, $\hat{\boldsymbol{p}}_\gamma = (0,0,1)$. Summing up the energy deposited in the TAS per photon generated then gives a relationship of the truth energy to the reconstructed energy. 10^4 photons were generated for this study with a uniform distribution over the energy range. Figure 5.14 shows the mean reconstructed photon energy per 0.2 GeV truth energy bin. Approximating this relationship with a linear fit represents the relationship well and yields a gradient of α=0.568. Such that the reconstructed energy of photons within the TAS actually represents a true energy of $E_{truth} = E_{recon}/0.568$. Applying this scale factor to the reconstructed photon energy then yields a close representation of the true reconstructed photon energy. Plotting $(E_{truth} - \alpha E_{recon})/E_{truth}$ on an event basis and fitting a Gaussian distribution of mean value μ=0.01 and σ=0.37 to the peak is shown in figure 5.15.

5.10.2 π^0 Invariant Mass

The invariant mass of the π^0, m_π, can be determined from the photon kinematics, $m_\pi^2 = p^\mu p_\mu = (q_1 + q_2)^2$, as shown in figure 5.16. In the lab frame, with E_1^γ and E_2^γ

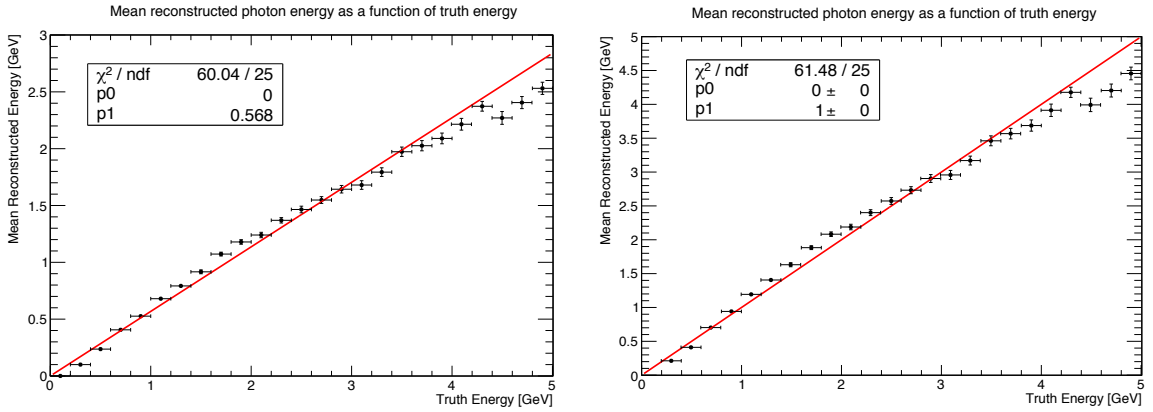

Fig. 5.14 The mean reconstructed energy of photons within the TAS as a function of truth energy both before (left) and after (right) scaling. Showing linear fits with gradients of 0.568 and 1 respectively. The mean is taken per truth energy bin width of 0.2 GeV and errors bars represent the standard error on the mean. 10^4 photons were simulated within the energy range and the plots only include non zero reconstructed values, which is represented by 8734 photons.

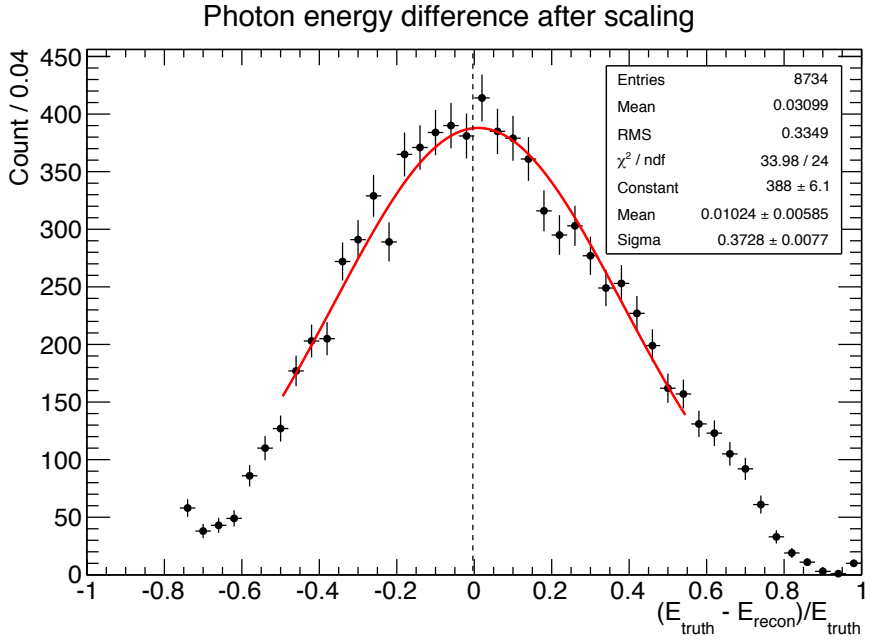

Fig. 5.15 The difference between the truth and reconstructed photon energies, $(E_{truth} - \alpha E_{recon})/E_{truth}$, within the TAS after the scaling factor of $\alpha = 0.568$ is applied. A Gaussian function is fitted to the peak of the distribution yielding a mean value of 0.01 and with a spread of $1\sigma = 0.37$.

the energies of the photons and α the angle between the two photons, the invariant mass squared can be determined by equation 5.8. The invariant mass of π^0 has been experimentally measured and has a well established result of $m_\pi = 134.98$ MeV [42]. Matching photon pairs to produce an invariant mass close to this value, using equation 5.8, can then indicate the photons originated from a π^0 with energy $E_\pi = E_1^\gamma + E_2^\gamma$.

$$m^2 = 4E_1^\gamma E_2^\gamma \sin^2\left(\frac{\alpha}{2}\right) \tag{5.8}$$

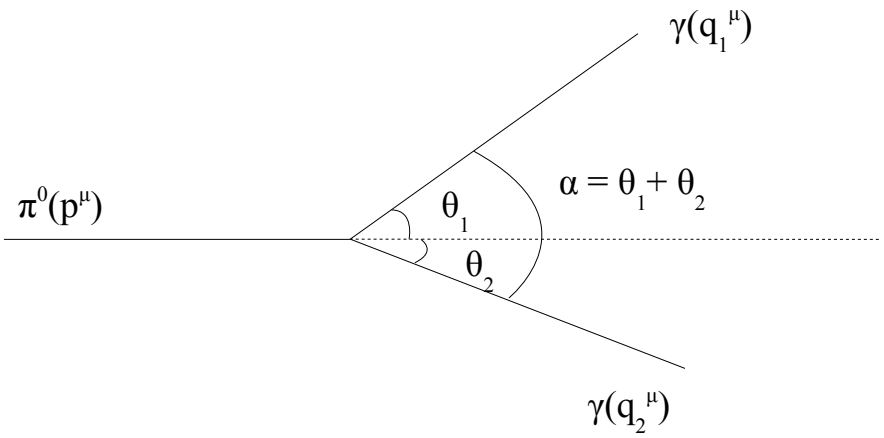

Fig. 5.16 An illustration of a π^0 of 4-momentum p^μ decaying into two photons of momentums q_1^μ and q_2^μ separated by an angle α in the lab frame.

Similar MC experiments to the photon tests were conducted also within the TAS to determine how well the invariant mass of single π^0s could be reconstructed. With an energy distribution of 0.2 - 10 GeV and momentum purely in the beam direction 10^4 π^0s were generated in the centre of the TPC. Tracking each outgoing photon and recording only hit information, the invariant mass is then calculated from equation 5.8. The energy of each photon is given by the sum of the total energy deposition along its trajectory, $E_i^\gamma = \sum_n^{hits} E_n^{deposited}$. The momentum of each outgoing photon is determined from the truth values. Photons which deposit no energy cannot provide a measurement of the invariant mass and are discounted. Other decay modes of π^0s are ignored from this study. An implicit photon energy cut of 50 MeV is applied to remove poorly reconstructed photon tracks, requiring both outgoing photons to have reconstructed energies above this threshold.

The effect of the reconstructed angle on the invariant mass is large and due to this no reconstruction on the angle is performed, with truth values for the photon

momentum being used instead. To fully estimate the detectors potential of measuring π^0s this effect needs to be studied further as it depends on the π^0 vertex location and hit locations of the 2 photons in the TAS, which are limited by track reconstruction and the position resolution in both the TPC and the TAS.

The reconstructed invariant mass can be seen in figure 5.17 without any scaling applied to the energies of the outgoing photons. A Gaussian distribution of μ=82.5 MeV and σ=27.8 MeV is fitted in the region of 45 to 125 MeV. This is far lower than the expected π^0 mass but upon scaling with the factor determined from fits to previous photon simulation data of α=0.568, taken from figure 5.14, a mean value of 143.8 MeV is determined from a similar fitting. The mean of the data is even closer to the true value at 135.7 MeV. However such scaling introduces a larger spread over the distribution and has an increased standard deviation of 48.2 MeV. The experimentally determined value of 134.98 MeV then lies well within 1 standard deviation of the fitted mean value.

The energy difference between the truth and the reconstructed values of the π^0s generated conforms well with a Gaussian distribution, both for pre and post scaling data sets. Figure 5.18 illustrates the differences from determination of the quantity $(E_{truth}$ - $E_{recon})/E_{truth}$.

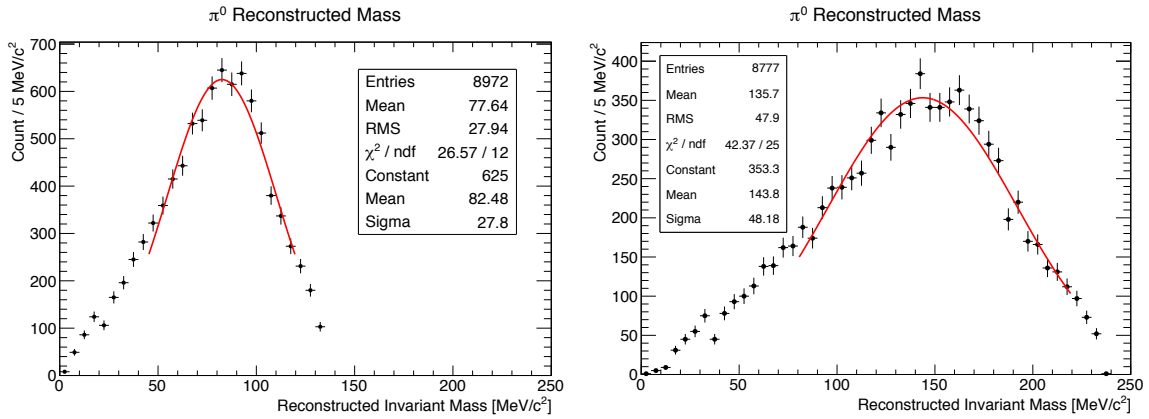

Fig. 5.17 The invariant mass of π^0s generated within the TPC using the energy deposition within the TAS to reconstruct the energy of each outgoing photon. Truth values of the separation angle in the lab frame are used in the reconstruction of the mass. Left: Unscaled photon energies. Right: Scaled photon energies by a factor of α^{-1}=1.76.

The lower energy photons contribute to the spreading of the distribution and it can be seen that adding more stringent selections on the photons tracks leads to a

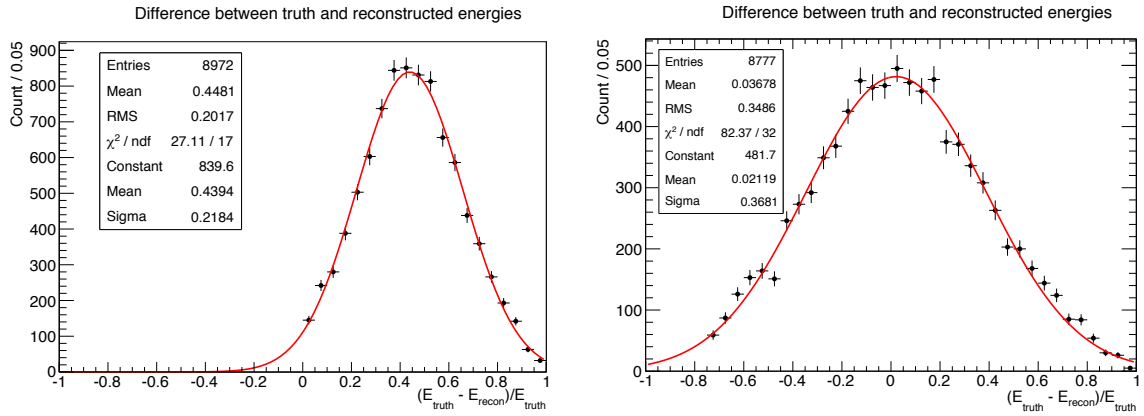

Fig. 5.18 The difference between the truth and reconstructed energies of π^0s generated in the TPC. Left: Unscaled photon energies. Right: Scaled photon energies by a factor of α^{-1}=1.76.

more precise value of the reconstructed mass. Requiring at least 4000 hits on each outgoing photon yields a better measurement on the reconstructed mass once fitted with a Gaussian distribution with a mean value of 134.9 MeV, as shown in figure 5.19. However the number of π^0s passing this selection is then reduced to 42.5%.

5.11 Estimating the Detector Performance

We finally try to estimate the ND performance based on the initial studies presented in this chapter. In order to so the main detector systematics are estimated and show how these contribute to the signal event normalisation uncertainty and the beam ν_e normalisation uncertainty. This study is based on an analysis using only CC interactions in the TPC fiducial volume, selecting events where the muon vertex is located within the fiducial volume and subsequently leaves the TPC. The relative difference of the transverse μ^- momentum to the ν_μ momentum in the TPC (truth values) as a function of the angle with respect to the beam axis is shown in figure 5.20 for these events to give a handle on how the muon flux represents the neutrino flux. It is clear from the figure that the majority of the muons are extremely forward going, with 56% of muons having a $\cos\theta$ value exceeding 0.98. From measurement of the muon direction, and hence angle, we can then impose a selection on the muons in the TPC to provide a closer representation of the true neutrino flux. Imposing a selection on smaller angles, $\cos\theta > 0.998$, 44.9% muons then are within 10% of the truth neutrino

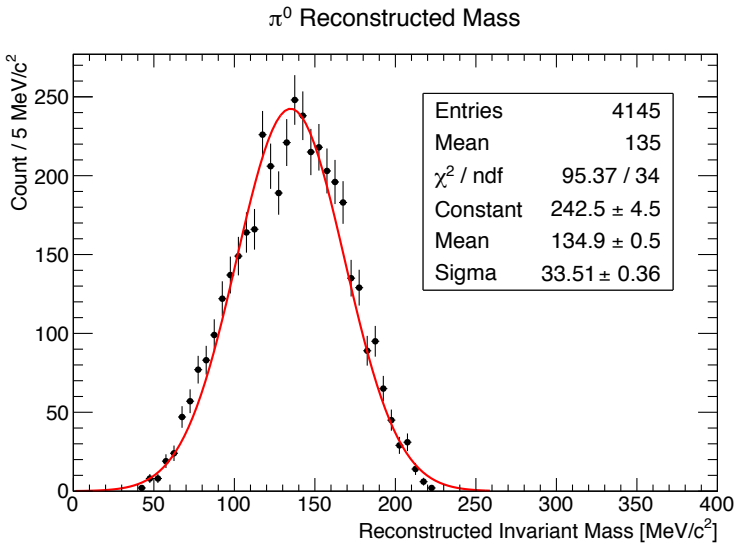

Fig. 5.19 The invariant mass of π^0s generated within the TPC using the energy deposition within the TAS to reconstruct the energy of each outgoing photon. Truth values of the separation angle in the lab frame are used in the reconstruction of the mass. Each outgoing photon energy is scaled by factor α^{-1}=1.76 and only photons with 4000 hits per track are included.

momentum. Based on this we then use the transverse momentum of the muon to give an indication of the ν_μ flux at the near detector. This aims to provide a first order estimation of the ND performance by directly looking at event rates, giving us the uncertainty on the flux × cross section which is used when extrapolating to the FD. For further, more accurate estimations of the neutrino flux from the muons we would impose these $\cos\theta$ selections with a hadronic cut to remove events that give poor estimation on the neutrino momentum. These are not realised in this analysis but are mentioned to motivate the use of the outgoing muon to provide a handle on the incident neutrino flux on the TPC.

5.11.1 Signal at Far Detector

Examining the appearance oscillation probabilities, which were presented in figure 3.1, we want to be sensitive to both first and second oscillation maxima. These occur at neutrino energies between 2 - 10 GeV and 1 - 2 GeV for first and second respectively, thus requiring a broad energy range selection of 1 - 10 GeV. Neutrinos of energies exceeding this threshold are discounted due to lack of signal statistics which are dramatically reduced for the 400 GeV PF beam option. As a lower threshold we

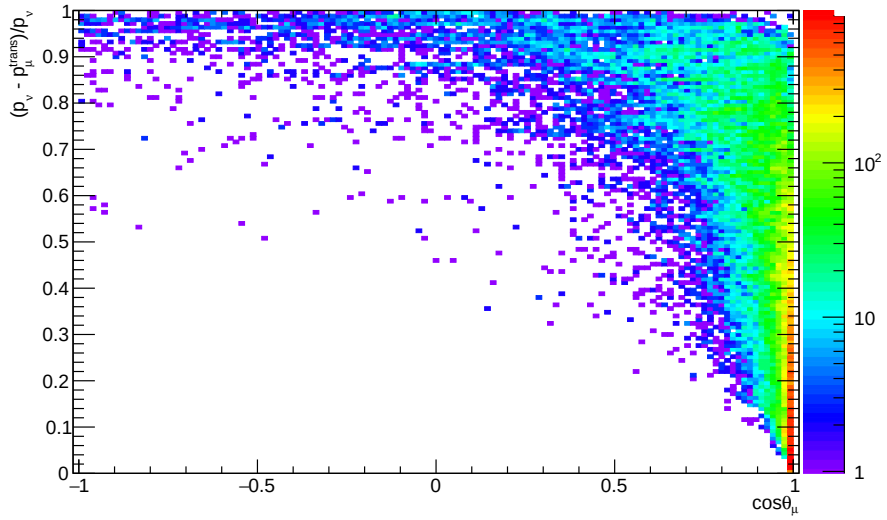

Fig. 5.20 The relative difference of the transverse μ^- momentum to the ν_μ momentum in the TPC (truth values) as a function of the angle with respect to the beam axis for ν_μ CC events in the TPC fiducial volume. The total number of events based on a simulation of exposure 9.6×10^{19} p.o.t.

use 500 MeV to avoid Fermi momentum and reduce the gamma background.

5.11.2 Statistics

In the LAGUNA-LBNO expression of interest [64] estimates for the beam power and number of p.o.t are established based on a pessimistic shared mode of the beam. The shared mode estimates 60% of the beam time dedicated for use in LBNO, providing 1.0 $\times$ 10^{20} p.o.t /year. Based on these numbers for the 400 GeV PF beam option we can expect $(67.5 \pm 0.3) \times 10^3$ ν_μ CC events / year at the ND within the fiducial volume with energies < 10 GeV/c, equivalent to a signal normalisation factor uncertainty, σ_{stat}^{sig} = 0.4%.

For ν_e CC events we can only estimate the statistical uncertainty by extrapolating the signal result. This is due to the extremely low ν_e composition in the beam that results in no electron neutrinos passing the fiducial volume at 800 m from the beam. This is an unfortunate result from the LAGUNA-LBNO collaboration, where the collaboration failed to provide an adequate simulation of the neutrino beam. Extrapolating the electron neutrino contamination result of $\alpha_{\nu_e}^{cont} = (\nu_e + \bar{\nu}_e)/(\nu_\mu + \bar{\nu}_\mu + \nu_e + \bar{\nu}_e) =$ 0.7%, determined earlier in section 4.7, we get a ν_e normalisation factor uncertainty

of $\sigma^{\nu_e}_{stat} = 1/\sqrt{\alpha^{cont}_{\nu_e} N^{sig}_{CC}} = 4.6\%$ for 1 year of running. For a duration of 5 years, this then drops to $\sigma^{\nu_e}_{stat} = 2.1\%$.

5.11.3 Fiducial Volume

In the ND studies a reduced TPC volume of $V_{fid} = 1.6 \times 1.6 \times 1.6$ m^3 $= 4.096$ m^3 represents the fiducial volume, employing a 20 cm cut from each of the TPC sides, resulting in a volume at 51.2% of the original size. By taking a vertex resolution of 1 mm, roughly 3 lengths of the estimated TPC position resolution of 300 μm, we estimate the uncertainty due to the difference in the volume. Given that the neutrinos are distributed isotropically within the fiducial volume provides good justification of this estimation. The systematic uncertainty arising from this choice of fiducial cut leads to a normalisation factor uncertainty, $\sigma_{FV} = (V^{'} - V^{''})/V_{fid}$, where $V^{'}$ and $V^{''}$ are the volumes for cuts of 199 mm and 201 mm respectively. We then have a fiducial volume uncertainty of $\sigma_{FV} = 0.8\%$.

5.11.4 TPC Momentum Scale

The TPC momentum scale uncertainty is estimated directly from the TPC momentum resolution. This arises due to the uncertainty in the measurement of the sagitta and the magnetic field strength across the TPC. We assume the effect of the track length uncertainty to be negligible in comparison to the uncertainties on the magnetic field and the sagitta measurement. Equation 5.9 shows the uncertainty calculation, which uses previous equations 4.2 and 4.3, arising from the uncertainty in the measurement of the sagitta. In estimating the TPC momentum resolution we have also included the uncertainty due to the magnetic field, which is estimated at a 1% fractional uncertainty in the field strength across the TPC. Since we look for a μ^- as our signal we can apply this to the μ^- transverse momentum spectrum on an event basis. With the muon a minimum ionising particle depositing ~0.07 MeV/cm in GAr, we estimate between 5 and 10 hits for a 1 m track, thus taking the lower bound of $N_p = 5$ in the estimation. This has been employed in equation 5.9.

$$\delta p_{trans} = p_{trans}\sqrt{(\delta s/s)^2 + (\delta B/B)^2} = p_{trans}\sqrt{\left[\frac{26.7\sigma_{xy}p^2_{trans}}{2\sqrt{2}l^2 B}\right]^2 + 0.01^2} \tag{5.9}$$

Using the truth values for the transverse muon momentum p^{trans}_{μ} we vary it as

equations 5.10 and 5.11 applied to all events, to give lower and upper variations on the total number of ν_μ CC interactions between 500 MeV/c and 10 GeV/c. Here $\Delta p_\mu^{trans} = \delta p_{trans}$. from equation 5.9.

$$p_{lower} = p_\mu^{trans} + \Delta p_\mu^{trans} \tag{5.10}$$

$$p_{upper} = p_\mu^{trans} - \Delta p_\mu^{trans} \tag{5.11}$$

We then have $N_{meas}^{CC} = 58368$ (truth events) with lower and upper bounds of $N_{lower}^{CC} = 56630$ and $N_{upper}^{CC} = 57037$ respectively, as shown in figure 5.21. To estimate the uncertainty on the TPC momentum scale we take the largest difference, this occurs for N_{lower}^{CC}, $\sigma_{mom.scale} = (N_{meas}^{CC}$ - $N_{lower}^{CC})/N_{meas}^{CC}$, yielding a value of 3.0%. The reason for this large uncertainty is due to small measurements of the sagitta for the high energy muons. At the mean momentum of 2.6 GeV/c we then have $\delta s/s$ ~4% (1 m track length), reaching $\delta s/s$ ~20% at 6 GeV/c.

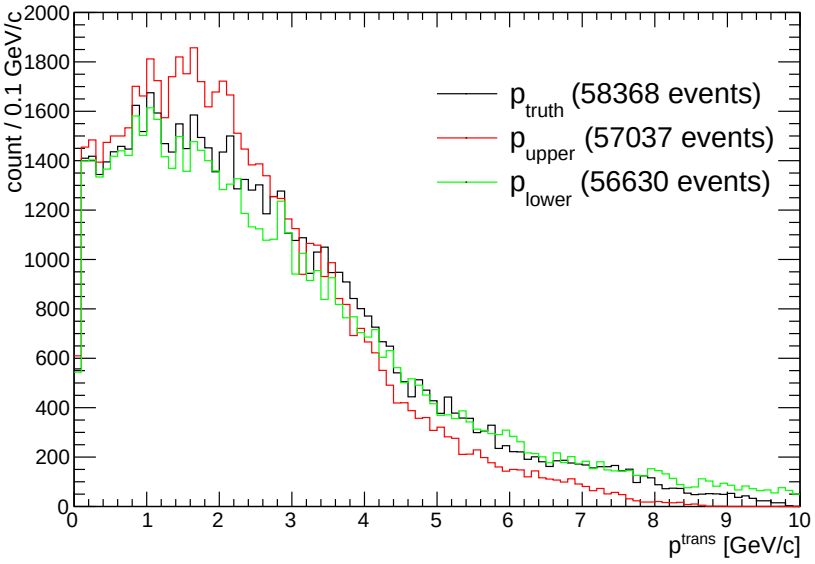

Fig. 5.21 The transverse muon momentum in the TPC for ν_μ CC events in the TPC fiducial volume. Truth values (black) are compared with upper (red) and lower (green) bounds, with the total number of events based on a simulation of exposure 9.6×10^{19} p.o.t.

5.11.5 External Backgrounds

The two main backgrounds are photons entering the TPC producing electrons which are in turn mis identified as μ^- and muons entering the TPC from external interactions (including sand muons).

5.11.5.1 Photons entering the TPC

It was shown earlier that the number of photons entering the TPC was extremely large at 125.0 ± 0.9 (stat) ppp (per proton pulse), from table 5.7. However when we examine the number of photons reaching the TPC which have energies of 200 MeV and above this number drops to 1.45 ± 0.08 (stat) ppp and for energies of 1 GeV and above it drops further to 0.13 ± 0.02 (stat) ppp. Figure 5.22 shows the full energy spectrum of photons reaching the TPC from background interactions.

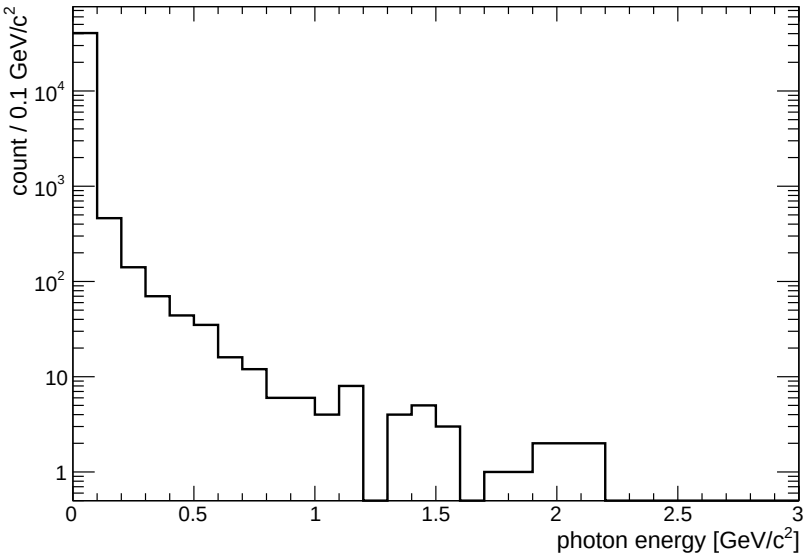

Fig. 5.22 The energy spectrum of photons entering the TPC from background neutrino interactions. Results based on a simulation of exposure 1.75 × 10^{16} p.o.t.

At these energies pair production interaction dominates and the cross section on argon can be approximated as constant between 0.1 - 10 GeV at 3.7 × 10^{-2} cm^2/g [86]. For a fiducial volume of mass 143.36 kg we then have a cross section, σ_{Ar} = 0.530432 m^2. Assuming we can use particle energy loss in the TPC to discriminate between e^- and μ^- below 500 MeV we only consider the effect of photons with energies ≥ 1 GeV.

At 0.13 ± 0.02 (stat) ppp the flux is then (8 ± 1) × 10^3 γ / m^2 / 10^{20} p.o.t, yielding an expected rate of (4.0 ± 0.7) × 10^3 γ / 10^{20} p.o.t. Taking the upper estimate at 4.7 × 10^3 γ / 10^{20} p.o.t, we then have an uncertainty due to external photons, σ_γ, of 7.0%(1 - $\epsilon_{e/\mu}$), where $\epsilon_{e/\mu}$ represents the discrimination efficiency factor between e^- and μ^- in the TPC, for energies above 500 MeV. For energies below this threshold we assume $\epsilon_{e/\mu} \sim 1$ due to TPC energy loss particle identification.

5.11.5.2 Muons entering the TPC

We have earlier determined the number of muons entering the TPC due to interactions in the rock (sand muons), detector and that originating from the beam. The total μ^- rate from table 5.9 was estimated at 114.5 ± 0.8 (stat) ppp, which corresponds to an extremely large rate of (1.047 ± 0.007) × 10^8 μ^- / 10^{20} p.o.t. Since the momentum of these muons is similar to the signal muon momentum we cannot impose any cuts on the momentum, however if the vertex can be resolved these events can be discounted. At (67.5 ± 0.3) × 10^3 ν_μ CC events / 10^{20} p.o.t we then have a normalisation uncertainty due to muon background, $\sigma_{ext.\mu}$, of (1.6 × 10^7)(1 - $\epsilon_{ext.\mu}$), where $\epsilon_{ext.\mu}$ is the discrimination efficiency between external and signal muons. To achieve a $\sigma_{ext.\mu}$ = 1.5% we then require an efficiency of $\epsilon_{ext.\mu} \sim 0.99999$.

5.11.6 Track Reconstruction

The studies presented have not examined track reconstruction techniques but in order to estimate the effect on the normalisation uncertainty we look at similar technologies in other experiments. Based on the T2K ND280 design and analysis we assume the value established in the ν_μ CCQE cross section analysis [87], estimating a track reconstruction normalisation uncertainty, $\sigma_{track.rec}$, of 0.6%.

5.11.7 Signal Event Normalisation Uncertainty

Assumptions on the event normalisation uncertainties have been used to estimate the oscillation sensitivities within LAGUNA-LBNO [88]. Although based on a combined two beam analysis we take the signal event normalisation uncertainty, f_{sig}, of 3% as the target for the ND requirements and estimate if the current design can obtain this. Having established estimates for the main detector systematics and signal backgrounds, as shown in table 5.11, it is clear that the TPC momentum scale uncertainty is already at this level when using a μ signal sample. To improve this value we would need to

have a stronger magnetic field, improve the TPC position resolution and/or increase the size of the TPC. All of these options would pose technical challenging, bringing high engineering risks and costs. The TPC position resolution would be difficult to increase with current technologies even for GAr. Out of all the options increasing the size of the TPC is the most viable and would prove the most effective as $\delta s/s$ goes as the inverse square of the track length, however requiring a larger pressure vessel. The need to increase the size of the TPC then demonstrates the need for gas instead of liquid argon as the target medium.

The overall signal event normalisation uncertainty f_{sig}, as given by equation 5.12, results in a value of 3.8%, exceeding the 3% level required for the LBNO study [88].

Uncertainty	**Normalisation Factor** [%]	**Requirement**
Statistics (σ_{stat})	0.4	-
Fiducial Volume (σ_{FV})	0.8	1 mm vertex resolution
TPC Momentum Scale ($\sigma_{mom.scale}$)	3.0	$B = 0.500 \pm 0.001$ T
External μ^- background ($\sigma_{ext.\mu}$)	1.5	$\epsilon_{ext.\mu} = 0.99999$
External γ background (σ_{γ})	1.3	$\epsilon_{e/\mu} = 0.821$
TPC track reconstruction ($\sigma_{track.rec}$)	0.6	-

Table 5.11 The uncertainty factors contributing to the signal event normalisation uncertainty.

$$f_{sig} = \sqrt{\sigma^2_{tot}} = \sqrt{\sigma^2_{stat} + \sigma^2_{FV} + \sigma^2_{mom.scale} + \sigma^2_{\gamma} + \sigma^2_{ext.\mu} + \sigma^2_{track.rec}} \tag{5.12}$$

5.12 Summary

This chapter has taken the requirements imposed on the LAGUNA-LBNO ND, presented and implemented the basic detector design in a software framework to be then able to perform detailed MC studies to acquire estimates for first order performance limitations. From examination of the signal event normalisation uncertainty imposed on the ND of 3% proves to low for this ND design when coupled with a CC signal sample based on the muon momentum measurement. We estimate using this method a value exceeding this at 3.8%. Although this estimated result only considers a few main contributing factors in a broad way it shows that clearly the ND design presented will not work to the level required for LBNO study. This is primarily due to

the nature of the high energy, broad band ν_μ beam using a large CC μ signal sample which is limited of the TPC momentum scale uncertainty, although rich in statistics. However we must consider that in the estimation we have overlooked other analysis methods we may be able to reduce this uncertainty, other possible methods would be to use a different signal sample, such as neutrino-electron scattering which would likely decrease the TPC momentum scale uncertainty but then statistical uncertainty could become an issue.

We must also consider the beam ν_e normalisation uncertainty for such a detector in order to compare with the value required used to estimate the oscillation sensitivities within LAGUNA-LBNO at 5% [88]. Due to the large statistical uncertainty of the ν_e component at 4.6% other detector uncertainties will have to fall below a total level of 1.7% (excluding fiducial volume and track reconstruction) in order to attain a 5% beam ν_e normalisation uncertainty. One detrimental factor to this estimation was the lack of input from the beam group within the LAGUNA-LBNO collaboration which resulted in a poor representation of the beam flux at the ND. If a more accurate simulation of the beam was used in the studies (with larger statistics of the ν_e component) then it may be possible to get a better understanding and estimation of the beam ν_e normalisation uncertainty.

This study has addressed the initial problems surrounding the ND design and sets the foundation for future studies. Much work still remains in the optimisation of the ND and more detailed studies are required to further probe the detectors reconstruction capabilities. Further focus is required for neutral particle detection, with focus on how to reconstruct neutron energies. It is clear from the design of the ND that one of the main weaknesses of a pressurised GAr TPC is the energy reconstruction of neutrinos due to the large amount of energy lost to neutrons and photons. However this is a difficulty that any other detector design will have to cover due to the high energy beam causing large numbers of DIS events. Coupling the TPC with the TAS aimed to reduce this effect and has indicated in these studies that it could reconstruct π^0s. The main advantage of the GAr target medium is to reduce the neutrino event rate, avoiding pile up, while maintaining good granularity and track reconstruction of charged particles.

The hardware for the ND has been omitted from this design study and to establish an accurate ND design the hardware and engineering effort needs to be properly addressed. Future designs, or continuations of this design, will need to determine how to instrument a detector within a high pressure chamber.

It must be stressed that this study addresses only the initial detector requirements and presents them in a very broad way. The simulation framework has been presented in depth and forms a large amount of the study. It is hopeful that this design and software framework can be further developed to be used in future ND designs based on GAr. It also allows similar proposed experiments probing the same energy regime of neutrinos to consider this design and take these studies as a foundation for future ND designs.

Chapter 6

The MODES-SNM Project

MODES-SNM (MOdular DEtection System for Special Nuclear Material) is a collaborative project concerned with tackling nuclear threats with a compact and portable approach [2]. A modular and mobile system design is considered with the capability of detecting and identifying radioactive and Special Nuclear Material (SNM). Within a period of only 30 months the project aimed to produce and test a fully integrated prototype of the system. Unlike LAGUNA-LBNO, this project is considerably smaller both financially and physically, however it has the potential to impact, not only the scientific community, but also the whole of modern society, enormously. This chapter presents an overview of the project with an introduction to potential uses and other current technologies.

6.1 Detecting Special Nuclear Materials

Nuclear terrorism is a modern day threat to society. Highly enriched uranium (^{235}U) and weapons grade plutonium (^{239}Pu) are SNM. Illicit trafficking of such material can suggest the intent to make or use Improvised Nuclear Devices (IND). It is understood that quantities of the order of 8 kg of plutonium or 25 kg of highly enriched uranium are required to build an IND [89].

SNM are high emitters of α and β particles, gammas and neutrons. With the former being stopped by a few centimetres of air, detection of the latter two provides the only viable indication of SNM. Detection of gammas can provide a strong signature of radioactive material, but they are heavily effected by source shielding. Shielding or masking of sources impedes dramatically on the ability to detect SNM and results in losses of sensitivity in detectors. It is therefore necessary to have a system that

is sensitive to shielded sources and employs an effective analysis to identify potential threats.

6.1.1 Current Technologies

Most modern technologies use gamma detectors to monitor radiation threats with the inclusion of optional neutron detectors for SNM. Examples are discussed in the following sections.

6.1.1.1 Gamma Detection

The three main processes in which gamma rays are detected are via the photoelectric effect, Compton scattering or pair production. These interactions all lead to the production of energetic electrons via partial or complete energy transfer from the photon.

NaI detectors are inorganic scintillator detectors that are the most frequently used technology for gamma ray detection. Inorganic scintillators are preferred to their organic counterpart due to the light yield production ($\sim$40,000 γ/MeV) but are quite slow in comparison [8]. The energy resolution of inorganic detectors are also fairly poor, with Full Width Half maximum (FWHM) values of between 5-15% for sources within the 0.1 - 1 keV range.

In order to gain better photon production efficiencies, impurities are added in the form of an activator. Due to these added impurities the energy band structure of the crystal lattice is altered and yields previously forbidden energy bands between the conduction and valence bands. In turn this results in the emission of visible fluorescent photons that can be collected. For NaI detectors, thallium (Tl) is the activator. NaI(Tl) technologies offer good detector efficiencies [8], as they can be produced in large crystals, good energy resolutions (when compared with other scintillator materials) and high light yields.

High Purity Germanium (HPGe) semiconductor detectors are also common place in gamma spectroscopy. Unlike scintillator detectors they rely on the detection of charge carriers produced from photon interactions. A photon upon energy deposition will move an electron to the conduction band producing a hole in the valence band. Applying an electric field will provide a net migration of the charge carriers which is then read out. Devices using HPGe boast very good energy resolutions in comparison to NaI(TI) but are limited to small sizes as fabrication of very high purity germanium

is difficult. As a result detection efficiency can be orders of magnitude worse than NaI detectors.

The far superior energy resolution of HPGe devices makes them extremely useful for resolving close gamma peaks in the energy spectra. NaI devices are poor in this respect. Although this is a very favourable trait a trade off occurs with detection efficiency, and for some applications it may be favourable to use NaI technology. Other devices such as plastic scintillator detectors are also used for gamma ray spectroscopy, however NaI and HPGe devices are by far the most common.

6.1.1.2 Neutron Detection

The detection of neutrons falls into two categories: slow and fast neutron detection. Almost all current technologies on the market for slow neutron detection rely on neutron capture. The subsequent recoiling nucleus, proton or alpha particle is then observed and measured in the detector. Technologies implementing this process however offer no knowledge of the incident neutron energy.

Materials such as ^{3}He, ^{6}Li, ^{10}B and ^{157}Gd are renowned for their high neutron absorption cross section, which can be seen in figure 6.1. Using these materials as the target medium then allows detectors to have smaller active volumes and can be used in smaller devices.

Fast neutron detection relies on elastic scattering which causes nuclear recoil, in turn creating ionisation. Shown previously in equation 1.8, it can be noticed that the ratio T_A/T_n can only give a 100% energy transfer for hydrogen. Due to these restrictions hydrogen is the predominately favoured technology for fast neutron detection. ^{3}He is also used as it can allow for up to 75% energy transfer per elastic scatter. It is clear from this, contrary to slow neutrons, that the energy of the incident neutron can be determined given an accurate measurement of the recoil nucleus energy deposition.

6.1.2 Current Systems

Several types of radioactive detection systems are currently employed at customs and borders worldwide to help combat potential nuclear threats. Most offer passive and non intrusive methods of screening and fall within three categories of instruments; fixed/automatic, portable/hand-held, and pocket-type [89].

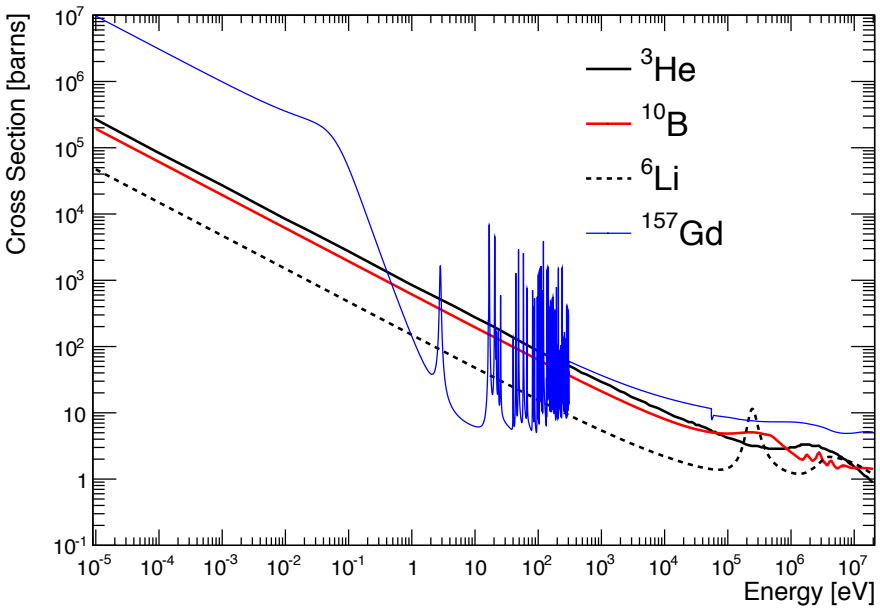

Fig. 6.1 The neutron total cross sections for ^{3}He, ^{6}Li, ^{10}B and ^{157}Gd. Data taken from the ENDF-VII.1 library [90].

6.1.2.1 Fixed and Automatic Systems

These types of instrument are commonly deployed as primary detector systems to act as the first barrier against nuclear threats. Such instruments are automatic and have the ability to screen large volumes of traffic. The continuous measurement of the gamma and neutron background levels and readjustment of the alarm threshold maintains a statistically constant false alarm rate. Occupancy sensors are then required to inform the system when to measure radiation levels of passing traffic. Background measurements are compared to the occupied measurement and an alarm is declared if it falls outside preset thresholds.

Radiation Portal Monitors (RPM) are currently the most prevalent of this type of technology, shown in figure 6.2. They are usually arranged in two parallel pillars placed either side of passing traffic. In this arrangement the system can probe cargo closely and symmetrically. Most RPMs will monitor both gamma and neutron rates. The most frequent technology for detection of the former is NaI scintillating crystals, while the latter relies on ^{3}He gas detectors. Large arrays of the detectors then form the basis of the RPM.

Fig. 6.2 An image of a fixed RPM used at an airport with a cargo truck passing through it. The RPM is the large yellow detectors placed either side of the passing vehicle.

6.1.2.2 Portable Systems

Secondary detection systems are employed for use if cargo or vehicles raise suspicion from the primary system. This usually involves the deployment of portable or hand-held systems. There are many variations of these particular systems but they all use common technology similar to the RPM, NaI detectors for gammas and ^{3}He or ^{6}Li for neutron detection. These type of detectors measure dose-rates with some more sophisticated systems able to perform identification. They can be deployed as primary detectors but are usually less sensitive due to the reduction of the active volume, especially for hand held devices. Longer exposure times compensate for the reduction of the active volume, and are why they work well as secondary devices.

6.1.2.3 Pocket-Type Systems

When only concerned with gamma radiation rates, these systems are cheap to produce and easily usable. However due to their size, they can only measure dose rates and cannot perform radionuclide identification. Such devices are commonly used to monitor individuals personal dose rates when exposed to potential radioactive areas, such as customs and border personnel. Only scintillation detectors are sensitive enough for use in these devices.

6.1.2.4 Issues

The are some severe issues with the current systems and their associated technologies. The generation of false alarms due to Naturally Occurring Radioactive Material (NORM) or other non threatening radioactive sources is a continuous nuisance. Reports suggest that 1% of alarms are due to NORM [91], and with large volumes of traffic it becomes more than an inconvenience. Other innocent alarms can originate from medical treatment (radio-pharmaceuticals), with ∼1 in every 2600 people crossing the U.S border triggering such an alarm [92]. These current levels of innocent alarm rates are a very costly disruption while monitoring the trafficking of illicit material. The sensitivity of these systems is also under scrutiny with new systems required to detect shielded or masked neutron sources. Coupled with the worldwide shortage of ^{3}He new technologies and techniques must be developed.

6.1.3 The Abundance of ^{4}He

With ^{3}He suffering from a severe supply shortage [93], other candidates for detection of neutrons are required. A potential candidate for its replacement is ^{4}He [94]. Although ^{3}He has a large cross section for neutron capture, at higher energies (∼500 keV and above) ^{4}He has a larger cross section due to elastic scattering. This can be seen in figure 6.3. Utilising this improved cross section requires a different detection technique as neutrons will elastically scatter off of ^{4}He atoms in the detection medium and the subsequent recoil of the ^{4}He atom will cause ionisation in the medium (gas), in turn producing scintillation light which can be collected. The number of collected photons is then proportional to the energy deposited by the incident neutron. Coupled with a high scintillation light yield of ∼18,000 VUV makes this technique possible.

This is a powerful technique when used for the detection of fast neutrons, especially for SNM, but for slow neutrons the difference in cross section is large, with a factor of ∼10,000 less at ∼1 eV. However adding a coating of ^{6}Li or another absorber then allows for neutron capture and the alpha emission can be seen in the active volume.

6.2 The MODES-SNM System

The MODES-SNM consortium was conceived in January 2012 in order to develop new technology and integrate it into a new generation of radiation detector systems. It consists of the following participants: University of Liverpool (UNILIV); Università

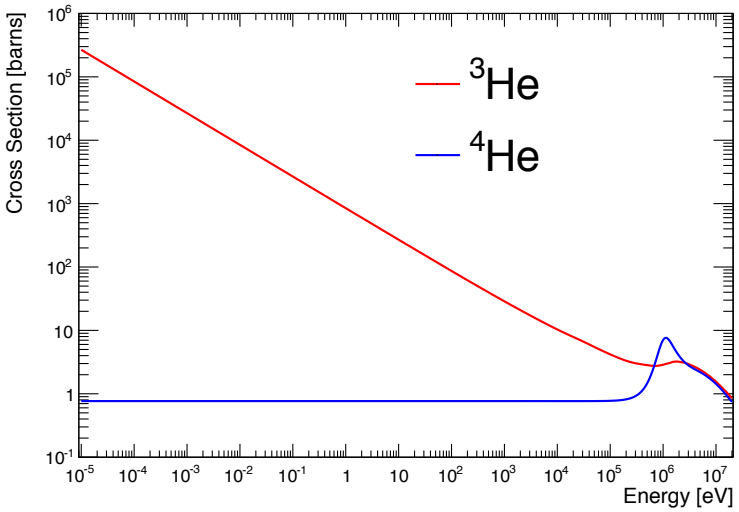

Fig. 6.3 The neutron total cross sections for ^{3}He and ^{4}He. Data taken from the ENDF-VII.1 library [90].

degli Studi di Padova, Italy (UNIPD); ARKTIS Radiation Detectors Ltd, Switzerland (ARKTIS); Narodowe Centrum Badań Jądrowych - National Centre for Nuclear Research, Poland (NCBJ); Eidgenössische Technische Hochschule Zürich, Switzerland (ETHZ); Costruzioni Apparecchiature Elettroniche Nucleari, Italy (CAEN); Università degli Studi dell'Insubria, Italy (UINS); Revenue Commissioners, Ireland (RC).

6.2.1 Sensitivity Requirements

Certain minimal requirements are imposed on the prototype based on the sensitivity recommendations set by the International Atomic Energy Agency (IAEA) [89]. Specific requirements imposed from the International Electrotechnical Commission (IEC) are integrated into these also [95]. With MODES-SNM being a portable/mobile system with the option to function as a fixed detector, like an RPM, it must support both mobile and fixed (RPM) criteria.

A true alarm is defined as an alarm that is raised in the presence of a radioactive source. Contrary to this a false alarm is an alarm raised when no radioactive source is present and the background is stable (false positive). The true alarm rate should be at or greater than 96/100 trials, corresponding to a probability of detection of 90% at a 95% confidence level [96]. The false alarm rate (FAR) should not exceed 1 alarm per hour, with the detector operating in stationary mode.

For gamma detection an alarm should be generated for a source of dose rate of

0.05 μSv/h at a minimum distance of 1 m separation from the instrument passing by with a speed of 0.5 m/s (1.8 km/h). Specifically this requirement shall be met for sources of ^{241}Am, ^{137}Cs and ^{60}Co, corresponding to an energy range of 50 keV to 1.5 MeV. The activities of these sources are listed in table 6.1, with their corresponding gamma emission energies and the required activities for a dose rate of 0.05 μSv/h at 1 m distance.

Source	Gamma Energy	Required Activity
^{60}Co	1.17, 1.33 MeV	160 kBq
^{137}Cs	662 keV	660 kBq
^{241}Am	59.5 keV	13 MBq

Table 6.1 The gamma sources with their associated energies and activities required to produce a dose rate of 0.05 μSv/h at 1 m distance.

For neutron detection an alarm should be generated for a ^{252}Cf source, of activity 1.2×10^4 neutrons/s, whilst in motion at a speed of 0.5 m/s (1.8 km/h). Again the distance between the source and the system should be no less than 1 m. This is equivalent to a static rate of 0.1 neutrons cm^{-2}s^{-1} at 1 m distance. For stationary screening, this requirement is increased such that the activity is reduced to $\sim 5 \times 10^3$ neutrons/s. This corresponds to 0.04 neutrons cm^{-2}s^{-1} at 1 m distance.

6.2.2 Nuclide Identification Requirements

In addition to the sensitivity requirements, radioactive source identification requirements are also set by the IEC [95]. The identification of the following radioactive sources: ^{152}Eu, ^{133}Ba, ^{22}Na (PET-type source), ^{51}Cr, ^{57}Co, ^{60}Co, ^{137}Cs, ^{241}Am should be performed within a 60 s exposure from rates of 50 nSv/h to 5.0 μSv/h.

6.2.3 The Detector Concept

The prototype system implements both gamma and neutron detection, with the latter consisting of thermal and fast neutrons. The technology behind all 3 detectors relies on high pressure noble gases used as scintillation volumes. ^{4}He is implemented for neutron detection while Xe is used for gamma detection. Design and development of detectors incorporating these gases have been performed by ARKTIS prior to and along side the MODES-SNM project. The Fast Neutron Detectors (FND) have been

developed independently prior to the MODES-SNM collaboration [94], whereas the development of the Slow Neutron Detectors (SND) and Gamma Detectors (GD) are part of the MODES-SNM project [97]. The SND and GD designs follow from an evolution of the design of the FND.

The 3 various types of detector all follow the same design. Each type consists of a cylindrical pressure vessel filled with an active gas of either ^{4}He or Xe. Lining the inside of the tubes exists a WaveLength Shifter (WLS) to reradiate scintillation light to the Vacuum Ultra Violet (VUV) range. Photo Multiplier Tubes (PMTs) are placed at either end of the tube with VUV transparent windows serving as the intermediary between the tube and the PMT for light collection. This is shown in figure 6.4.

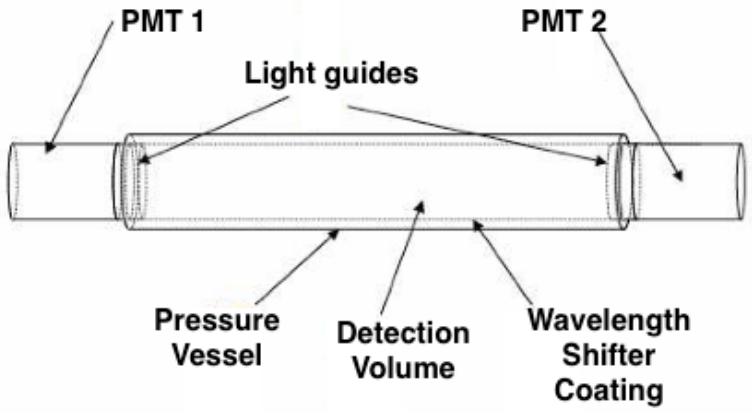

Fig. 6.4 The basic design of the detectors used in MODES-SNM.

This detector design does not allow for recirculation of the gas which is a common method of purifying the gas. As a result high purity is required to achieve high scintillation yields.

6.2.3.1 Fast Neutron Detectors

With low atomic number (Z=2) and low mass number (A=4), ^{4}He is well suited as a medium for neutron detection. Due to kinematic restrictions, only 64% of the incident neutrons kinetic energy can be transferred to the nucleus per elastic scatter, calculated from equation 1.8. Although not as good as hydrogen it is the highest energy transfer for the nobel gases. helium

The FND contain pressurised ^{4}He at ∼180 bar in tubes of active volume of ∼714 cm^3 (470 mm length and 44 mm diameter). At this pressure the corresponding density is 0.03 gcm^{-3} at room temperature. Studies close to this pressure at 200 bar have shown ^{4}He is a fairly good scintillator with a light yield of approximately 18,000 VUV photons / MeV deposited by neutrons [94] [8]. That is just less than half that of NaI detectors (∼40,000). The scintillation light produced in ^{4}He has a wavelength of the order of 70 nm (∼18 eV).

Gamma rejection is important for neutron detection in order to discrimination against source masking or NORM radiation. helium is excellent for this due to four main reasons:

- A low atomic number results in low sensitivity to gammas, having a cross section of a factor ∼20 less than neutrons around ∼1 MeV.
- Low energy deposition from recoiling electrons in the gas due to gamma interactions, hence low ionisation.
- Low light yield for gamma interactions due to electron recoil, as opposed to nuclear recoil for neutrons. Recombination of electron-ion pairs in pressurised ^{4}He is considered as an inefficient process.
- Pulse Shape Discrimination (PSD) is a powerful tool that can be applied to scintillation signals, due to the fast and slow components of scintillation light.

Given that the average exposure time of the detector is between 2-3 seconds, a conservative limit of R = 10 neutrons s^{-1} is assumed. To estimate the number of required detectors, N, equation 6.1 is used. Table 6.2 shows the parameters used in the calculation with some extracted from sources [94],[90] and [13].

$$N = \frac{mR}{\rho V_0 \sigma \phi} \tag{6.1}$$

Although the fission neutron spectrum from ^{252}Cf is actually continuous, it is a good approximation to assume a mono-energetic flux as both the cross section and flux peak at the same energy, making contributions from other energies far less important. From equation 6.1 it is then estimated that at least 7 detectors are required to gain sensitivities set by the IEC and IAEA.

Parameter	Value	Description
E	1 MeV	Peak neutron energy from ^{252}Cf spontaneous fission [13]
σ	$\sim 10^{-27}$ m^2	Neutron cross section on ^{4}He at peak energy [90]
m	6.68×10^{-27} kg	^{4}He atomic mass
R	10 n/s	Neutron detection rate
V_0	$\sim$714 cm^3	Active volume of each neutron detector [94]
ρ	30 kgm^{-3}	Density of ^{4}He at 180 bar and room temperature
ϕ	400 n m^{-2}s^{-1}	Neutron flux assumed to be mono energetic at 1 MeV

Table 6.2 The parameters used for estimating the number of fast neutron detectors required.

6.2.3.2 Slow Neutron Detectors

The SND are almost identical to the FND, however one key difference exists. A coating of ^{6}LiF is applied to the internal lining of the SND, due to the large neutron capture cross section of ^{6}Li. However with the same technology as the FND they remain sensitive to fast neutrons. Given the larger cross section of ^{6}Li at thermal energies, less active volume is needed and only 2 detectors are used.

6.2.3.3 Gamma Detectors

With a much higher atomic number (Z=54) than ^{4}He, xenon is much more sensitive to gammas. It is also far more dense than helium, at 0.4 gcm^{-3} at 50 bar pressure and 293 K. Although using liquid xenon would increase this density ($\sim$3 gcm^{-3}) it is beneficial however to use gas as it omits the need for cryogenics, making it far more practical in mobile systems. It has also been shown that the energy resolution is better in gas as opposed to liquid [98], achieving 6.1% FWHM at 662 keV. The scintillation light produced from xenon corresponds to a wavelength of 175 nm, which is in the VUV range. The cross sections comparing Xe and He for gammas are shown in figure 6.5, data taken from [86].

The critical point of xenon occurs at 289.77 K and 58.41 bar, at this pressure and room temperature (293K) it is in a supercritical phase. Operating a detector in this phase can then be problematic due to strong pressure increases with small temperature increases. Large fluctuations in scintillation light yield also arise due to light propagation in a supercritical fluid. It is therefore favourable to have lower pressures than the neutron detectors to avoid these problems and for the detector to

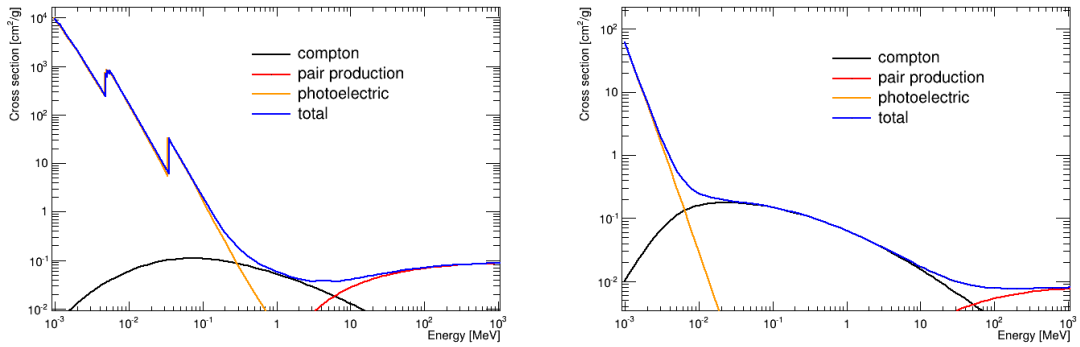

Fig. 6.5 The cross sections for gamma rays incident on Xe (left) and He (right). Data taken from [86].

maintain a fairly constant pressure. The isochoric curves for xenon are shown in figure 6.6 with the critical point also shown.

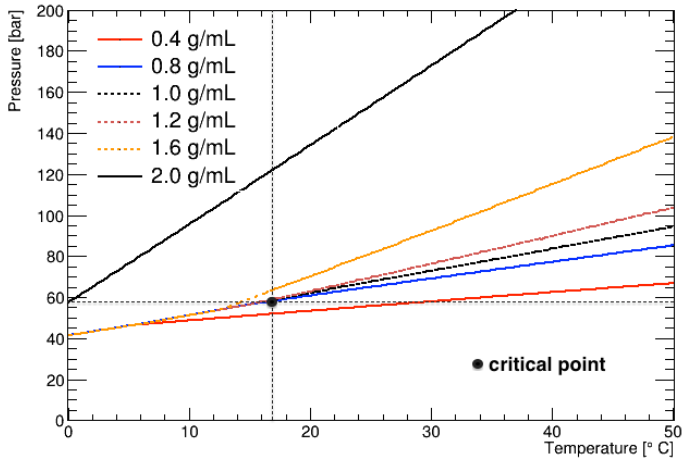

Fig. 6.6 The isochoric curves for xenon at various densities.

The system will need to operate at room temperature, with a total operation range of 0 - 50 °C, to account for most climates around the world. To avoid the supercritical fluid regime the pressure is set at ∼40 bar, corresponding to a density of ∼0.3 gcm^{-3} at room temperature.

The xenon detector has an active volume of ∼1570 cm^3 (10 cm diameter and 20 cm length). Two xenon detectors are proposed for use within the MODES-SNM system.

6.2.4 Light Readout

Hamamatsu R580 PMTs are used for scintillation light readout, with two placed within each detector. An image of the PMTs is shown in figure 6.7. The spectral response of the R580 PMT lies between 300 to 650 nm, with a peak quantum efficiency of 27% at 420 nm [99].

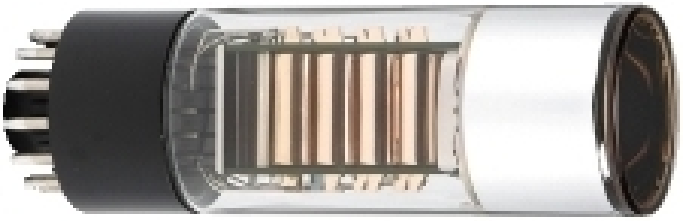

Fig. 6.7 The Hamamatsu R580 Photo Multiplier Tube used in the detectors.

6.2.5 The Electronics System

The processing of scintillation information, detector monitoring and system power supply is all provided by an electronics system, consisting of five hardware subsystems.

- The fully digital Front End electronic system (FE)
- The Data Acquisition system (DAQ)
- The High Voltage Power Supply system (HV-PS)
- The Battery Management System (BMS)
- The Information System (IS)

6.2.5.1 The Front End System

The FE system acts to digitise the raw scintillation signals from each PMT within the detector assembly. Three 8 channel 14-bit 500 MS/s DT5730 digitisers form the FE system. These units are developed by CAEN specifically for the MODES-SNM project and can be seen in figure 6.8. The DT5730 performs analogue to digital conversion with a dead timeless acquisition. After conversion to a digital waveform its

internal firmware provides information on timing and pulse charge (energy). Ultimately yielding two charge collection measurements, the short and long components of the digitised waveform, Q_{short} and Q_{long} respectively. These quantities represent the charge collection between the two gates, short (fast component) and long (total), summarised in figure 6.9. The Pulse Shape Discrimination (PSD) value is then determined from these two parameters, as shown in equation 6.2. The PSD value then represents the ratio of the tail to the total integrated spectrum. Due to the different slow component times of neutrons and gammas it is a powerful tool for discrimination between the two particle types.

$$\text{PSD} = (Q_{long} - Q_{short})/Q_{long} \tag{6.2}$$

Fig. 6.8 The three 8 channel 14-bit 500 MS/s DT5730 digitisers that form the FE system.

6.2.5.2 The Backend System

The output from the FE is fed to the DAQ to be processed by the IS. The IS consists of a standard desktop computer (PC) with a Linux based operating system and the bespoke software, designed by University of Padova, already installed. A wireless modem and GPS are connected to the PC in order to communicate with external

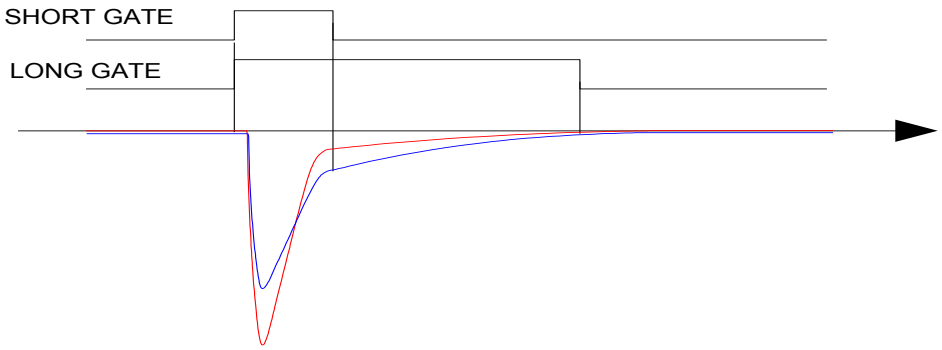

Fig. 6.9 An illustration indicating the two different waveforms with the indications of the short and long gates. Image taken from [59]

devices to control the system. The HV-PS is required to provide the necessary high voltages for the PMTs on each detector. The intermediary between the electronics and the battery is the BMS, which monitors and regulates the current and voltage supplied by the battery.

6.3 The Software

The software installed on the IS is designed to process signals from the DAQ, monitor pressures and temperatures of the detectors, while allowing users to manage and control the system. Calibration and data acquisition are also handled by the IS and are integrated into the software. The ROOT package provides the necessary analysis tools required for the system and with the CAEN libraries (used for the FE system) also written in C/C++, a C/C++ framework is a natural choice for the software framework. The software itself is composed of several layers to allow this functionality, this is summarised by figure 6.10.

1. The control system for data acquisition, the FE system and the HV-PS (FE&DAQ)
2. The initialisation and automated calibration process - Setup and Calibration Control System (SU&CCS)
3. The decision making algorithms and data analysis (DT)
4. The graphic user interface - Man Machine Interface (MMI)

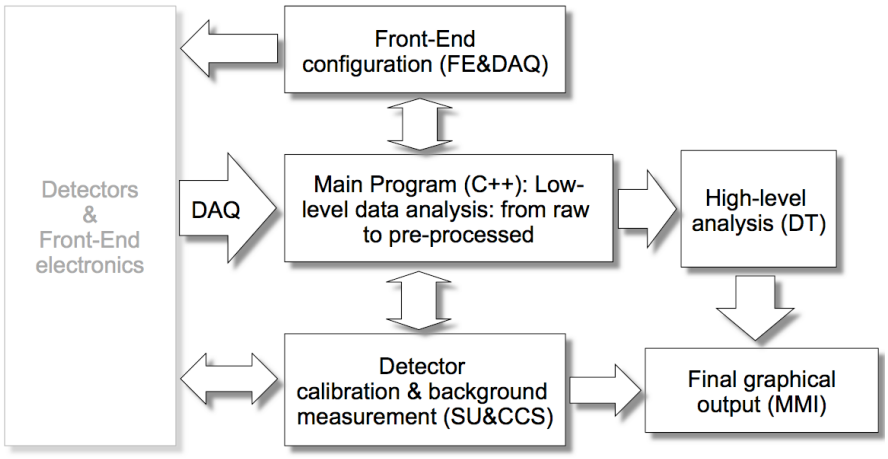

Fig. 6.10 The IS software modular breakdown. Image taken from [59]

6.3.1 Uses

MODES-SNM is not intended to compete with or replace current RPM systems but instead will serve as a selected screening device, to be deployed as a mobile secondary detection unit. This will allow screening on a risk analysis and intelligence basis. However this does not omit it from being deployed as a primary unit and can be used in conjunction with other radioactive detection systems.

The MODES-SNM system will most likely be used at border controls relating to maritime, air, road, rail and postal traffic. These are locations were RPMs are commonly installed.

It can be easily envisioned that such a system with mobile capabilities would be best deployed for use scanning where threats are occasional and temporary. If deployed with other systems such as X-ray scanners, users would gain additional benefit.

Chapter 7

The MODES Detector and System Integration

The detector assembly and integration of the whole system is a formidable task. Spanning from the design phase to the full installation phase of the project, all phases are presented in this chapter.

7.1 System Requirements

There are four main requirements imposed on the system and are fundamental to the system integration design. These are:

- **Modularity** - The system must allow for users to move and mount the detector array in any desired fashion. This requires that the system can be broken down to several key modules that form the base of the system. In order to be assembled by a single user then imposes a weight restriction on each module of 25 kg.
- **Portability** - The system must be portable. The ability to relocate and operate is absolutely necessary and the assembled system must be able to probe while in motion.
- **Durability** - The system must be able to operate for extended periods of time without failure. Due to the other requirements this is very important as the system must be able to withstand being disassembled and relocated.
- **Safety** - The system must be safe to assemble and operate for all users, including non-experts. Measures must be introduced to reduce the risk of accidents and

provide maximum protection in case such events occur.

7.2 The Detectors

The prototype consists of 8 fast neutron, 2 thermal neutron and 2 gamma detectors. The detectors are of cylindrical design with an extrusion in the form of the valve. The fast neutron detector tube is 1000 mm in length and has a diameter of 70 mm at the widest part, shown in figure 7.1. With the inclusion of the valve gives a height of 200 mm. The thermal neutron detectors match these dimensions and only differ by having a ^{6}LiF coating internally. Each neutron detector tube is composed of steel and has a total weight of 5.0 kg.

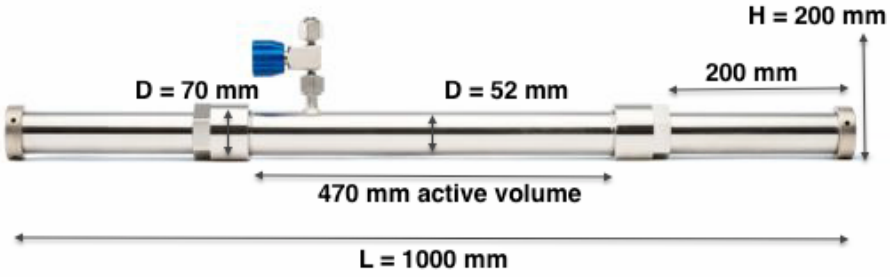

Fig. 7.1 The dimensions of the fast and thermal neutron detectors.

The gamma detectors are larger in diameter, at 140 mm, but shorter in length, at 607 mm, and with the inclusion of the valve the height is 290 mm. This is shown in figure 7.2. They are considerably heavier than the neutron detectors at approximately 11 kg. The gamma detector vessel is made from Titanium.

In order to satisfy the system requirements these detectors must be housed in appropriate containers. It is obvious that this cannot be done with one container alone, as this would exceed the 25 kg limit without taking into account the weight of the container itself. Therefore the choice of the container skin, and hence the material, is crucial in the design of the detector casing.

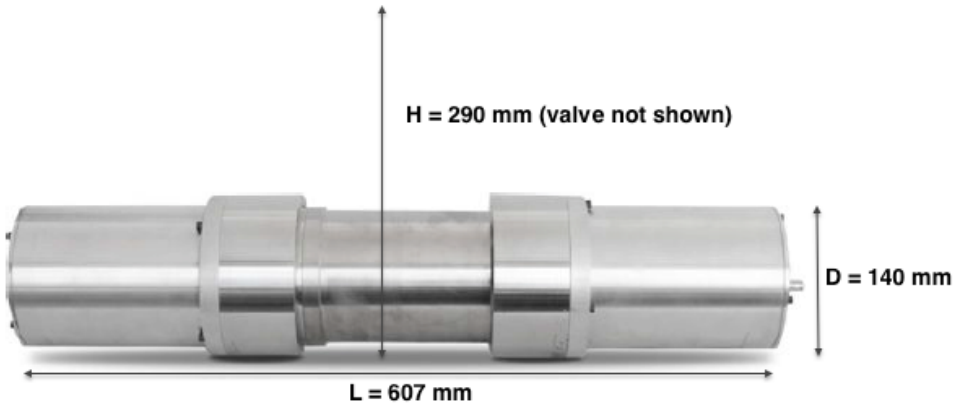

Fig. 7.2 The dimensions of the gamma detectors.

7.3 Detector Container Design

Rectangular boxes are implemented for the container designs, this makes them easily configurable and can then be stacked upon each other. The neutron detectors are paired and housed in containers of external dimensions 1255 × 170 × 250 mm, shown in figure 7.3. Due to the larger dimensions and weight of the gamma detectors these are housed individually in boxes of external dimensions 1005 × 170 × 300 mm, shown in figure 7.4.

7.4 Detector Container Material

A suitable detector container material must be lightweight while maintaining structural support and protection for the detectors. Radiation shielding is also a key factor when deciding on the material and heavy consideration must be focused on minimising this effect.

Carbon fiber is a seemingly perfect candidate for the detector material, as it is renowned for its high tensile strength while maintaining a very low density. However it is expensive to produce and would not provide shielding from ElectroMagnetic (EM) noise. This could be overcome by adding a layer of conductive material but it would prove difficult to manufacture for a casing design. Plastics, such as polyethylene and polypropylene, are very light but are also soft and would not provide enough structural support. In order to provide EM shielding as well, metals are the primary candidate,

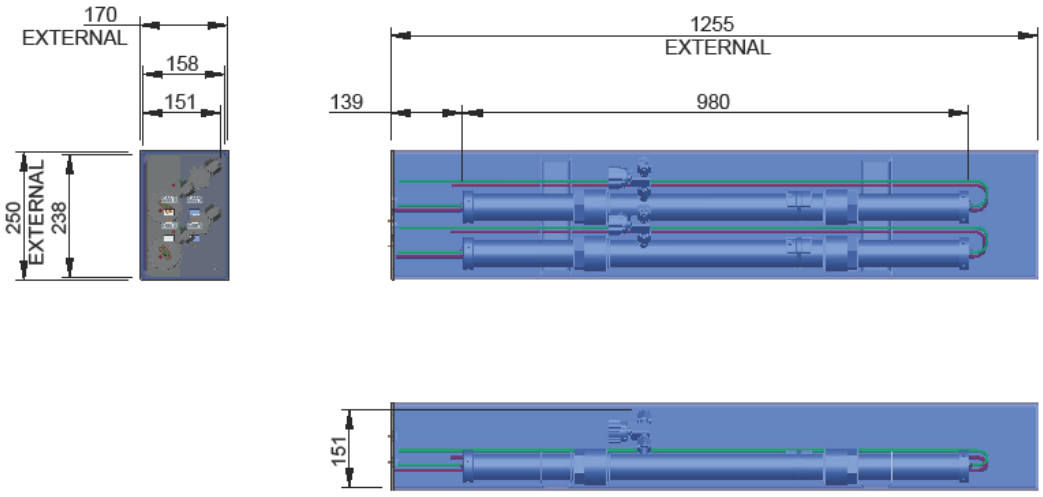

Fig. 7.3 The dimensions of the neutron detector container. All dimensions are shown in mm.

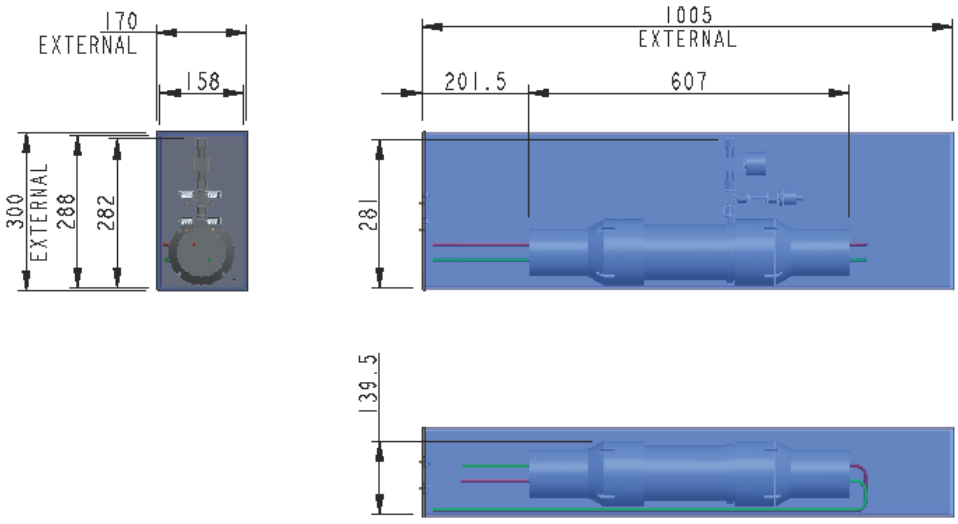

Fig. 7.4 The dimensions of the gamma detector container. All dimensions are shown in mm.

with a composition of metals and materials favourable. The materials considered are shown in the table 7.1.

Material	Composition	Density	Youngs Modulus	Electrical Conductivity
-	-	gcm^{-3}	GPa	Sm^{-1}
Carbon fiber	C_3H_3N	1.4-1.8	∼50-100	-
Polyethylene	C_2H_4	0.9	∼0.1-2	-
Polypropylene	CH_2=$CHCH_3$	0.9	∼1.5-2	-
Aluminium	Al	2.7	∼69	3.5×10^7
Magnesium	Mg	1.7	∼45	2.2×10^7
Iron	Fe	7.87	∼200	1.0×10^7
Lead	Pb	11.35	∼16	4.9×10^6

Table 7.1 Summary of potential materials considered for the casing.

Of the metals shown, aluminium is the most ideal candidate due to its reasonably low density, relative strength and high conductivity. Iron and lead are far too dense to be considered and have lower conductivities, whereas magnesium is less dense but is brittle and is susceptible to corrosion. Compared to carbon fiber aluminium is rather dense at 2.7 gcm^{-3}, which will severely impede on the weight restrictions. To reduce the weight, a honeycomb aluminium structure is considered. The effect is significant on the weight as the equivalent density of the honeycomb layer is 0.29 gcm^{-3}. The honeycomb structure is of 5.2 mm thickness and is then sandwiched between two thin aluminium sheets, each of 0.5 mm, to maintain the structural support. The casing material is shown in figure 7.5.

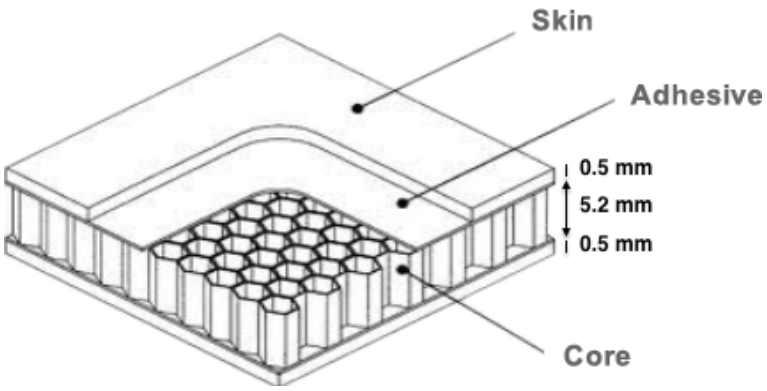

Fig. 7.5 The honeycomb aluminium structure used for the containers skin.

7.4.1 Monte Carlo Studies

Monte Carlo (MC) simulations are implemented to gain an understanding of the effects such a casing would introduce to the incident energy spectra of neutrons and gammas. Geant4 [75] is used to study particle interactions within the casing and record information on these for large amounts of events. A hypothetical source of neutrons and gammas with a flat and isotropic kinetic energy spectrum is implemented in the simulation. With energies ranging from 50 keV to 15 MeV the energy regime of interest for the MODES-SNM project can be probed. The source is implemented at a distance of 0.5 m from the casing with source dimensions of $1 \times 1 \times 1$ cm^3. One layer of the casing is modelled as a solid sheet of 1.0 mm thick aluminium (100% $^{27}_{13}$Al), density 2.7 gcm^{-3}, on top of a sheet of the same aluminium composition but with 5.2 mm thickness and a lower density of 0.29 gcm^{-3}. This casing plate then has dimensions of 1000 mm $\times$ 1000 mm $\times$ 6.2 mm, shown on the left of figure 7.6. The source and casing plate are situated in a vacuum with the complete experimental setup shown on the right of figure 7.6.

Only information on the primary particle is of interest for this study and tracking is setup to propagate the primary until it is either outside the main experimental boundaries or it is absorbed. The particles kinetic energy, momentum and position are recorded upon reaching the casing and once more upon leaving the casing. All primaries are recorded that pass through the casing boundary, regardless if energy is deposited or not. 1×10^6 primary particles are generated at the source, with a sixth of these, 1.67×10^5, reaching the casing boundary.

7.4.2 Casing Efficiencies

In order to quantify the effect of the detector casing, efficiencies are calculated on a energy binned basis. The efficiency ϵ, as a function of incident kinetic energy is defined by equation 7.1.

$$\epsilon_{bin} = \frac{N_p^{bin}}{N_T^{bin}} = \frac{\text{number of particles in energy bin that pass through casing}}{\text{number of particles in energy bin that are incident on casing}} \quad (7.1)$$

When a particle is incident on the detector it can either: not interact, scatter with forward momentum, scatter with backward momentum or be absorbed. Only particles that match the former two cases are considered successful. Particles that are then back scattered or absorbed do not pass the selection criteria. The efficiencies are then

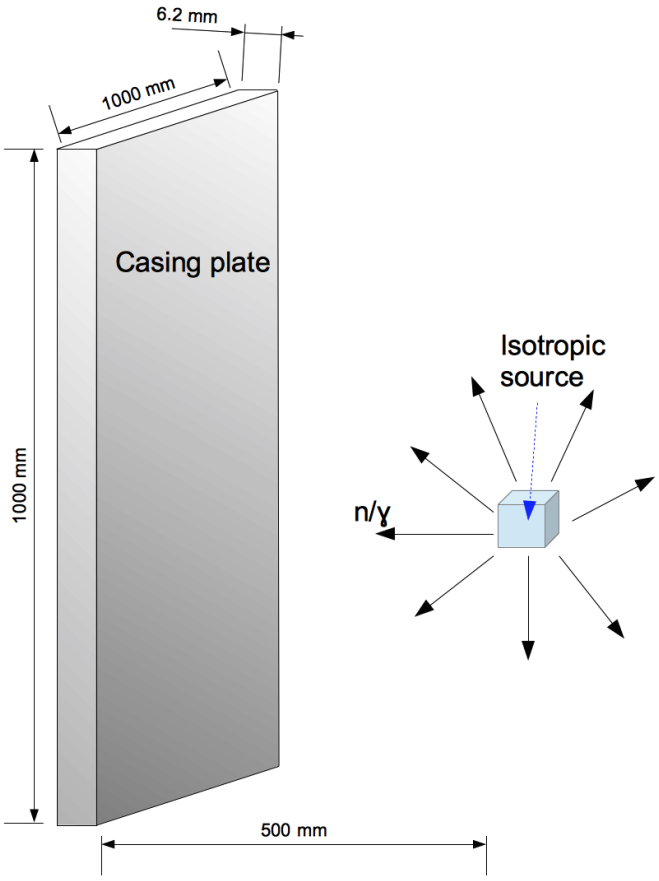

Fig. 7.6 One layer of the casing plate of aluminium with dimension labels (left) and the experimental setup (right).

calculated from the particle counts for each kinetic energy bin.

7.4.2.1 Examining Multiple Layers

Depending on the detector array arrangement some detectors may encounter up to five layers of the casing in their path. It is then necessary to measure the effect that this would have on the energy spectra. To give a comparison of introducing additional layers, efficiencies as a function of incident energy for numbers of 1,2,3,4 and 5 layers are shown in figure 7.7. With energies of 2 MeV and below of particular interest, efficiencies in this range are shown separately in figure 7.8.

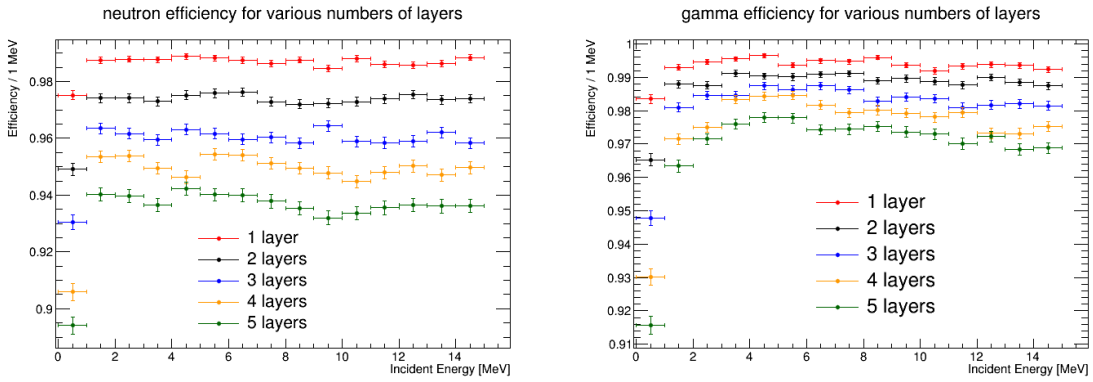

Fig. 7.7 The neutron (left) and gamma (right) efficiencies for 1,2,3,4 and 5 layers of the aluminium casing.

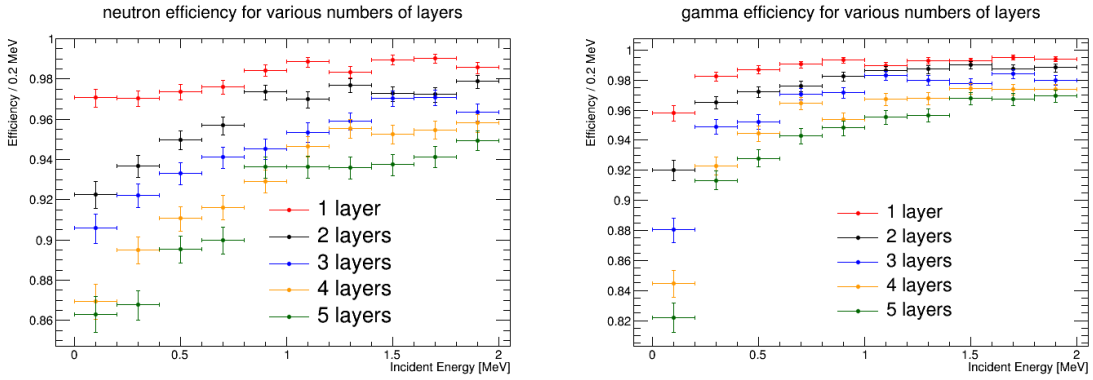

Fig. 7.8 The neutron (left) and gamma (right) efficiencies for 1,2,3,4 and 5 layers of the aluminium casing in the energy region of 0 - 2 MeV.

In can be noticed that neutron efficiencies can exceed 97% for 1 layer of the aluminium casing. Similarly for photons efficiencies can surpass 98% when the <100

keV regime is excluded. In this low energy region it falls to just below 96% however. Both particles show efficiencies that are largely independent of the incident energy but with it slightly improving at energies above 1 MeV. When considering 5 layers of the material these efficiencies are reduced to ∼94% and ∼97% for neutrons and gammas respectively for energies above 1 MeV. In the case for particles <1 MeV, efficiencies fall to as low as 86% for neutrons and 82% for gammas.

It is important to realise that due to kinematic restrictions from elastic scattering, neutrons can only transfer up to 14% of their kinetic energy per scatter on aluminium, calculated using equation 1.8. This can be noticed when taking the ratio of the kinetic energy of incident neutrons to the kinetic energy of the neutrons leaving the casing, shown left in figure 7.9. For photons however no such kinematic restrictions exist on elastic scattering, shown right in figure 7.9.

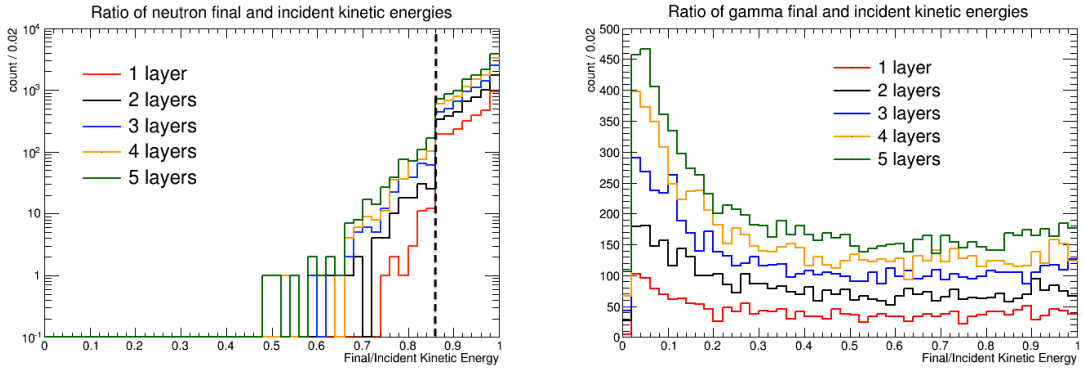

Fig. 7.9 The ratio of kinetic energies for the neutrons (left) and gammas (right) upon leaving the casing to entering it for 1,2,3,4 and 5 layers of the casing. The dashed line on the neutron plot indicates the maximum possible energy transfer from one scatter of 14%.

7.4.2.2 Other Materials

Some of the other potential candidates for casing materials are also implemented for comparison. The two other materials tested are carbon fiber (C_3H_3N), density of 1.8 gcm^{-3} and Iron (100% $^{56}_{26}Fe$), density of 7.87 gcm^{-3}. These are tested for casings of 1,3 and 5 mm thicknesses against aluminium, density 2.7 gcm^{-3}. Their associated efficiencies are shown in figure 7.10, with separate efficiencies calculated for the lower energy range of 0 to 2 MeV in figure 7.11.

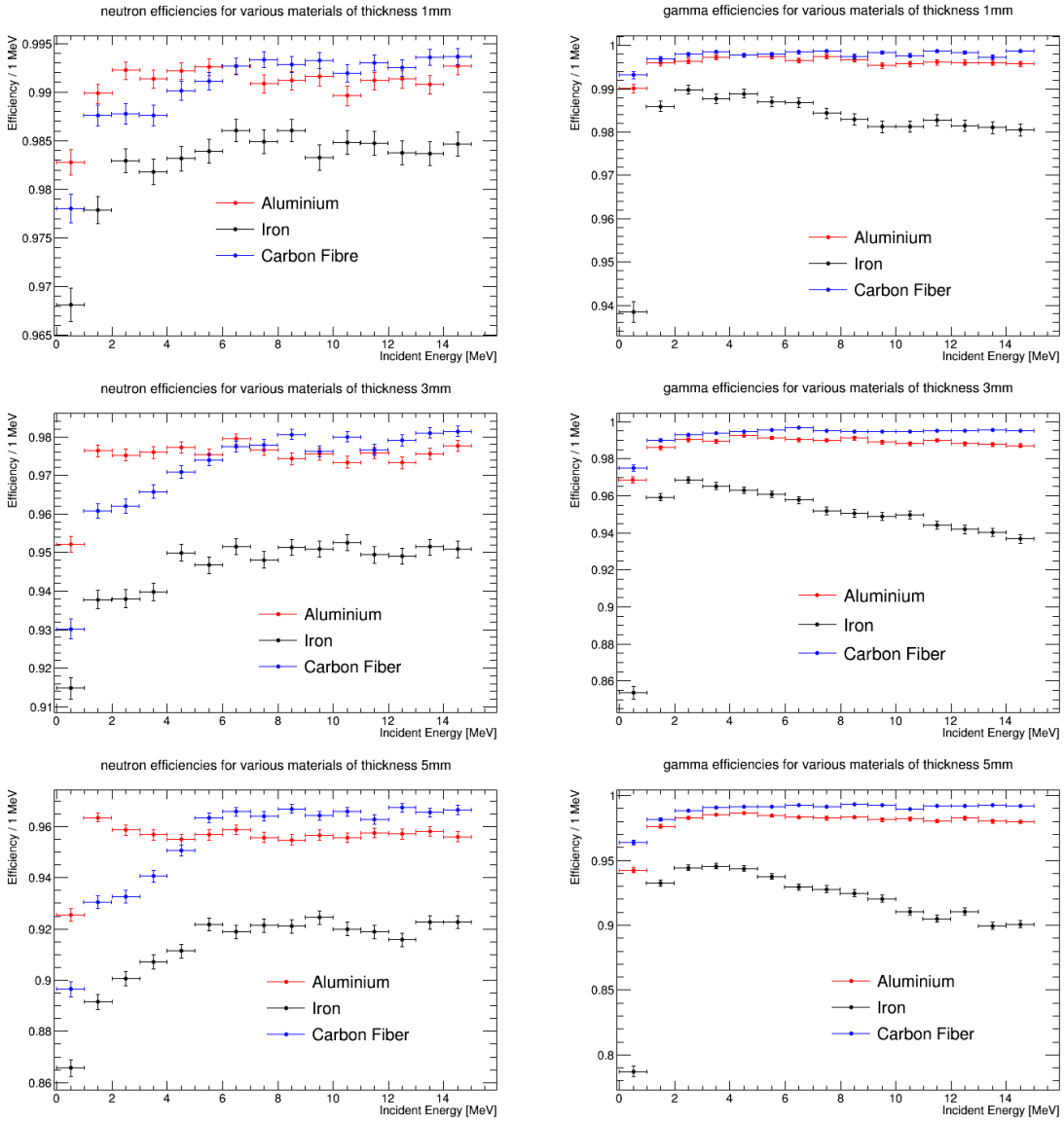

Fig. 7.10 The neutron (left) and gamma (right) efficiencies for carbon fibre, Iron and aluminium casings of 1 (top), 3 (middle) and 5 mm (bottom) thicknesses.

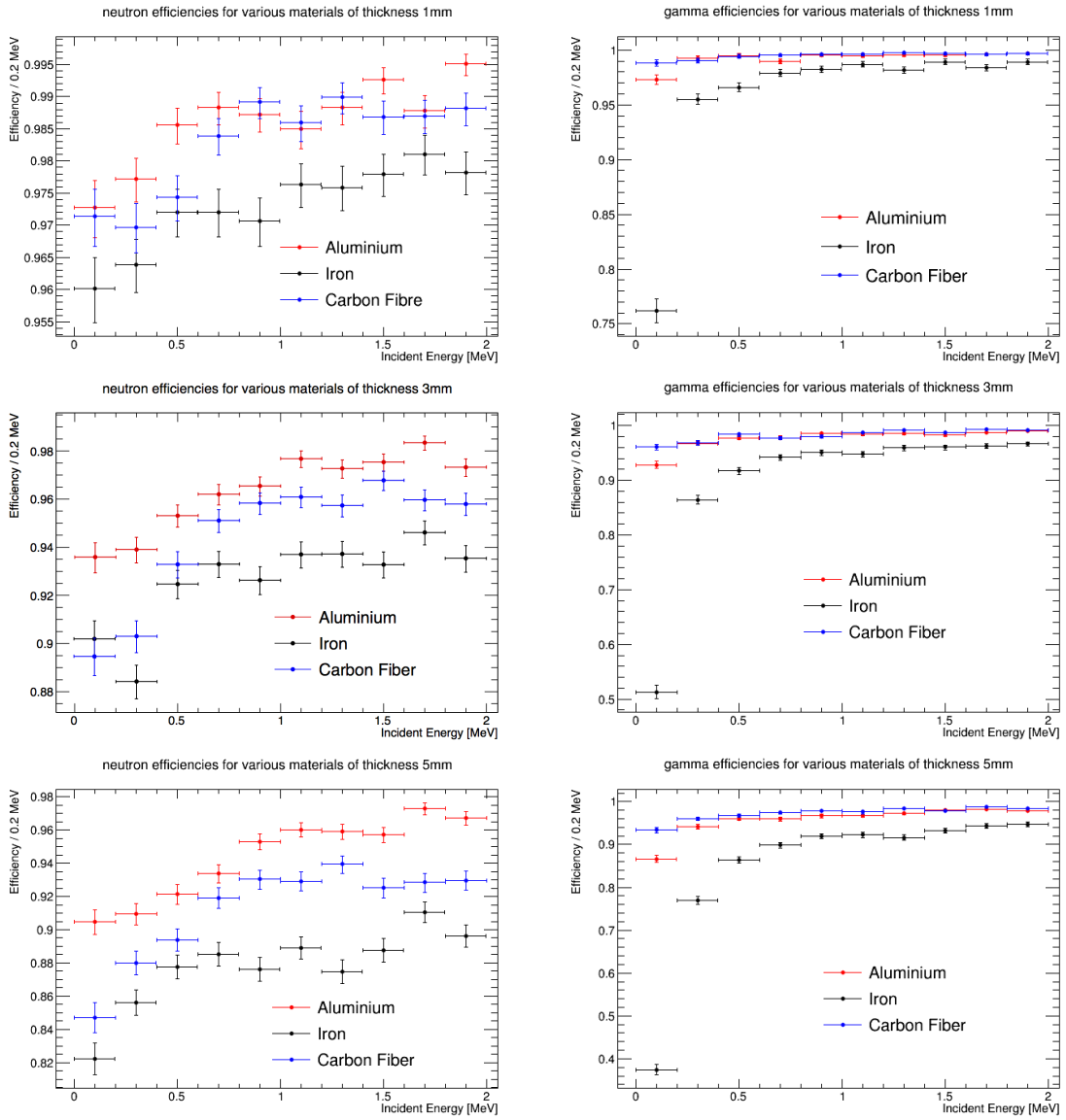

Fig. 7.11 The neutron (left) and gamma (right) efficiencies for carbon fibre, Iron and aluminium casings of 1 (top), 3 (middle) and 5 mm (bottom) thicknesses for lower energies between 0 and 2 MeV.

Due to the Hydrogen atoms in the carbon fiber, the neutron efficiencies are not as great as aluminium at lower energies. Neutrons incident on hydrogen can transfer up to 100% of their energy from one scatter alone, as opposed to aluminium at 14% per scatter. This results in an increase in absorbed neutrons for carbon fiber. With a lower density than aluminium the efficiencies improve at higher energies however. At almost three times as dense as aluminium and four times as dense as carbon fibre, Iron is unsurprisingly much less efficient than the two.

7.5 Electronics and Connection Design

With the detectors in separate containers, the rest of the system can be localised into two separate boxes, one containing the FE, DAQ, HV-PS, IS and BMS, while the other is the battery used to provide power to the system. Figure 7.12 shows the system architecture.

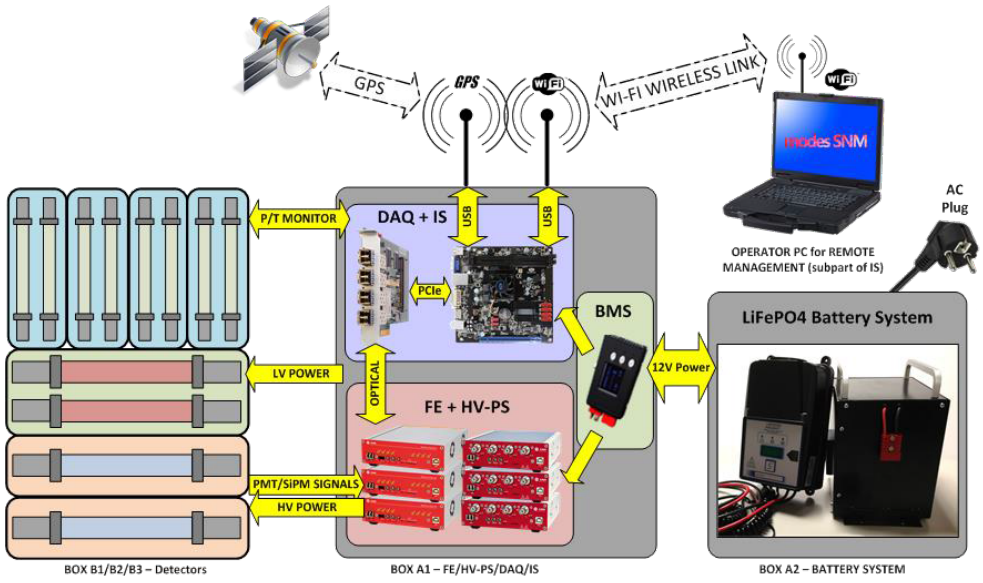

Fig. 7.12 The system architecture.

7.6 Container Construction

The University of Liverpool were responsible for the design and production of the containers needed for the detectors, electronics and computer system.

7.6.1 Detector Containers

The construction of the main body of the detector containers involves two C-shape panels bonded together with open ends for the detector installation. The end plates are made from a different material to the casing, 4.15 mm thick aluminium composite with a Polyethylene core. The material for the end plates is not of concern to the detection efficiency as they do not obstruct the detectors path of detection. The external connectors are fitted through one end of these plates, which are described later. The weight of each end is 0.2 kg for the neutron detector container and 0.24 kg for the gamma detector container, with each box requiring two, one for each end. The weight of the neutron and gamma containers are then 4.7 kg and 4.4 kg respectively.

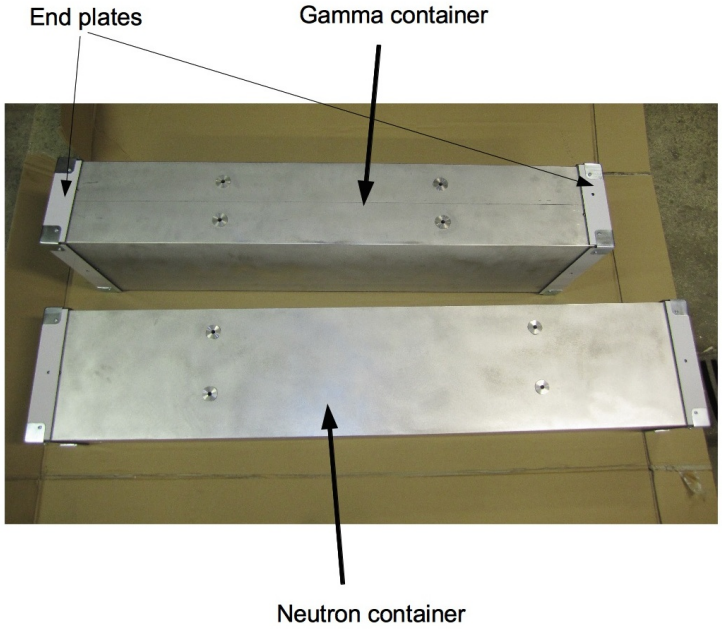

Fig. 7.13 The detector containers.

7.6.2 The Neutron Detector Rack

To support each pair of neutron detectors inside the containers requires a stable and secure structure. Aluminium is again used for the brackets to hold the detectors such that they do not obstruct the detection volume and are clamped on the external part of the PMT tube casing. A silicon resin is applied on the inside of the saddles to hold the detectors securely and after detector installation are fastened shut with screws.

This can be seen in figure 7.14. The whole support structure has a total weight of 0.542 kg and can be seen in figure 7.15. In contrast there is no such structure needed for the gamma detectors and is simply fastened to the case via two raised aluminium and plastic blocks, shown in figure 7.16.

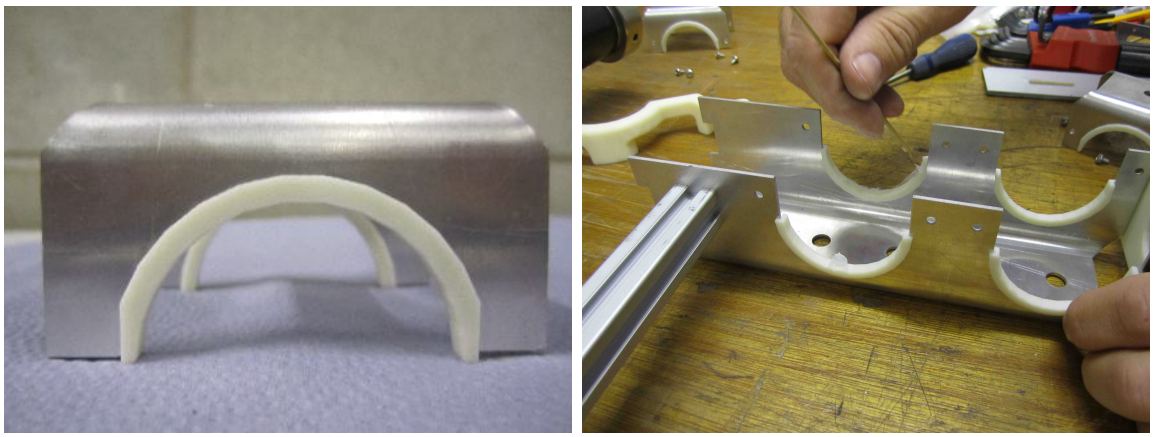

Fig. 7.14 The components of the neutron detector support structure. Left: The saddle clasp applied once detectors are installed. Right: The resin applied to the main structure just before inserting the detectors.

7.6.3 The Electronics and Computer Equipment Container

The housing for the electronics and the computer, along with all the corresponding equipment is made from the same aluminium composite used for the detector container ends. The box has dimensions 350 × 450 × 450 mm and is split into two compartments, shown in figure 7.17. The lower compartment is to be used for all cabling and the top compartment is then to be used for the HV-PS, FE, DAQ, BMS and the IS. The lower floor also acts to provide ventilation to the equipment above. Each face of the box is held with screws which are fastened to a box frame. Thus each panel can be removed easily and allows internal access if equipment is in need of repair or replacement. Two C-shaped plastic handles are attached on the top face to allow users to easily and safely carry the box.

The battery does not require a container as it is already encased in a protective casing. It has one single external connection, which is protected by thick plastic shielding to prevent users from electrocution and only the matching connector will complete the connection, shown in figure 7.18. The weight of the battery is 17.3 kg.

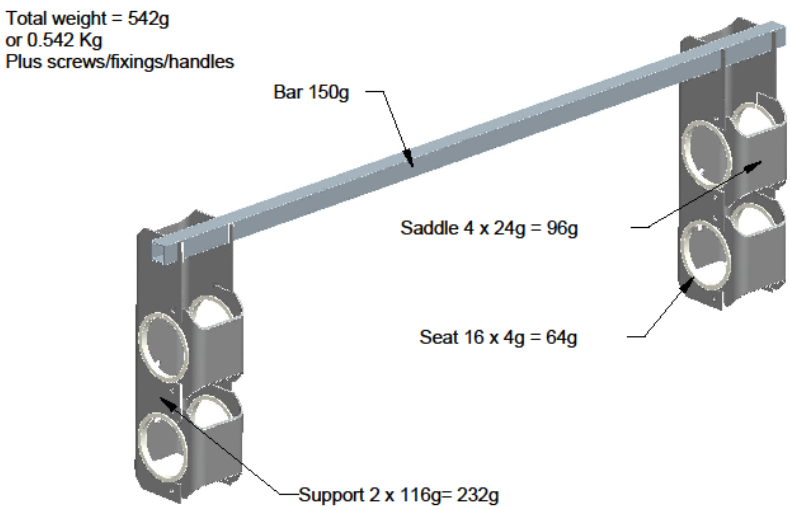

Fig. 7.15 The neutron detector support structure.

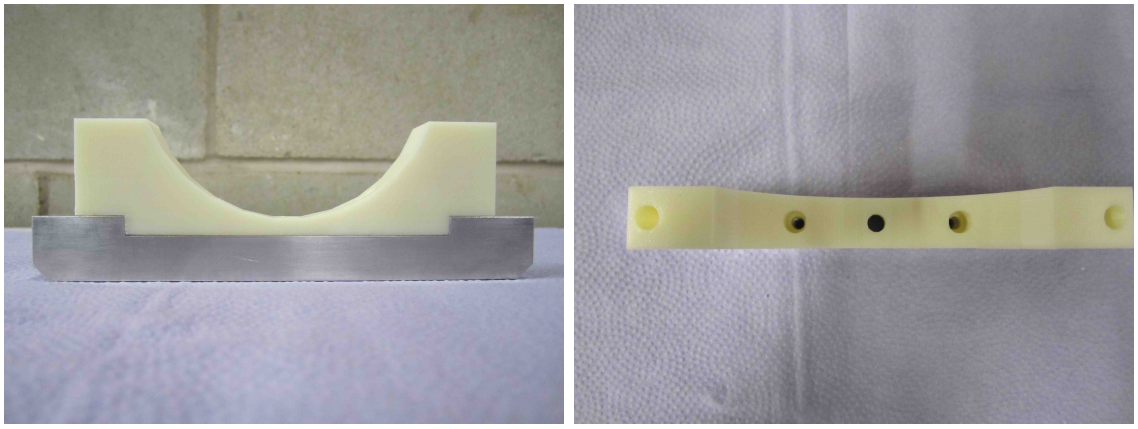

Fig. 7.16 The gamma detector support structure. Left: Side view. Right: Birds eye view.

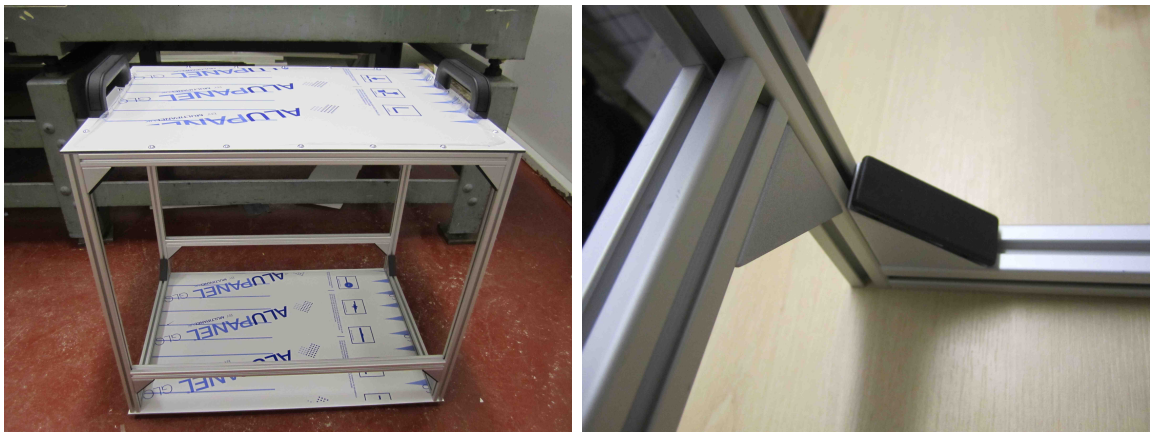

Fig. 7.17 Left: The container for the electronics and computer system. Right: The frame structure of the box.

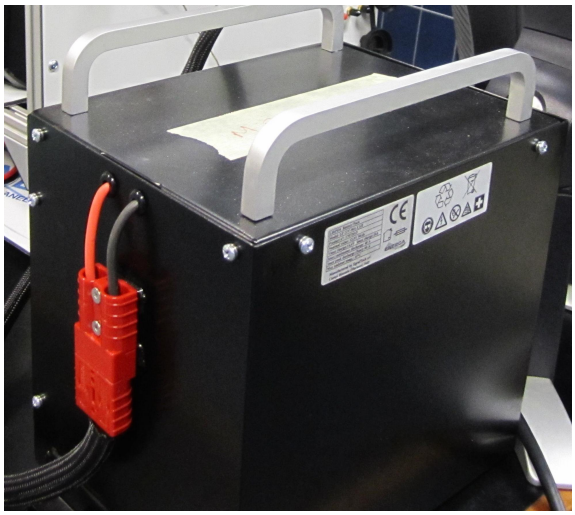

Fig. 7.18 The battery connected with the correct cable.

7.7 Integration

With the exception of the detector and electronics containers, all of the equipment (detectors, computer, cables and connectors) was brought together and tested at Arktis Laboratories in Zurich. On completion of this, these parts were then shipped to the University of Liverpool for the integration phase of the prototype system.

7.7.1 Installation of the High Pressure Gas Detectors

From the twelve detectors described only ten arrived at Liverpool, with one fast neutron and one gamma detector missing from the inventory. Due to technical issues they were tested independently, then subsequently shipped and installed after the integration at Liverpool.

Each neutron tube is inserted in the detector rack with the resin applied to each clasp and then fixed shut with screws and a bolt fasten, shown in figure 7.19. A plastic angular holder, shown in figure 7.20, is used to hold them parallel to each other and avoid slipping inside the container. The tubes are then slid into the containers via the open ends and fastened with screws, this can be seen in figure 7.22. The cables for the PMT's and the readout are then tied neatly and fed to one end of the box. To enable external connection with each container an end plate is fixed to the boxes which provides such an interface, shown left in figure 7.23. The cables are matched with numerical labels and each end is fixed with screws. A plastic C-shaped handle is placed on each end of the box to enable the user to lift the box, shown in figure 7.23. The total weight of the neutron box upon installation is then 18.6 kg, well below the 25 kg limit imposed.

For the gamma detector, the support structure is fixed to the container base with screws and bolts. The detector is then placed on these fixings and fastened with an aluminium clasp, this can be seen in figure 7.24. A thin compressible pad (1 cm thick) is inserted between the detector and the container base to provide shock relief, as the detector may come into contact with the container base. An additional feature on the gamma containers is a small coin shaped slot on the side facing the detector allowing calibration sources to be placed inside the container, right in figure 7.24. Also a similar entry point is inserted on the end of the container to allow placement of sources internally via a rod, this is covered with a plastic cap and is shown in figure 7.25. The fully installed gamma box has a total weight of 17.5 kg.

Temperature and pressure sensors were added separately after installation of the

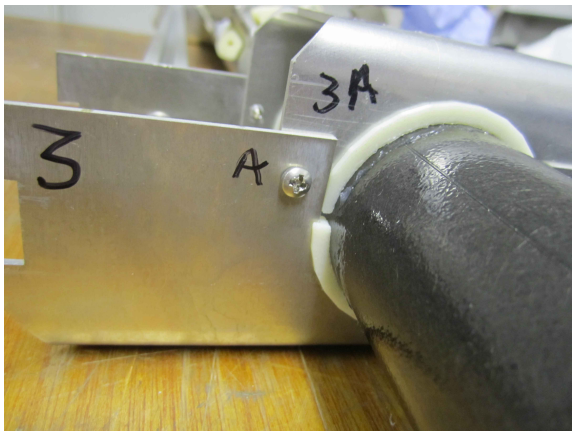

Fig. 7.19 The neutron detectors fixed inside the rack with the clasp fixed.

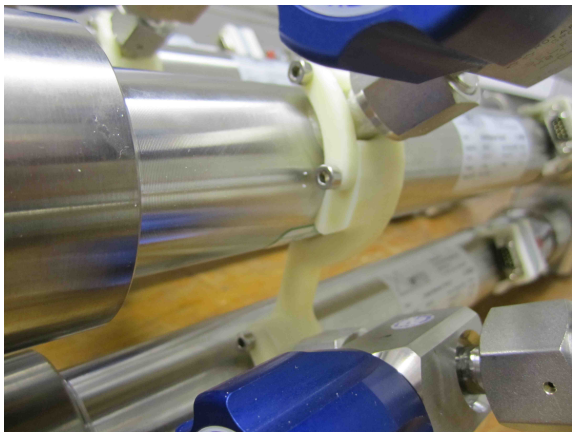

Fig. 7.20 The plastic piece used to hold the detectors parallel and securely inside the box.

Fig. 7.21 The neutron detectors ready for insertion in the containers.

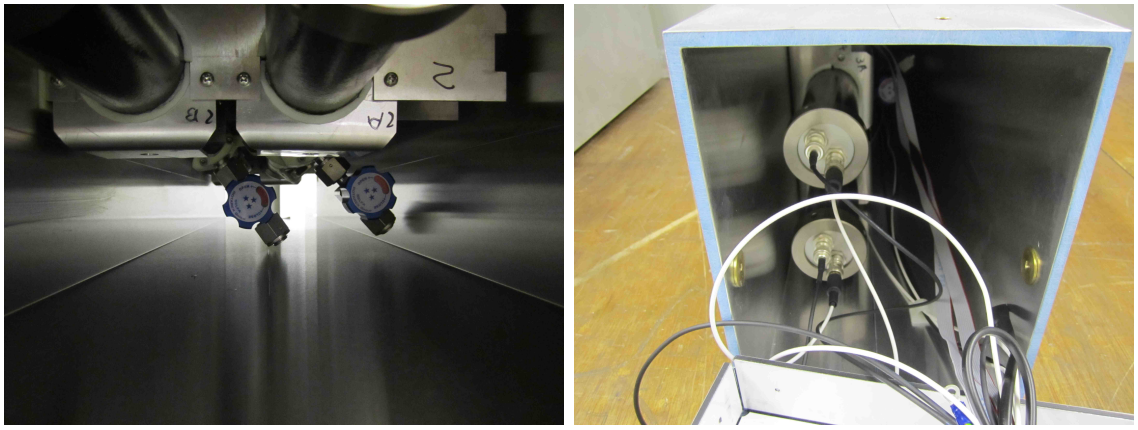

Fig. 7.22 The neutron detectors installed in the containers.

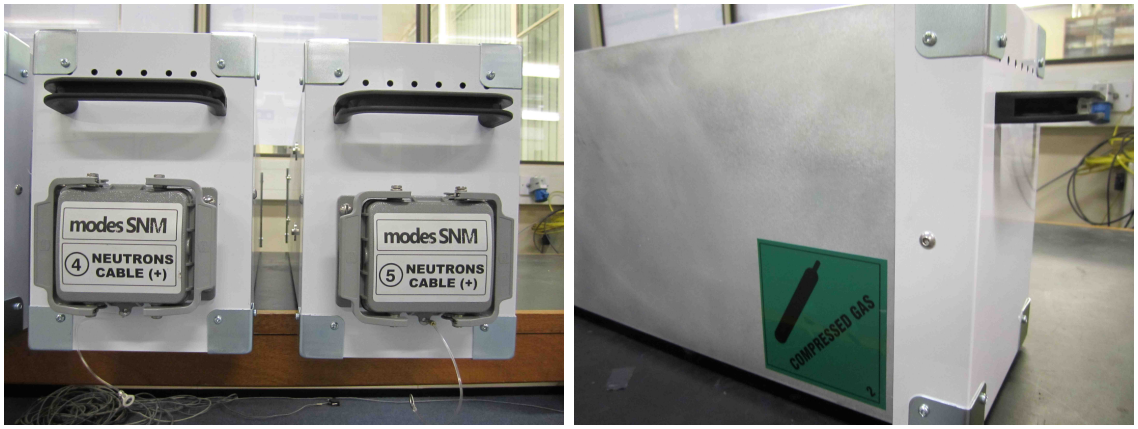

Fig. 7.23 The neutron detector container ends. Left: Cable connection side. Right: Blank side.

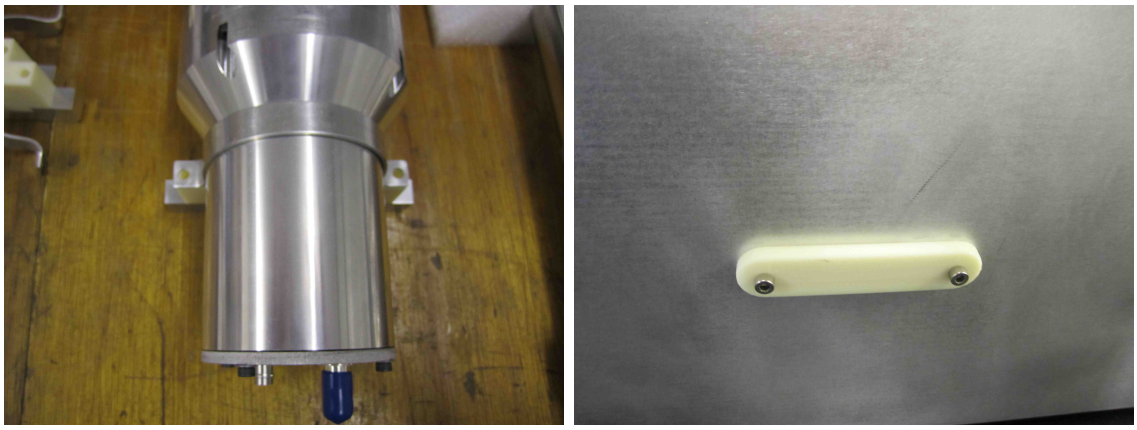

Fig. 7.24 Left: The gamma detector fixed with the clasp, ready for installation in the box. Right: A coin shaped slot on gamma detector container with a retractable plastic piece to hold a small calibration source.

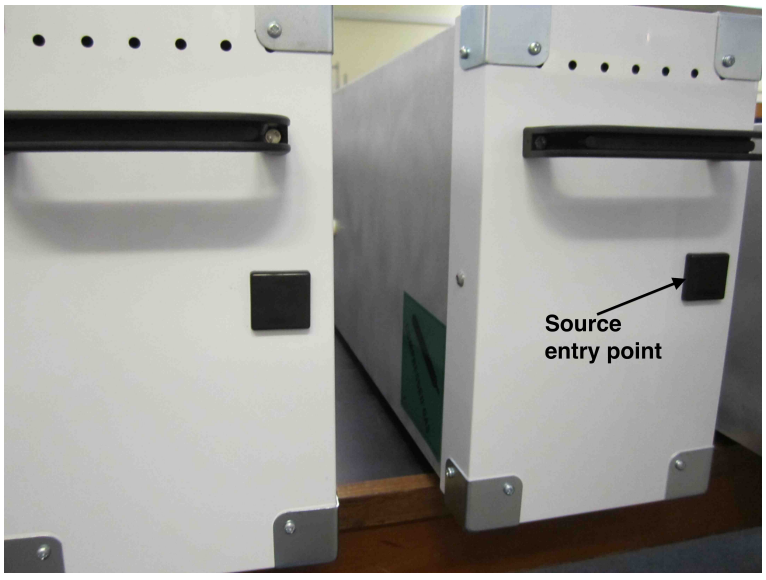

Fig. 7.25 The gamma detector container end with the entry point for sources.

detectors. These were omitted from the Liverpool integration and fitted inside the containers at a facility in Poland prior to preliminary tests of the system.

7.7.2 Installation of the Electronics and Computer

The electronics system cabling can be summarised by figure 7.26. It contains three HV-PS modules, each with four output connections and three 14-bit 500 MS/s FE modules (labelled as digitizer), each with 8 input connections. With two PMT's per detector four cables into the FE are required for each neutron box and two for the gamma box. Only one high voltage cable is required for each detector. An optical connection from FE + HV-PS unit to the PC is established via the DAQ (labelled as A3818). This is mounted inside the PC through the x8/x16 PCI Express slot and can solely handle all 6 of the front end modules. The HV-PS, FE and DAQ are all produced by CAEN but the modules used were developed for bespoke use in the MODES-SNM project, all shown in figure 7.27.

The BMS, GPS and Slow Control (SC - labelled RS485) all follow USB protocol connection to the core of the IS, the PC. The SC is used to control the gas pressure, temperature and PMT voltages for each detector, while the BMS monitors and regulates the current and voltage supplied from the battery to the system.

The computer and components all require 12 V input which is supplied from the battery. An external mechanical switch is required outside the container to control this power supply. Wired in series with the PC and the Power Distribution (PD) the battery can then be disconnected from the system, acting as a kill switch, using a key which is shown left in figure 7.28. The PD consists of a series of conducting connectors in order to provide voltage across the WiFi router, FE and HV-PS, right in figure 7.28.

The three HV-PS and three digitisers are stacked upon each other and are secured via four aluminium pillars on each corner of the module tower. Each is fastened to the containers raised floor with the top joined by two parallel metal bars. There is a $\sim$1 cm gap between each layer due to small rubber feet under each component, providing stability. This structure design does not impede on the component fans, which are located on the side of each component, and allows plenty of ventilation. The PC unit is fastened to the same floor in the container using existing holes in the factory casing of the PC. The WiFi router is then fastened on top of this.

Although most components have built-in fans, additional ventilation is required for the container itself to dissipate heat from cabling and the components inside the container. The total system in operation draws $\sim$21 A of current, this is a considerable

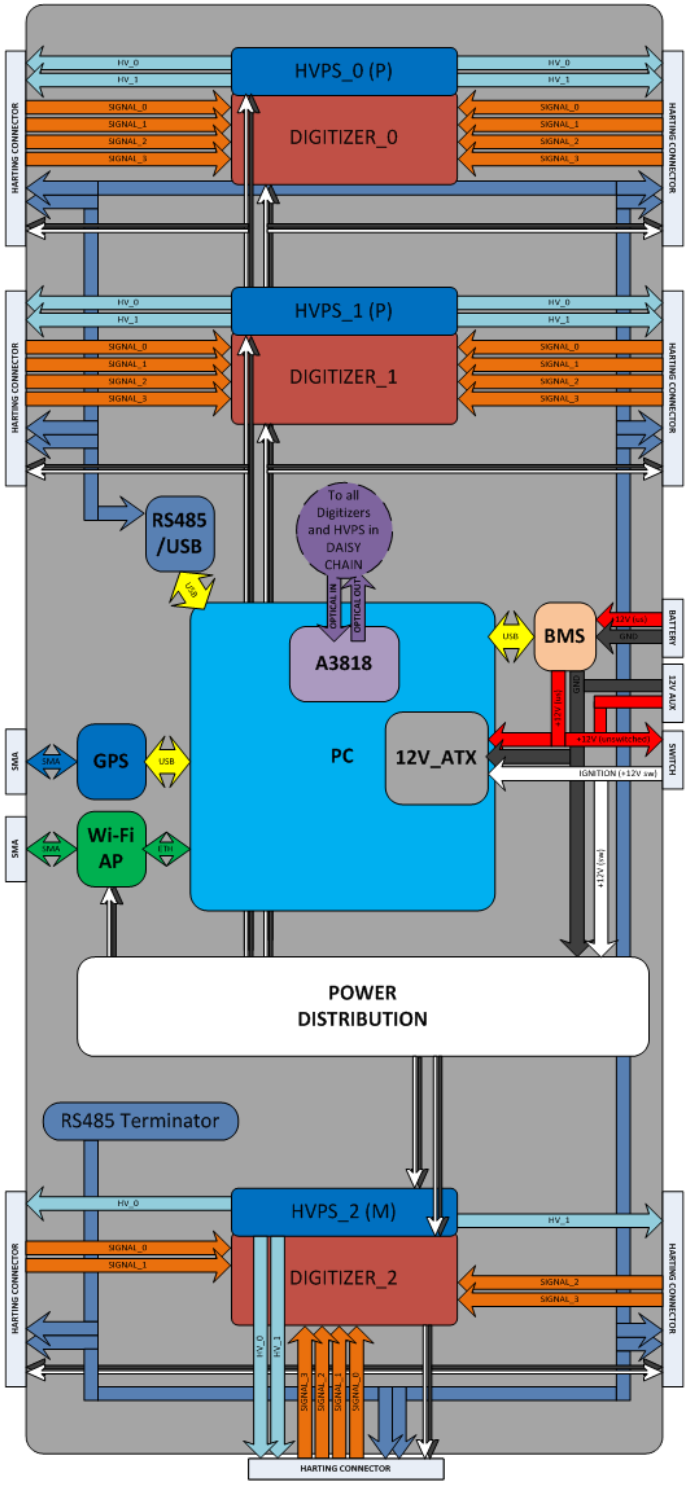

Fig. 7.26 The overview of the internal cabling required for the HV-PS, FE, DAQ, BMS and the IS.

Fig. 7.27 From top left clockwise: The HV-PS, FE and DAQ produced and developed by CAEN.

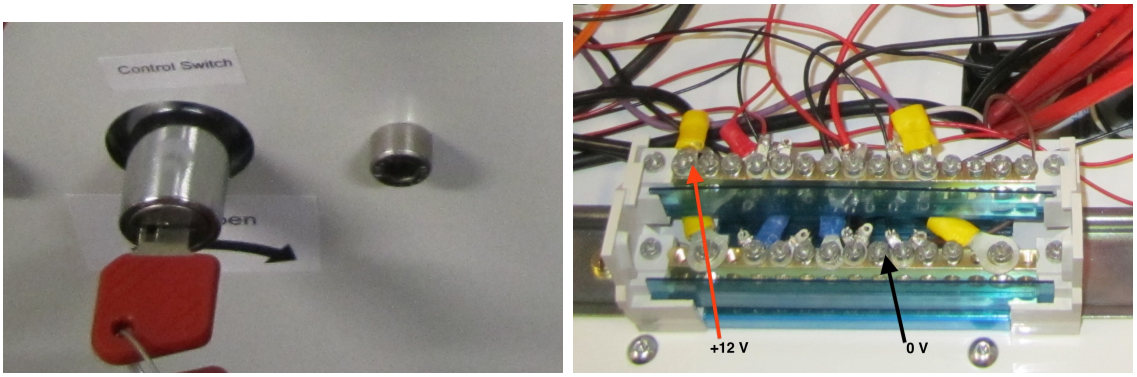

Fig. 7.28 Left: The external mechanical switch located on the electronics container. Right: The power distribution used to supply 12 V to the HV-PS, FE and WiFi router fully wired up.

power consumption of ∼250 W. Fans are implemented to maintain room temperature inside the box, although the system can operate in temperatures varying 0 - 45 °C. Considering the increase in power consumption from the addition of fans and the surface area restrictions on the box, four small 0.25 mA fans are used. Mounting these on two opposite container sides, one near the top and one near the bottom, repeated on the opposite face, provides adequate cooling. The two on the bottom provide external air into the box with the top two operated in reverse expelling warmer air to the outside of the box. This was tested with the temperature monitored every 30 mins for a 3 hour continuous run. The temperature increased by 4 °C above room temperature at the end of the running period, but this level was reached within an hour and an increase of 2.5 °C after just 30 minutes. This is a perfectly acceptable level of temperature increase as the system remained fully operational throughout and considering that the battery can last no longer than 8 hours is a very reasonable testing time.

To allow external connection to the components, panels are removed from two opposite sides of the container to facilitate this. To make the electronics and computer easily accessible incase of a component failure or a wiring fault, it is necessary to restrict all external connections to only 2 of the 4 side faces. Seven holes are required for the detectors, four for the fans, one for the key, one for the battery, one for the mains supply, one for the antenna and then five for various USB, ethernet and VGA connections. This can be seen in figure 7.29. Harting connectors are used as the external cables to connect each module. These are shown in figure 7.30.

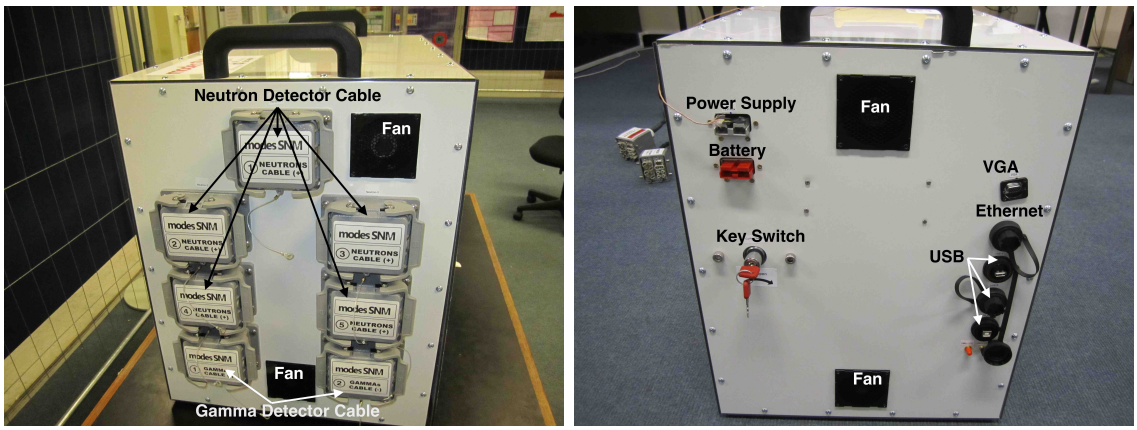

Fig. 7.29 The left and right sides of the electronics box with the full fittings and connectors mounted.

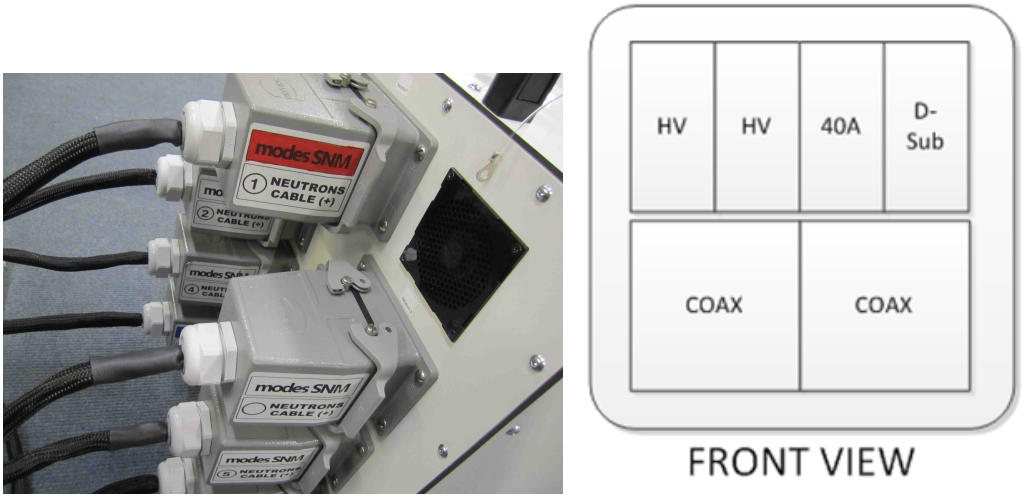

Fig. 7.30 Left: The Harting cables connected to the electronics box. Right: The front end view of the Harting connectors.

The fully integrated electronics and computer system can be seen installed in the container with all cabling in figure 7.31. With the inclusion of two handles on top of the container the total weight of the closed electronics box is 32.7 kg. This weight exceeds the limit of 25 kg imposed on each module but this restriction is relaxed for the electronics box as it is preferable to have one single module for the electronics. A large contribution of the total weight is due to the detector connectors, as each weighs $\sim$2 kg. This was unforeseen in the design but is acceptable for a prototype model.

The total weight of the whole MODES-SNM prototype is then close to 185 kg. This however omits the weight of the Harting cables. The full prototype can be seen in figure 7.32.

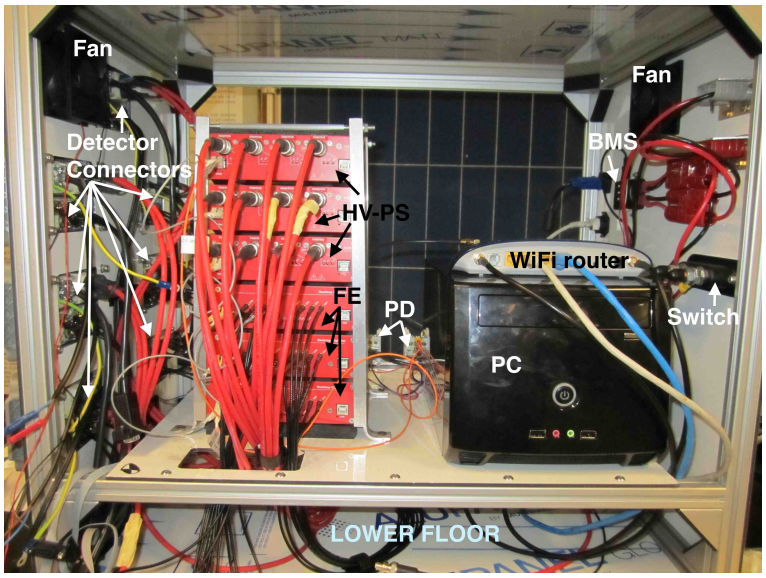

Fig. 7.31 The fully installed electronics and computer system cabled in the container with the two front and back panels removed.

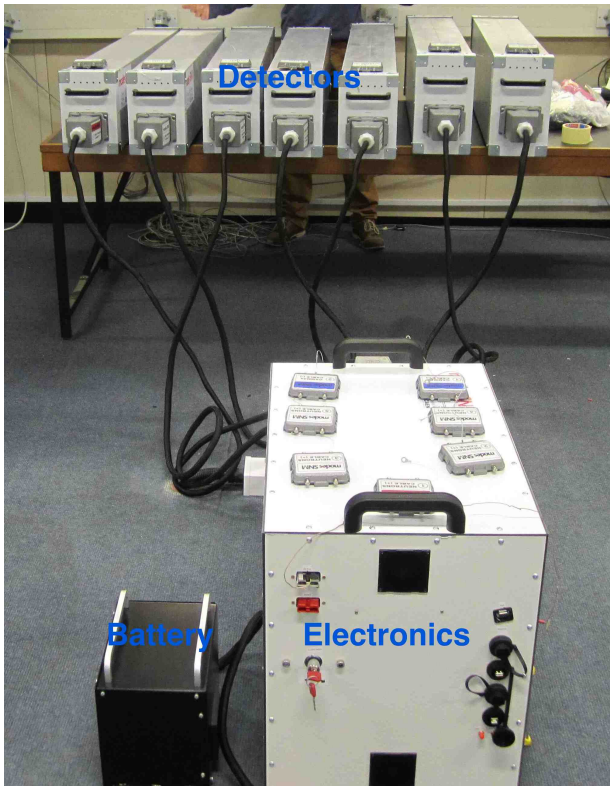

Fig. 7.32 The full system prototype.

Chapter 8

Live Deployment in Real Life Applications

The aim of the MODES-SNM project is to produce a working prototype of a mobile system which is able to detect and identify a wide range of nuclear radiation. Such systems exist on the market but high false alarm rates, low sensitivities and expensive products require a new generation of technology with higher standards and cheaper alternatives than current commercial systems. If the prototype system would be deemed successful this would then lead to development of a commercial product to be used in all areas tackling nuclear threats. Such a device could be used to supersede current systems or to be used in parallel as a secondary device with existing infrastructure. Lab tests alone do not reflect the real life situations that the system would encounter if it where to be commercialised and in order to stringently test and develop such a system, live demonstrations are a necessity.

Several locations for demonstrations of the MODES system were chosen across Europe to perform adequate field tests. The two most common areas where MODES would be used, and where other systems are currently deployed, are shipping ports and airports.

8.1 Prototype Setup

The MODES prototype setup consists of the detector array, electronics box and battery, all fixed and mounted on a movable frame placed inside a medium wheelbase van. Although the frame is movable, for the demonstrations it is fixed inside the van, with the detector array facing parallel to the drivers side panel. In this position the

Fig. 8.1 The MODES system setup in the van.

detectors are closest to the vans side door and while in operation this door can be opened to improve detection efficiency, depending on the weather. This can be seen in figure 8.1. This setup however means the system is biased to one side for screening and is not bidirectional in operation but as it is a mobile system this is not an issue.

8.2 Software Interface

The MODES prototype is operated and monitored through a software interface which is accessible via any device with a wireless connection. Devices such as laptops and smartphones can connect to the Graphical User Interface (GUI) at a distance of up to 20 m from the van, shown in figure 8.2.

The software is accessible in two modes, normal and expert. Normal mode can only access the main control page, 'CONTROL' tab, which is shown in figure 8.2 and is designed for users with no scientific background. This will be the default mode of operation and retains all functionality that an end user would need. The simplistic design of the interface is specifically tailored to such an end user with no background in nuclear physics. Expert mode should only be used as stated, by an expert, personnel who have substantial knowledge and understanding of nuclear radiation. In

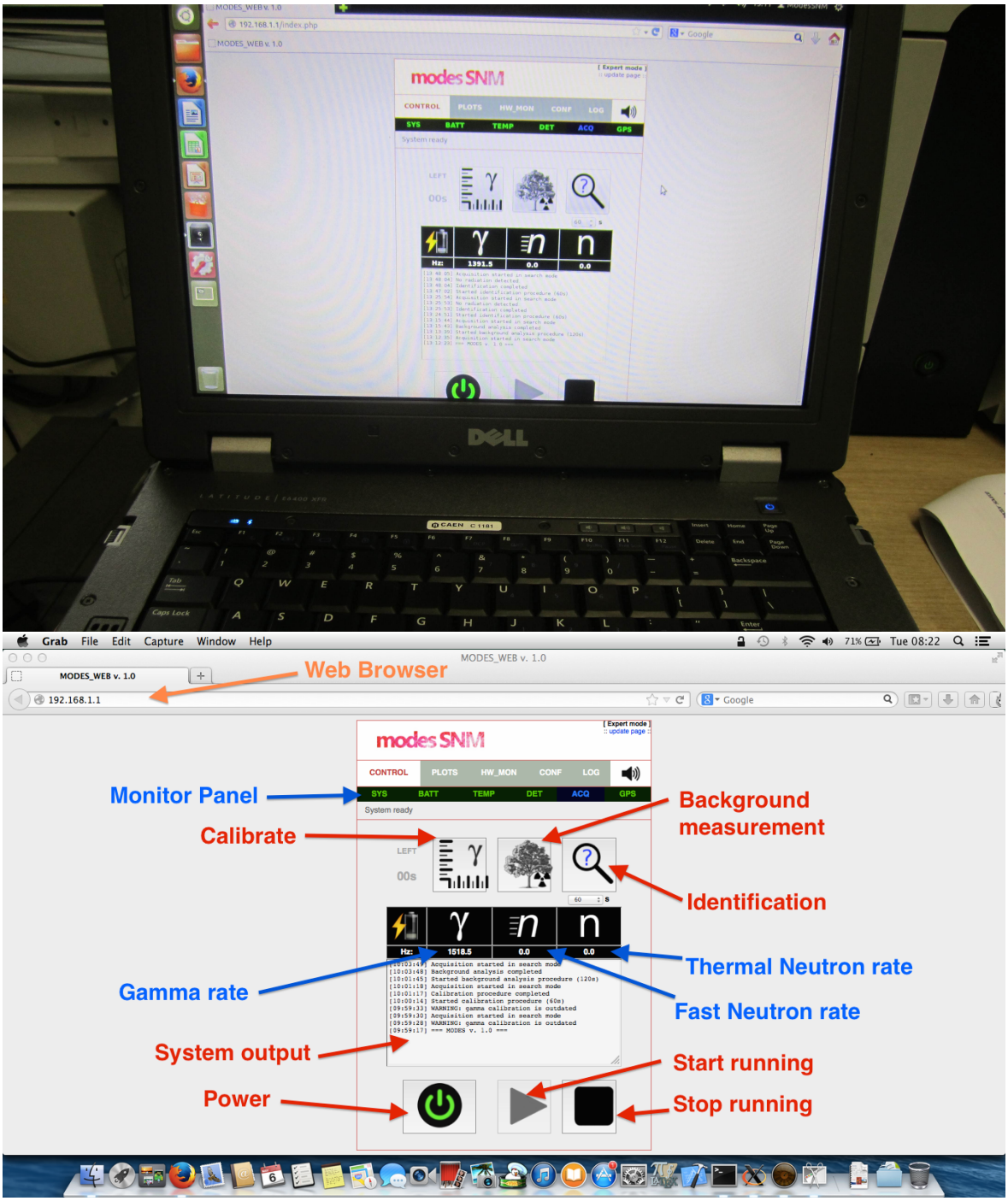

Fig. 8.2 Top: The software interface show on a laptop. Bottom: The control page of the software shown in an internet browser with labels.

this mode energy spectra can be observed for each of the tubes in the detector array under the 'PLOTS' tab. Details on pressures, temperatures and voltages on the tubes are viewable under the 'HW_MON' tab with these parameters configurable via the 'CONF' panel. An extensive log file is accessible, under the 'LOG' tab, which is far more heavily detailed than the one shown to the user in normal mode, showing energy spectrum peak values with corresponding $\chi^2/d.o.f$ values for fitting.

The procedure to start up the system and begin data acquisition is a simple 5 minute operation. With the battery connected to the electronics box the mechanical ignition key can be switched on and provide power to the whole system. Once the wireless connection has been established with the device used to control the system, in the case for demonstration this is the laptop, the user can then begin the procedure. A calibration run must first be performed, involving a 60 s exposure of a weak ^{60}Co source (40 kBq) held close to the NaI detector via the coin sized slot on the side of the contatiner. Such a source is deemed safe to handle by a user and can be placed in the slot on the detector. Internal calibration is also continually performed but does not need interaction from the user. Following this a background measurement is then needed, which involves a 120 s exposure. The system output will print out details of the procedure to the user and notify when each step is completed. Upon completion of these steps the system is ready to begin data acquisition and is considered active. The various radiation rates: gamma, fast and thermal neutrons, are shown on the control page.

8.2.1 Energy Calibration

For calibration of the MODES system two sources are used. One ^{40}K source (1 kg KCl ∼32 kBq), is used internally in the NaI detector, which is continually present and the second is a ^{60}Co source (40 kBq) that is used externally upon start up of the system. ^{40}K emits a 1.46 MeV photon in around 10% of decays via electron capture. The two peaks at 1.17 and 1.33 MeV originate from ^{60}Co beta decay and then the subsequent nuclear de-excitation. These can be seen in the spectra when calibration is being performed figure 8.3.

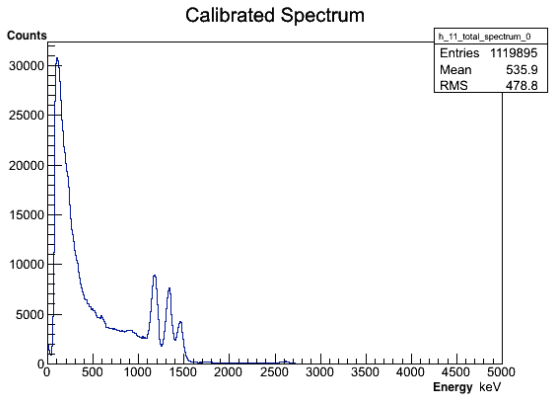

Fig. 8.3 The energy spectrum upon calibration as measured by the NaI detector.

8.3 Joint Research Centre, Ispra Laboratory Tests

Ispra Research Laboratories, located in Ispra, Italy, are one of Europe's leading research facilities dedicated for experimental activities used for the development and testing of new technologies. It is then well suited to perform controlled laboratory tests on the MODES system. Such tests were performed at Ispra prior to the live demonstrations in order to test the system with SNM sources, as this would hopefully not be encountered at the demonstrations. Also it enabled the capability to test the system with known moving sources.

An IAEA requirement imposed on any potential radiation detection device is to raise a neutron alarm for a ^{252}Cf source, of activity of 1.2×10^4 neutrons/s, whilst in motion at a speed of 0.5 m/s (1.8 km/h) [89]. It is also required that the distance between the source and the system $\geq$1 m. This is equivalent to a static rate of 0.1 neutrons cm^{-1}s^{-1} at 1 m distance. Such tests successfully met this requirement with the results shown in table 8.1. Other neutron sources were also used to test the neutron detection capabilities, all conducted at the speed of 1.8 km/h, table 8.2.

Speed	Alarms	Trials	Success Rate
km/h	-	-	%
1.8	**30**	**30**	**100.0**
4.3	28	30	93.3
7.9	23	30	76.7

Table 8.1 The speed tests for a ^{252}Cf source (1.2×10^4 n/s) at 1 m distance performed at Ispra

Source	Alarms	Trials
AmBe	10	10
AmBe shielded 1cm lead + 1 cm iron	10	10
Am/Be shielded 1cm lead + 1 cm iron + 8 cm poly	10	10
Pu (6 g - 61% enriched in ^{239}Pu)	5	5
Pu shielded 1cm lead + 1 cm iron	5	5
Pu shielded 1cm lead + 1 cm iron + 8 cm poly	5	5
^{252}Cf 1cm lead + 1 cm iron + 8 cm poly	5	5

Table 8.2 Various neutron sources used to test the MODES system in laboratory conditions with a separation of 1 m from the detector.

The IAEA also impose a requirement for the dynamic sensitivity of gamma radiation such that the system shall generate an alarm for ^{241}Am, ^{137}Cs and ^{60}Co sources whilst in motion at a speed of 0.5 m/s (1.8 km/h) [89]. Once again the distance of closest approach should be no less than one meter between the source and the detection system. The gamma results met this requirement and are shown in table 8.3. Given the variable activities of the sources, the distance of closest approach was varied in order to compensate. Identifications were also performed on the sources in a 60 s exposure while probing in stationary mode. Ten attempts at identification were performed on each with each attempt successful.

Source	Dose Rate	Speed	Alarms/Trials
-	nSv/h	km/h	-
^{60}Co	50	$\leq$7.9	30/30
^{133}Ba	10	$\leq$7.9	30/30
^{241}Am	50	1.8	30/30
^{241}Am	50	4.3	20/30

Table 8.3 Various gamma sources used to test the MODES system in laboratory conditions.

8.4 London Heathrow Airport Demonstration

London Heathrow International airport is the busiest airport in the UK, with an average of $\sim$1200 aircraft movements daily. In 2013 the cargo tonnage passing through

the airport reached over 1.4 million tonnes [100]. It is therefore a perfect environment to perform field tests for the prototype system.

The UK Border Force (UKBF) are responsible for monitoring all cargo that is imported and exported via Heathrow. However only shipments for import into the airport are scanned for radiation. All cargo is loaded on to vehicles, consisting of vans and trucks, to be transported around the airport. Every vehicle must first pass through a control area at the airport, where it is scanned, before it is fit for import.

8.4.1 Current System and Procedure

At the entrance to the control area, a large RPM is mounted, this is the UKBFs primary radiation detection system, shown in the left of figure 8.4. If the RPM is triggered when a truck is passing, an alarm is raised via lights and a siren. The vehicle in question is then stopped and guided to an examination area for further investigation. Upon examination of the vehicle, the UKBF use secondary detectors, identiFINDERs (produced by FLIR) [101], shown in the right of figure 8.4, to help identify the source of radiation. The identiFINDER uses NaI detectors to identify gamma radiation sources, with optional ^{3}He detectors to detect neutron radiation.

The RPM has a laser tracking system, used to trace out the vehicle outline as it passes the detectors. Coupled with the measurement of the count rate with time, gives the user the ability to localise the source position on the truck, within a distance of around a meter. With cargo containers of the order of a 1 m in length this can help deduce which container is the cause for concern. From this information the secondary inspection device, the identiFINDER, can be used more successfully, homing in on the source.

On secondary inspection the count rate is measured and an identification is performed. If the count rate is considered safe and the source identification matches the corresponding documentation for the cargo, the cargo is suitable for import and released from the control area. However if an identification proves inconclusive or yields an unknown source after repeated measurements, then external advice is required. A Radiation Protection Advisor (RPA) is an external entity that has expert knowledge on radiation and is called upon when the system fails to identify the source correctly. It is then up to the RPA to decide the fate of the cargo given data and information from the RPM software, including energy spectra and rates.

Fig. 8.4 Left: The RPM in use at Heathrow Airport to scan and monitor all shipments arriving for import. Right: The identiFINDER, produced by FLIR, used for secondary investigation after the RPM alarm is raised

8.4.2 Setup

The van is setup with the detector array facing the road upon which the cargo vehicles travel. At this position the typical distance between the MODES van and the passing traffic is no more than 1.5 m and in operation the door is left open.

8.4.3 Stationary Mode - Passing Vehicle Testing

While the system was operational in stationary mode for testing passing cargo, a total of 635 vehicles passed the system, covering a 20 hour period. From these passing vehicles one false positive alarm and one true positive alarm occurred only. Many gamma alarms occurred also when no vehicles were present, with an average of 3 alarms per hour, totalling to ∼60 such incidents. These occur due to a low threshold setting in the system and fluctuations in the background can trigger such alarms. Although no vehicles were present, future designs and upgrades for the system must consider removing these alarms if the system is to survive the scrutiny from potential buyers.

Fig. 8.5 The MODES system mounted in a medium wheelbase van. Left: The detector array mounted on the frame. Right: The MODES van with the side door open to expose the detector array.

8.4.4 False Positive Alarm

On the second day of testing, after 140 vehicles had already passed the system without an alarm, a false positive alarm was raised by a passing vehicle. The alarm was short and the gamma count rate was similar to the background rate of ∼1400 Hz, initially raising suspicion that this may a false positive. However following procedure the vehicle was instructed to stop at the examination area for further probing. At a distance of 0.5m from the vehicle MODES failed to pick up any signs of radiation after repeated measurements of exposures from 60 to 300 seconds. The gamma count rate decreased upon approach to the vehicle to a value ∼ 1100 Hz, due to vehicle shielding. The identiFINDER also failed to detect any radiation. Cargo itinerary revealed oil mining equipment which is fit for transport and not a radiation threat. The vehicle was subsequently released.

It was a displeasing result and highlights that the sensitivity of the system is an issue as it increases the number of false alarms. The probability of such an event occurring due to background fluctuations is much smaller than observed however. As in the 20 hour period 635 vehicles passed the detector, with each taking ∼6-8 s to fully pass the van. Hence on average ∼6% of the time a vehicle was present. With an average of 3 alarms raised when no vehicles were present per hour, but with a maximum of 4 per hour, and each lasting ∼2 s, yields an upper limit that ∼0.2% of the time an alarm is triggered by the background. For these two events to both occur results in ∼0.014% probability, which would mean we can expect 1 false alarm for every ∼7,400 passing vehicles. Thus from the 635 vehicles observed we would expect 0.09 false alarms while a vehicle is present but we observed 1 false alarm event. In terms of Poisson statistics an observation of one false alarm, with a mean of 0.09 false alarms, corresponds to P(n=1) = 8.2% and P(n≥1) = 8.6% for one or more false alarms. Highlighting that this was quite an improbable occurrence but for large volumes of traffic this would not be acceptable and reasserts the need to lower the rate at which alarms are triggered from background fluctuations.

8.4.5 True Positive Alarm

On the fourth day of the demonstration, after a cumulative count of 319 vehicles passing MODES, the 320^{th} such vehicle raised an alarm upon passing the MODES van. The vehicle was instructed to stop and moved to the examination area for further investigation. With the van parallel to the drivers side of the alarmed vehicle and at a

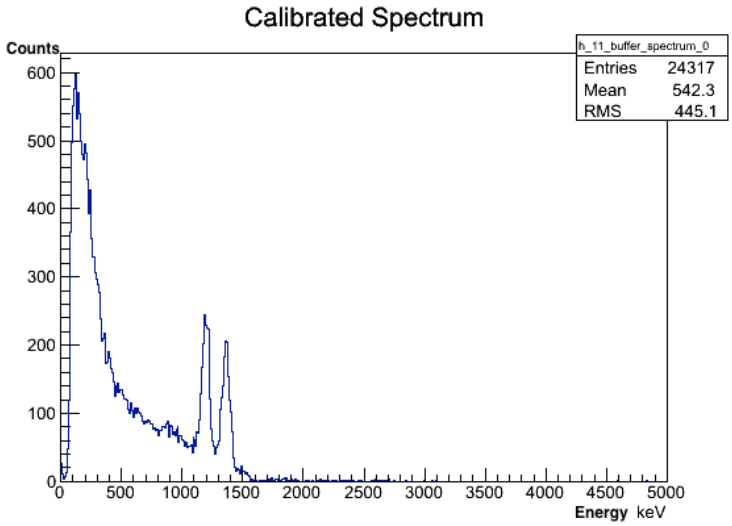

Fig. 8.6 The energy spectrum of a ^{60}Co source found on a cargo passing the MODES system for a 2 s exposure time. The two peaks at 1.17 and 1.33 MeV indicate ^{60}Co.

distance of 0.5 m away, the van probed it while in motion at <8 km/h. Moving from the front to the rear of the vehicle the count rate increased sharply until a maximum of 7400 gamma counts s^{-1} was reached near the centre. In comparison the background rate, at more than 10 m from the vehicle, was 1400 counts s^{-1}. After locating the maximum count rate position, a 60 s exposure led to an identification of a ^{60}Co source on the first attempt. Repeated measurements yielded the same source with the peaks matched with a fit of $\chi^2/d.o.f = 0.198$. The spectrum for a 2 s exposure can be seen in figure 8.6.

The two peaks at 1.17 and 1.33 MeV, are a clear signature of ^{60}Co. These occur following the beta decay of the isotope which leaves the daughter nucleus, ^{60}Ni, in an excited nuclear state which subsequently emits two photons at these energies following from de-excitation. ^{60}Co is not a naturally occurring isotope and is created artificially by the bombardment of neutrons on ^{59}Co. The paperwork for the alarmed vehicle details that it contains two sources of ^{60}Co of 500 kBq and 7.4 MBq, shielded by stainless steel. However other sources present of ^{137}Cs (1.9 GBq) and ^{125}I (activity not stated) were not picked up by the MODES system. ^{125}I does not currently exist in the software spectrum library and could not be matched but ^{137}Cs does exist in the library. ^{137}Cs emits a 0.66 MeV photon 93.5% of the time, but this is not seen in the spectrum in figure 8.6. This source may have been shielded much more than the ^{60}Co and as a result cannot be identified. In terms of eligibility for transport the

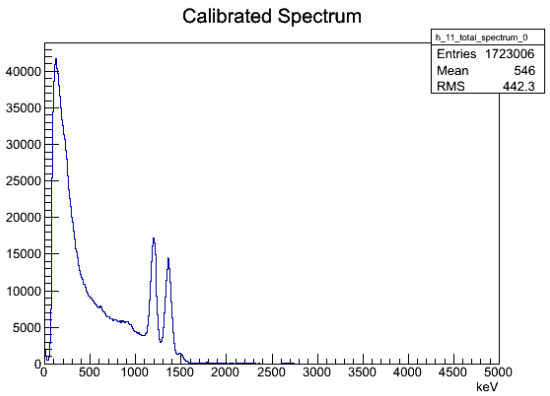

Fig. 8.7 Left: A container holding various radioactive substances, of ^{60}Co, ^{137}Cs, ^{232}Th and ^{222}Rn, with the MODES van positioned along side it. Right: The energy spectrum from the container.

cargo ranks a category of Class 7, which label radioactive materials fit for transport. The vehicle was subsequently released.

This was a pleasing result and thoroughly impressed the UKBF. It was a perfect example of the sensitivity the MODES-SNM system possesses.

8.4.6 Container of Radioactive Sources at Heathrow

At the control area a large container is used to hold confiscated radioactive sources that were not eligible for import. The sources in the container were known to the UKBF but a blind test was performed with the MODES van to see if it could identify any of the sources in the container. The sources in the container were: ^{60}Co, ^{137}Cs, ^{232}Th and ^{222}Rn. The alarm was raised initially at a distance of almost 10 m as the van approached the container. At 1 m away from the container with the detector modules facing the containers side, a gamma count rate in excess of 15000 Hz was observed (∼11 times the background). Several exposures of 60 s correctly identified the ^{60}Co source but failed to identify the remaining 3 sources. The activity of the sources is not known but the ^{60}Co source originates from stainless steel bowls which were not classed as Class 7 on import. Isotopes ^{232}Th and ^{222}Rn could not be identified, with the 0.66 MeV photon from ^{137}Cs not noticeable in the energy spectra, shown in figure 8.7.

Once again it was an impressive result, especially with the alarm raised at such a far distance from the source. The identification of ^{60}Co was well received by the UKBF

but of the sources found this was the most anticipated. The remaining sources were unidentified and it was a slight disappointment. It would of been productive to repeat the test without the ^{60}Co source in the container and to then see if the remaining sources were identifiable, however it was not possible to perform such a test.

8.4.7 System Stability and Reliability

Over a period of five non consecutive days, the MODES system ran fully operational for the majority of demonstration. There were few minor problems with the system, with 3 software crashes in total, which were overcome with a simple laptop restart. Considering that the van had travelled over 2000 miles before arrival to Heathrow illustrates that the system fully fulfils the reliability requirement of the prototype while remaining mobile.

8.5 Other Demonstrations

Other demonstrations were also performed at Rotterdam, Dublin and Switzerland, a summary is given for each.

8.5.1 Rotterdam Port Demonstration

The port of Rotterdam is the largest port in Europe and acts as a passage to the EU. On an annual basis more than 12 million cargo containers (Twenty-feet Equivalent Units based on 2014 statistics) pass through the port [102]. The Dutch Customs are responsible for the scanning of such containers and detecting illicit radioactive and nuclear materials. They currently employ a range of fixed, mobile and hand held detection devices to aid them in this task.

Dutch Customs tested the MODES system in their daily use in the Port of Rotterdam. Similar procedures were employed at the port with trucks carrying cargo required to pass their primary detectors. Trucks that alarmed from the primary fixed RPMs were pulled over and investigated using secondary detectors. At ports large containers are common place and large lorries are required to transport them, seen in figure 8.8, unlike Heathrow were cargo is held in much smaller volumes.

The port experiences far more traffic than at Heathrow and as a result experiences many more alarms. Several different techniques were employed to fully test the MODES system. This consisted of MODES being deployed as a stationary and mobile

Fig. 8.8 Left: A typical lorry carrying a container under inspection with the MODES system and the currently used mobile system at the port by the Dutch Customs. Right: The truck passing the RPM at the port with the MODES system in front being used as a primary detector.

probe while used as a primary detector, with some radioactive tests also performed with known samples used.

As a fixed primary detector positioned along side the RPM, pictured in figure 8.8, several alarms were raised but no identifications were performed in this mode. During these tests vehicles passed the system at speeds ranged from 12 - 25 km/h at a distance of ∼1 m away. These alarms were all matched by the RPM. However a few gamma alarms were also raised when no vehicles were present.

While being deployed in primary mobile mode as a container probe, the MODES van was driven around stacked containers at a distance of ∼0.5 m away at a speed of ≤10 km/h, shown in figure 8.9. Several alarms were raised with sources of ^{40}K, ^{137}Cs and ^{60}Co being correctly identified in a container of tiles and ^{232}Th and ZnOx being correctly identified in a container of polymers. However the remaining alarms were unable to be resolved with MODES, as it was unable to identify the source, some of which also contained ^{40}K and ^{232}Th.

Radioactive tests were performed with some weak sources placed on a tripod ∼1 m away from the van with the side door closed. With van speeds of 10 km/h MODES was able to identify a ^{133}Ba source, 0.45 MBq. AmBe was also identified but only when the van was slowed to 5 km/h, after a 60 s exposure yielded shielded neutron source. After this it was removed from the lead shield and a further identification gave AmBe and ^{241}Am sources. The neutron rate recorded was 1.5 Hz, with a gamma alarm of 1400 Hz.

Fig. 8.9 The MODES van probing containers at the port while in motion.

Fig. 8.10 The MODES van being tested in mobile mode with known radioactive test samples on a tripod.

Fig. 8.11 The Nuctech X-ray scanner used at the Dublin Port.

The system also suffered from many alarms when no containers were present, similar to as in Heathrow tests. Another problem encountered is the wifi connection with the system, as many times the connection would be lost and needed to be restarted. This was much more frequent than at Heathrow but is most likely due to the fact the door was closed for the testing at Rotterdam, whereas at Heathrow the door was left open, avoiding Faraday cage effects.

8.5.2 Dublin Port Demonstration

The port of Dublin is the largest port in Ireland. MODES was also deployed here to be used in conjunction with an X-ray scanning operation at the Coastal compound at the port. The MODES system was deployed in stationary mode ∼50 m from the 6 MeV mobile X-ray scanner (Nuctech). At this distance the MODES system did not experience any interference. The scanner is pictured in figure 8.11.

In stationary operation a total of 83 containers and vehicles with cargo were scanned by the MODES system and no alarms were raised in them passing, however several alarms were raised when none were present. Two known containers of NORM were probed and raised an alarm both times in coherence with the X-ray scanner. These two cases of gamma alarms were triggered by containers holding ceramic tiles and clay pots. While both containers had been profiled as containing NORM, MODES yielded an erroneous identification of AmBe for the clay pots.

It was also used in mobile operation to probe 60 containers but all failed to trigger an alarm. In absence of high traffic at the port the van was taken to the University College Dublin (UCD) to test against a Pu/Be source (37 GBq). The source was

Fig. 8.12 The MODES prototype system scanning at the Swiss Customs, Basel.

heavily sealed by tantalum and stainless steel capsules, containing 16 g of ^{239}Pu oxide mixed with beryllium metal. The source was held in a paraffin-filled drum, 0.51 m in height and 0.36 m in diameter. The drum was placed in a van and driven past the MODES system, at a speed of 8 km/h at ∼1 m away. This was increased to 4 m and the speed to 20 km/h, on both occasions the MODES system triggered gamma, neutron and thermal neutron alarms.

8.5.3 Switzerland Field Tests

Two locations in Switzerland were chosen for live field tests, the first at the Swiss border in Basel and the second at a Heavy Goods Traffic Center in Uri. These were the concluding tests for the demonstration period.

8.5.4 Swiss Customs, Basel

At the Swiss Customs, Basel, the MODES system was setup in stationary mode and was used as a primary detector along side the Swiss Customs mobile X-ray scanner. Vehicles passing the border, pass both systems at speeds of ∼8 km/h. 38 vehicles were scanned over a period of 6 hours, no alarms were triggered. The background rate was measured at between 1.8 and 2.0 kHz, which fell to 1.2 - 1.5 kHz when vehicles passed the system, due to vehicle shielding.

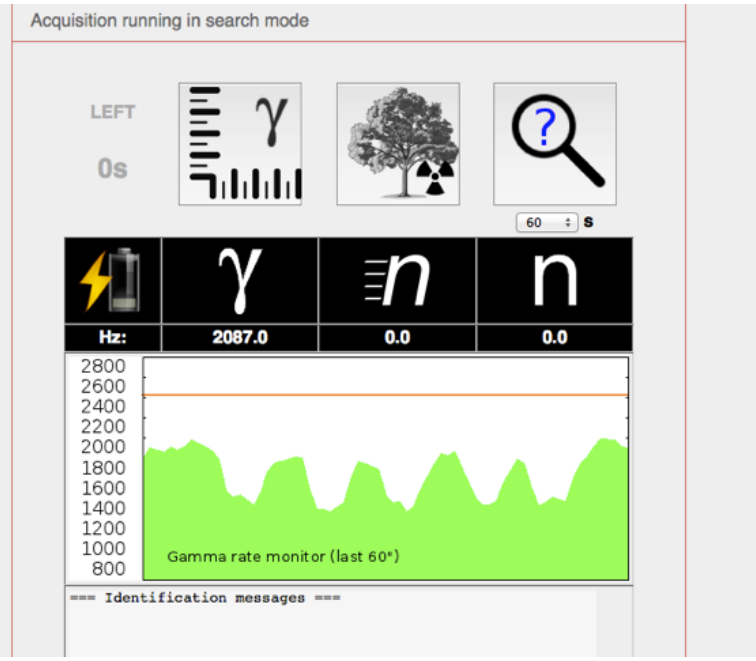

Fig. 8.13 The user interface after the software upgrade, showing count rate as a function of time. This example shows the background suppression when five trucks pass the system.

8.5.5 Software Upgrade

After the first Swiss test an upgrade was applied to the software, addressing some key issues that were raised during the previous demonstrations. These were:

- False alarm rate higher than expected
- Occasional low power to some detector tubes
- Conflict of GUIs when accessing from different devices
- Lack of data export tools
- More user information, count rate as a function of time
- Better compatibility with mobile devices

A key upgrade was the inclusion of the count rate as a function of time, as fluctuations can be obvious to the user and it can be used to localise radioactive material on vehicles, figure 8.13.

8.5.6 Heavy Goods Traffic Centre, Uri

Located in front of the Gotthard tunnel in Switzerland, the heavy goods traffic centre sees 1300-1500 trucks pass through every day. This is ∼75% of all trucks driving through the Swiss border. The gamma background in Uri was twice the level of that in Basel, due to large amounts of Radon in Uri, with rates of ∼200-400 Bq/m^3 on average in this area, compared to ∼80-100 Bq/m^3 on average in Basel [103].

Over a 2.5 hour window, 218 trucks were probed while the system was stationary. The speeds of the vehicles ranged from 5 - 25 km/h. No alarms occurred during this period, however 4 sharp peaks could be noticed, which involved short rapid increase in count rate, while no vehicles were present. These did not raise any false alarms due to the software upgrade.

8.6 Summary

The laboratory tests show the system meets the requirements of the IAEA and the demonstrations ultimately prove the durability, reliability and portability of the system. While traveling over 10,000 km across Europe the system, which was mounted in the van continuously over a period of 2 months, remained fully functional. It is also worth noting that the system traversed both land and sea on its journey. With the exception of wifi connection problems, the system worked without any major problems throughout the tests and each time it was easy to setup and use. Some key issues with the system were addressed before the final demonstration which most importantly removed the false alarm rate due to background fluctuations. Other issues still remain however with the need to extend the library to include medical isotopes persisting, as a lot of cargo transported via Heathrow involves medical isotopes.

For the majority of the demonstrations the system was deployed as a primary stationary detector, but ideally this system would be used as a secondary device. Although not tested as stringently as in primary mode, the demonstrations give an indication that this system is very capable of competing with current secondary devices.

The officials at each demonstration site were very impressed with the prototype. Many of the officials were especially keen on the simplicity and usability aspects of the system, with it very easy for non experts to use. They look forward to further developments from the system and retain close interest to its potential in the near

future.

Chapter 9

Data Analysis and Source Identification Techniques

Laboratory tests on the MODES-SNM system were performed at a controlled environment at NCBJ in Poland. The collected data was the first that the prototype was exposed to and was used to characterise the system. Some studies are initially presented that were conducted by the collaboration members from NCBJ to quantify the basic properties of the detectors and examine the detector requirements. The chapter then focusses on the techniques employed to analyse the collected data, with the aim to discriminate between neutron and gamma sources for real world applications. This is an alternative analysis to the one implemented in the prototype and the one used in the live demonstrations, as it aims to improve on the existing analysis and to be implemented in future MODES-SNM like systems.

9.1 Laboratory Characterisation

Laboratory characterisation of the system was performed at NCBJ and the following section summarises the results of the work performed by the NCBJ contributors of the MODES-SNM project [59]. The primary objective was to perform preliminary tests on the prototype system, specifically to assess the detectors response, efficiencies, resolutions and durability.

9.1.1 Gamma Detector Response

^{137}Cs (662 keV) and ^{241}Am (59.6 keV) sources were introduced at 0.5 m from the centre of the xenon container to measure the detectors response. Figure 9.1 shows the xenon detector's response for the two sources, also compared to the background counts (no source). The signal amplitude is determined as the ADC counts measured in the long gate, corresponding to the Q_{long} value from equation 6.2. The non-linearity of this response is illustrated in figure 9.2, it can be seen that the detectors energy response for gammas is no longer linear for energies less than ∼200 keV. This is due to increased scintillation efficiencies at these lower energies. Each point in figure 9.2 was determined from matching peaks in the signal amplitude to known energies from 9 different radioactive sources (14 peak energies between 50 keV and 1.5 MeV), using both channels on one of the xenon detectors. The measured peaks were normalised to that of the ^{137}Cs source at 662 keV. The maximum linear deviation was observed at the 60 keV peak for which a measured difference of 8% and 10% for channels 0 and 1 respectively.

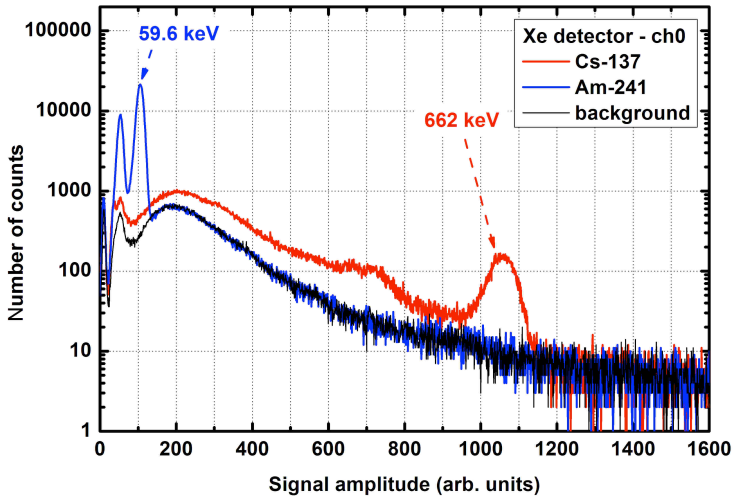

Fig. 9.1 The energy spectrum (signal amplitude) from one of the PMTs in the xenon detector for a ^{137}Cs source (red line) and an ^{241}Am source (blue line). The counts due to the absence of a nearby localised radioactive source is shown by the black line. Plot taken from [59].

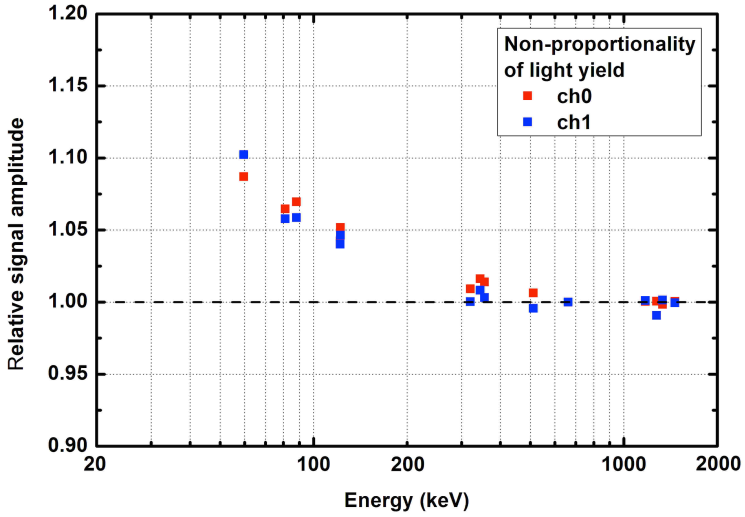

Fig. 9.2 The relationship between the measured relative signal amplitude and the measured peak energy arising from several gamma sources. The signal amplitude is normalised to the 662 keV peak energy photon emission from a ^{137}Cs source. Data points correspond to 14 measured energy peaks between 50 keV and 1.5 MeV for 9 known gamma sources, using both channels (channel 0 in red and channel 1 in blue) for one of the xenon detectors. Plot taken from [59].

9.1.1.1 Energy Resolution

Defining the energy resolution as the FWHM (Full Width at Half Maximum) divided by the signal amplitude, measurements of the energy resolution for gammas in the xenon detector where established using the same 9 sources previously used for the linearity tests. Again only one of the xenon detectors was tested with both channels used. An energy resolution of between 6.7% and 7.0% [59] was established for both channels on the detector at 662 keV, a value comparable to NaI detectors. The left of figure 9.3 shows the energy resolution as a function of the source energy, showing resolutions less than 6% for energies around 1.5 MeV but very poor resolutions for energies below 200 keV.

Although the xenon detector showed good energy resolutions at the higher energy range these studies showed very poor efficiencies also (<1% above >1 MeV), with the detector failing to identify ^{22}Na and ^{60}Co sources. The right of figure 9.3 shows the Peak Detection Efficiencies (PDEs) for the same 9 sources. The maximum efficiency is achieved at ∼100 keV reaching ∼50% with it dropping off below this energy due to interactions in the Titanium vessel and decreasing above this energy due to decreased

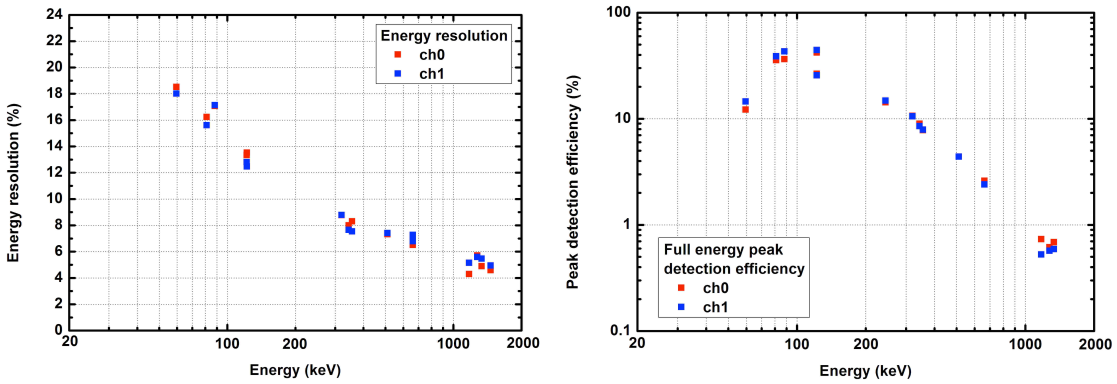

Fig. 9.3 The xenon gamma detectors energy resolutions (left) and efficiencies (right) based on peak matching from 9 gamma sources with energies between 50 keV and 1.5 MeV. Plot taken from [59].

cross section.

9.1.1.2 Detector Stability

The ^{137}Cs source was used to measure the stability and temperature response of the xenon detector. Measurements of the signal amplitude were taken at the 662 keV peak at 15 minute exposures, over a period 14 days to determine the detector stability. The left of figure 9.4 shows the measured amplitudes for both channels, showing a fairly stable response (maximum ∼2.2% deviation) over this period varying between 1130 - 1155 and 955 - 970 for the signal amplitude for channel 0 and 1 respectively.

The variation in the signal amplitude over this period cannot be solely attributed to the temperature variation as this was also measured independently by controlled cooling of the detector between 12°C and 20°C. The maximum deviation for this variation was at ∼0.9%, this is negligible in comparison to the energy resolution at 662 keV of ∼7.0%.

9.1.1.3 Detection Rates

To fulfil the prototype requirements controlled tests on the xenon detector were performed to determine the probability of detection and FAR for the three sources: ^{241}Am, ^{137}Cs and ^{60}Co. The setup in figure 9.5 shows the xenon detector placed at a variable distance away from the source fixed securely to a stand. The experiment was conducted in a large experimental hall to reduce the influence from wall interactions and

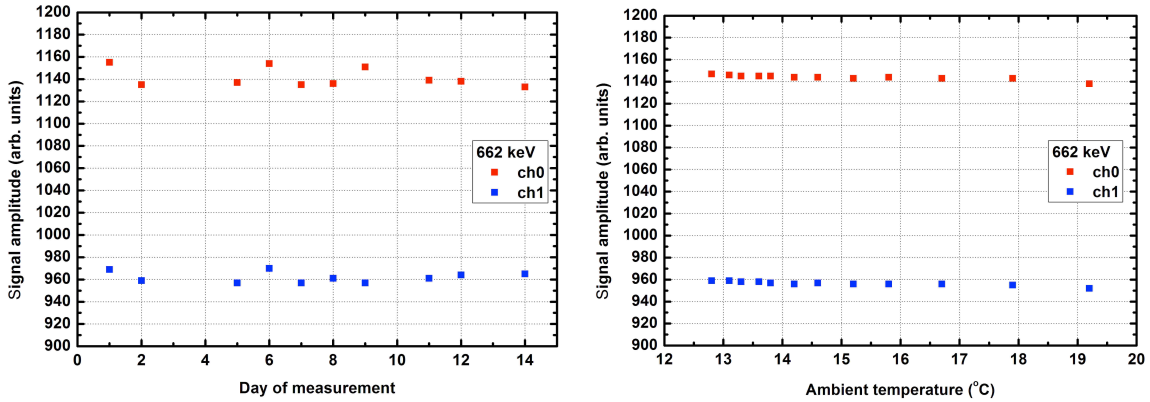

Fig. 9.4 The stability (left) and temperature dependance (right) and of the signal amplitude measured for a ^{137}Cs source for both PMTs of the xenon detector. Plot taken from [59].

the distance was varied to compensate for the variable strengths of the sources. The room temperature was measured between 20.3°C and 21.6°C with ∼35% humidity and pressure ∼100 kPa. The gamma radiation background was measured at ∼0.11μSv/h.

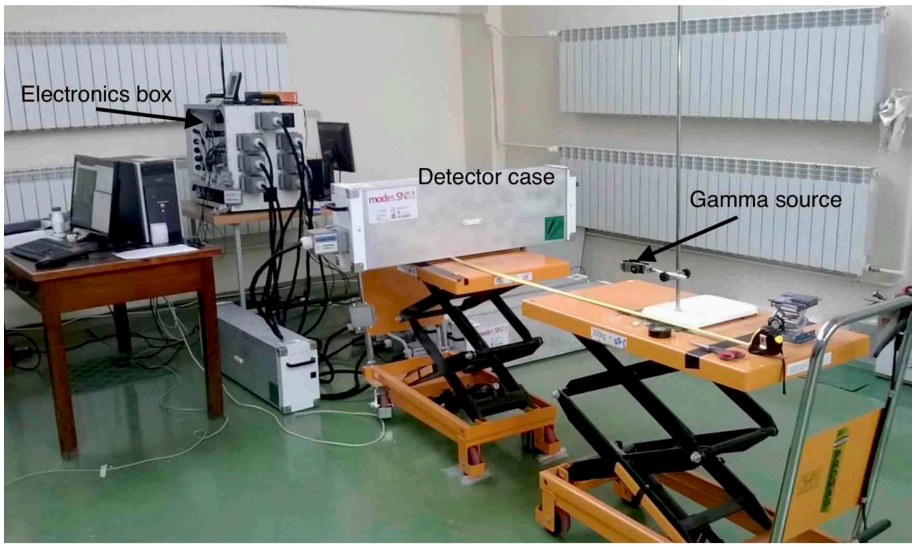

Fig. 9.5 The experimental setup for detection rate tests on the xenon detector. The source is fixed to the clamp stand facing the detector box. Plot taken from [59].

A total of 450 consecutive tests were conducted for each of the three sources, each with an exposure time of 2 seconds. All the tests yielded a 100% success rate, measuring a 97.6% probability of detection at 95% C.L [59]. The FAR did not exceed 1 per hour.

For source identification 9 sources were used: ^{137}Cs (662 keV), ^{60}Co (1.17 & 1.33 MeV),^{22}Na (511 keV & 1.28 MeV), ^{152}Eu (122, 245, 344, 779 keV & 1.41 MeV), ^{51}Cr (320 keV), ^{133}Ba (81, 276/303 & 356/384 keV), ^{57}Co (122 keV), ^{241}Am (59.6 keV) and ^{109}Cd (22 & 88 keV). The exposure times were increased to 60 second per identification and sources were adjusted by distance to provide 50 nSv/h dose rates at the detector. The experimental environment and apparatus was otherwise not altered. For sources with peak energies below 1 MeV, 60 s was an adequate exposure time with the system able to identify the source correctly in this time frame. However for energies above this threshold the detector efficiencies were too low to provide a successful identification for ^{60}Co, with nether peak shown in the spectra, shown in figure 9.6.

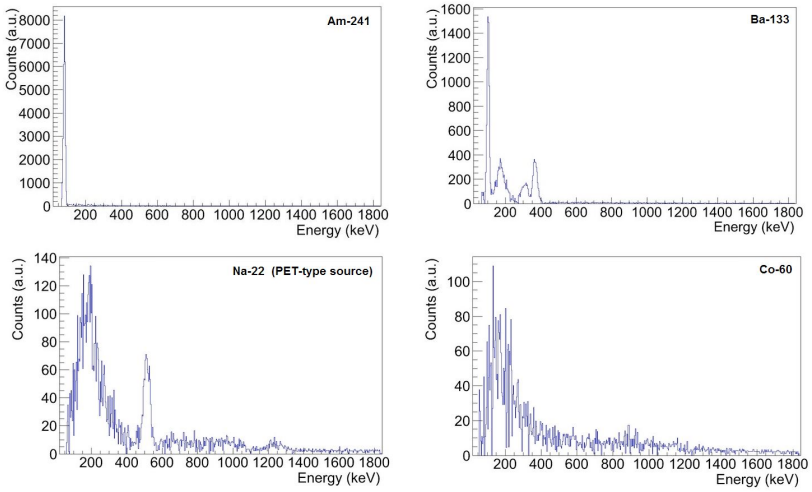

Fig. 9.6 The energy spectra measured with the channel 0 of the xenon detector for sources: ^{241}Am (upper left), ^{133}Ba (upper right), ^{22}Na (lower left) and ^{60}Co (lower right). The peaks can be noticed for all sources except the 1.28 MeV on ^{22}Na and both for ^{60}Co. Plot taken from [59].

9.1.2 Fast Neutron Detector Response

Good gamma rejection is an important property for the neutron detectors as this can be a cause for an increased false alarm rate. The neutron gamma discrimination is performed by use of the PSD value, equation 6.2, by comparing the difference between the long and short gate integrations with the pulse height, which is proportional to the long gate integration. Figure 9.7 shows the PSD value binned as a function of pulse height for a fast neutron detector exposed to a neutron/gamma source. Two clear

groups of events can be noticed, showing neutrons occupying the higher PSD region at a fairly constant value of 0.8, compared to the gammas with a more variable lower PSD value. The difference can be attributed to neutrons causing recoil of the ^{4}He nucleus and therefore very localised energy deposition compared to the electron recoil for gamma interactions which deposits less energy (tens of keV/cm). Studies have shown [94] that while the short gate integration (fast component) for both interactions is ∼120 mV for a typical event in ^{4}He, the slow scintillation component is ∼3-4 times larger for neutrons.

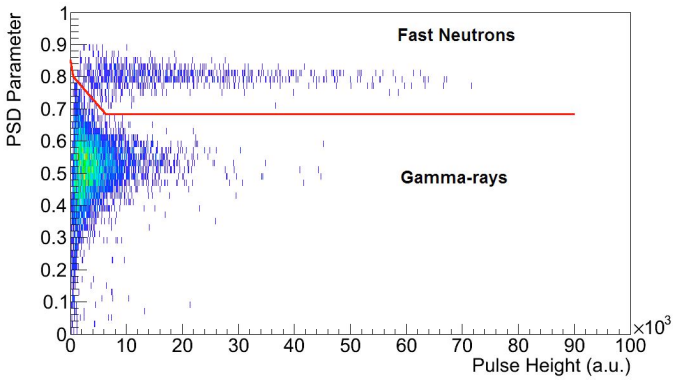

Fig. 9.7 The PSD value binned as a function of the pulse height (proportional to the total integrated charge) an event by event basis from events in the fast neutron detector from a neutron/gamma source. Both channels on the neutron detector are used. Plot taken from [59].

9.1.2.1 Detection Rates

To measure the probability of detection for the fast neutron detectors, each detector case (2 in each) was exposed to a ^{252}Cf source following the same method and setup as the xenon detector. The ^{252}Cf source of 570 kBq activity was placed at 2.28 m from the detector case to provide a 0.1 $ns^{-1}cm^{-2}$ at the detectors. Again 2 second exposures were used to keep the FAR below 1 per hour and 449 trials were conducted [59]. By summing the neutron events from each of the eight detectors the probability of detection reached 97.4% at 95% C.L, with 448/449 trials successful. It can be noted that with only half the detectors included a probability of detection of almost the required level (90% at 95% C.L) was reached with a probability of detection of 89.4% at 95% C.L [59]

9.1.3 Thermal Neutron Detector Response

Determination of thermal neutrons is performed by comparison of the fast and slow components of the scintillation light. These values are equivalent to the Q_{short} and Q_{long} - Q_{short} values respectively, which are determined from the integration gates. Figure 9.8 shows the 2-dimensional scatter plot binned by short and long scintillation components for events in the thermal neutron detector. The cuts shown are used within the MODES-SNM software to discriminate between fast neutrons, thermal neutrons and gammas within the thermal neutron detector. Optimisation studies within the collaboration have been performed to set these thresholds via exposure to intense neutron and gamma sources [59]. The separation between fast and thermal neutrons is set at 1100 a.u on the fast component and the separation between thermals and gammas is set 600 a.u on the slow component.

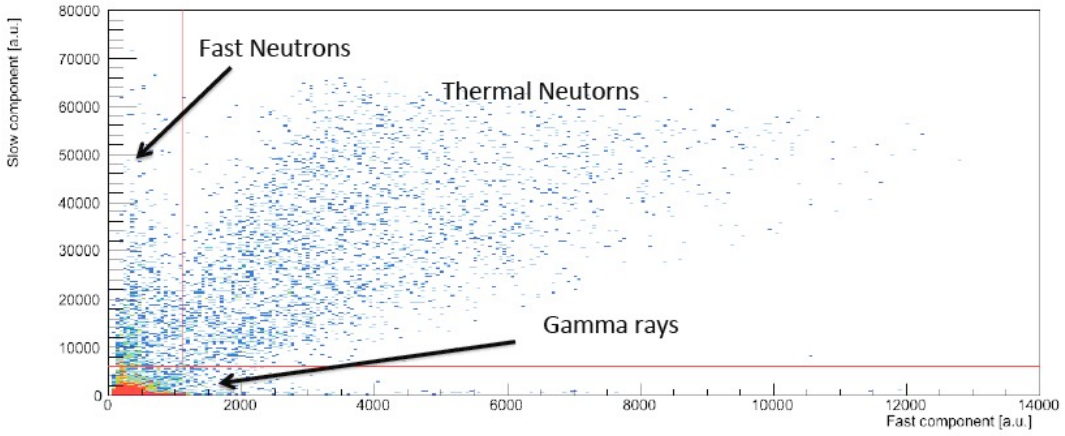

Fig. 9.8 A 2-dimensional plot for events in the thermal neutron detector binned according to each fast and slow component (Q_{short} and Q_{long} - Q_{short} respectively) of the scintillation light. Two thresholds are set, shown as red lines, in order to discriminate between fast and thermal neutrons (1100 a.u on the fast component) and between gammas and thermal neutrons (600 a.u on the slow component). Plot taken from [59].

Thermal neutrons are used within the MODES-SNM system to detect the presence of a hydrogen rich shield around the source. Fast neutrons will interact with polyethylene such that it is possible for 100% kinetic energy transfer per scatter, this can thermalise neutrons and increase their detection rate while reducing the fast neutron rate. A significant difference in fast/thermal neutron ratios can suggest a shielded source.

For the purpose of an experiment, polyethylene was used as a shield to surround the ^{252}Cf source. Blocks of the material were used to completely cover the source such that each face had 10 cm thick of polyethylene, except for the side facing the detector with only 5 cm thick polyethylene, as seen in figure 9.9.

Measurements of the fast and thermal neutron rates were made in 60 second exposures for with and without the shielding present. The distance between the front of the detector case and the centre of the source was kept at 40 cm for both the shielded and unshielded source.

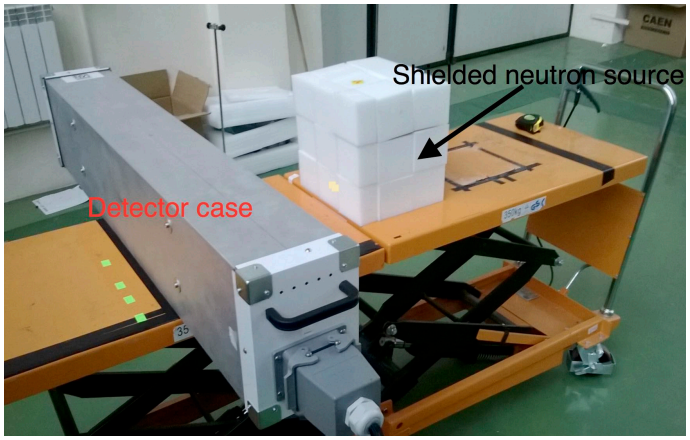

Fig. 9.9 The shielded ^{252}Cf source placed inside a polyethylene casing. Plot taken from [59].

It was observed that the thermal neutron area in the 2D slow-fast component plot was already quite heavily populated for the unshielded scenario. This heavy background can be attributed to neutron interactions with the detector casing and other apparatus. Taking the ratio of the counts in the populated areas, defined in figure 9.8, for fast and thermal neutrons as N_f and N_t respectively, we define the quantity $\alpha = N_t/N_f$. This value was determined as $\alpha_{unshielded} = (0.20 \pm 0.27)$ % for the unshielded case and $\alpha_{shielded} = (3.26 \pm 0.18)$ % for the shielded case. Using this quantity as the benchmark for whether a source is shielded a reasonable value of $\alpha > 0.5$ is used to establish this as true [59].

9.2 Initial System Review

The MODES-SNM system performed well in the initial tests by surpassing the requirements and showing good stability and reliability in a laboratory environment.

However it was obvious that the xenon detector efficiencies at higher energies would need to be improved as this would significantly impair on the system performance and source identification for spectra above 1 MeV. To resolve this issue an additional detector of different technology, a NaI detector, was used to replace the second xenon detector. This has been studied and characterised previously [59]. The dimensions of this detector are $12.5 \times 12.5 \times 25.0$ cm^3.

9.3 Neutron Gamma Discrimination

The rest of this chapter focuses on the data collected from the fast neutron detectors only and presents an analysis for neutron-gamma (n-γ) discrimination, proposed and implemented independently from the MODES-SNM collaboration. Due to this, the following analysis is not implemented in the MODES-SNM prototype system and forms a separate analysis to depict an alternative solution to the problem. It came to light that in the field tests the false alarm rate was quite high and although increasing the threshold is a possible solution, it would decrease sensitivity to radioactive material. The existing discrimination techniques only apply per channel and as a result a fluctuation in one isolated channel will trigger a false alarm whereas a further improvement would be to examine all channels when performing the discrimination. The analysis presented here uses a similar technique to that implemented in the prototype, using a Pulse Shape Discrimination (PSD) technique, but is employed in such a way to make use of all channel data when discriminating between neutrons and gammas. This then aims to improve the n-γ discrimination and reduce the false alarm rate that was observed in the field tests.

It is important to discriminate between neutron and gamma events to maximise neutron detection efficiency and reduce the false alarm rate. In this chapter we examine how to discriminate between the two particles using both the fast and slow components of the scintillation light. We have shown that the neutron detectors meet the requirements when a strong neutron source, such as ^{252}Cf is used, but when gamma sources are used these can trigger a neutron alarm. To combat this issue we use known sources of PuBe, ^{137}Cs and ^{60}Co to show the discrimination potential of the fast neutron detectors following various selection procedures. The latter two sources being gamma emitters and PuBe being a strong neutron source.

To motivate the need for particle discrimination a single channel on one neutron detector is used, ignoring the 7 other detectors. Data was collected in a laboratory

environment, as previously described earlier in the chapter. However the detectors operating parameters can vary over time, including pressure, temperature and voltages across the PMTs. Both temperature and pressure have an effect on the density of the gas and hence the cross section, which would yield inconsistent event rates. To overcome this dependancy the collected data is normalised to the total number of events collected. Furthermore this also makes the data independent of the source activities. The voltages across the PMTs though do have direct impact on both Q_{long} and Q_{short} values, as it directly affects the charge amplification and charge readout. However the results made available from the tests in Poland were limited and resulted in a severely restricted data set which could be used for the analysis. With limited information on all operating parameters, including voltages, it was not possible to investigate the effect of the voltages on the discrimination power. To overcome this restriction, the processes and algorithms used in this discrimination analysis are designed such that any conclusions and results drawn are to be independent of the operating parameters.

9.3.1 Energy Spectra

Comparing the energy spectra of the sources measured on the fast neutron detector shows little discrimination between the gamma sources but PuBe is notably different from the gamma sources. Figure 9.10 shows the Q_{long} value recorded in the fast neutron detector, normalised to the number of events measured in a given time interval. The data collection period of 300 s is chosen to accumulate enough events to reduce statistical errors, at least (1×10^6 events) for each source. The notable difference between the neutron and gamma sources is clear but shows a large overlap in the spectra at the low energy region, at $\sim$1000 ADC counts. To increase the separation we examine the PSD value of each event.

9.3.2 Pulse Shape Discrimination

Pulse Shape Discrimination (PSD) methods are an established technique employed by scintillation fast neutron detectors when needing to discriminate against γ-ray backgrounds. With that very much the case in MODES-SNM it is used as the main method of discrimination between fast neutrons and gammas. If we examine the signal signature of both a neutron and gamma event read by each PMT we can notice clear differences between them, as shown in figure 9.11. For a neutron event the energy deposition occurring from the recoiling nucleus within the gas is spread over a larger

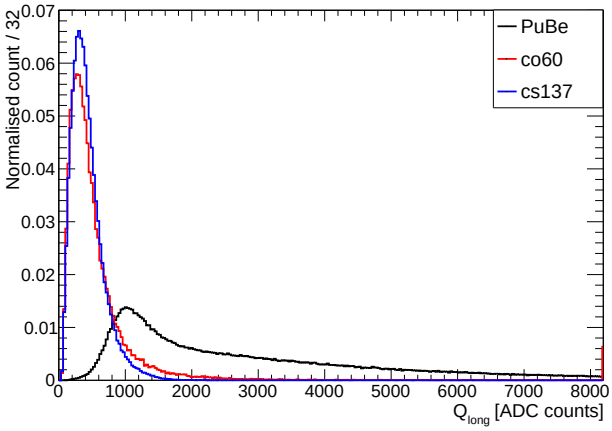

Fig. 9.10 The total integrated charge measured, Q_{long}, on channel 0 of one of the fast neutron detectors. Each source is normalised to the number of events recorded - 124148 PuBe events, 589223 ^{60}Co events and 239418 ^{137}Cs events. The data used is that corresponding to one channel on one of the fast neutron detectors.

time period ($\sim$1.4-2.0μs) with narrow peaks of charge collection (spikes). Contrary to this the gamma event is typically shorter in its energy deposition ($\sim$0.2-0.4μs). Thus the PSD value, governed by the difference in the charge collected between the short and long gates, is notably different for each particle.

Using the PSD value the separation between neutron and gamma sources becomes much more apparent than just comparing their spectra, as seen in figure 9.12. The neutron source has a narrow distribution centred around a high PSD value, at $\sim$0.76, whereas the gamma sources have a broader distribution centred at a lower PSD value of $\sim$0.55. Again each distribution has been normalised to the number of total entries within the data collection period of 300 s. Although the n-γ separation is clearer using the PSD value compared to their spectra, there still remains a large area of overlap. To quantify this we introduce the efficiencies, purities and figure of merits to optimise a selection criteria for discriminating between the two particles.

9.3.2.1 Discrimination Optimisation

Defining the neutron detection efficiency, ϵ, as equation 9.1 we impose a selection on the collected events based on the PSD value to optimise the discrimination. Here n_i corresponds to the number of entries in the i^{th} bin. A bin width of 0.01 is taken as this provides good granularity while assuring at least one event per bin. Labelling the

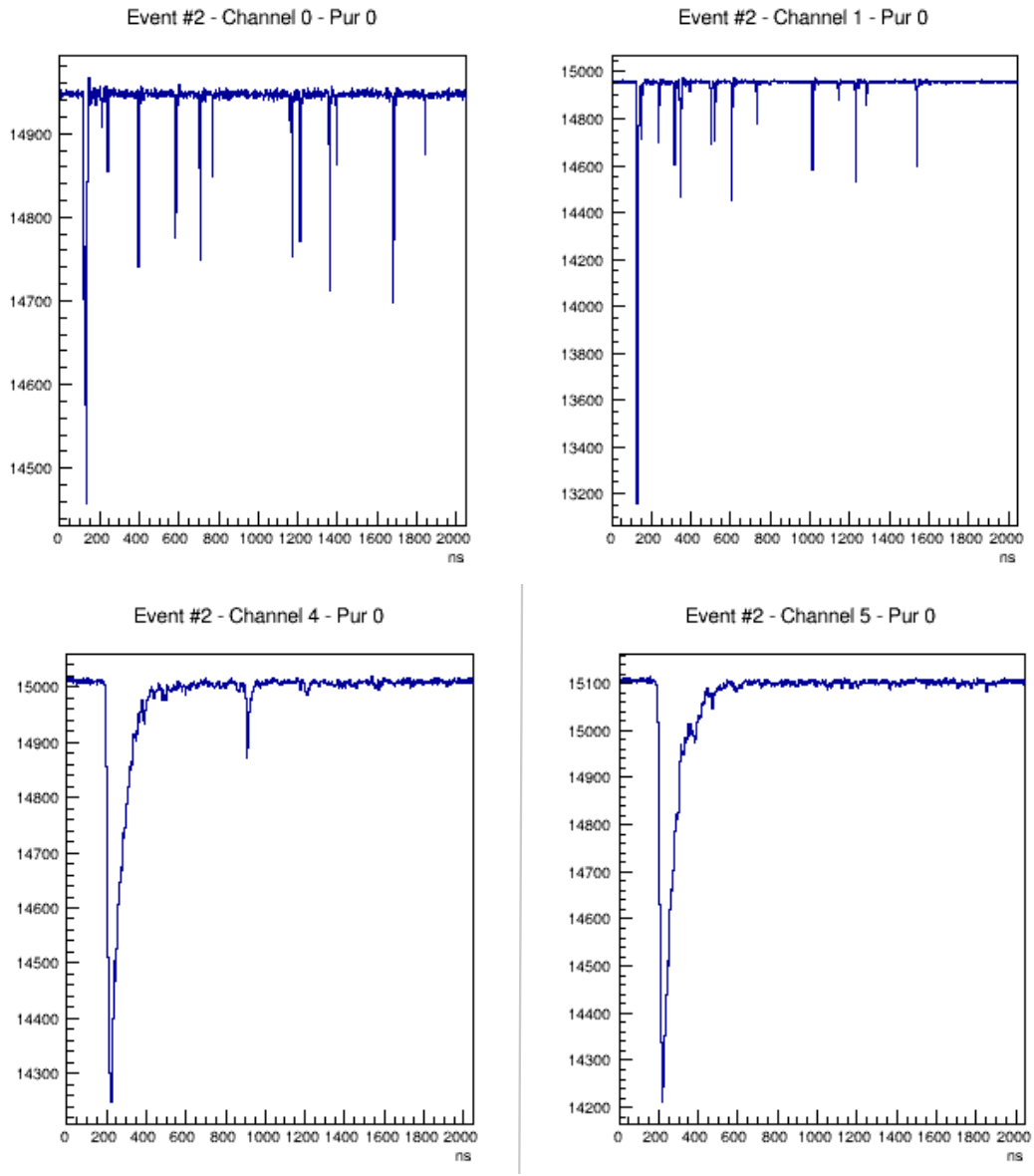

Fig. 9.11 Top: A neutron event recorded by one detector showing the charge as a function of time collected by both detector channels. Bottom: A gamma event recorded by one detector showing the charge as a function of time collected by both detector channels. Figure taken from [59].

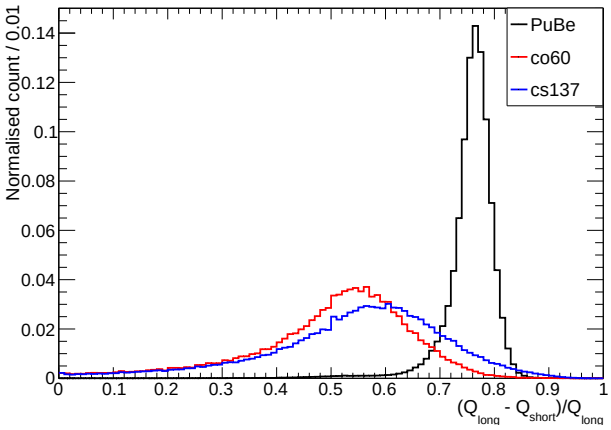

Fig. 9.12 The PSD value measured on one channel of one of the fast neutron detectors. Each source is normalised to the number of events recorded - 124148 PuBe events, 589223 ^{60}Co events and 239418 ^{137}Cs events. The data used is that corresponding to one channel on one of the fast neutron detectors.

first bin as 0 includes all binned entries, indicating an efficiency equal to unity, and the final bin as 99 represents the last bin. In this manner the efficiency of the j^{th} bin is determined as a function of the selection, such that j=0,1,2,..N=99.

$$\epsilon_j = \frac{n_j}{n_0} = \frac{\sum_{i=j}^{N} n_i}{\sum_{i=0}^{N} n_i} \tag{9.1}$$

The uncertainty associated with ϵ_j is determined using standard binomial treatment of which the uncertainty of the j^{th} bin is given by equation 9.2.

$$\Delta\epsilon_j = \sqrt{\frac{\epsilon_j(1-\epsilon_j)}{n_0}} \tag{9.2}$$

In a similar fashion we define the purity, η, by comparing a signal distribution to a background distribution, in this case a neutron source against a gamma source. The purity of the j^{th} bin is then defined by equation 9.3, with n_i representing the number of signal entries in the i^{th} bin and l_i representing the number of background entries in the i^{th} bin. This analysis aims to provide discrimination between neutron and gammas based solely on distribution shape and no information on the source is used other than if it is a neutron or gamma source. Scale factors of α_s and α_b represent the inverse of the total number of events in the detector due to signal (PuBe) and background (^{137}Cs or ^{60}Co) events. From this definition we can define the purity in terms of their

efficiencies, ϵ^s and ϵ^b, for signal and background respectively.

$$\eta_j = \frac{\alpha_s \sum_{i=j}^{N} n_i}{\left(\alpha_s \sum_{i=j}^{N} n_i + \alpha_b \sum_{i=j}^{N} l_i\right)} = \frac{\epsilon_j^s}{\left(\epsilon_j^s + \epsilon_j^b\right)} \tag{9.3}$$

The uncertainty associated with η_j follows from the combination of binomial errors from the signal and background efficiencies, given by equation 9.4. In limiting cases this can lead to an incorrect treatment of the uncertainties and can provide non physical results. Due to this we impose $0 < \Delta\eta_j < 1$ and that $\epsilon_j^s > 0$.

$$\Delta\eta_j = \frac{\eta_j^2}{\epsilon_j^s}\sqrt{\left(\frac{\epsilon_j^b}{\epsilon_j^s}\right)^2 (\Delta\epsilon_j^s)^2 + (\Delta\epsilon_j^b)^2} \tag{9.4}$$

The product of these two parameters, $\lambda = \eta\epsilon$, is then a good indication of the optimal selection criteria and is used as the figure of merit. Figure 9.13 shows the comparison of the efficiencies and purities for the neutron source compared with a background gamma source of either ^{137}Cs or ^{60}Co. Their figure of merit is also overlaid onto the same plots.

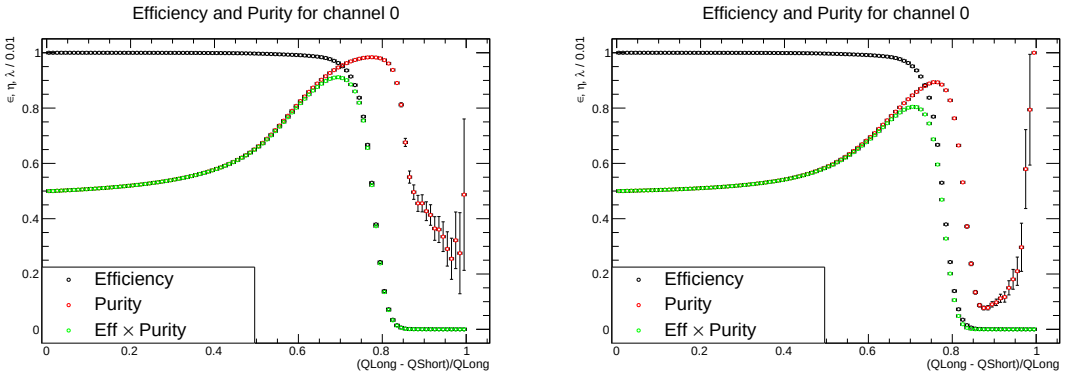

Fig. 9.13 The efficiencies, purities and figure of merits comparing the neutron source with the gamma sources, PuBe-^{60}Co (left) and PuBe-^{137}Cs (right). The data used is that corresponding to channel 0 on one of the fast neutron detectors.

The highest figure of merit values for each of the two plots can be seen in table 9.1. Both comparisons showed fairly consistent values for the optimal selection value, at 0.695 ± 0.005 and 0.705 ± 0.005. However the figure of merit values are relatively different with PuBe/^{60}Co at $\lambda_{max} = 0.9118 \pm 0.0006$ and PuBe/^{60}Co at $\lambda_{max} = 0.8046 \pm 0.0007$. This is due to the larger tail in the ^{137}Cs distribution which could be due to the lower energy photons having a smaller slow scintillation component. For the

MODES system to be able to discriminate between neutrons and gammas at a level to match the system requirements, these values need to be vastly improved.

Source	Background	λ_{max}	Best PSD cut value
PuBe	^{60}Co	0.9118 ± 0.0006	0.695 ± 0.005
PuBe	^{137}Cs	0.8046 ± 0.0007	0.705 ± 0.005

Table 9.1 A table showing the best cut on the PSD value to yield the highest figure of merit, λ_{max}, for PuBe against each of the two gamma sources.

9.3.2.2 Multiple Channels

Up until now we have examined only a single channel on one of the fast neutron detectors, using a long data capture time window of 300 seconds. However in reality such a time window would be unachievable and far lower times are to be expected, ∼2 seconds. Therefore it is beneficial to combine data collected from multiple detectors to increase statistics while also achieving a larger coverage area. This can be useful if the source is partially shielded or directed differently.

For the MODES-SNM system prototype 8 fast neutron detectors are to be used, however at the time of testing only 4 detectors were available for data collection, totalling to 8 channels. If we examine the raw data collected for the PuBe and ^{60}Co sources it can be noticed that there is a large variation between each channel in both amount of events collected and distribution shape. Figures 9.14 and 9.15 show the long and short components of the integrated charge collected at each channel with the neutron source in black and the gamma source in red. Again the distributions have been normalised to the number of events collected. No restrictions or selections are imposed on the collected events with the figures showing only raw data. Each two consecutive channels (0&1, 2&3, 4&5, 6&7) represent one detector.

The largest difference in events can be seen between detectors 1 and 3, channels 0&1 and 4&5 respectively, for the neutron source with the latter recording ∼2.5 times less events. For the gamma source the difference is much larger but detectors 1 and 3 having considerable more events than detectors 2 and 4, a factor of ∼85 between detectors 2 and 3. In both cases this is most likely due to the placement of the source with respect to the arrangement of the detector arrays. As detectors 1 and 2 are housed in the same box (box 1), as are detectors 3 and 4 (box 2), when the data was collected for the neutron source, box 1 was most likely placed closer to the neutron source with box 2 directly behind box 1. This would then explain why the events

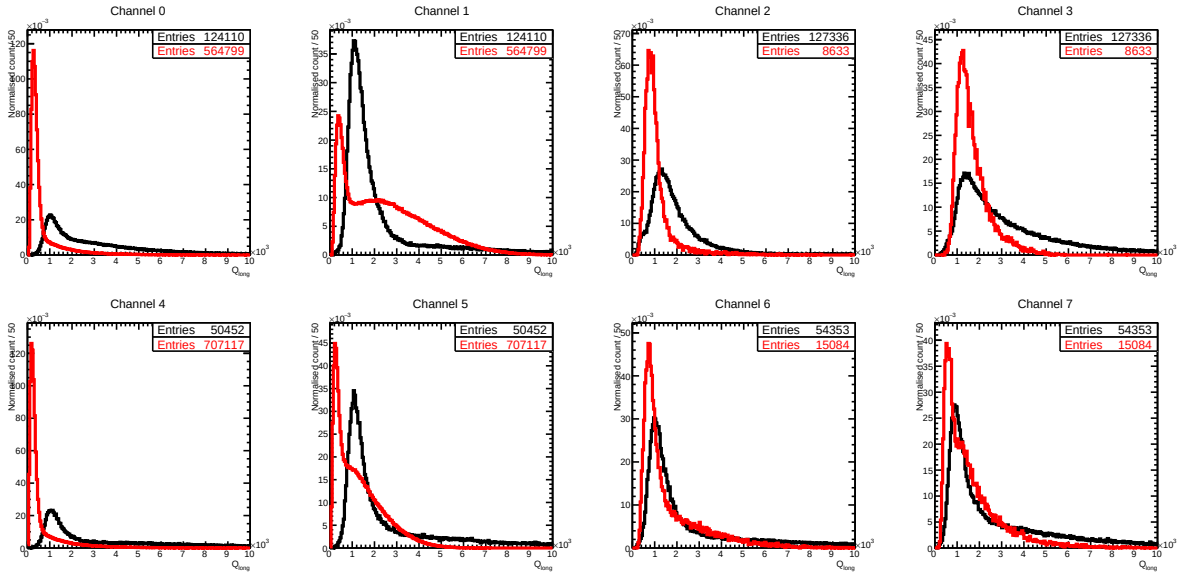

Fig. 9.14 The total integrated charge measured, Q_{long}, on 4 fast neutron detectors (8 channels) for a PuBe neutron source (black line) and a ^{60}Co gamma source (red line). Each source is normalised to the number of events recorded in that channel and no restrictions or selections are imposed on the collected events.

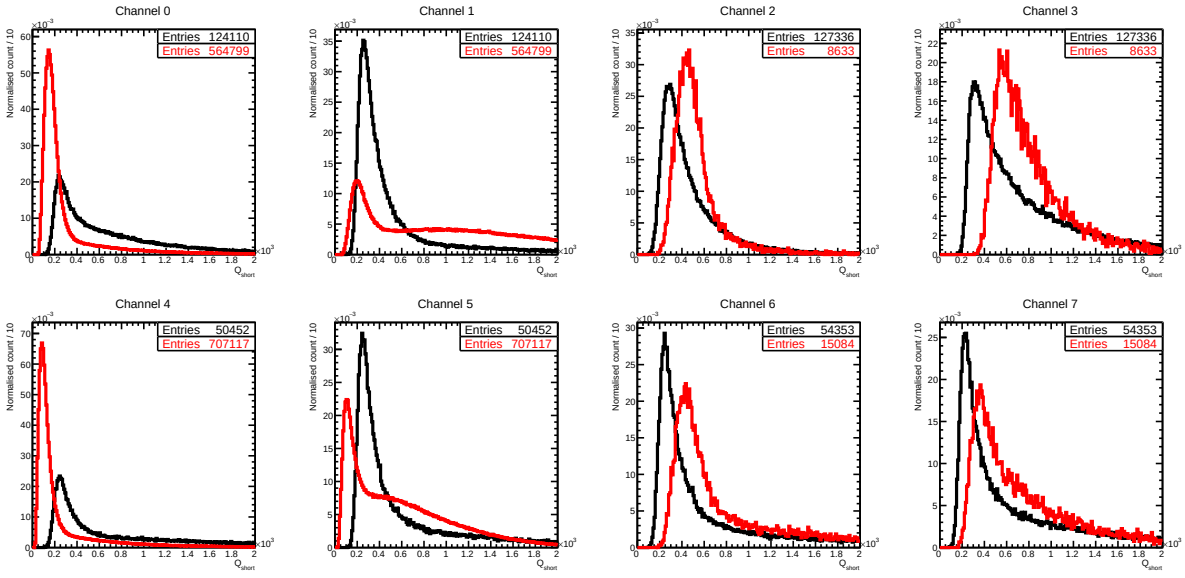

Fig. 9.15 The integrated charge measured in the short gate, Q_{short}, on 4 fast neutron detectors (8 channels) for a PuBe neutron source (black line) and a ^{60}Co gamma source (red line). Each source is normalised to the number of events recorded in that channel and no restrictions or selections are imposed on the collected events.

are similar across detectors 1 and 2 and detectors 3 and 4. However the setup for the gamma data collection is likely to have differed such that the boxes were placed together with the source placed on top of both boxes. This would then shield the lower detectors and heavily reduce the gamma events incident on the lower detectors. The arrangement of the detector boxes in the prototype system would need to optimise the positions such that large coverage can be achieved while maintaining high statistics for both neutrons and gammas. For the purpose of this analysis, the difference in the number of events across detectors is not an issue as each channel is normalised to the number of events per channel. However imposing the same number of events per detector should be included to reduce detector noise.

The variation in the distributions across the channels is most noticeable between channels 0 and 1, for both long and short components. Both of these channels represent the same detector yet channel 1 has a large amount of noise, showing a second peak at higher charge.

Examining the PSD values removes the noise and shows a stronger correlation between the distributions, as can be seen in figure 9.16. Each distribution follows a similar shape for both neutrons and gammas and a Gaussian peak is fitted to each channel PSD distribution. By fitting a Gaussian function to within 70% of the peak value using a χ^2 $/n.d.f$ best fit allows each channel to be quantified. The fit parameters are shown in the figure and are summarised in table 9.2. The requirement of having the same number of events in a single detector tube, is also enforced in the PSD distributions.

	Mean value ($\bar{\mathbf{x}}$)		**Sigma value** (σ)	
Channel	**PuBe**	**^{60}Co**	**PuBe**	**^{60}Co**
0	0.7626 ± 0.0002	0.5276 ± 0.0004	0.0228 ± 0.0003	0.0915 ± 0.0008
1	0.7556 ± 0.0002	0.5304 ± 0.0002	0.0258 ± 0.0003	0.0492 ± 0.0003
2	0.7553 ± 0.0002	0.4760 ± 0.0030	0.0320 ± 0.0004	0.1000 ± 0.0080
3	0.7650 ± 0.0001	0.5150 ± 0.0020	0.0220 ± 0.0003	0.0490 ± 0.0030
4	0.7657 ± 0.0002	0.5566 ± 0.0003	0.0202 ± 0.0003	0.0921 ± 0.0007
5	0.7650 ± 0.0002	0.5402 ± 0.0002	0.0216 ± 0.0004	0.0593 ± 0.0004
6	0.7500 ± 0.0003	0.4880 ± 0.0020	0.0236 ± 0.0006	0.0710 ± 0.0040
7	0.7477 ± 0.0003	0.4900 ± 0.0020	0.0250 ± 0.0005	0.0590 ± 0.0040

Table 9.2 A table showing the parameters and their uncertainties of the Gaussian function fitted to the peak value on the PSD distribution for PuBe and ^{60}Co sources.

From examination of the mean values presented in table 9.2 it is apparent that the values are not consistent with each other when using the fit errors. The mean

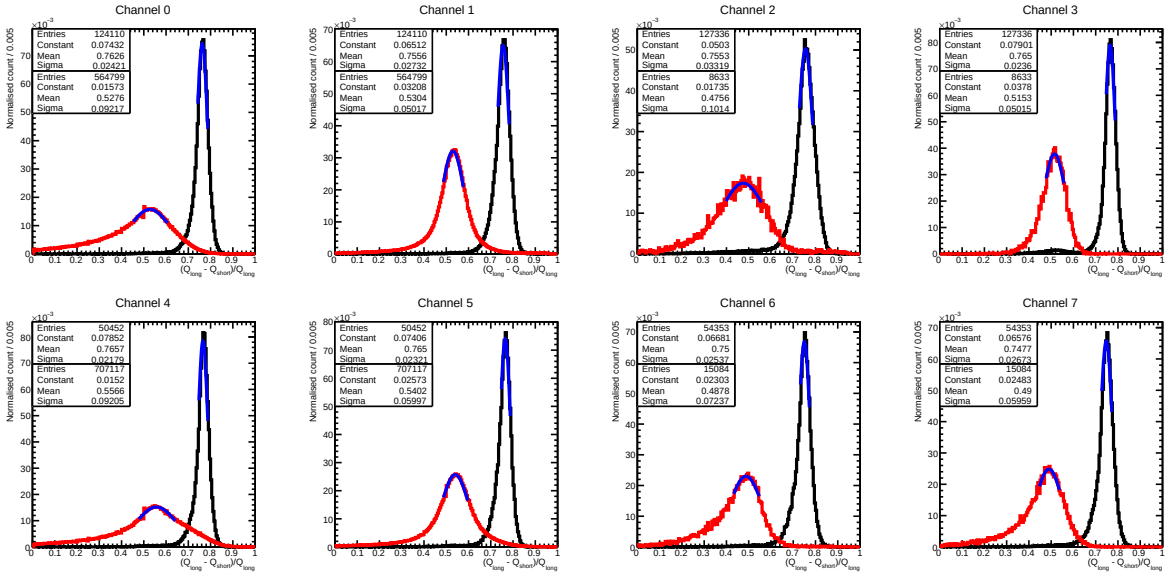

Fig. 9.16 The PSD distributions measured on 4 fast neutron detectors (8 channels) for a PuBe neutron source (black) and a ^{60}Co gamma source (red). Each source is normalised to the number of events recorded in that channel and is fitted with a Gaussian distribution on the PSD peak value.

values across the channels are 0.758 and 0.51 for PuBe and ^{60}Co respectively. By taking the variance of this mean value, $\bar{x_0}$, across the 8 channels yields a considerable difference between the two sources, 0.007 and 0.03 for PuBe and ^{60}Co respectively. When examining the channels within the same detector the mean PSD values differ less, suggesting that the differences occur due to the detector properties (pressure differences of the gas), playing a larger factor than variance in PMT properties, such as voltage. The uncertainties associated with the fit values represent that of the fit alone and their low values highlight how well the fit represent the peaks. If the standard deviation, σ, values from the Gaussian fits are used to represent the uncertainty of the means then it is clear the results are fairly consistent, as shown in figure 9.17.

To achieve an analysis that uses data collected from all/multiple channels, it is best to treat each channel/detector independently when optimising the selection for n-γ discrimination. This can be seen in figure 9.18 which shows the efficiencies, purities and figure of merits varying for each channel also. Establishing a n-γ selection on a channel by channel basis we can then identify the particle and combination of the rates can occur after selection. Due to non-linear effects it is not possible to calibrate each channel by shifting channel peaks to a common value without greater understanding

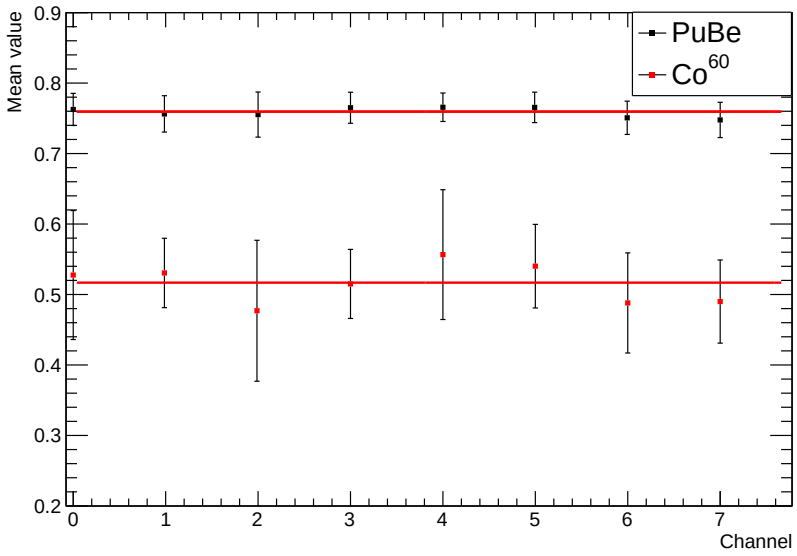

Fig. 9.17 The mean values obtained from the Gaussian fit to the peak of the PSD distributions for each channel. The error bars represent $\pm$ 1σ values from the fit. The red lines indicate the best fit value over all channels, 0.759 $\pm$ 0.008 and 0.52 $\pm$ 0.02 for PuBe and ^{60}Co respectively.

and information on the detector conditions, the data acquired is insufficient. The best figure of merits values are shown in table 9.3 along with their associated PSD selection values.

9.3.2.3 Improving the Selection

Examining the maximum figure of merit values, λ_{max}, from table 9.3 there is large variation between the channels with the lowest value at 0.8327 $\pm$ 0.0009 and the highest value reaching 0.9550 $\pm$ 0.0010. With the figure of merit a strong indicator of detection efficiency and purity, even at this highest value the efficiencies would be far below the limit imposed on the detector requirements. We propose to improve the figure of merit and hence the efficiencies for each channel via a method of sampling the collected data and measuring the PSD mean within the sample. Using the mean PSD value should then provide a more accurate PSD distribution for both neutrons and gamma sources which can then be used to establish a higher figure of merit. The algorithm can be summarised as the following:

1. Select an appropriate average sample size - $\bar{n}$

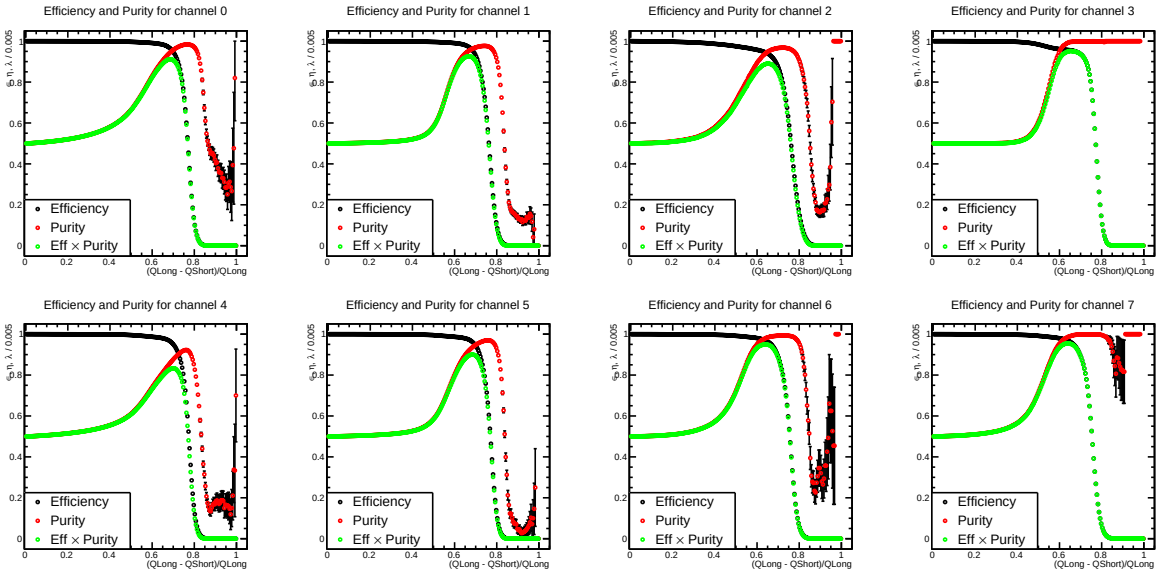

Fig. 9.18 The efficiencies, purities and figure of merits comparing a neutron source, PuBe, with gamma source ^{60}Co, for 8 channels across 4 fast neutron detectors.

2. Get the number of events from the channel with the lowest number - m_{min}
3. Establish the total number of experiments such that all channels have the same number of experiments - $N_{exp} = m_{min}/\bar{n}$
4. Establish a value for the sample size for each experiment based on the mean value from a Poisson distribution - n
5. From the full data set of the channel take n random events
6. Require the same sample size for both channels in the detector tube
7. Calculate the mean of the PSD values for the channel
8. Fill the mean PSD value in the appropriate bin in the histogram
9. Increase the number of experiments performed
10. Take a new sample - go to step 4
11. Repeat until N_{exp} is reached per channel
12. Optimise n-γ PSD selection based on maximising the figure of merit value

Channel	**Highest figure of merit value** ($\lambda_{\mathbf{max}}$)	**PSD Selection value**
0	0.9117 ± 0.0006	0.695 ± 0.005
1	0.9260 ± 0.0006	0.675 ± 0.005
2	0.8910 ± 0.0020	0.655 ± 0.005
3	0.9514 ± 0.0009	0.655 ± 0.005
4	0.8327 ± 0.0009	0.705 ± 0.005
5	0.8999 ± 0.0009	0.695 ± 0.005
6	0.9500 ± 0.0010	0.645 ± 0.005
7	0.9550 ± 0.0010	0.645 ± 0.005

Table 9.3 A table showing the highest achieved figure of merit values, λ_{max}, when optimising the PSD selection on a channel basis.

Taking an initial sample size of 100 events, results in a total of 80 experiments given the data samples for all channels and sources. Performing the analysis steps discussed above results in figure of merits of unity for all channels, with the PSD distributions shown in figure 9.19 and the efficiencies, purities and figure of merits shown in figure 9.20. However such a sample size would be unrealistic in real life deployment where much lower statistics are expected. To study the effect of the sample size on the PSD distributions and hence the figure of merit values, samples were reduced to sizes of 10, 8, 6, 4 and 2 events. The choice of these sizes were taken as λ_{max} only began to drop below unity when the mean sample size dropped below 12 events The best figure of merit values can be seen in figure 9.21 for each channel and for each of the different sample sizes.

There is considerable variation between the figure of merit values over the channels at lower sample sizes with channel 4 reaching the lowest value at 0.906 ± 0.005. At this low sample size no channels figure of merit exceeded 0.98 but at the larger sample sizes of 8 and 10 the figure of merit is much improved with values exceeding 0.994 and with many channels at $\lambda_{max} = 1$. Although the figure of merit takes both the efficiency and purity into account, such that the optimal PSD selection can be determined, the efficiency is the important parameter for particle discrimination. Taking the efficiencies at the optimal PSD selection, $\epsilon^{optimal}$, for each channel can then be used to define the total n-γ discrimination efficiency for the 4 fast neutrons detectors combined. This will provide an insight to the expected efficiency of the full MODES-SNM system and hence we can determine if the false alarm rate is below the acceptable level. Simply, the n-γ discrimination efficiency, ϵ_{tot}, can be described by equation 9.5. This then describes the number of neutrons that pass the cut, i.e. the number of neutrons that

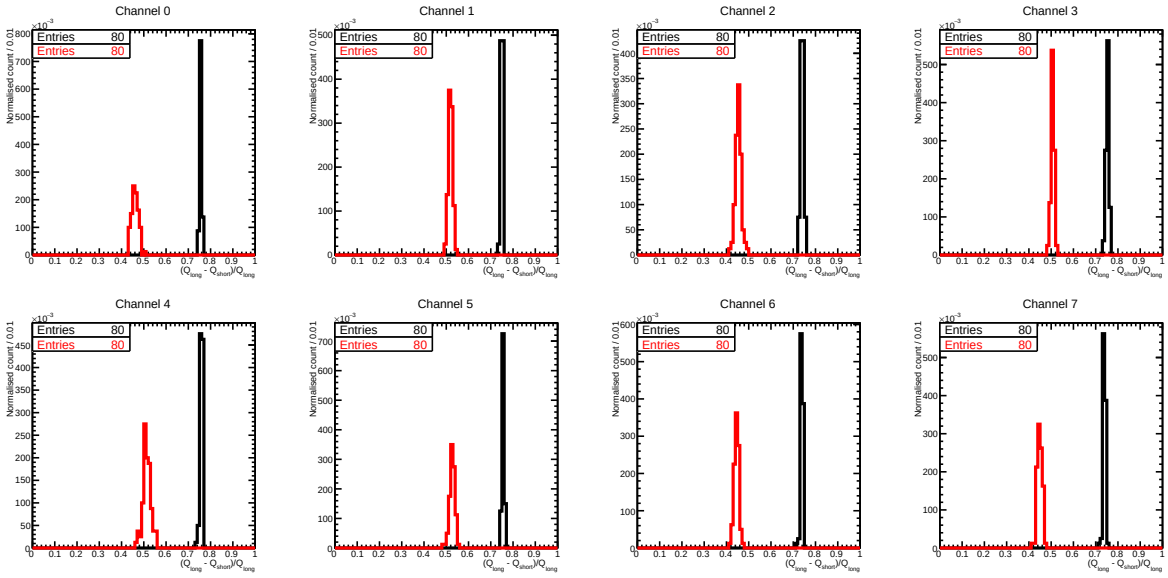

Fig. 9.19 The mean PSD values binned in a histogram for a neutron source, PuBe (black), and a gamma source ^{60}Co (red), for 8 channels across 4 fast neutron detectors. A sample size of 100 events were used with a total of 80 experiments performed over the data set.

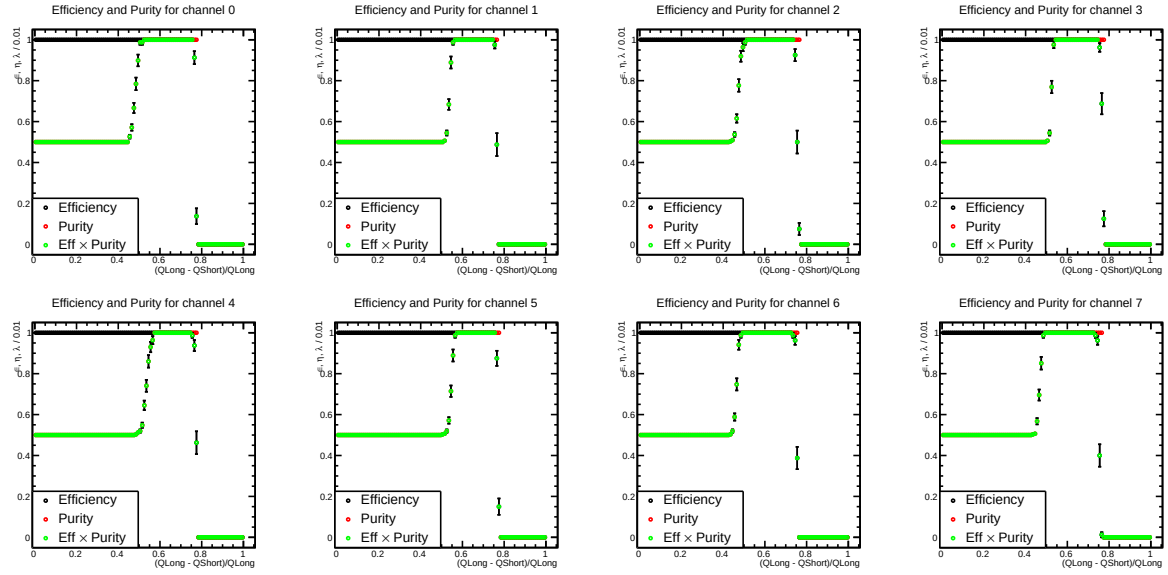

Fig. 9.20 The efficiencies, purities and figure of merits based on the mean PSD values for a sample size of 100 events with 80 experiments performed. The comparison is between a neutron source, PuBe, and a gamma source ^{60}Co, for 8 channels across 4 fast neutron detectors.

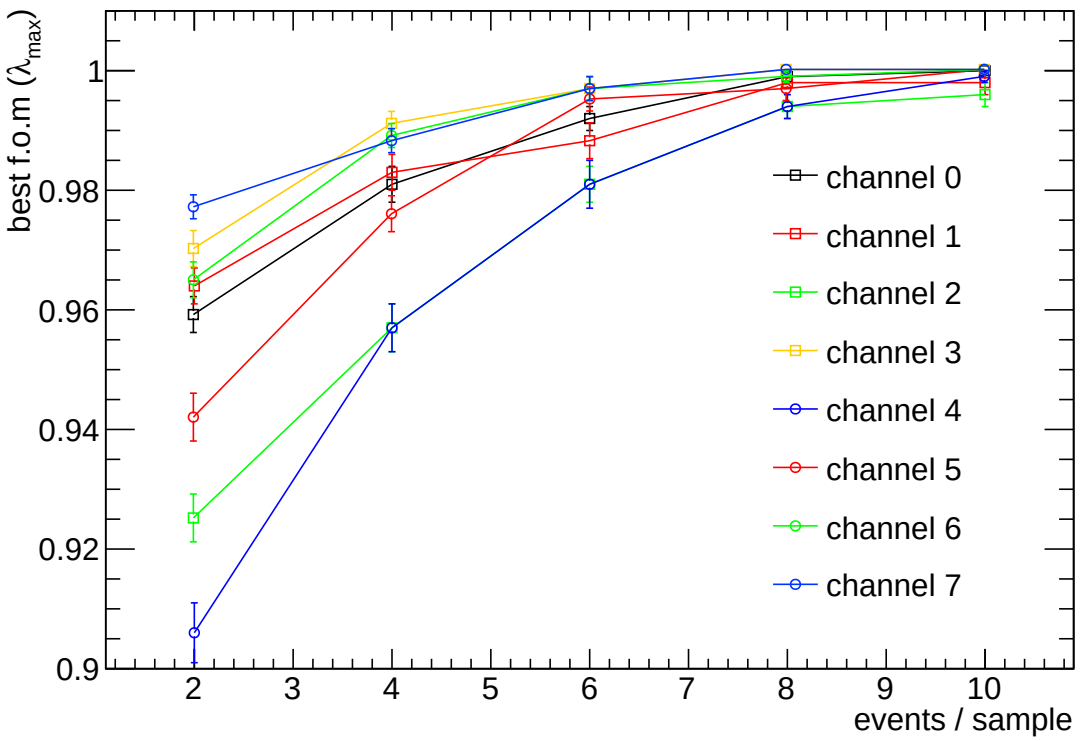

Fig. 9.21 The highest figure of merit values achieved, λ_{max}, when optimising the PSD selection on a channel basis. The values are shown for mean sample sizes of 10, 8, 6, 4 and 2 events, for all 8 channels. The number of experiments varied for each event sample size, with 3734, 2113, 1431, 1075 and 857 experiments for mean sample sizes of 2, 4, 6, 8 and 10 respectively.

are detected as neutrons, for all channels combined. Since the number of experiments are used, denoted by N_i, is fixed for all channels and only varies depending on the sample size, ϵ_{tot} is simply equal to the average value across the channels. These values are shown for each mean sample size in table 9.4.

$$\epsilon_{tot} = \frac{\sum_{i=0}^{ch=7} N_i \epsilon_i^{optimal}}{\sum_{i=0}^{ch=7} N_i} = \frac{1}{8} \sum_{i=0}^{ch=7} \epsilon_i^{optimal} \tag{9.5}$$

Combined channel neutron detection efficiency				
10 events	**8 events**	**6 events**	**4 events**	**2 events**
857 exp	**1099 exp**	**1431 exp**	**2113 exp**	**3734 exp**
0.9996 ± 0.0017	0.9980 ± 0.0036	0.9961 ± 0.0049	0.9891 ± 0.0064	0.9737 ± 0.0076

Table 9.4 A table showing the neutron detection efficiencies for 4 fast neutron detectors, combining all 8 channels. The efficiency values are shown for mean sample sizes of 10, 8, 6, 4 and 2 events, along with their corresponding number of experiments.

For all event sample sizes, we exceed the requirement of 96/100 neutron detection efficiency, with 10 mean events/sample reaching an efficiency of 0.9996 ± 0.0017 and 0.9737 ± 0.0076 for just 2 mean events/sample.

Similarly for misidentification alarms, we examine the number of γ's that pass that selection, that is photons that are detected as neutrons. This is again determined in a similar fashion using equation 9.5 but now the efficiencies relate to γ's that have a psd larger than the optimal selection, where 0 efficiency represents a 0 misidentification rate. Table 9.5 shows these rates. These values do not translate directly to false alarms, as a false alarm by definition is an alarm raised without explanation, that is when no source is present and the detectors are in a stable background. To translate these numbers to produce a estimate of the fast neutron detector false alarm rate we must first estimate an upper bound for the gamma background.

Combined channel gamma misidentification efficiency				
10 events	**8 events**	**6 events**	**4 events**	**2 events**
857 exp	**1099 exp**	**1431 exp**	**2113 exp**	**3734 exp**
0.0013 ± 0.0025	0.0022 ± 0.0034	0.0044 ± 0.0053	0.0120 ± 0.0110	0.0240 ± 0.0099

Table 9.5 A table showing the gamma misidentification detection efficiencies for 4 fast neutron detectors, combining all 8 channels. The efficiency values are shown for mean sample sizes of 10, 8, 6, 4 and 2 events, along with their corresponding number of experiments.

Due to the requirements set on the gamma detectors, a ^{60}Co source of activity of C = 160 kBq should be placed at a distance of $r = 1$ m. Using this activity as the upper limit for an expected gamma background it can then be translated to an expected number of events across all 8 fast neutron detectors. In a $T = 2$ second window, using equation 9.6 and detector parameters from table 6.2, yields ∼87 gamma events. Note that a factor of two is used as ^{60}Co produces 2 outgoing photons per disintegration (>99% of the time) and the cross section on He^4, $\sigma_{\gamma \to He}$, is taken as a constant value of 0.01 m^{2}kg^{-1}, which is roughly valid between 0.1 to 1 MeV.

$$N_{events} = \frac{8C\sigma_{\gamma \to He}\rho V_0 T}{4\pi r^2} \tag{9.6}$$

At this level of statistics, an average sample size of $\bar{n} = 100$ would be unfeasible but $\bar{n} = 10$ would, in this time frame to provide a enough experiments to perform the discrimination. However this would lead to a total of ∼20 false alarms per hour on average, much higher than permitted by the requirements. Given that λ_{max} for mean sample sizes of ∼12 and above yield maximal efficiency and zero misidentification alarms for ^{60}Co against PuBe, would provide remove all false alarms. To achieve mean samples sizes of 12, then we require at least 96 events across the 8 fast neutron detectors, which can be achieved in 3 s exposure.

9.3.2.4 Using the ^{137}Cs Gamma Source

Following the same procedure using a ^{137}Cs gamma source requires larger mean sample sizes, $\bar{n} \geq 50$, to reach optimal λ_{max} values across all channels. However the requirements for a ^{137}Cs demand a larger activity of 660 kBq, 4.125 times larger than ^{60}Co. At this activity this number of events can be achieved within a 3 s exposure at 1 m distance.

9.3.2.5 Contamination Levels

To emulate a real neutron source in the presence of a gamma background it is necessary to understand the effect of signal contamination on the efficiencies and purities. Signal contamination is the process of supplementing the neutron source (PuBe) with different levels of gamma (^{60}Co) events.

Due to the requirements imposed on the system we can estimate the gamma background rate at the detectors. The minimum gamma dose rate for detection at 1 m distance is 0.05 μSv/h, which is equivalent to a source of ∼160 kBq activity. This

translates to a gamma flux at of $\phi_\gamma = 25.4 \times 10^3$ $\gamma \mathrm{m}^{-2}\mathrm{s}^{-1}$ at 1 m from the source, which is independent of whether the system is in stationary or mobile detection mode. If we define this value as the upper limit for the background rate then we can define the contamination rate relative to the neutron flux.

The minimum neutron flux required for detection is defined as $\phi_n^s = 0.4 \times 10^3$ neutrons $\mathrm{m}^{-2}\mathrm{s}^{-1}$ and $\phi_n^m = 0.94 \times 10^3$ neutrons $\mathrm{m}^{-2}\mathrm{s}^{-1}$ for stationary and motion detection modes at 1 m from the source respectively. Considering the neutron and gamma peak emission is around 1 MeV we take a constant cross section for neutrons at 1 MeV of $\sigma_{n\to He}$ ∼0.2 m^2 kg^{-1} and $\sigma_{\gamma\to He}$ ∼0.01 m^2 kg^{-1} for γ's at the same energy, as a rough estimate. Thus the ratio of cross sections is $\sigma_{n\to He}/\sigma_{\gamma\to He}$ ∼20. The γ contamination level is then given by $\delta = N_\gamma/(N_n + N_\gamma) = \phi_n\sigma_{n\to He}/(\phi_n\sigma_{n\to He} + \phi_\gamma\sigma_{\gamma\to He})$. For mobile neutron detection this corresponds to a level $\delta^m = 57.5\%$ gamma contamination with it increasing to $\delta^s = 76.0\%$ for stationary neutron detection.

Through choice of an average sample size, $\bar{n}$, we establish the number of neutron events per experiment as $N_n = n - N_\gamma$, where both n and N_γ are taken from a Poisson distribution with mean values of $\bar{n}$ and $\bar{n}\delta$ respectively. Both n and N_γ are also determined per experiment, where the former represents the total number of contaminated events and the latter representing the number of gamma events for a signal experiment. Conversely the background experiments contain only gamma events, hence assuming a zero neutron contamination level.

Taking N_n events from the PuBe data set and N_γ events from the ^{60}Co data set per experiment, for 1×10^5 experiments, we then estimate the neutron detection efficiency and the gamma misidentification efficiencies as a function of the average number of contaminated events, $\bar{n}$. Both N_γ and N_n are determined on a tube basis, as the same number of neutrons and gammas interact within one tube, but PSD values are taken on a channel basis to avoid differences in channel parameters such as PMT voltage. Again all 8 channels are combined using equation 9.5. The left of figure 9.22 shows the neutron detection efficiency as a function of $\bar{n}$ and with the right of figure 9.22 showing the misidentification efficiencies also a function of $\bar{n}$.

At a 2 second exposure we can expect to achieve $\bar{n}^s$ ∼116 and $\bar{n}^m$ ∼154 for stationary and motion detection modes respectively. For a 3 second exposure these increase to $\bar{n}^s$ ∼174 and $\bar{n}^m$ ∼231. Since motion detection has a lower contamination level it therefore achieves better efficiencies and yields higher statistics when compared to the stationary detection mode. For motion detection at a 3 second exposure we can expect to achieve a neutron detection efficiency of $\epsilon_{sig} = 1.00000 \pm 0.00001$ with a misidenti-

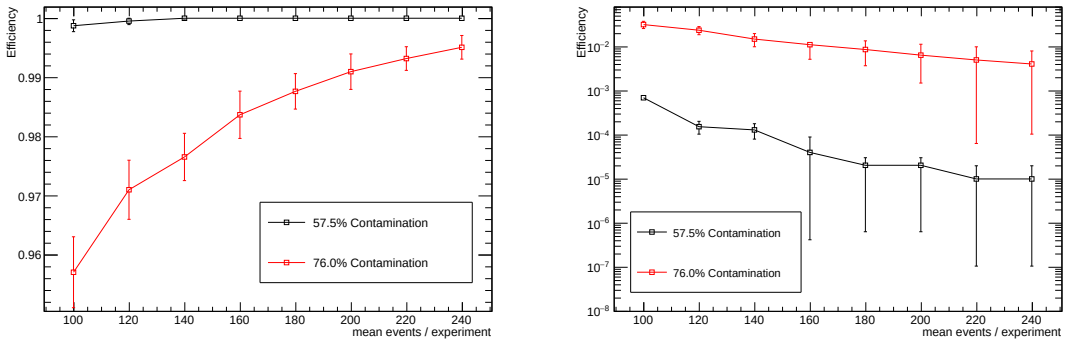

Fig. 9.22 Left: The neutron detection efficiencies as a function of the mean number of events per experiment. Right: The misidentification efficiencies as a function the mean number of events per experiment. Both show efficiencies for 57.5% (black line) and 76.0% (red line) levels of contamination corresponding to motion and stationary detection modes respectively.

fication efficiency of $\epsilon_{bkg} = (1.0 \pm 0.1 \times)\ 10^{-5}$. Although the impact of reducing the exposure to 2 seconds only slightly reduces the efficiencies to $\epsilon_{sig} = 0.9999^{+0.0001}_{-0.0003}$ and $\epsilon_{bkg} = (1.5 \pm 0.1) \times 10^{-5}$. For stationary detection however the efficiencies are worse with $\epsilon_{sig} = 0.988 \pm 0.003$ and $\epsilon_{bkg} = 0.009 \pm 0.004$ for a 3 second exposure, with $\epsilon_{sig} = 0.967 \pm 0.005$ and $\epsilon_{bkg} = 0.023 \pm 0.006$ for a 2 second exposure.

Due to requirements imposed on the system, the false alarm rate should not exceed 1 per hour, we can estimate how this translates to the misidentification efficiencies. We assume that per period of exposure of T seconds, $\bar{n}$ events are accumulated, which then translates to 1 experiment. The resultant PSD value of this 1 experiment will then either pass or fail the PSD selection, hence we have $k = 60^2\epsilon_{bkg}/T$, false alarms in one hour due to γ's misidentified as neutrons. For motion detection this equates to 0.012 ± 0.001 and 0.027 ± 0.002 false neutron alarms per hour for 3 and 2 second exposures respectively. However for stationary detection we exceed the required rate with much higher rate of 11 ± 5 and 41 ± 11 false neutron alarms per hour for 3 and 2 second exposures respectively. Although for stationary detection the exposure period can well exceed 2/3 s periods and so higher statistics and better efficiencies can be achieved. Increasing the period to T= 6 s, ϵ_{bkg} is reduced to 0.0010 ± 0.0005, which then passes the requirement by achieving a false alarm rate of 0.6 ± 0.3 per hour.

We can conclude that the presented analysis demonstrates that n-γ discrimination can be performed with the MODES-SNM system while maintaining the imposed detector requirements. Although these conclusions have been drawn from using a single

^{60}Co source, the analysis has been formed in such a way as to make it independent of the source, given that other γ sources with similar energy spectra could be used to produce similar results. However some assumptions have been made in the process with the approximations used on the expected number of interactions based on estimates of source activities. The corresponding activity of ^{60}Co was used as the upper background estimation, given that the minimum gamma detection should be 0.05/h μSv at 1 m from the source. This activity would translate differently for other similar gamma sources and it would be interesting to perform a similar analysis on sources such as ^{137}Cs and ^{241}Am to examine if the results still hold. A limiting factor on the analysis was the amount of data provided, given that I was not present for data collection and time was heavily restricted for testing. It must also be noted that these results are based on only 4 out of the possible 8 fast neutron detectors and it would of been also interesting to study the different effects of the detector array arrangement.

Chapter 10

Conclusions and Outlook

This thesis has been comprised of two independent sections with one underlying and unifying theme, neutral particle detection in noble gases. In the first two chapters we introduced how neutral particles, particularly neutrinos, neutrons and photons can be detected by means of noble gases and discussed the benefits of using them while also exploring the technical feats that must be overcome to make them viable detection mediums.

Chapters 3 to 5 presented the LAGUNA-LBNO project, proposed as the next generation long baseline neutrino experiment in Europe, with the focus on the near detector. The design, simulation and evaluation of a newly proposed near detector design was performed using a bespoke software framework encompassing several Monte Carlo packages. With this being the initial study of the near detector, previous studies on such a detector did not exist, and due to this a lot of the preliminary and base work was covered within this thesis. Loosely based on the T2K ND280 detector, we were able to use similar parameters to help in the design. From the results of several Monte Carlo studies we have managed to quantify the basic detector capabilities and set the path for future detectors of similar design. We have shown for a TPC of $2 \times 2 \times 2$ m^3 at 20 bar the expected number of neutrino interactions is 0.1785 ± 0.0003 p.p.p for the 400 GeV in positive focusing. Considering only ν_μ with energies of 10 GeV and less, within a fiducial volume at $1.8 \times 1.8 \times 1.8$ m^3, this is reduced to 0.0628 ± 0.0002 p.p.p for the same beam. CCQE interactions are then 0.00779 ± 0.00007 ν_μ p.p.p for the same selection.

Background rates were also heavily examined in the ND design studies, with μ's the particles of biggest concern we found that 44.5 ± 0.5 p.p.p for the 400 GeV in positive focusing were reaching/passing the TPC due to interactions from outside the TPC.

Although they contribute to only 14.5% of the total particles entering the TPC from background interactions, they pose the largest threat to pileup with energies similar to that expected from interactions within the TPC. It was shown that 75.6% of these arise due to rock interactions are therefore hard to minimise, however when compared to the number arising from the beam (punch through muons) their contribution is smaller at 36.7% compared to the 61.1% of beam muons at 70 p.p.p. Thus with $\sim$1/2 μ tracks/ m^2 / μs and drift times of $\sim$100 μs, pile up is unavoidable but manageable assuming the vertex can be resolved to within $\sim$1 μ tracks/ 700 cm^2 / spill.

Ultimately a pressurised GAr TPC ND design will not achieve the requirements of the LAGUNA-LBNO proposal using current technologies. With a required signal event normalisation uncertainty of 3% a first order analysis using only the final state μ indicates that this is not achievable, estimating an uncertainty at 3.8%. The difficulty with the presented design is primarily due to the high number of DIS events expected at that TPC, 50.3% of CC interactions, due to the high energy beam where large amounts of energy are lost to neutrons and π^0s. The main benefit of the GAr medium with its great track and position reconstruction capabilities, due to the high granularity of the detector, is then lost due to the energy lost to neutral particles.

Overall with the main aim of the project to determine the mass hierarchy of the neutrinos to beyond the 5σ threshold, other ND detector designs should be considered if this is to be achieved. However at the time of writing, the continuation of the LAGUNA-LBNO project has been halted due to economical and political reasons, with costs expected to exceed the 100 million EUR estimate. It is important to note that Liverpool University and myself drove the ND design and created initial discussions on its requirements. I played a large role in the design and the study has led to interesting work within the neutrino community, paving the way for other very long baseline neutrino experiments, with LBNX becoming the focus of future neutrino experiments. The software framework created largely by myself can then be used for these future designs and take the information gained from this investigation to design an improved ND for high energy, broad spectrum beams.

Chapters 6 to 9 presented the MODES-SNM project which discussed a new and novel way of detecting nuclear radiation, neutrons and gammas, in a portable manner. From the conceptual design of using pressurised ^{4}He gas, instead of the conventionally used ^{3}He, right through to the construction and testing of a fully working prototype, we have shown that the MODES-SNM system can be used in the combat against radionuclide trafficking.

We have shown that both gamma and neutron radiation sources can be detected with successful identification of the gamma sources: ^{60}Co, ^{241}Am, and ^{133}Ba while in both stationary and motion detection modes. Other gamma sources have been identified in laboratory conditions with AmBe, Pu and ^{252}Cf neutron sources being detected successfully even upon shielding. Real life demonstrations have also showed promising results with many end users interested in the potential of the MODES-SNM prototype.

We have presented a new analysis to be used to discriminate between neutrons and γ's showing that even in high levels of gamma contamination (up to 76%) we can achieve higher than required detection efficiencies, exceeding 96%, while maintaining reasonable false alarm rates (< 1 per hour).

The MODES-SNM prototype has paved the way to becoming a new commercial system that could be a very competitive alternative to current systems, with it showing lower false alarm rates with cheaper costs due to the rising costs of ^{3}He. The MODES-SNM collaboration has been largely successful and a great achievement considering we managed to deliver a working prototype on time and to budget.

References

[1] A. Bernstein *et al.*, "Nuclear reactor safeguards and monitoring with antineutrino detectors," *J. Appl. Phys.*, vol. 91, 2002.

[2] G. Viesti, "Modes-snm: http://www.modes-snm.eu," January 2012.

[3] M. Planck, "Ueber das gesetz der energieverteilung im normalspectrum," *Annalen der Physik*, vol. 309, pp. 553–563, 1901.

[4] A. Einstein, "Über einen die erzeugung und verwandlung des lichtes betreffenden heuristischen gesichtspunkt," *Annalen der Physik*, vol. 322, pp. 132–148, 1905.

[5] A. Einstein, "Über die entwicklung unserer anschauungen über das wesen und die konstitution der strahlung," *Physikalische Zeitschrift*, vol. 10, pp. 817–825, 1909.

[6] A. H. Compton, "A quantum theory of the scattering of x-rays by light elements," *Physical Review*, vol. 21, pp. 483–502, 1923.

[7] G. N. Lewis, "The conservation of photons," *Nature*, vol. 118, pp. 874–875, 1926.

[8] G. F. Knoll, *Radiation Detection and Measurement*. John Wiley & Sons, 1999.

[9] E. Aprile, A. Bolotnikov, A. Bolozdynya, and T. Doke, *Noble Gas Detectors*. Wiley-VCH, 2006.

[10] *Bakerian Lecture: Nuclear Constitution of Atoms*, Proceedings of the Royal Society, 1920.

[11] V. Ambartsumian and D. Ivanenko, "Les electrons inobservables et les rayons," *Compt. Rend. Acad Sci. Paris*, vol. 190, p. 582, 1930.

[12] J. Chadwick, "Possible Existence of a Neutron," *Nature*, vol. 129, p. 312, 1932.

[13] A. B. Smith, P. R. Fields, and J. H. Roberts, "Spontaneous fission neutron spectrum of ^{252}Cf," *Physical Review*, vol. 108, no. 2, 1957.

[14] F. Scott, "Energy Spectrum of the Beta-Rays of Radium E," *Phys. Rev*, vol. 48, pp. 391–395, 1935.

[15] C. Cowan *et al.*, "Detection of the free neutrino: A confirmation," *Science*, vol. 124, p. 103, 1956.

[16] G. Dandy *et al.*, "Observation of High-Energy Neutrino Reactions and the Existence of Two Kinds of Neutrinos," *Phys. Rev. Lett*, vol. 9, pp. 36–44, 1962.

[17] DONUT Collaboration, "Observation of Tau Neutrino Interactions," *Phys. Lett. B*, vol. 504, pp. 218–224, 2001.

[18] R. Davis, D. S. Harmer, and K. Hoffman, "Search for neutrinos from the Sun," *Phys. Rev. Lett*, vol. 20, pp. 1205–1209, 1968.

[19] Q. R. Ahmed *et al.*, "Measurement of the rate of interactions produced by ^{8}B solar neutrinos at the Sudbury Neutrino Observatory," *Phys. Rev. Lett.*, vol. 87, no. 071301, 2001.

[20] S. Schael *et al. Phys. Rept.*, vol. 427, pp. 257–454, 2006.

[21] B.Pontecorvo *Zh.Eksp.Teor.Fiz*, vol. 33, no. 549, 1957.

[22] C. Guinti and C. W. Kim, *Fundamentals of Neutrino Physics and Astrophysics.* Oxford University Press, 2007.

[23] G. Christodoulou, *A measurement of the electron neutrino component in the T2K beam using the tracker detectors and the electromagnetic calorimeter at the near detector ND280.* PhD thesis, University of Liverpool, 2011.

[24] L. Wolfenstein, "Neutrino oscillations in matter," *Physical Review*, vol. D17, pp. 2369–2374, 1978.

[25] S. P. Mikheev and A. Y. Smirnov, "Precision electroweak measurements on the z resonance," *Sov. J. Nucl. Phys.*, vol. 42, pp. 913–917, 1985.

[26] S. K. Raut, R. S. Singh, and S. U. Sankar, "Magical properties of 2540 km baseline Superbeam Experiment," *arXiv:0908.3741v1*, 2009.

[27] *T2K ND280 Conceptual Design Report (T2K internal document)*, 2005.

[28] T. Schwetz, M. Tortola, and J. W. F. Valle, "Global neutrino data and recent reactor fluxes: status of three-flavour oscillation parameters," *arXiv:1103.0734v2*, 2011.

[29] V. Barger, D. Marfatia, and K. Whisnant, "Observation of electron-antineutrino disappearance at Daya Bay," *Phys. Rev.*, vol. D65, no. 073023, 2012.

[30] K. Abe and others (T2K Collaboration), "Indication of electron neutrino appearance from an accelerator-produced off-axis muon neutrino beam," *Phys. Rev. Lett.*, vol. 107, no. 041801, 2011.

[31] S. Agostinelli *et al.*, "Observation of reactor electron antineutrino disappearance in the reno experiment," *arXiv:1204.0626v2*, 2012.

[32] G. Fogli, E. Lisi, A. Marrone, D. Montanino, A. Palazzo, and A. Rotunno, "Global analysis of neutrino masses, mixings, and phases: Entering the era of leptonic CP violation searches," *Phys. Rev. D*, vol. 86, p. 013012, Jul 2012.

[33] S. Petcov and M. Piai, "The LMA MSW solution of the solar neutrino problem, inverted neutrino mass hierarchy and reactor neutrino experiments," *Physics Letters B*, vol. 533, pp. 94–106, 2002.

[34] C. Kraus *et al.*, "Final results from phase ii of the mainz neutrino mass search in tritium β decay," *Eur. Phys. J*, vol. C40, pp. 447–468, 2005.

[35] J. A. Formaggio and G. Zeller, "From eV to EeV: Neutrino cross sections across energy scales," *Rev. Mod. Phys.*, vol. 84, pp. 1307–1341, Sep 2012.

[36] J. N. Bahcall and C. Pena-Garay, "Solar models and solar neutrino oscillations," *New J. Phys.*, vol. 6, 2004.

[37] C. Walter, "The super-kamiokande experiment," *arXiv:0802.1041*, 2008.

[38] D. Vignaud, "The GALLEX solar neutrino experiment," *Nuclear Physics B - Proceedings Supplements*, vol. 60, no. 3, pp. 20 – 29, 1998.

[39] J. Abdurashitov *et al.*, "Measurement of the solar neutrino capture rate with gallium metal," *Phys. Rev. C*, vol. 60, p. 055801, Oct 1999.

[40] N. Ferrari, S. d'Angelo, W. Hampel, K. Ebert, and G. Cerichelli, "GALLIUM NEUTRINO OBSERVATORY,"

[41] J. Boger *et al.*, "The sudbury neutrino observatory," *Nuclear Instruments and Methods in Physics Research Section A: Accelerators, Spectrometers, Detectors and Associated Equipment*, vol. 449, no. 1–2, pp. 172 – 207, 2000.

[42] C. Amsler and others (Particle Data Group), "Particle listings - $\pi^{\pm}$," *Physics Letters*, vol. B667, 2008.

[43] R. Becker-Szendy *et al.*, "The electron-neutrino and muon-neutrino content of the atmospheric flux," *Phys. Rev.*, vol. D46, pp. 3720–3724, 1992.

[44] D. B. Collaboration, "A precision measurement of the neutrino mixing angle θ_{13} using reactor antineutrinos at daya bay," *arxiv:hep-ex/0701029v1*, 2007.

[45] J. K. Ahn *et al.*, "Observation of reactor electron antineutrinos disappearance in the reno experiment," *Phys. Rev. Lett.*, vol. 108, p. 191802, May 2012.

[46] Y. Abe *et al.*, "Indication of reactor $\overline{\nu}_e$ disappearance in the double chooz experiment," *Phys. Rev. Lett.*, vol. 108, p. 131801, Mar 2012.

[47] The T2K Collaboration, "The T2K Experiment," *Nuclear Instruments and Methods in Physics Research Section A: Accelerators, Spectrometers, Detectors and Associated Equipment*, vol. 659, pp. 106–135, 2011.

[48] M. Ahn *et al.*, "Measurement of neutrino oscillation by the k2k experiment," *Phys. Rev. D*, vol. 74, p. 072003, Oct 2006.

[49] J. Evans, "The minos experiment: results and prospects," *arXiv:1307.0721*, 2013.

[50] R. Patterson, "The NOvA Experiment: Status and Outlook," *Nucl.Phys.Proc.Suppl.*, vol. 235-236, pp. 151–157, 2013.

[51] M. Titov, "Gaseous detectors: recent developments and applications," *arXiv:1008.3736*, 2010.

[52] C. Amsler and others (Particle Data Group), "Review of Particle Physics," *Physics Letters B*, vol. 667, 2008.

[53] National Weather Service, "The atmosphere." `http://www.srh.noaa.gov/jetstream//atmos/atmos_intro.htm`. Accessed: 2014-08-26.

[54] R. Betzendahl, "Rare gases: A fast growing global commodity." `http://bgcspecgas.com/media/Rare$20Gases$20Supply$20$26$20Demand$206-07.pdf`. Accessed: 2015-06-21.

[55] J. Emsley, *Natures Building Blocks*. Oxford University Press, 2001.

[56] W. Blum, W. Riegler, and L. Rolandi, *Particle Detection with Drift Chambers*. Springer, 2008.

[57] G. Charpak *et al. Nucl. Instrum. Methods*, vol. 262, 1968.

[58] A. Grün and E. Schopper *Naturforsch*, vol. 6A, 1951.

[59] *MODES−SNM internal collaboration - Deliverable*, 2014.

[60] T. Patzak, "Laguna-lbno: Large apparatus studying grand unification and neutrino astrophysics and long baseline neutrino oscillations," *J. Phys. Conf. Ser.*, vol. 375, 2012.

[61] A. Badertscher *et al.*, "Giant Liquid Argon Observatory for Proton Decay, Neutrino Astrophysics and CP-violation in the lepton sector (GLACIER)," *arXiv:1001.0076v1*, 2009.

[62] A. de Bellefon *et al.*, "MEMPHYS: A large scale water Cerenkov detector at Frejus," *arXiv:0607026v1*, 2006.

[63] M. Wurm *et al.*, "The next-generation liquid-scintillator neutrino observatory LENA," *arXiv:11045620v3*, 2012.

[64] The LAGUNA consortium, "Expression of interest for a very long baseline neutrino oscillation experiment (LBNO)," 2012.

[65] *LAGUNA−LBNO internal document*, 2013.

[66] J. Beringer and others (Particle Data Group) *Phys. Rev.*, vol. D86, 2012.

[67] CERN, "Cern beam complex." `http://cern-accelerators-optics.web.cern.ch/cern-accelerators-optics`. Accessed: 2014-08-20.

[68] D. J. Blundell, R. Freeman, and S. Mueller, *A Continent Revealed: The European Geotraverse, Structure and Dynamic Evolution.* Cambridge University Press, 1992.

[69] A. Ferrari, R. P. Sala, A. Fassò, and J. Ranft, *FLUKA : A multi-particle transport code.* Geneva, 2005.

[70] A. Curioni, E. Noah, Y. Karadzhov, and T. Stainer, "LBNO Near Detector Description - Technical Note," 2013.

[71] *LAGUNA−LBNO internal presentation*, 2013.

[72] R. Gluckstern, "Uncertainties in track momentum and direction, due to multiple scattering and measurement errors," *Nuclear Instruments and Methods*, vol. 24, no. 0, pp. 381 – 389, 1963.

[73] C. Andreopoulos *et al.*, "The GENIE Neutrino Monte Carlo Generator," *Nucl. Instrum. Meth.*, vol. A614, pp. 87–104, 2010.

[74] R. Gilgen, R. Kleinrahm, and W. Wagner, "Measurement and correlation of the (pressure, density, temperature) relation of argon i. the homogeneous gas and liquid regions in the temperature range from 90 k to 340 k at pressures up to 12 mpa," *Journal of Chemical Thermodynamics*, vol. 26, pp. 383–398, 1994.

[75] S. Agostinelli *et al.*, "Geant4 - a simulation toolkit," *Nuclear Instruments and Methods in Physics Research Section A: Accelerators, Spectrometers, Detectors and Associated Equipment*, vol. 506, pp. 250–303, 2003.

[76] C. L. Smith, "Neutrino Reactions at Accelerator Energies," *Phys.Rept.*, vol. 3, pp. 261–379, 1972.

[77] A. Bodek and U. K. Yang, "Higher twist, ξ_ω scaling, and effective LO PDFs for lepton scattering in the few GeV region," *J. Phys.*, vol. G29, pp. 1899–1906, 2003.

[78] D. Rein and L. Sehgal, "PCAC and the Deficit of Forward Muons in π^+ Production by Neutrinos," *Phys.Lett.*, vol. B657, pp. 207–209, 2007.

[79] D. Rein and L. Sehgal, "Neutrino-excitation of baryon resonances and single pion production," *Ann. Phys.*, vol. 133, pp. 79–153, 1981.

[80] "Geant4 physics reference manual." `http://geant4.web.cern.ch/geant4/UserDocumentation/UsersGuides/PhysicsReferenceManual/BackupVersions/V10.0/fo/PhysicsReferenceManual.pdf`. Accessed: 2014-08-25.

[81] R. Brun and F. Rademakers, "ROOT - An Object Oriented Data Analysis Framework," *Nuclear Instruments and Methods in Physics Research Section A: Accelerators, Spectrometers, Detectors and Associated Equipment*, vol. 389, pp. 81–86, 1997.

[82] K. A. Olive *et al.*, "Review of Particle Physics," *Chin. Phys.*, vol. C38, p. 090001, 2014.

[83] W. P. R. Chytracek, J. McCormick and G. Santin, "Geometry Description Markup Language for Physics Simulation and Analysis Applications," *IEEE Trans. Nucl. Sci.*, vol. 53, pp. 2892–2896.

[84] N. Abgrall *et al.*, "Time projection chambers for the T2K near detectors," *Nuclear Instruments and Methods in Physics Research Section A: Accelerators, Spectrometers, Detectors and Associated Equipment*, vol. 637, no. 1, pp. 25 – 46, 2011.

[85] M. Buhler-Broglin *et al.*, "General description of the CERN project for a neutrino beam to Gran Sasso (CNGS)," *CERN AC Note*, 2000.

[86] M. Berger *et al.*, "Xcom: Photon cross sections database." `http://physics.nist.gov/PhysRefData/Xcom/html/xcom1.html`. Accessed: 2014-07-21.

[87] K. Abe *et al.*, "Measurement of the ν_μ CCQE cross section on carbon with the ND280 detector at T2K," 2014.

[88] S. K. Agarwalla *et al.*, "The LBNO long-baseline oscillation sensitivities with two conventional neutrino beams at different baselines," 2014.

[89] IAEA, "Detection of radioactive materials at borders (technical document)," 2002.

[90] M. Chadwick, M. Herman, P. Obložinský, *et al.*, "ENDF/B-VII.1 nuclear data for science and technology: Cross sections, covariances, fission product yields and decay data," *Nuclear Data Sheets*, vol. 112, no. 12, pp. 2887 – 2996, 2011. Special Issue on ENDF/B-VII.1 Library.

[91] J. Ely *et al.*, "The use of energy windowing to discriminate snm from norm in radiation portal monitors," *Nuclear Instruments and Methods in Physics Research Section A: Accelerators, Spectrometers, Detectors and Associated Equipment*, vol. 560, pp. 373–387, 2006.

[92] R. T. Kouzes and E. R. Siciliano, "The response of radiation portal monitors to medical radionuclides at border crossings," *Radiation Measurements*, vol. 41, pp. 499–512, 2006.

[93] D. A. Shea and D. Morgan, "The helium-3 shortage: Supply, demand, and options for congress," *Congressional Research Service*, 2010.

[94] R. Chandra *et al.*, "Fast neutron detection with pressurized ^{4}He scintillation detectors," *Journal of Instrumentation*, 2012.

[95] IEC, "Radiation protection instrumentation installed radiation monitors for the detection of radioactive and special nuclear materials at national borders," *INTERNATIONAL STANDARD IEC 62244*, 2006.

[96] D. Gilliam, S. Leigh, A. Rukhin, and W. Strawderman, "Pass-fail testing: Statistical requirements and interpretations," *Journal of Research of the National Institute of Standards and Technology*, vol. 114, no. 3, 2009.

[97] F. Resnati *et al.*, "Suitability of high-pressure xenon as scintillator for gamma ray spectroscopy," *arXiv:1212.4050*, 2012.

[98] A. Bolotnikov and B. Ramsey, "The spectroscopic properties of high-pressure xenon," *Nucl. Instr. and Meth.*, vol. 396, pp. 360–370, 1997.

[99] Hamamatsu, "Photomultiplier tube r580." `http://www.hamamatsu.com/us/en/R580.html`. Accessed: 2014-07-23.

[100] Heathrow Airport, "Heathrow statistics page." `http://www.heathrowairport.com/about-us/investor-centre/results-and-performance/traffic-statistics`. Accessed: 2014-06-30.

[101] Flir, "identifinder technical data." `http://gs.flir.com/uploads/file/products/data-sheets/DS-identiFINDER2-en.pdf`. Accessed: 2014-06-30.

[102] "Port statistics 2014." `https://www.portofrotterdam.com/en/the-port/port-facts-and-figures`. Accessed: 2015-07-04.

[103] Federal Office of Public Health FOPH, "Radon risk in switzerland." `http://www.bag.admin.ch/themen/strahlung/00046/11952/index.html?lang=en`. Accessed: 2014-08-12.